eman ta zabal zazu

Universidad del País Vasco

Euskal Herriko Unibertsitatea

Facultad de Medicina y Enfermería

Departamento de Neurociencias

Exploring pro-resolution mediator ATL and complement receptor CR3 as potential therapeutic targets for Alzheimer's disease

Tesis doctoral para optar al grado de Doctor, presentada por:

Celia Luchena Moreno

2022

Directoras de tesis:

Dra. Estibaliz Capetillo González de Zarate y Dra. Elena Alberdi Alfonso

Esta tesis doctoral ha sido realizada gracias a una beca de contratación para la realización de tesis doctorales en neurociencias de la Fundación Tatiana Pérez de Guzmán el Bueno (Madrid, España) durante el periodo 2017-2022.

El trabajo experimental ha sido financiado por el Centro de Investigación Biomédica en Red de Enfermedades Neurodegenerativas (CIBERNED), proyectos del Ministerio de Economía y Competitividad (SAF2016-7592-R), proyectos de grupos consolidados del Gobierno Vasco (IT02-13) y proyectos ELKARTEK: Ayudas a la investigación colaborativa en áreas estratégicas (KK2017/00067, KK2019/00058 y KK2020/00034) y proyectos de Investigación Básica y/o Aplicada (PI-2016-1-0009).

Agradecimientos

Esta tesis doctoral es el resultado de más de cuatro años de esfuerzo y aprendizaje que no habrían sido posibles sin la ayuda de mis supervisoras, mi familia y mis compañeros. Ha sido un largo viaje, con sus altos y sus bajos, pero también una aventura preciosa.

En primer lugar, me gustaría agradecer a mis directoras de tesis, Esti y Elena. He tenido la inmensa suerte de tener, no sólo una, sino dos mujeres científicas como mentoras. Dos mujeres amables y brillantes que siempre van a ser referentes para mí. Gracias a Elena, por tu apoyo y ayuda durante estos años, y por transmitirme tu pasión por la ciencia. Y un millón de gracias a Esti, por tu generosidad y por confiar en mí cuando sólo era una estudiante de biología que apenas sabía manejar una pipeta. Siempre me has hecho sentir valorada y me has animado a expresar mis ideas y a mejorar cada día.

En segundo lugar, tengo que agradecer a la Fundación Tatiana Pérez de Guzmán el Bueno por financiar mi trabajo. He tenido la inmensa suerte de poder contar con su apoyo económico, que me ha permitido comenzar mi carrera profesional como investigadora. Me han tratado de forma muy amable y cercana, y siempre han intentado mejorar las condiciones de todos sus becarios.

Gracias a todo el Laboratorio de Neurobiología y a nuestro director Carlos Matute. Valoro mucho tus ideas y tus consejos, y me siento muy afortunada de haber podido formar parte de esta gran familia. Por supuesto, también a todos los miembros veteranos del grupo: Vicky Sánchez, María Domercq, Susana Mato, Vanja Tepavcevic, Asier Ruiz, Fabio Cavaliere, Federico Soria, Fernando Pérez y Alberto Pérez. Gracias a todos por recibirme con los brazos abiertos y siempre estar dispuestos a ofrecer vuestros conocimientos y vuestra ayuda. Por supuesto, gracias también a las técnicos de laboratorio Ainara Martínez y Zara Martínez, cuyo trabajo ha sido y es fundamental para que nuestra gran familia funcione. También me gustaría agradecer a todo el centro Achucarro Basque Center for Neuroscience, que ha sido mi casa durante todo este tiempo, y en especial a Laura Escobar por su infinita paciencia y su sentido del humor.

I would also like to thank Michael T. Heneka, who kindly welcomed me in his laboratory at the DZNE Center in Bonn (Germany) for three months, and Francesco Santarelli and Christina Ising, who helped me a lot.

Durante esta etapa he tenido la oportunidad de conocer a muchas compañeras y compañeros de los que me llevo muy buenos recuerdos. Compañeras como Jone Zuazo, que me ayudó desde el principio a instalarme en un ambiente que era completamente nuevo para mí, y como Raffaela Cipriani, con la que he compartido trabajo, cafés y conversaciones. También Maialen Martínez, a la que he intentado enseñar lo mejor que he podido, y a la que deseo toda la suerte del mundo. Y, por supuesto, Fátima Zallo, a la que voy a estar eternamente agradecida por hacerme mucho más llevadero el último año de tesis con sus consejos y sus risas. Muchas gracias a todas. Por otro lado, tengo que mencionar a todos los inmigrantes sureños y no tan sureños que nos mudamos a Vizcaya para disfrutar de su cultura y sus paisajes, aunque no tanto de su clima. María Ardaya, Ana Palma, Alejandro Montilla, Álvaro Moreno, Laura Bayón, Teresa Colomer y Juan Carlos Chara; gracias por los buenos ratos.

Thank you Ali, for your love, your optimism and your support. Thanks for broadening my horizons and helping me fight my own prejudice.

Por último, y precisamente más importante, quiero agradecer a mi familia. A mis padres Valentina y Vicente, por darme la vida, por educarme y por seguir guiándome cada día. Espero que estéis orgullosos de mí. Os quiero mucho.

«…Malditas sean las guerras y los canallas que las hacen.»

Don Julio Anguita González (1941-2020)

Para mi abuela Dolores.

El Alzheimer se llevó tus recuerdos,

pero no pudo con tu sentido del humor.

(1928-2017)

Table of content

Abbreviations

5-, 12-, 15-LOX	5-, 12-, 15-lipoxygenase.
15-HPETE	15-hydroxyperoxyeicosatetraenoic acid.
3xTg	Triple transgenic mouse model of Alzheimer's disease.
AD	Alzheimer's disease.
AGER, RAGE	Receptor for Advanced Glycosylation End-products.
AICD	APP Intracellular Domain.
ALX/FPR2	Formyl Peptide Receptor-2.
AMIGO2	Adhesion molecule with Ig like domain 2.
ANOVA	Analysis of variance.
APOE	Apolipoprotein E.
APP	Amyloid Precursor Protein.
ArgI	Arginase I.
ASC	Apoptosis-associated Speck-like Protein containing a Caspase recruitment domain.
ATL	5(S),6(R),15(R)-trihydroxy-7,9,13-trans-11-cis-eicosatetraenoic acid, aspirin-triggered 15-epi-lipoxin A_4.
ATP	Adenosine triphosphate production-linked oxygen consumption rate.
A.u.	Arbitrary units.
Aβ	Amyloid β peptide.
BBB	Blood-brain barrier.
BR	Basal respiration.
BSA	Bovine serum albumin.
CAA	Cerebral amyloid angiopathy.
COX-2	Cyclooxygenase-2.
CM-H2DCFDA	5,6-chloromethyl-2'7dichlorodihydrofluorescein diacetate acetyl ester.
CNS	Central nervous system.
CR3	Complement Receptor 3.
CSF	Cerebrospinal fluid.

CSF1R	Colony-Stimulating Factor 1 Receptor.
Ct	Cycle threshold.
ddH_2O	Double distilled water.
DIV	Days *in vitro*.
DMEM	Dulbecco's modified Eagle medium.
DMSO	Anhydrous dimethylsulfoxide.
DPI	Diphenylene iodonium chloride.
DRP1	Dynamin-Related Protein 1.
EDTA	Ethylenediamine tetraacetic acid.
ELISA	Enzyme-linked immunosorbent assay.
EOAD	Early-onset Alzheimer's disease.
FBS	Fetal bovine serum.
FCCP	Carbonyl cyanide-p-trifluoromethoxyphenyl-hydrazone.
FDA	Food and Drug Administration.
FdU/U	5-fluoro-2′-deoxyuridine and Uridine.
Fis1	Mitochondrial fission 1 protein.
GAPDH	Glyceraldehyde-3-phosphate dehydrogenase.
GFAP	Glial Fibrillary Acidic Protein.
GM-CSF	Granulocyte-Macrophage Colony-Stimulating Factor.
GSSG	Oxidized glutathione.
GSH	Reduced glutathione.
HBSS	Hanks' balanced salts.
HFIP	Hexafluoroisopropanol.
Homer1	Homer scaffold protein 1.
HRP	Horseradish peroxidase.
HS	Horse serum.
ICC	Immunocytochemistry.
IDE	Insulin Degrading Enzyme.
IFN-γ	Interferon-γ.
IHC	Immunohistochemistry.

IL-1β	Interleukin-1β.
IMDM	Iscove's modified Dubecco's medium.
iNOS	Inducible Nitric Oxide Synthase.
iPSC	Induced pluripotent stem cell.
IRF8	Interferon Regulatory Factor 8.
kDa	Kilodaltons.
LAMP1	Lysosomal Associated Membrane Protein 1.
LOAD	Late-onset Alzheimer's disease.
LPS	Lipopolysaccharide.
LTP	Long-term potentiation.
LXA_4	Lipoxin A_4.
LXB_4	Lipoxin B_4.
MAC	Membrane Attack Complex.
MAP2	Microtubule-Associated Protein 2.
MAPT	Microtubule-Associated Protein Tau.
MCM	Microglia conditioned medium.
M-CSF	Macrophage Colony-Stimulating Factor.
MFN1, 2	Mitofusin-1, -2.
MIDAS	Metal Ion-Dependent Adhesion Site.
MMP	Matrix metalloproteinase.
MMSE	Mini-mental state examination.
MRC1	Mannose Receptor C-type 1.
MSR1	Macrophage Scavenger Receptor 1.
MUR	Maximal respiratory capacity.
NADPH	Nicotinamide adenine dinucleotide phosphate.
NCM	Neuron conditioned medium.
NGS	Normal goat serum.
NLRP3	Nucleotide-binding Domain-Like Receptor Protein 3.
NMDAR	N-Methyl-D-Aspartate Receptor.
NOX2	Nicotinamide adenine dinucleotide phosphate oxidase 2.

oAβ	Oligomeric Amyloid β_{1-42}.
OCR	Oxygen consumption rate.
OPA1	Optic Atrophy Protein 1.
PBS	Phosphate-buffered saline.
PDL	Poly-D-lysine.
PET	Positron emission tomography.
PFA	Paraformaldehyde.
PI	Propidium iodide.
PiB	Pittsburgh compound B.
PL	Proton leak.
PLAT	Tissue plasminogen activator.
PSEN-1, -2	Presenilin 1 and 2.
PSD-95	Post-Synaptic Density protein 95.
ROS	Reactive oxygen species.
Rot/AA	Rotenone/antimycin A
RT	Room temperature.
SDS	Sodium dodecyl sulfate.
SEM	Standard error of the mean.
SOD	Superoxide dismutase.
SPI1	Transcription factor PU.1.
SPM	Specialized pro-resolving mediator.
SSA	5-sulfosalicylic acid.
STAT1	Signal Transducer and Activator of Transcription 1.
TBS	Tris-buffered saline.
TGF-β1	Transforming Growth Factor-β1.
ThS	Thioflavin S.
TNF-α	Tumor Necrosis Factor-α.
TREM2	Triggering Receptor Expressed on Myeloid cells 2.
tTau	Total Tau.
TYROBP	Tyrosine kinase-binding protein.

Veh	Vehicle.
VGlut1	Vesicular glutamate transporter 1.
WB	Western blotting.
WT	Wild type.

Abstract

Alzheimer's disease (AD) is the most common cause of dementia. Its main histopathological features are amyloid β (Aβ) plaques and tau neurofibrillary tangles. Excessive Aβ production and aggregation can trigger tau deposition and neuroinflammation, which lead to widespread neurotoxicity and dementia symptoms. Neuroinflammation plays a key role in AD progression, with inflammation mediators, especially microglia, promoting cytokine release, oxidative stress, mitochondrial dysfunction, synapse loss and neuronal death.

In this work, we targeted inflammation resolution and microglial function to study AD pathology and treatment, using *in vitro* and *in vivo* models. Additionally, we developed a triple co-culture with neurons, microglia and astrocytes to study cellular communication in Aβ pathology and neurodegeneration.

Firstly, we studied how using lipoxins to enhance resolution of neuroinflammation could be beneficial for AD. We found that lipoxins *in vitro* were able to decrease Aβ-induced ROS generation and restore mitochondrial function. Lipoxins also reduced amyloid accumulation, tauopathy and glial activation in a mouse model of AD, and prevented synapse loss and mitochondrial dysfunction. These results suggest that lipoxins are interesting therapeutic candidates to reduce AD pathology and progression.

Second, we analyzed Complement Receptor 3 (CR3) in microglia using the inhibitor XVA143. CR3 inhibition altered cellular morphology and reduced microglial migration capacity. It also altered the expression of genes related to the immune response, including cytokines and the complement system. CR3 seems to play key roles in microglial function, and further research is required to understand how this receptor affects microglia-mediated AD pathology.

Lastly, we established a triple co-culture model to study cellular communication. In this triple co-culture, neurons had a more complex morphology, microglia were less inflammatory, and astrocytes were less reactive compared to primary cultures. We were also able to recapitulate Aβ pathology, which will allow us to study neurodegeneration and neuroinflammation processes relevant to AD in future studies.

Introduction

Introduction

1. Alzheimer's disease pathology.

AD is a neurodegenerative disorder characterized by progressive memory loss and cognitive impairment. AD is the most common form of dementia with around 50 million patients worldwide, and estimated to reach over 150 million by 2050 (Breijyeh and Karaman, 2020). Psychiatrist Alois Alzheimer was the first to report the disease in 1907. He described a patient, 51-year-old woman Auguste D, who had developed severe memory loss, disorientation and language impairment. *Post mortem* analysis of her brain revealed widespread atrophy, unusual extracellular deposits and intracellular neurofibrillary tangles (Alzheimer and A., 1907; Strassnig and Ganguli, 2005). Later on, extracellular deposits were identified as senile plaques made of Aβ and intracellular tangles were identified as hyperphosphorylated tau protein (Miyakawa *et al.*, 1982; Grundke-Iqbal *et al.*, 1986) (**Figure 1**). To this day, senile plaques and neurofibrillary tangles are the main histopathological features of AD (Long and Holtzman, 2019).

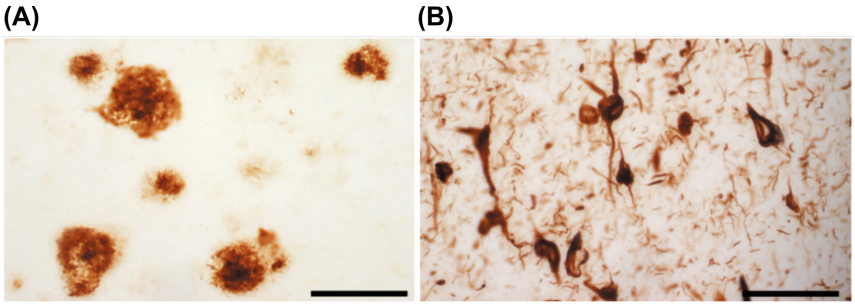

Figure 1. Senile plaques and neurofibrillary tangles in the AD brain. (A) Amyloid plaques stained with anti-$A\beta_{42}$ antibody. Scale bar = 125 μm. **(B)** Neurofibrillary tangles with anti-PHF1 antibody. Scale bar = 62.5 μm (adapted from LaFerla and Oddo, 2005).

AD can manifest with diverse cognitive symptoms, although memory loss is the most prominent (reviewed in Apostolova, 2016). Patients become incapacitated and complications such as malnutrition, venous thrombosis or infections ultimately arise. These complications are often the cause of death in AD patients, generally 5-12 years after the onset of the symptoms.

The deposition of Aβ occurs in the AD brain following a distinctive anatomical pattern. Amyloid deposits start developing in the neocortex, they spread to cholinergic nuclei, brainstem nuclei and, finally, to the cerebellum (Thal *et al.*, 2002). Alternatively, neurofibrillary tangles spread following a different anatomical pattern, starting in the transentorhinal region, all the way into the neocortex (Braak and Braak, 1995). Six stages of the disease are defined based on the areas affected by the gradual deposition of fibrillary tangles. Stages I-II, or transentorhinal, are preclinical stages with no symptoms. Stages III–IV, or limbic, coincide with incipient and moderate symptoms. Finally, stages V–VI, or neocortical, are fully developed AD. Several studies have suggested that tau tangles do not spread into the neocortex in the absence of Aβ (reviewed in Long and Holtzman, 2019), so Aβ might be a prerequisite to develop tau pathology.

The most significant risk factor for AD is aging. The majority of cases emerge after 65 years of age, constituting late-onset AD (LOAD), while only around 5% of cases appear before age 65, constituting early-onset AD (EOAD) (Lanoiselée *et al.*, 2017). Most cases of EOAD are familial, inherited in an autosomal dominant manner and linked to mutations in genes such as Amyloid Precursor Protein (APP), γ-secretase components Presenilin 1 and 2 (PSEN-1, PSEN-2), and Apolipoprotein E (ApoE). Mutations in other genes like Clusterin, or Triggering Receptor Expressed on Myeloid cells 2 (TREM2) also increase the risk of AD, although to a lesser extent. Environmental factors such as infections, cardiovascular disease or diabetes are also linked with higher risk of AD (reviewed in Breijyeh and Karaman, 2020).

Since 1984, the standard for AD diagnosis has been the National Institute of Neurological and Communicative Disorders and Stroke - Alzheimer's Disease and Related Disorders Association (NINCDS–ADRDA) criteria, which combines the clinical history of patients with *post mortem* neuropathological examinations (McKhann *et al.*, 1984). However, new techniques such as positron emission tomography (PET) imaging and cerebrospinal fluid (CSF) and plasma biomarkers now allow *ante mortem* diagnosis with reasonable accuracy (reviewed in Long and Holtzman, 2019).Brain Aβ deposits in cognitively normal adults, using PET amyloid tracer Pittsburgh Compound B (PiB), are associated with high risk of AD (Morris *et al.*, 2009). Besides, individuals with preclinical or mild AD confirmed by

PET-PiB have reduced $A\beta_{42}$ and increased tau levels in CSF and plasma (Fagan *et al.*, 2006, 2007; Fossati *et al.*, 2019).

To this day, there is no cure for AD. Although some medications can stabilize patients and delay cognitive decline. The acetylcholinesterase inhibitors donepezil, galantamine and rivastigmine, and the N-Methyl-D-Aspartate Receptor (NMDAR) antagonist memantine were the only medications approved by the American Food and Drug Administration (FDA) for AD since 2003 (reviewed in Yiannopoulou and Papageorgiou, 2020). However, in 2021 the FDA approved the first disease-modifying drug Aducanumab, a human monoclonal antibody that selectively targets Aβ aggregates (Sevigny *et al.*, 2016). While promising, the decision has been controversial, because the drug did not prove robust clinical improvements in two phase III clinical trials (Knopman *et al.*, 2021). More than 200 clinical trials for AD have failed in the past (www.clinicaltrials.gov, accessed January 17, 2022). Possible explanations for this fact could be that therapies started too late in the disease progression, or that the selected targets were not adequate (reviewed in Yiannopoulou *et al.*, 2019). Up to the year 2020, there were 121 ongoing clinical trials for AD, with a progressive shift from Aβ and tau to alternative targets, such as synapse protection, neurogenesis and neuroinflammation (Cummings *et al.*, 2020).

1.1. Amyloid cascade hypothesis.

The most accepted hypothesis to explain the onset and progression of AD is the amyloid cascade hypothesis (Selkoe, 1991; Hardy and Higgins, 1992; Hardy and Selkoe, 2002; Selkoe and Hardy, 2016). It was based on the discovery of Aβ as the main constituent of senile plaques (Glenner and Wong, 1984; Kang *et al.*, 1987), and the identification of mutations in APP in familial AD (Levy *et al.*, 1990; Chartier-Harlin *et al.*, 1991). The hypothesis postulates that AD pathology is ultimately caused by an abnormal accumulation of Aβ in the brain, due to enhanced production and/or reduced elimination of the peptide (Hardy and Higgins, 1992; Dickson, 1997). Aβ is a 4.5 kDa peptide derived from the proteolytic processing of APP (Haass *et al.*, 1992).

APP is a 100-140 kDa transmembrane glycoprotein with a single domain and a long extracellular N-terminus, which is involved in physiological functions like brain development, neurite growth and cell migration (Herms *et al.*, 2004; Young-Pearse *et al.*, 2007). APP is produced and metabolized very rapidly (Lee *et al.*, 2008), following two main alternative pathways (**Figure 2**). APP can be sequentially cleaved by α-secretase and γ-secretase following the non-amyloidogenic pathway, generating APP Intracellular Domain (AICD) and extracellular peptide p3. Alternatively, APP can be cleaved by β-secretase and γ-secretase following the amyloidogenic pathway, which generates AICD and Aβ (reviewed in O'Brien and Wong, 2011). Non-amyloidogenic cleavage is the dominant pathway, although the amyloidogenic pathway is favored under pathological conditions (Ehehalt *et al.*, 2003).

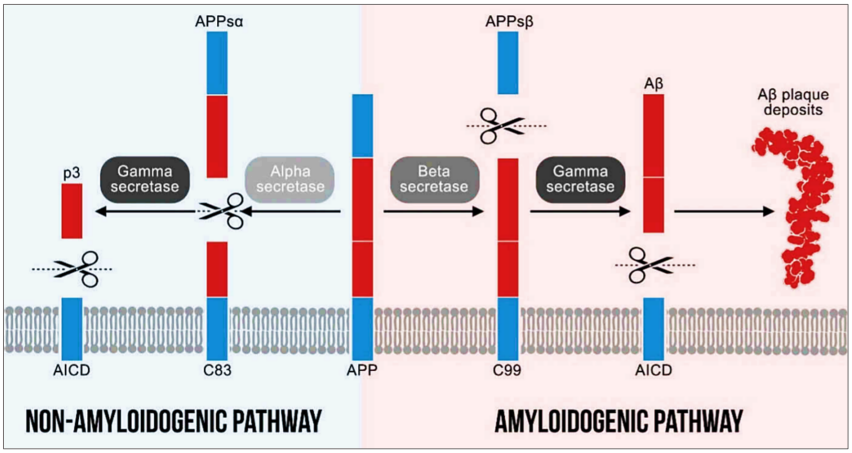

Figure 2. Diagram of APP processing. In the non-amyloidogenic pathway, the sequential proteolytic cleavage by α- and γ-secretases generates AICD and p3. In the amyloidogenic pathway, β- and γ-secretases generate AICD and Aβ, which can form oligomers, fibrils and, ultimately, senile plaques (adapted from Sasmita, 2018).

Depending on the point of cleavage by γ-secretase, mainly three forms of Aβ can be produced, consisting of 38, 40 or 42 amino acid residues. $A\beta_{40}$ is the most abundant, while $A\beta_{42}$ is more prone to aggregate forming oligomers and fibrils (Burdick *et al.*, 1992). Thus, increased $A\beta_{42}/A\beta_{40}$ ratio can rise Aβ aggregation and trigger neurodegeneration (Pike *et al.*, 1991; Geula *et al.*, 1998). According to the amyloid cascade hypothesis, when the $A\beta_{42}/A\beta_{40}$ ratio is increased, $A\beta_{42}$ oligomerization and accumulation are favored. This ratio can

increase by excessive Aβ production, for example by mutations in APP and PSEN-1 and -2, or by insufficient Aβ clearance (Suzuki *et al.*, 1994; Scheuner *et al.*, 1996). Oligomeric $A\beta_{42}$ alters synaptic function, and senile plaques start to accumulate and trigger local inflammation and oxidative stress. Disruption of neuronal homeostasis and altered kinase and phosphatase activities induce tau hyperphosphorylation and formation of neurofibrillary tangles that, in turn, contribute to neurotoxicity. The cascade leads to widespread neuronal dysfunction and cellular death, leading to the onset of dementia symptoms (reviewed in Haass and Selkoe, 2007).

Aβ oligomers are more toxic than other aggregated forms, in part due to the fact that they can interact with a wide variety of targets (reviewed in Kayed and Lasagna-Reeves, 2013). Aβ oligomers are present in AD brains, and they are a better correlate for disease severity than senile plaques (Darocha-Souto *et al.*, 2011). Soluble Aβ oligomers are able to induce abnormal synaptic spine morphology and neuronal death (Lambert *et al.*, 1998; Lacor *et al.*, 2007), induce oxidative damage (Alberdi *et al.*, 2018), and trigger release of inflammatory mediators in microglia and astrocytes (White *et al.*, 2005; Kim *et al.*, 2014).

On the other hand, hyperphosphorylated forms of the tau protein are also highly neurotoxic. Tau, or Microtubule-Associated Protein Tau (MAPT), is primarily expressed by neurons in the central nervous system (CNS), and it participates in microtubule assembly and stabilization of neuronal axons (reviewed in Long and Holtzman, 2019). Hyperphosphorylation, mediated by tau kinases, changes the protein conformation, causing misfolding and aggregation (reviewed in Ballatore *et al.*, 2007) that contribute to synapse loss, microglial activation and neurodegeneration (Yoshiyama *et al.*, 2007). Longitudinal PET studies have revealed tau as a robust predictor of cognitive impairment (Hanseeuw *et al.*, 2019), while tau-related cognitive decline is worse in individuals with high Aβ levels (Aschenbrenner *et al.*, 2018). Evidence reveals the close interaction between Aβ and tau in AD, with Aβ aggregation taking place upstream of tau, and tau accumulation further spreading the pathology and contributing to neurotoxicity in collaboration with Aβ (reviewed in Bloom, 2014).

1.2. Synaptic dysfunction and synapse loss.

Synapses are specialized structures that allow neuronal communication. Presynaptic terminals synthesize, store and release neurotransmitters that bind postsynaptic terminals, also known as spines, in order to transmit electrical signals or activate signaling pathways (reviewed in Burns and Augustine, 1995).

Impaired synaptic transmission and synapse loss happen in early stages of AD. Multiple authors have reported synapse loss in neocortex and hippocampus of AD patients (Davies *et al.*, 1987; Catalá *et al.*, 1988; Scheff *et al.*, 2007), and it is considered the most reliable correlate of memory impairment (DeKosky *et al.*, 1996; Sze *et al.*, 1997). As aforementioned, there is a strong link between soluble Aβ oligomers and synaptic dysfunction, and even picomolar concentrations of Aβ oligomers can reduce the density of dendritic spines in organotypic slices (Shankar *et al.*, 2007). Tg2576 AD mice, which overexpress APP695 and the Swedish mutation (KM670/671NL), show a drastic inhibition of long-term potentiation (LTP) with age (Fernández-Fernández *et al.*, 2016). Triple transgenic (3xTg) AD mice, which carry PSEN1M146V, Swedish, and tauP301L transgenes, also displays a deficit in LTP in the hippocampus as early as 4 months of age (Oddo *et al.*, 2003*b*; Billings *et al.*, 2005). Aβ oligomers can also disrupt glutamate, the most abundant excitatory neurotransmitter in the CNS. Aβ oligomers can impair glutamate uptake by astrocytes (Han *et al.*, 2016), and also trigger astrocytic glutamate release (Harkany *et al.*, 2000). This excessive glutamate accumulates around synapses and can induce excitotoxicity (reviewed in Tu *et al.*, 2014).

Synaptic transmission relies on mitochondrial energy supply in order to maintain ion gradients and support neurotransmitter release and reuptake (reviewed in Cai and Tammineni, 2017). Thus, damaged mitochondria directly threaten synaptic function. It has been reported that Aβ induces mitochondrial swelling and reduces synaptic markers in rat synaptosomes (Mungarro-Menchaca *et al.*, 2002). Aβ also impairs mitochondrial recruitment to synapses by inhibiting axonal transport, resulting in reduced energy availability and further contribution to synaptic dysfunction in AD (Rui *et al.*, 2006).

Along with synaptic dysfunction, active elimination of synapses takes place in the AD brain (reviewed in Cardozo *et al.*, 2019). This elimination can occur through autonomous neuronal mechanisms, or through glial cells. Cultured neurons from Tg2576 mice display reduced expression of both pre- and post-synaptic markers, and a reduction of Glutamate receptor ionotropic 1, which suggests that Aβ can induce synapse loss in a cell-autonomous way in neurons via downregulation of glutamate receptors (Almeida *et al.*, 2005).

Synapses can also be eliminated by the interaction with glial cells. Astrocytes are involved in synapse elimination during CNS development via Megf10 and Mertk phagocytic pathways (Chung *et al.*, 2013). Besides, reactive astrocytes near Aβ plaques can engulf dystrophic neurites in hippocampus of APP/PS1 AD mice, which carry Swedish and PSEN1L166P mutations, as well as AD patients (Gomez-Arboledas *et al.*, 2018). Besides, microglia participate in synaptic elimination in AD, mainly through components of the complement system. Schaffer *et al.* (2012) first reported this process in mammalian CNS development. Years later, Hong *et al.* (2016) proved that this microglia-dependent synaptic loss was also present in pre-plaque J20 AD mice, which carry APP mutations Swedish and Indiana, and APP/PS1 mice.

Complement components C1q and C3, and receptor CR3 are the main effectors of microglia-dependent synaptic elimination (Hong *et al.*, 2016) (**Figure 3**). The presence of Aβ induces C1q, initiator of the classical complement cascade, to be recruited to the synapse. This leads to the activation of C3, whose cleavage product C3b labels the synapse for elimination. Interaction of C3b with CR3 in the microglia finally results in the engulfment of the synapse (reviewed in Luchena *et al.*, 2018). Numerous publications have reported that genetic ablation of C1q, C3 or CR3 is able to prevent Aβ-induced synaptic loss in AD mouse models (Hong *et al.*, 2016; Lui *et al.*, 2016; Shi *et al.*, 2017). In addition, C1q and C3 expression is increased in hippocampus of AD patients (Yasojima *et al.*, 1999).

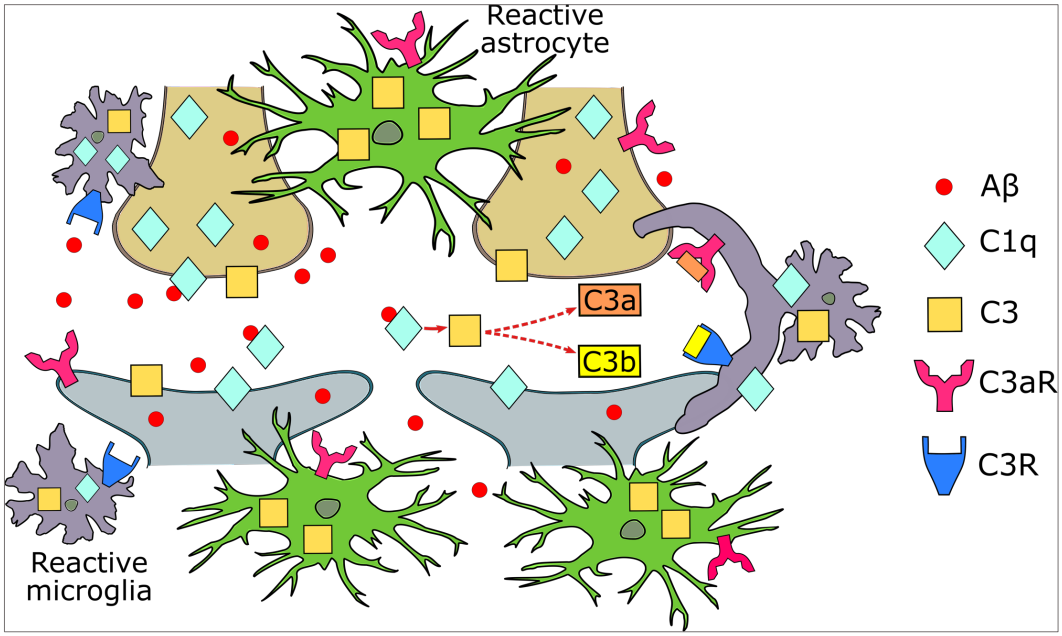

Figure 3. Diagram of microglia-dependent synaptic elimination. In AD, C1q is recruited to synapses and interacts with Aβ. This triggers the activation of complement protein C3, which is cleaved into C3a and C3b. C3a binds to receptor C3aR, linked to inflammation. C3b labels the synapses and binds to microglial CR3, which leads to the removal of the synapse (adapted from Luchena *et al.*, 2018).

1.3. Oxidative stress.

Increasing evidence reveals that oxidative stress plays a major role in the pathophysiology of AD (Huang *et al.*, 2016). The brain has limited antioxidant capacity in comparison with other organs, in part because it has high oxygen and energy demands, so it is particularly vulnerable to oxidative damage. There is evidence of oxidative damage in the brain of AD patients, with increased protein oxidation (Hensley *et al.*, 1995; Aksenov *et al.*, 2001), lipid peroxidation (Markesbery and Lovell, 1998), and reduced antioxidant activity in plasma (Zafrilla *et al.*, 2007).

Byproducts derived from oxygen metabolism are known as reactive oxygen species (ROS). Among this group of metabolites are hydrogen peroxide (H_2O_2), nitric oxide (NO) and superoxide anion (O_2^-). ROS are constantly produced in the cell during normal metabolism, and there is a balance between production and clearance. Oxidative stress occurs when balance is disrupted and there is an uncontrolled ROS production and/or limited antioxidant activity.

Excessive ROS leads to cellular damage, driven by protein and enzyme oxidation, lipid peroxidation, and mitochondrial and nuclear DNA damage. ROS are mainly generated by mitochondrial oxidative metabolism and Nicotinamide adenine dinucleotide phosphate (NADPH) oxidases or NOX, while superoxide dismutases and glutathione are the most prominent detoxification agents (reviewed in Bresciani *et al.*, 2015).

The human NOX family includes seven isoforms that catalyze the production of superoxide radicals by transferring electrons from NADPH to oxygen. NOX2 is the most studied in the brain, mainly expressed by microglia (Dohi *et al.*, 2010) and, to a lesser extent, by astrocytes (Abramov *et al.*, 2005) and neurons (Tammariello *et al.*, 2000). NOX2 consists of two transmembrane proteins, $p22^{phox}$ and the catalytic subunit $gp91^{phox}$, and four cytosolic components, $p47^{phox}$, $p67^{phox}$, $p40^{phox}$, and G-protein Rac (reviewed in Brandes *et al.*, 2014) (**Figure 4**). Activation of NOX2 requires phosphorylation of p47 and p67, and the activation of Rac, so that all cytosolic components can translocate to the membrane. NOX2 is located in the cytoplasmic membrane and can be activated in lipopolysaccharide (LPS)-induced immunity (Parajuli *et al.*, 2013), or in response to neurodegeneration stimuli like Aβ (Della Bianca *et al.*, 1999) and α-synuclein (Hou *et al.*, 2018).

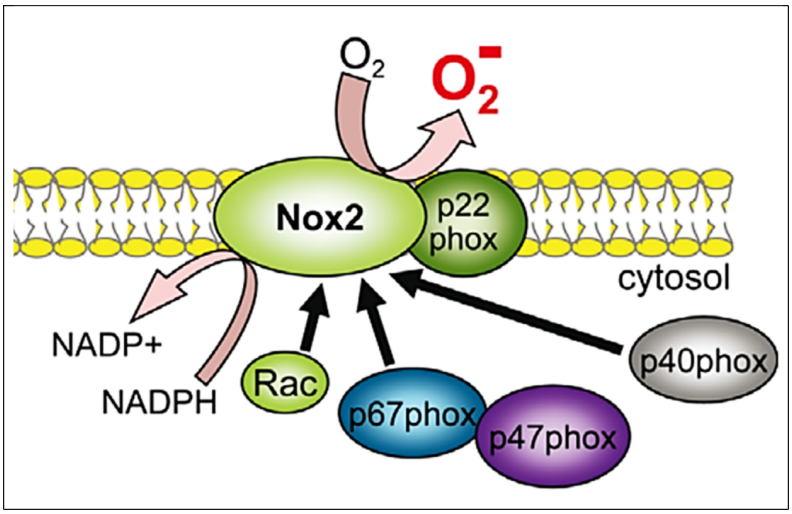

Figure 4. Structure of enzyme NOX2. NOX2 consists of transmembrane subunits $p22^{phox}$ and $gp91^{phox}$, and cytosolic components $p47^{phox}$, $p67^{phox}$, $p40^{phox}$ and Rac. Recruitment of cytosolic components to the membrane activates the enzyme, producing superoxide anions (adapted from Brandes *et al.*, 2014).

In the context of AD neurodegeneration, there is a sustained oxidative damage triggered by the combination of enhanced ROS production and reduced antioxidant activity (Cheignon *et al.*, 2018). Besides, NOX2 is activated in AD patients (Shimohama *et al.*, 2000), and Aβ is a potent enhancer of NOX-mediated ROS generation (Della Bianca *et al.*, 1999; Shelat *et al.*, 2008). Tg2576 mice display high levels of ROS in the cortex coincident with the onset of senile plaques (Apelt *et al.*, 2004). NOX2 is especially relevant in microglia, where it mediates ROS generation in response to pro-inflammatory cytokines Tumor Necrosis Factor-α (TNF-α), Interleukin 1β (IL-1β) and Interferon-γ (IFN-γ) (Yang *et al.*, 2007). Inversely, ROS can act as secondary messengers activating pro-inflammatory pathways in microglia (reviewed in Simpson and Oliver, 2020). Regarding ROS clearance, AD patients display low activity of antioxidant enzymes SOD and glutathione reductase in plasma (Zafrilla *et al.*, 2007). Genetic ablation of SOD-2 in J20 mice accelerates behavioural alterations and neuronal damage (Esposito *et al.*, 2006), while overexpression of the same SOD-2 in Tg2576 mice reduces superoxide radicals and prevents memory deficits (Massaad *et al.*, 2009). A number of antioxidants have been tested to reduce oxidative damage in AD (reviewed in Oliver and Reddy, 2019). For instance, naturally occurring polyphenols rutin, morin and magniferin are able to reduce ROS generation, enhance SOD activity and attenuate mitochondrial damage induced by $A\beta_{42}$ in neurons (Wang *et al.*, 2012; Alberdi *et al.*, 2018).

Glutathione is a thiol-containing molecule that is key in the antioxidant response to oxidative stress (reviewed in Dringen, 2000). The reduced form GSH can turn into the oxidized form GSSG during ROS detoxification, and then can be regenerated in the glutathione redox cycle (**Figure 5**). Alterations in the GSSG/GSH balance can leave cells vulnerable to oxidative damage (reviewed in Pocernich and Butterfield, 2012). Studies have revealed increased levels of GSSG in cerebrum, cerebellum, hippocampus and blood of APP/PS1 mice with age (Zhang *et al.*, 2012). In addition, GSSG levels are significantly higher in erythrocyte and plasma samples of AD and mild cognitive impairment patients, compared to age-matched controls (Calabrese *et al.*, 2006; Bermejo *et al.*, 2009), thus GSSG and GSH in blood have been proposed as biomarkers for AD progression.

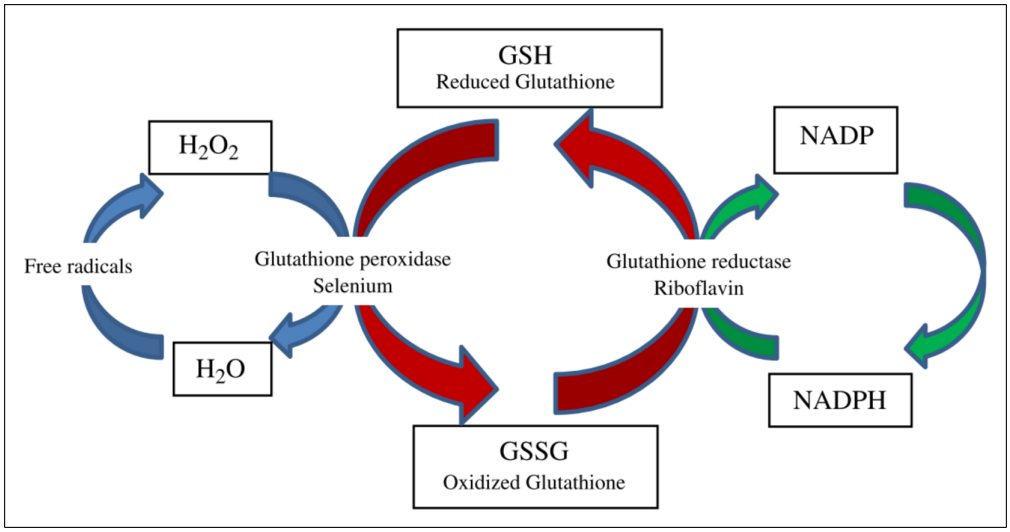

Figure 5. Glutathione cycle of oxidation and reduction. Glutathione protects against oxidative damage by ROS detoxification. Glutathione peroxidases convert GSH into the oxidized form GSSG, while glutathione reductases convert GSSG into the reduced form GSH (adapted from Patel *et al.*, 2014).

1.4. Mitochondrial dysfunction.

Mitochondria play a critical role in brain bioenergetics and metabolism, so any disruption will significantly contribute to AD pathology (reviewed in Cai and Tammineni, 2017). Besides, mitochondria are both the main source of ROS generation in the cell, and one of the organelles most vulnerable to oxidative damage (reviewed in Sastre *et al.*, 2003). The main function of this organelle is to generate energy in form of adenosine triphosphate by oxidative phosphorylation, in which electrons are transferred down the mitochondrial respiratory chain to power adenosine triphosphate synthase. Mitochondria carry out many other functions like Ca^{2+} storage, maintenance of the redox balance, and apoptosis (reviewed in Belenguer *et al.*, 2019). These dynamic organelles undergo continuous changes in number and shape depending on cellular needs. Mitochondrial fusion is mainly mediated by proteins Mitofusin-1 (MFN1), Mitofusin-2 (MFN2) and Optic Atrophy Protein 1 (OPA1), while mitochondrial fission is mediated by Mitochondrial fission 1 protein (Fis1) and Dynamin-Related Protein 1 (DRP1) (reviewed in Chan, 2012). Imbalance between fusion and fission leads to impaired mitochondrial motility and function (Cai and Tammineni, 2017).

Mitochondrial dysfunction is part of the pathophysiology of AD. Increased expression of DRP1 and Fis1 and reduced expression of MFN1, MFN2 and OPA1 was found in the frontal cortex of AD patients, indicating excessive mitochondrial fragmentation (Calkins *et al.*, 2011). Human neuroblastoma cells overexpressing APP Swedish mutation display increased Fis1 and reduced OPA1, along with fragmented mitochondria with an abnormal distribution around the perinuclear area (Wang *et al.*, 2008). Female 3xTg mice also have low levels of MFN2 and high levels of DRP1 in hippocampus and cortex (Djordjevic *et al.*, 2020).

Together with mitochondrial dynamics, Aβ can alter normal mitochondrial metabolism. Several authors have demonstrated that $A\beta_{42}$ impairs the activity of respiratory chain components *in vitro* (Bobba *et al.*, 2013; Alberdi *et al.*, 2018). Oxidative phosphorylation is also reduced in 3xTg mice, with alterations in the expression of respiratory chain complexes (Yao *et al.*, 2009; Djordjevic *et al.*, 2020). Cytochrome C, IV component of the respiratory chain, is reduced in Tg2576 mice compared with wild type (WT) littermates (Manczak *et al.*, 2006).

Defective mitochondrial metabolism can be partially explained by an increase in oxidative stress. Aβ oligomers increase mitochondrial ROS levels in rat hippocampal neurons (Wang *et al.*, 2009), and Tg2576 mice accumulate Aβ oligomers in the inner mitochondrial membrane together with high levels of H_2O_2 (Manczak *et al.*, 2006). It is also known that enzyme NOX4, found in mitochondrial membranes, produces H_2O_2 and specifically inhibits the activity of respiratory chain complex I (Kozieł *et al.*, 2013).

Some studies suggest that mitochondrial dysfunction precedes the onset of AD pathology. For instance, in 3xTg mice, impaired mitochondrial respiration and increased oxidative stress manifest as soon as three months of age, before the onset of amyloid plaques (Yao *et al.*, 2009). Thus, mitochondrial dysfunction and Aβ and tau pathologies would exacerbate each other in a vicious cycle that ultimately drives AD neurodegeneration (reviewed in Kim and Mook-Jung, 2019).

2. Neuroinflammation in AD.

Neuroinflammation is a feature that has gained relevance in the pathophysiology of AD over the last decades. Acute inflammation can take place in the brain as a defensive response to harmful stimuli like pathogens or injuries (reviewed in Lyman *et al.*, 2014). However, if the negative stimulus persists, inflammation is not resolved and becomes chronic, contributing to further tissue damage. Numerous authors argue that chronic inflammation is key to the progression of neurodegenerative diseases, and especially AD (reviewed in Calsolaro and Edison, 2016). Recent studies using PET imaging suggest that microglial activation is necessary for amyloid pathology to progress to tau pathology, and that the conjunction of Aβ, tau and microglial activation is a robust predictor for cognitive impairment (Pascoal *et al.*, 2021). Over the years, genome-wide association studies have revealed a number of variants in inflammation-related genes that are associated with increased risk of AD, such as complement receptor CR1 and clusterin (Lambert *et al.*, 2009), myeloid cell surface antigen CD33 (Naj *et al.*, 2011), and TREM2 (Sims *et al.*, 2017), among others. Besides, AD patients display ongoing inflammation in the brain, characterized by reactive astrocytes or astrogliosis (Kato *et al.*, 1998; Serrano-Pozo *et al.*, 2011), as well as reactive microglia or microgliosis (Dickson *et al.*, 1988; Vehmas *et al.*, 2003) concentrated around amyloid plaques. Interestingly, amyloid pathology can act as both cause and consequence of neuroinflammation. For example, Aβ oligomers induce the release of IL-1β and TNF-α by microglia *in vitro* (Weldon *et al.*, 1998; Parajuli *et al.*, 2013). On the other hand, the expression of APP can be enhanced in murine neurons after exposure to IL-1β (Forloni *et al.*, 1992). Along with resident microglia and astrocytes, inflammation in the brain is also joined by infiltrating leukocytes and monocytes/macrophages due to a disruption of the blood-brain barrier (BBB) (reviewed in Hohsfield and Humpel, 2015) (**Figure 6**). It has been shown that AD patients can display abnormalities in the capillary endothelium (Stewart *et al.*, 1992), and cerebral amyloid angiopathy (CAA) (Vinters *et al.*, 2009), where Aβ deposits in blood vessels walls and leads to damage and rupture. Tg2576 mice also display CAA and structural disruption of blood vessels (Christie *et al.*, 2001).

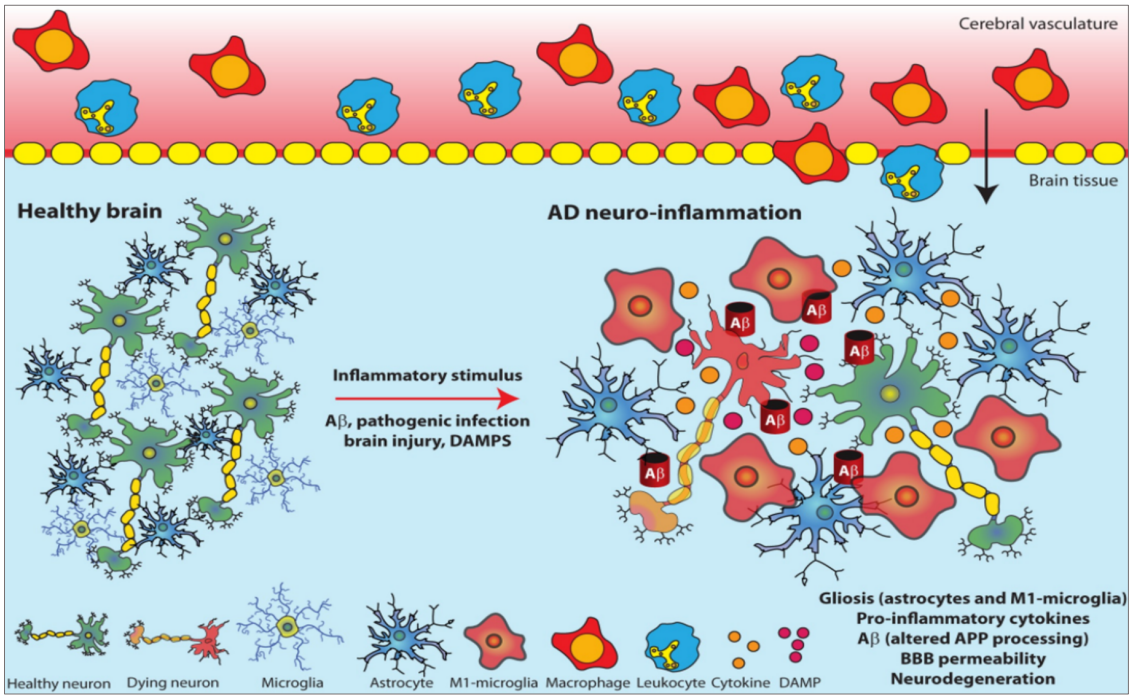

Figure 6. Neuroinflammation is a key process in AD pathology. Stimuli like Aβ deposition, infections or brain injury trigger an inflammatory response. Microglia and astrocytes become reactive and secrete pro-inflammatory cytokines, and BBB disruption allows the recruitment of peripheral immune cells to the inflammation site. In AD, neuroinflammation becomes chronic, which leads to a neurotoxic environment (adapted from Minter *et al.*, 2016).

Non-cellular mediators of inflammation are widespread in the AD brain. High levels of pro-inflammatory cytokines are found in plasma of AD patients (Swardfager *et al.*, 2010), including TNF-α (Gezen-Ak *et al.*, 2013), IL-1β (Honma *et al.*, 2013) and Macrophage Colony-Stimulating Factor (M-CSF) (Laske *et al.*, 2010). Besides, *in vitro* microglia derived from AD patient autopsies increase their production of cytokines IL-1β, IL-6, TNF-α and M-CSF after treatment with $A\beta_{42}$ aggregates (Lue *et al.*, 2001).

Other well-known non-cellular mediators of inflammation pathways are inflammasomes. There are four different inflammasome complexes, and Nucleotide-binding Domain-Like Receptor Protein 3 (NLRP3) has been extensively studied in the context of neurodegeneration (reviewed in Freeman and Ting, 2016). NLRP3 inflammasome consists of the sensor protein NLRP3, the adaptor protein Apoptosis-associated Speck-like Protein containing a Caspase recruitment domain (ASC) and pro caspase-1. Assembly and activation of this complex leads to the cleavage of pro IL-1β and pro IL-18 into their bioactive

forms (reviewed in Gold and El Khoury, 2015). Caspase-1 and NLRP3 (Saresella *et al.*, 2016), as well as ASC (Liu and Chan, 2014) are increased in AD patients, and genetic ablation of either caspase-1 or NLRP3 has positive effects on memory loss and amyloid deposition in APP/PS1 mice (Heneka *et al.*, 2013).

2.1. Microglia.

Microglia, first described more than a century ago by Spanish researcher Pío del Río Hortega, are the principal resident immune cells of the brain. Microglia make up to 5-12% of the total CNS cells, they originate in the embryonic yolk sac, and are capable of self-renewal (reviewed in Helmut *et al.*, 2011). These cells carry out three crucial tasks: they promote neuronal homeostasis and normal function, they constantly survey their environment in search for external threats or injuries, and they act as the first defense against such threats to provide neuroprotection (reviewed in Hickman *et al.*, 2018). Microglia can display diverse morphologies (reviewed in Olah *et al.*, 2011) (**Figure 7**). Ramified microglia, with small cell bodies and numerous processes, are characteristic of healthy or homeostatic conditions. Meanwhile, hypertrophic microglia are associated with reactive microglia and can be found after acute injury or around amyloid plaques in AD. Depending on the authors, hypertrophic microglia can display enlarged cell bodies with few short ramifications (Shahidehpour *et al.*, 2021), or enlarged cell bodies with numerous ramifications (Wyatt-Johnson *et al.*, 2017). Dystrophic microglia, characterized by cytoplasmic swelling and few discontinuous processes, can be found in AD and other forms of dementia (Shahidehpour *et al.*, 2021). Microglia can also adopt an amoeboid shape in conditions of high phagocytic activity, with completely retracted processes and an almost rounded soma. There is a fifth microglial morphology known as rod shape, with elongated cell bodies and very short processes (Taylor *et al.*, 2014). This rod-shaped microglia has been associated with aging (Bachstetter *et al.*, 2017) and AD (Wierzba-Bobrowicz *et al.*, 2002), although its function remains poorly understood.

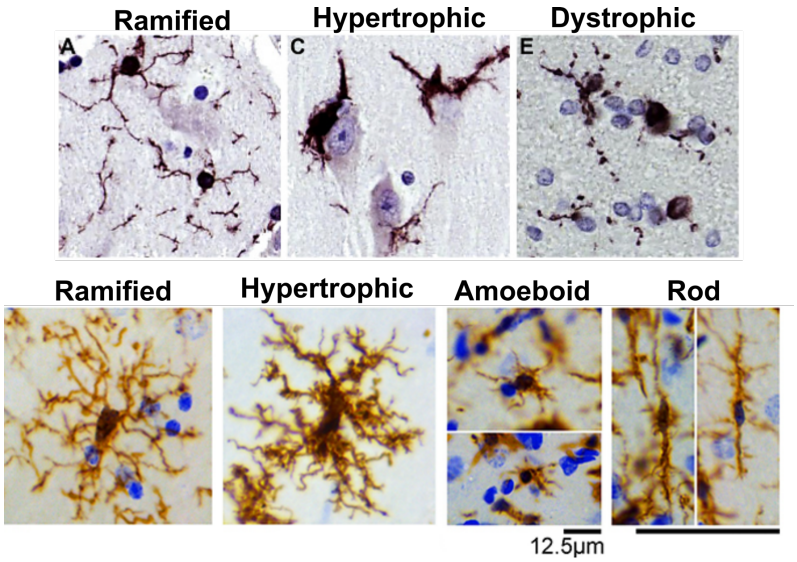

Figure 7. Microglial morphology in the human brain, associated with neurodegeneration (up) and epilepsy (down). Microglia stained with Iba1 in different morphological states. Big scale bar = 50 µm (adapted from Wyatt-Johnson *et al.*, 2017; Shahidehpour *et al.*, 2021).

In response to stimuli like injury or pathogens, microglia migrate to the affected area thanks to the release of chemotactic factors such as extracellular adenosine triphosphate, which microglia can follow (Honda *et al.*, 2001). Once in the area, microglia will try to remove the negative agent by producing pro-inflammatory cytokines, generating ROS and inducing phagocytosis (reviewed in Garden and Möller, 2006). In response to LPS, *in vitro* microglia become amoeboid, increase the production of cytokines IL-1β, IL-6 and TNF-α, and generate nitric oxide (Nakamura *et al.*, 1999) due to the upregulation of Inducible Nitric Oxide Synthase (iNOS) (Possel *et al.*, 2000). LPS-stimulated microglia also increase their capacity to engulf synaptosomes (He *et al.*, 2021) and apoptotic neurons (Fricker *et al.*, 2012). This microglial response is considered neuroprotective and helps the tissue return to physiological conditions.

Amyloid and tau act as microglial activators in the context of AD. Reactive microglia are able to remove fibrillar Aβ (Koenigsknecht and Landreth, 2004) and neurons accumulating phosphorylated tau (Brelstaff *et al.*, 2018). However, persistent production and accumulation of Aβ and tau overwhelm microglia, and their clearance ability is reduced (Mawuenyega *et al.*, 2010). Some studies also suggest that microglia can contribute to tau propagation (Asai *et al.*, 2015). Evidence supports the idea of microglia as a double-edged sword that can

promote neuroprotection with acute activation, but can become neurotoxic if the activation is sustained and becomes chronic (reviewed in Kwon and Koh, 2020). In fact, partial depletion of microglia in 3xTg mice using PLX5622, an inhibitor for Colony-Stimulating Factor 1 Receptor (CSF1R), resulted in improved learning and memory (Dagher *et al.*, 2015). Another CSF1R inhibitor, PLX3397, depleted 80% of microglia in 5xFAD mice, rescuing synaptic and neuronal loss and reducing neuroinflammation (Spangenberg *et al.*, 2016). These studies strongly suggest that microglia become detrimental in AD, supporting the development of therapeutics focused on mitigating microglial activation and/or proliferation (reviewed in Spangenberg and Green, 2016).

AD mouse models like Tg2576 (Benzing *et al.*, 1999), 3xTg (Belfiore *et al.*, 2019) and 5xFAD (Oakley *et al.*, 2006) display microgliosis, especially in the form of hypertrophic and amoeboid microglia surrounding amyloid plaques. Besides, microglial activation markers such as Major histocompatibility complex II, CD68, CD45, Iba1 and CD11b are elevated in AD brains (Hopperton *et al.*, 2017). Aβ induces microglia to produce and release pro-inflammatory cytokines IL-1β, IL-6 (Meda *et al.*, 1999) and TNF-α (Meda *et al.*, 1995) that have neurotoxic effects. IL-1β can interfere with neurotrophic factors and reduce neuronal survival (Tong *et al.*, 2008), while TNF-α inhibits neurite outgrowth (Neumann *et al.*, 2002). Interestingly, microglial Aβ phagocytosis is impaired in the presence of IL-1β and TNF-α *in vitro* (Pan *et al.*, 2011). Similarly, in APP/PS1 mice there is a reduction in Aβ binding receptors like CD36 and Receptor for Advanced-Glycosylation End products (RAGE) at the same time as IL-1β and TNF-α are increased, suggesting a negative correlation between cytokine release and Aβ clearance capacity (Hickman *et al.*, 2008). Finally, microglia are also a source of oxidative stress in the AD brain. Aβ can activate NOX (Zhang *et al.*, 2011) and iNOS (Weldon *et al.*, 1998) in microglia to produce ROS, leading to impaired mitochondrial respiration and neuronal death (reviewed in Kaur *et al.*, 2019).

2.2. Astrocytes.

Astrocytes make up to 20-40% of cells in the CNS, and they participate in a long list of processes to maintain homeostasis and normal neuronal function (reviewed in Westergard and Rothstein, 2020). Astrocytes maintain the BBB, regulate blood flow, provide energy to neurons, and participate in tripartite synapses regulating neurotransmission (reviewed in Perea *et al.*, 2009). In case of injury, astrocytes can remove dead cells, release pro-inflammatory mediators and form a glial scar around areas of tissue damage (reviewed in Kaur *et al.*, 2019). Astrocytes are morphologically heterogeneous, with as many as nine distinct groups, depending on their location, their function and their state of activation (Emsley and Macklis, 2006; Escartin *et al.*, 2021). Protoplasmic astrocytes are located in the cortical grey matter, distributed uniformly with minimum overlapping, and they have a complex morphology with numerous fine processes. In pathological conditions, astrocytes undergo diverse morphological changes, including elongation, extension toward injuries, and domain overlap (reviewed in Escartin *et al.*, 2021). Astrocytes can also become hypertrophic, with enlarged cell bodies, high number of ramifications, and upregulated expression of Glial Fibrillary Acidic Protein (GFAP) (reviewed in Oberheim *et al.*, 2012).

Hypertrophic astrocytes are associated with amyloid plaques and neurofibrillary tangles in the neocortex of AD patients, and this astrogliosis negatively correlates with cortical thickness (Serrano-Pozo *et al.*, 2011). Astrocytic markers GFAP and S100β are increased in brain tissue, CSF and plasma of AD patients (Mecocci *et al.*, 1995; Fukuyama *et al.*, 2001; Wyssenbach *et al.*, 2016). In addition, astrogliosis can be observed in AD models like 3xTg (Oddo *et al.*, 2003*a*) and 5xFAD (Girard *et al.*, 2014). Aβ-stimulated astrocytes trigger an inflammatory response increasing the expression of IL-1β, TNF-α and iNOS (Akama and Van Eldik, 2000). Aβ causes sudden increases in astrocytic cytoplasmic Ca^{2+} (Alberdi *et al.*, 2013) that are associated with higher NOX-dependent ROS generation and neuronal death (Abramov *et al.*, 2005).

Similar to microglia, astrocytic activation can be beneficial or detrimental. On one hand, astrocytes have the capacity to bind and degrade $A\beta_{42}$ (Wyss-Coray *et al.*, 2003), and to release extracellular enzymes like matrix

metalloproteinases 2 and 9 (MMP2, 9) that contribute to Aβ clearance (Yin *et al.*, 2006). On the other hand, reports suggest that astrocytes exacerbate Aβ neurotoxicity and promote tau phosphorylation *in vitro* (Garwood *et al.*, 2011), and inhibition of astrocytic activation pathway Calcineurin/Nuclear Factor of Activated T cells results in improved cognition and lower Aβ levels in APP/PS1 mice (Furman *et al.*, 2012).

2.3. Complement system.

The complement system is a component of the innate immune response involved in defense against pathogens, and it has over 50 components between soluble proteins and membrane receptors (reviewed in Ghebrehiwet, 2016). The complement cascade can be activated by the classical, the lectin and the alternative pathways (reviewed in Mathern and Heeger, 2015) (**Figure 8**). The classical pathway is initiated by C1q, a multimeric protein made up by A, B and C chains. Activation of C1q leads to the formation of complex C1, which cleaves C2 and C4 to C2a + C2b and C4a + C4b, respectively. C2b and C4b form the C3 convertase, which cleaves C3 into C3a + C3b. In the lectin pathway, C3 cleavage is triggered by mannose-binding lectins and ficolins. In the alternative pathway, complement activation occurs constitutively at low rates thanks to factors B and D, which act as C3 convertases. C3 cleavage is the central amplification step of the complement cascade, with multiple C3b products recruiting more C3 convertases. C3 convertases bind C3b products to form C5 convertases, which in turn cleave C5 into C5a and C5b. Anaphylatoxins C3a and C5a mediate inflammatory response and immune cell recruitment. C3b participates in opsonization and phagocytosis, while C5b initiates the formation of the Membrane Attack Complex (MAC), composed by proteins C5b, C6, C7, C8 and C9, in order to induce lysis in cell membranes. There are four complement receptors, CR1-4, that mediate C3b actions on lymphocyte activation, opsonization and phagocytosis (reviewed in Carpanini *et al.*, 2019).

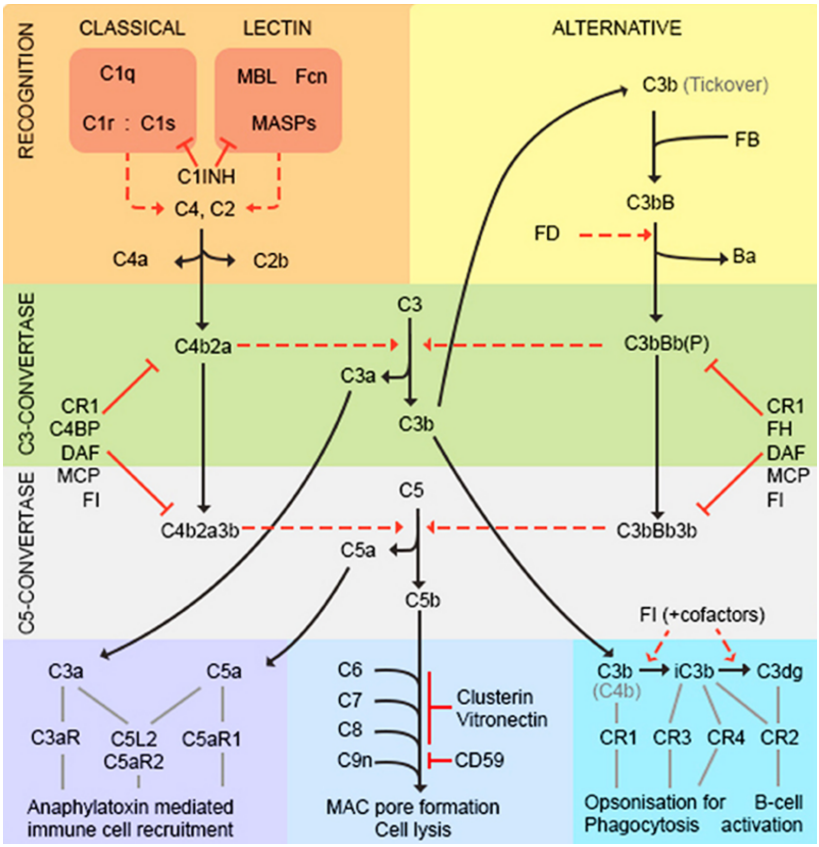

Figure 8. The complement cascade. The classical pathway is activated by C1q through antibody/antigen recognition. Complex C1 generates C3 convertase C4b2a. The alternative pathway is constitutively active, and it is mediated by factors B and D. Three pathways converge in C3 cleavage, generating anaphylatoxin C3a, and C3b. C3b takes part in C5 convertases that cleave C5 into anaphylatoxin C5a and C5b. C3a and C5a bind their respective receptors to recruit immune cells. C5b binds C6, C7, C8 and C9 to form the MAC. C3b participates in opsonization, phagocytosis and B-cell activation. The cascade can be stopped in every step by factors like receptor CR1 or clusterin (adapted from Carpanini *et al.*, 2019).

Aβ can directly bind and activate C1q (Rogers *et al.*, 1992; Jiang *et al.*, 1994), which can be found in association with senile plaques in the brain of AD patients (Ishii and Haga, 1984; Afagh *et al.*, 1996). Expression of components C1-C9 is increased in temporal cortex and hippocampus (Walker and McGeer, 1992; Shen *et al.*, 1997), and levels of C3 and C4 are elevated in CSF of AD patients (Daborg *et al.*, 2012). Besides, variants in complement components CR1 and clusterin are linked to increased AD risk (Lambert *et al.*, 2009). In the adult brain, C1q is mainly produced by microglia (Fonseca *et al.*, 2017), which can respond to C1q with release of pro-inflammatory cytokines and ROS generation in a way similar to LPS exposure (Färber *et al.*, 2009). Authors have also found a steady increase of C1q accumulation in the aging human and mouse brain in

areas like the hippocampus and localized in the proximity of synapses (Stephan *et al.*, 2013). Interestingly, genetic ablation of C3 prevented aging-induced synaptic loss and memory impairment in WT mice (Shi *et al.*, 2015). The role of the complement system in AD pathology is controversial (reviewed in Luchena *et al.*, 2018). Some authors argue that the complement has neuroprotective effects. For instance, aged APP mice lacking C3 have higher levels of $A\beta_{42}$ deposition and increased neuronal loss (Maier *et al.*, 2008). Moreover, soluble complement receptor-related protein Y, a complement inhibitor, increases Aβ deposition and neuronal degeneration in APP mice (Wyss-Coray *et al.*, 2002). On the other hand, other authors have shown the complement system can be detrimental for neurons. C3 coming from astrocytes alters synaptic morphology and disrupts neuronal function *in vitro* (Lian *et al.*, 2015), and genetic ablation of C1q or C3 reduces synapse loss in J20 and APP/PS1 mice (Hong *et al.*, 2016). As in glial cells, the apparent dual function of the complement system might be due to differences in acute and chronic activation. For instance, in primary microglia, acute C3 activation enhances phagocytosis, whereas chronic C3 activation attenuates it (Lian *et al.*, 2016). Finally, the complement system is also involved in tau-induced synaptic loss, with C1q accumulation in synapses and increased microglial phagocytosis in the mouse model of tauopathy Tau-P301S (Dejanovic *et al.*, 2018).

2.4. Resolution of inflammation.

Acute inflammation is a protective response against pathogens or injuries to defend the host and restore homeostasis (reviewed in Lyman *et al.*, 2014). This response includes the release of cytokines, chemokines and lipid mediators, as well as the recruitment of neutrophils and monocytes/macrophages. Once the threat has been removed, the inflammatory response must be stopped so that tissues can heal. Resolution of inflammation is an active process highly regulated by specialized pro-resolution mediators (SPMs) including lipoxins, resolvins, protectins and maresins. Failure to resolve results in chronic inflammation, which is involved in the pathogenesis of diseases like asthma, arthritis, multiple sclerosis and AD (reviewed in Whittington *et al.*, 2017).

Resolution of inflammation takes place when there is a switch in the production of pro-inflammatory mediators to the production of SPMs (reviewed in Serhan *et al.*, 2015). Lipoxins are derived from endogenous arachidonic acid, while resolvins, protectins and maresins are produced from dietary fatty acids (**Figure 9**). Lipoxin synthesis can occur through different pathways. The first and second pathways are led by 5-, 12- and 15-lipoxygenases (5-, 12, 15-LOX), while the third pathway can be triggered by aspirin, which leads to the acetylation of cyclooxygenase-2 (COX-2), switching its activity from producing pro-inflammatory thromboxane and prostaglandins, to lipoxins. On the other hand, resolvins are synthesized from ω-3 fatty acids. Resolvins from the D-series, protectins and maresins derive from docosahexaenoic acid, while E-series derive from eicosapentaenoic acid (reviewed in Serhan *et al.*, 2015).

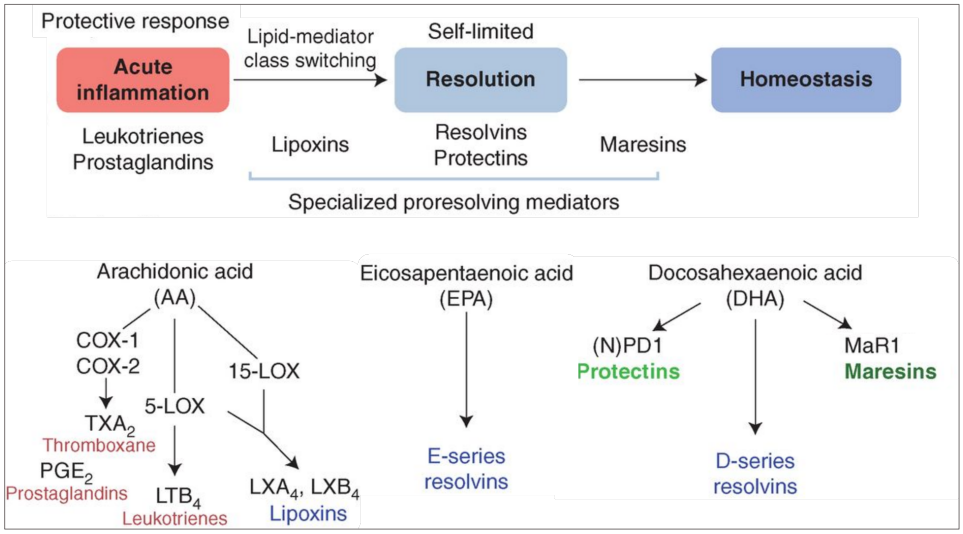

Figure 9. Resolution of inflammation is mediated by SPMs. Acute inflammation, driven by leukotrienes and prostaglandins, undertakes resolution, driven by SPMs, in order to re-establish homeostasis. Lipoxins are biosynthesized from arachidonic acid, while resolvins, protectins and maresins are derived from eicosapentaenoic acid and docosahexaenoic acid (adapted from Serhan *et al.*, 2015).

SPMs implement a number of anti-inflammatory functions (reviewed in Freire and Van Dyke, 2013). For instance, studies report that lipoxins inhibit neutrophil recruitment and enhance phagocytosis (Serhan *et al.*, 2003; Tobin *et al.*, 2012). Resolvins reduce prostaglandins and promote tissue healing (Hasturk

et al., 2006; Norling *et al.*, 2012). Protectins regulate macrophage function (Duffield *et al.*, 2006) and maresins reduce cell migration (Shinohara *et al.*, 2012).

Neurodegenerative diseases, including AD, are characterized by a state of chronic inflammation, with high levels of pro-inflammatory mediators (reviewed in Whittington *et al.*, 2017). An increasing number of publications suggests that failed inflammation resolution is key to the development of AD. For instance, Wang *et al.* (2015*a*) discovered that senescence-accelerated mice SAMP8 display high levels of pro-inflammatory markers and low levels of SPMs. They also found a correlation between SPM-synthesis enzymes and Aβ and tau. Besides, levels of maresins, protectins and resolvins are low in the entorhinal cortex of AD patients compared to controls, while levels of prostaglandin are higher in AD patients (Lukiw *et al.*, 2005; Zhu *et al.*, 2016). This evidence supports the idea that SPMs are a potential therapeutic target for AD.

3. Strategies to modulate neuroinflammation.

Given the key role of neuroinflammation in the progression of AD, efforts are directed towards finding new therapeutic targets that can modulate this process. Neuroinflammation comprises a wide range of events that are greatly dependent on each other, which complicates the search for adequate targets (reviewed in Wenzel and Klegeris, 2018). Nonsteroidal anti-inflammatory drugs like Naproxen or Rofecoxib have shown disappointing results (Reines *et al.*, 2004; Breitner *et al.*, 2011). Other approaches, like naturally occurring curcumin and resveratrol have shown promising preclinical results, but limited efficacy in clinical trials (reviewed in Bronzuoli *et al.*, 2016). A number of ongoing clinical trials are focused on modulating microglia (reviewed in Moore *et al.*, 2019). For instance, Sargramostim, a recombinant form of Granulocyte-Macrophage Colony-Stimulating Factor (GM-CSF), has shown promising results in a phase II clinical trial in reducing cognitive impairment (Potter *et al.*, 2021). Emerging preclinical evidence targeting inflammation and microglia suggest beneficial effects in AD, so further research is needed in order to find targets with translational potential.

3.1. Lipoxins as inflammation solvers.

Lipoxins are pro-resolving molecules, derived from arachidonic acid, and secreted by immune cells such as neutrophils and macrophages (reviewed in Chandrasekharan and Sharma-Wali, 2015). Lipoxins can be synthesized following three pathways (reviewed in Serhan *et al.*, 2015) (**Figure 10**). In the first pathway, arachidonic acid is converted to leukotriene A_4 by 5-LOX, and then leukotriene A_4 is converted to lipoxins A_4 and B_4 (LXA_4, LXB_4) by 12- or 15-LOX. In the second pathway, arachidonic acid is converted to 15-hydroxyperoxyeicosatetraenoic acid (15-HPETE) by 15-LOX, and subsequently converted to LXA_4 and LXB_4 by 5-LOX. The third pathway is triggered by aspirin via COX-2 acetylation. Acetylated COX-2 turns arachidonic acid into 15-HPETE, and then 15-HPETE is converted to epi-lipoxins A_4 and B_4, also known as aspirin-triggered lipoxins (ATL), by 5-LOX. Interestingly, aspirin has a sex-dependent impact on ATL production. ATL increases in plasma of aged women taking low doses of aspirin, while it decreases in men (Chiang *et al.*, 2006).

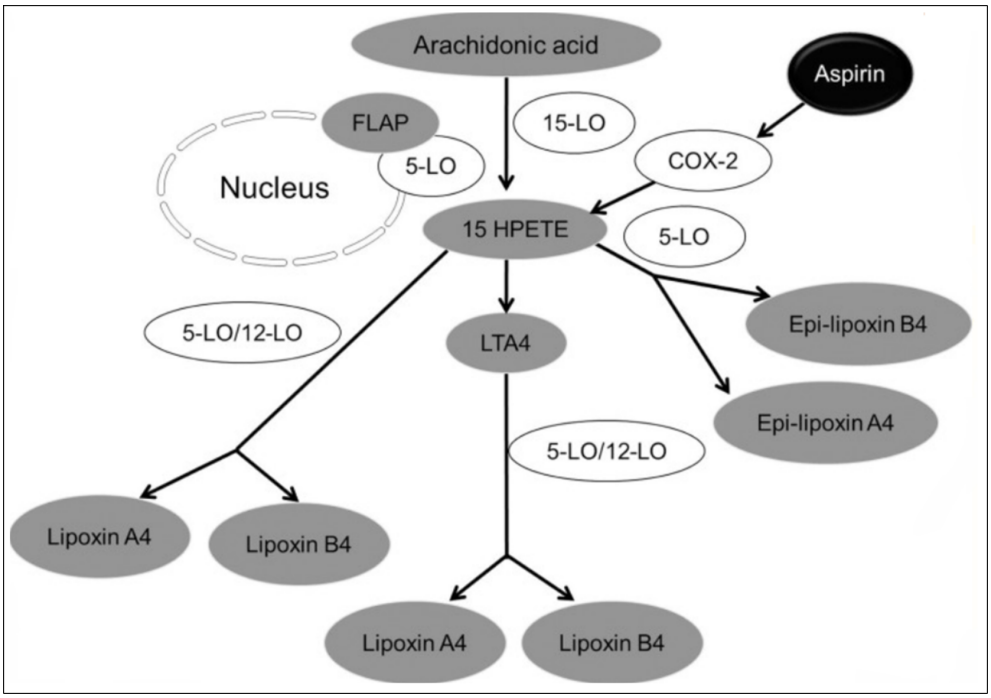

Figure 10. Lipoxins biosynthesis pathways. Arachidonic acid is converted into lipoxins by three main lipoxygenases, 5-, 12- and 15-LOX (LO in the image). Aspirin can also trigger lipoxin synthesis via COX-2 acetylation (adapted from Chandrasekharan and Sharma-Wali, 2015).

Lipoxins carry out their anti-inflammatory actions binding the high-affinity Formyl Peptide Receptor 2 (ALX/FPR2), a G protein-coupled receptor (Romano *et al.*, 2015; Ge *et al.*, 2020). Binding to ALX/FPR2 triggers numerous cytoplasmic signaling pathways. For instance, lipoxins control cytokine release through pathways like NF-κB (reviewed in Chandrasekharan and Sharma-Wali, 2015).

AD is characterized by a deficient resolution of inflammation. AD patients display lower levels of LXA_4 in CSF and hippocampus compared to control individuals, and these levels negatively correlate with Mini-mental state examination (MMSE) scores. Interestingly, Aβ has the ability to bind ALX/FPR2 and trigger antagonistic effects (Le *et al.*, 2001). Several authors have demonstrated that lipoxins can countervail Aβ-induced pro-inflammatory effects. In mice injected with $Aβ_{42}$, LXA_4 reduce the overexpression of IL-1β and TNF-α in a dose-dependent manner (Wu *et al.*, 2011). The effects of LXA_4 and ATL have been extensively studied in microglia. BV2 cells, a microglia-like murine cell line, drastically increase pro-inflammatory cytokines and oxidative stress in response to LPS, while treatment with ATL can reduce expression of iNOS, IL-1β and TNF-α via inhibition of NF-κB nuclear translocation (Wang *et al.*, 2011). ATL is also capable of reducing LPS-induced ROS generation in BV2 cells by NOX2, inhibiting the translocation of subunit $p47^{phox}$ to the cell membrane (Wu *et al.*, 2012*b*). Lipoxins have anti-inflammatory effects on astrocytes as well. ATL reduces the production of nitric oxide and prostaglandins in LPS-treated astrocytes *in vitro* (Yao *et al.*, 2014), and LXA_4 induces astrocyte-mediated neuroprotection following acute injury in a mouse model of glaucoma (Livne-Bar *et al.*, 2017).

Several authors have tested the neuroprotective effects of lipoxins in AD mouse models. In APP/PS1 mice, stimulation of COX-2 acetylation increased the production of LXA_4 and resolvins E1 and D1 (Lee *et al.*, 2020). This increase of SPMs led to resolution of inflammation, enhanced microglial phagocytosis and cognitive improvements. 5xFAD mice, which carry APP mutations Swedish, Florida (I716V), and London (V717I) as well as PSEN1 mutations M146L and L286V, exhibit low levels of SPMs in the hippocampus. Combined treatment with resolvin E1 and LXA_4 strongly reduced soluble Aβ levels, amyloid plaque load, astrogliosis and microgliosis (Kantarci *et al.*, 2018). Treatment also reduced

levels of pro-inflammatory cytokines IFN-γ, IL-1β and TNF-α, among others. On the other hand, treatment with ATL has also proved positive results. In Tg2576 mice, ATL improved memory, reduced brain Aβ levels and restored synapses (Medeiros *et al.*, 2013). ATL also reduced astrogliosis and microgliosis, as well as pro-inflammatory cytokines and chemokines. Later on, the same research group found that ATL also has a positive effect on cognition, Aβ levels, tau phosphorylation and gliosis in 3xTg mice (Dunn *et al.*, 2015). This evidence supports the idea of lipoxins as a therapeutic option for AD and other neurodegenerative diseases (reviewed in Martini *et al.*, 2014).

3.2. Complement receptor CR3 as microglial modulator.

Receptor CR3, also known as Mac-1, is a glycoprotein member of the β_2 integrin family that, in the intact brain, is exclusively expressed by resident microglia (Hickman *et al.*, 2013). The β_2 integrin family of adhesion molecules contains four members: $\alpha_L\beta_2$ (LFA-1, CD11a/CD18), $\alpha_M\beta_2$ (CR3, Mac-1, CD11b/CD18), $\alpha_X\beta_2$ (CR4, CD11c/CD18) and $\alpha_D\beta_2$ (CD11d/CD18). All of them form heterodimers that contain one CD18 β_2 subunit and one CD11 α subunit (reviewed in Vorup-Jensen and Jensen, 2018). These receptors participate in key inflammation processes, including cell adhesion and migration. The functionality of this family does not rely much on upregulation and decay of gene expression, but rather subunits are stored in the cytoplasm and recruited to the cell membrane upon activation of immune cells. B_2 integrins use outside-in and inside-out bidirectional signaling. Outside-in refers to the response to ligands by activation of intracellular signaling, while inside-out refers to the modulation of their activity by signals generated by other receptors (reviewed in Hynes, 2002).

CR3 is the most promiscuous receptor of the β_2 integrin family, with almost 100 reported ligands including fibrinogen, Intercellular adhesion molecule-1, iC3b and Aβ (reviewed in Lamers *et al.*, 2021). It mediates migration of immune cells into inflammation sites, NF-κB activation and phagocytosis of opsonized complexes (reviewed in Ross, 2002). In response to infections like *P. gingivalis*, CR3 induces the release of TNF-α, IL-1β and IL-6 (Hajishengallis *et al.*, 2008).

CR3 is also involved in NOX2 activation. Genetic ablation of CD11b reduces ROS generation by blocking the recruitment of subunit $p47^{phox}$ to the cell membrane in response to α-synuclein (Zhang *et al.*, 2007; Hou *et al.*, 2018) and Aβ (Zhang *et al.*, 2011). Both subunits, CD11b and CD18, are elevated in microglia of AD patients (Akiyama and McGeer, 1990). Numerous publications have demonstrated the role of CR3 in Aβ clearance and complement-mediated synaptic elimination, not only in AD but other neurological diseases such as West Nile neuroinvasive disease (Vasek *et al.*, 2016). Genetic ablation of CR3 *in vitro* and *in vivo* results in impaired fibrillar Aβ uptake by microglia. Czirr *et al.* recently demonstrated that even when CR3 absence impairs phagocytic activity in microglia, Aβ accumulation is reduced in APP mice due to an increased secretion of extracellular Aβ degrading enzymes like tissue plasminogen activator (PLAT) (Czirr *et al.*, 2017). Other researchers have demonstrated that ablation of CR3 reduces complement-dependent synapse loss in J20 and APP/PS1 mice (Hong *et al.*, 2016). All of these reports confirm the key role of CR3 in AD pathogenesis, and its potential as therapeutic target.

Small molecule XVA143, developed by Hoffmann-La Roche (Switzerland), is an allosteric antagonist of β_2 integrins that binds the CD18 subunit and blocks transmission of activation signals to the CD11 subunit (Yang *et al.*, 2006). This inhibitor has been used to study immune cells adhesion and migration in response to pathogens. XVA143 changes cell morphology from polarized to round shapes in lymphocytes and impairs adhesion and transendothelial migration *in vitro* and *in vivo* (Salas *et al.*, 2004; Yang *et al.*, 2006). In models of bacterial infections, XVA143 recovers CR3-mediated cytokine production and CR3-dependent phagocytosis (Hajishengallis *et al.*, 2007; D'Elia *et al.*, 2011). XVA143 is also capable of blocking microglial phagocytosis *in vitro* and improving microglia-mediated pruning of neuronal networks in brain development in mice (Madore *et al.*, 2020).

4. *In vitro* models for the study of Aβ pathology and neurodegeneration.

AD is a multifactorial disease that involves many interacting pathways, which frequently potentiate each other as the disease progresses (reviewed in Gong *et al.*, 2018). The contribution of glial cells to the development of the pathology is becoming more relevant every day, so understanding the crosstalk between neurons and glial cells is essential in order to identify new pathways with therapeutic potential. In animal models of AD, targeting glial cells and neuroinflammation can ameliorate the disease progression. For instance, genetic ablation of microglial CD11b results in reduced plaque deposition and enhanced extracellular Aβ degradation in APP/PS1 mice (Czirr *et al.*, 2017). Selective deletion of ApoE in astrocytes ameliorates memory deficits and reduced Aβ accumulation (Zheng *et al.*, 2017). Pharmacological interventions with anti-inflammatory drugs also reduce memory deficits and amyloid plaque load (Gasparini *et al.*, 2005; Ou *et al.*, 2018).

Although *in vivo* animal models allow researcher to study the full complexity of neuroinflammation, they are expensive and require long time frames. Besides, large numbers of animals are required. On the other hand, *in vitro* models such as cell lines, primary cultures and, more recently, induced pluripotent stem cells (iPSCs) require shorter time frames and are more susceptible to experimental manipulation, but cell cultures of only one cell type lack the complexity of whole organisms. In order to have *in vitro* models with a little bit more complexity, co-culture models were developed in recent years. In addition, conditioned media have been extensively used to study cell communication via secreted factors. For instance, conditioned media from microglia stimulated with Aβ stimulates neurotoxicity via secreted TNF-α and NMDA receptors in mouse primary neurons (Floden *et al.*, 2005). Secreted factors from astrocytes can also affect neuronal function. Conditioned media from immature astrocytes containing thrombospondins-1 and -2 promotes synaptogenesis in retinal ganglion cells (Christopherson *et al.*, 2005). In another study, conditioned media from microglia activated with LPS rich in IL-1α, TNF and C1q, induced reactive astrocytes that had reduced capacity to promote neuronal survival (Liddelow *et al.*, 2017). Other researchers have developed co-culture

models where two different cell populations share the medium but have no physical contact. For instance, Du *et al.* (2018) established a co-culture with iPSC-derived neurons and astrocytes transwell inserts, and they found that astrocytes rescued mitochondrial dysfunction in neurons treated with mitochondrial toxins. A relevant advantage of co-cultures is that they can alleviate the drastic transcriptomic modifications that cells, especially microglia, undergo due to experimental manipulation. Transcriptome profiling of human and mouse microglia have shown significant alterations in expression of genes related to immune signaling and stress responses, among other, in *in vitro* conditions compared to *ex vivo* (Gosselin *et al.*, 2017). Microglia *in vitro* and in the brain can also differ in their response to Aβ. Murine primary microglia display rapid transcriptional changes in response to Aβ, that *in vivo* microglia do not display, suggesting that primary microglia poorly recapitulate physiological conditions (McFarland *et al.*, 2021). Fortunately, studies have shown that culturing microglia with neurons can mitigate this problem. iPSC-derived microglia express key microglia-specific markers and display dynamic when co-cultured with neurons, and they also show a more anti-inflammatory cytokine profile than monocultures (Haenseler *et al.*, 2017).

In recent years, complex co-cultures have been developed with up to three cell populations in order to study intercellular communication. Park *et al.* (2018) developed a triculture model using human neurons, astrocytes, and microglia in a 3D microfluidic platform. With this model, they could recapitulate AD features such as Aβ aggregation, tau phosphorylation, and microglial recruitment. They were also able to demonstrate neurotoxic effects derived from neuron-glia interactions. In a different study, a tri-culture system with hiPSC-derived neurons, microglia and astrocytes was used to study complement component C3 (Guttikonda *et al.*, 2021). They observed that crosstalk between microglia and astrocytes that resulted in increased C3 in AD conditions. Given that not all laboratories have access to newly developed iPSC-derived cells, there is a need for an inexpensive and straightforward murine triple co-culture model that can be used to study cellular communication in the context of amyloid pathology and neuroinflammation.

Hypothesis and objectives

Hypothesis and objectives

Neuroinflammation, driven mainly by microglia and astrocytes, is a key feature in Alzheimer's disease progression that contributes to Aβ accumulation, tau hyperphosphorylation and, ultimately, neurodegeneration. Several studies have reported that oxidative stress can trigger mechanisms that cause neurotoxicity, and other immune pathways such as the complement system can directly participate in synaptic elimination. Microglia are central to these events, which makes these cells an interesting target in the pursuit of new therapeutic targets. In addition, there are limited *in vitro* models that allow researchers to study neuroinflammation in the context of neuron-glia interactions, which would also be a powerful tool for drug discovery. In this project, we hypothesize that modulating microglial function and enhancing inflammation resolution can reduce oxidative damage and glial activation, leading to an improvement of AD pathology. In order to investigate this hypothesis, we plan to target microglial function exploring two different pathways, inflammation resolution and the complement system, using pharmacological interventions. On the other hand, we aim to advance *in vitro* models focused on the communication between neurons and glial cells, which will allow us to better approach neurodegeneration and neuroinflammation in the context of AD.

To test this hypothesis, the following specific objectives were addressed:

Aim 1. To evaluate the effect of pro-resolving mediator aspirin-triggered 15(R)-lipoxin A_4 (ATL) on oxidative stress, mitochondrial dysfunction and glial activation in Alzheimer's disease.

Aim 2. To analyze the role of complement receptor CR3 in microglial function in the context of amyloid β pathology, using the allosteric antagonist XVA143.

Aim 3. To establish and characterize a triple co-culture model with neurons, astrocytes and microglia that can be used to study neuroinflammation.

Experimental procedures

Experimental procedures

1. Human samples.

Prefrontal cortex samples of seven control subjects and nine AD patients were obtained from the Neurological tissue bank Hospital Clínic IDIBAPS Biobank (Barcelona, Spain) (**Table 1**). AD samples were classified as Braak stages V-VI (Braak and Braak, 1995), and as stage C by CERAD classification (Mirra *et al.*, 1991). Patients signed informed consents for clinical investigations, which were performed in accordance with the Declaration of Helsinki.

Table 1. Information of control and AD subjects, categorized as Braak stages V-VI and CERAD stage C. *Time (h) between death and sample extraction.

Case number	Ref. number	Braak stage (NFT)	CERAD (senile plaque)	Gender	Age	Mean age ± S.E.M.	Post-mortem delay*
C1	1378	-	-	M	78	78.5 ± 3.72	6:00
C2	1491	-	-	M	83		13:00
C3	1648	-	-	M	73	79.2 ± 1.3	6:10
C4	1733	-	-	M	76		11:30
C5	1536	-	-	M	79		4:45
C6	1423	-	-	F	82		5:00
C7	695	-	-	M	80		10:00
AD1	1286	V	C	M	79	76.4 ± 0.6	5:00
AD2	1622	V	C	M	76		5:00
AD3	1392	VI	C	M	77		5:00
AD4	1445	VI	C	F	73		3:30
AD5	1456	VI	C	F	74		3:30
AD6	1645	VI	C	F	77		5:30
AD7	1198	VI	C	F	77		5:00
AD8	1585	VI	C	F	74		6:30
AD9	1637	VI	C	M	78		7:00

2. Animals.

All animal experiments were compliant with the requirements of the Animal Ethic and Welfare Committees of the University of the Basque Country (UPV/EHU), following the Spanish Real Order 53/2013 and the European Communities Council Directive 2010/63/EU. Animals were housed with standard 12 h light cycle and *ad libitum* access to water and food. All possible efforts to maintain animal wellbeing and to reduce the number of animals used were made.

Primary cultures and organotypic cultures were obtained from wild-type Sprague Dawley rats. *In vivo* procedures were performed with wild-type 129 mice and 3xTg mice. 3xTg mice carry the Swedish mutation in the human APP, the presenilin knock-in mutation (PS1M146V), and TauP301L mutant transgene (TauP301L) (Oddo *et al.*, 2003*b*). Both homozygous and heterozygous mice for the PS1M146V mutation were used. For the treatments with ATL, 16-17 months old female mice were distributed into four groups: wild-type mice vehicle (N = 4), wild-type mice treated with ATL (N = 4), 3xTg mice vehicle (N = 7) and 3xTg mice treated with ATL (N = 7). Animals were given a daily intraperitoneal injection for eight weeks with 10 µg/kg ATL or vehicle (0.05% ethanol), in saline.

3. Cell cultures.

3.1. Primary cultures of cortical neurons.

Neurons were obtained from E18/E19 Sprague-Dawley rat embryos as previously described (Ibarretxe *et al.*, 2006), with modifications. Cortical lobes were digested in 0.2% trypsin and 0.02% deoxyribonuclease I in Hanks' balanced salts (HBSS) no calcium, no magnesium (Sigma-Aldrich, MO, USA) for 5 min at 37ºC. The enzymatic digestion was stopped with neurobasal medium supplemented with 2% B27 (Gibco, MA, USA) (Brewer *et al.*, 1993), 1% penicillin-streptomycin (Lonza, Switzerland) and 0.5 mM L-glutamine (referred to as B27 neurobasal from now on), plus 10% fetal bovine serum (FBS) (Gibco, MA, USA). After incubating 10 min at 37ºC, cells were centrifuged for 5 min at 200 g, and the resultant pellet was resuspended in B27 neurobasal plus 10% FBS. Cells were mechanically dissociated by trituration (20 strokes with 21, 23 and 25-gauge needles), filtered through a 41 µm nylon mesh and seeded onto poly-D-lysine-coated (PDL) (Sigma-Aldrich, MO, USA) plates as needed. After one day, the medium was replaced by serum-free B27 neurobasal. Cultures were maintained at 37°C and 5% CO_2 for eight to nine days *in vitro* (DIV) before use.

3.2. Primary cultures of cortical glia.

Mixed glial cell cultures were prepared from the cortical lobes of P0/P1 Sprague-Dawley rat pups as described elsewhere (McCarthy and De Vellis,

1980). Cortical lobes were incubated with 0.2% trypsin and 0.01% deoxyribonuclease I in HBSS for 15 min at 37ºC. The digestion was stopped by adding Iscove's modified Dubecco's medium (IMDM) (Gibco, MA, USA) with 1% antibiotic-antimycotic, plus 10% HyClone™ FBS (Cytiva, MA, USA). Cells were centrifuged for 6 min at 250 g, and the pellet was resuspended in IMDM plus 10% HyClone™ FBS. This pellet was mechanically dissociated by trituration (20 strokes with 21 and 23-gauge needles) and recentrifuged. Cells were resuspended in IMDM plus 10% HyClone™ FBS and plated onto PDL-coated 75 cm^2 flasks (about four cortices per flask). One day later, the medium was replaced by fresh IMDM plus 10% HyClone™ FBS for primary astrocytes, or by Dulbecco's modified Eagle medium (DMEM) high glucose, pyruvate (Gibco, MA, USA) with 1% penicillin-streptomycin plus 10% FBS for primary microglia. Cultures were maintained at 37°C and 5% CO_2 for one week to collect astrocytes, or for two weeks to collect microglia.

Primary astrocytes were obtained from source mixed glial cultures as previously described (McCarthy and De Vellis, 1980; Alberdi *et al.*, 2013). After one week of incubation, medium was removed and flasks were washed twice with HBSS. Cells were trypsinized by incubating with trypsin and Ethylenediamine tetraacetic acid (EDTA) 0.05% (Gibco, MA, USA) for 5 min at 37ºC. IMDM plus 10% HyClone™ FBS was added to stop the enzymatic reaction and cells were centrifuged for 5 min at 300 g. The cell pellet was resuspended in IMDM plus 10% HyClone™ FBS, and astrocytes were plated onto PDL-coated plates as needed. Serum-free medium was added one day prior to experimentation. Cultures were maintained at 37°C and 5% CO_2.

Primary microglia were also obtained from source mixed glial cultures as previously described (Majumdar *et al.*, 2011). After growing for two weeks, microglia were harvested by orbital shaking for 1 h at 400 rpm in DMEM plus 10% FBS. Cells were centrifuged for 6 min at 250 g, and plated onto PDL-coated plates as needed. Serum-free medium was added one day prior to experimentation. Cultures were maintained at 37°C and 5% CO_2.

3.3. Triple co-culture procedures.

In order to obtain all possible combinations of neuron-glia co-cultures (neuron-astrocyte, neuron-microglia and neuron-astrocyte-microglia), primary cell cultures were prepared as stated above. Adequate conditions for the co-cultures were optimized based on previous publications (Hernangómez *et al.*, 2012; Correa *et al.*, 2013). The co-cultures started by plating astrocytes onto PDL-coated plates. Three days later, when a monolayer of astrocytes was obtained, neurons were plated in a proportion of 5 neurons to 2 astrocytes. After 24 h, the medium was replaced by serum-free B27 neurobasal, and antimitotic agents 5-Fluoro-2′-deoxyuridine and Uridine (FdU/U) (Sigma-Aldrich, MO, USA) were added at a concentration of 10μM to control glial proliferation. Cells were incubated at 37ºC and 5% CO_2, and more FdU/U could be added every two days for further control of proliferation. After six days, microglia were added to the cultures in a proportion of 1 microglia to 5 neurons (**Figure 11**). Cultures were ready to process for analysis two days later. The co-cultures were maintained for a total of 13 DIV at 37°C and 5% CO_2. In order to make all conditions comparable, serum-free B27 neurobasal medium was added to the cultures one day prior to experimentation. For experiments with oligomeric $A\beta_{1-42}$ (oAβ), a treatment of 3 μM oAβ for 24 h was used.

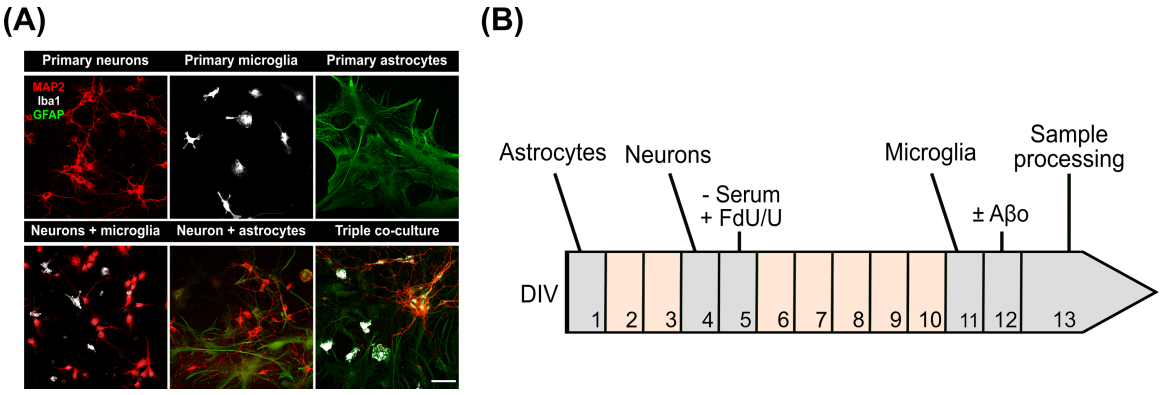

Figure 11. (A) Representative image of the triple co-culture model. MAP2 was used to mark neurons, GFAP to mark astrocytes and Iba1 to mark microglia. Scale bar = 50 μm. **(B)** Protocol diagram. Triple co-cultures started with a monolayer of astrocytes. Neurons were plated three days later (ratio: 5 neurons to 2 astrocytes), and microglia were added six days after that (ratio: 1 microglia to 5 neurons). Cultures were incubated for a total of 13 DIV before analysis.

3.4. BV2 cell line.

The immortalized murine microglia-like cell line BV2 was maintained in DMEM medium plus 10% FBS and 1% penicillin-streptomycin at 37°C and 5% CO_2. When cultures were 80-90% confluent, they were incubated with trypsin-EDTA 0.05% for 5 min at 37ºC. DMEM plus 10% FBS was added to stop the enzymatic reaction and cells were centrifuged for 3 min at 300 g. The cell pellet was resuspended in DMEM plus 10% FBS and plated onto PDL-coated plates, or tissue culture Petri dishes for further passages. One day prior to experimentation, serum-free medium was added to the cells.

3.5. Organotypic cultures.

Organotypic cultures were obtained from P5/P6 Sprague-Dawley rat pups and prepared as previously described (Stoppini *et al.*, 1991; Ortiz-Sanz *et al.*, 2020), with modifications. Brains were extracted in ice cold HBSS, and chopped into 400 µm thick slices using a vibratome (VT 1200S, Leica, Germany). Corticostriatal and hippocampal slices were isolated under a dissection microscope, and transferred onto Millicell culture inserts with 30 mm in diameter (EMD Millipore, MA, USA). In the lower compartment of the inserts, neurobasal medium was added (supplemented with 25% horse serum (HS), 22% HBSS, 1% D-glucose 550 mM, 1% L-glutamine 200 mM and 1% antibiotic-antimycotic). Slices were maintained for 14-15 DIV at 37°C and 5% CO_2, and the medium was renewed every other day. One day before treatment, medium was replaced by neurobasal supplemented with 1% HS, 25% HBSS, 1.8% D-glucose 550 mM, 1% L-glutamine 200 mM and 1% antibiotic-antimycotic. For experiments with oAβ, slices were treated with 3 µM oAβ for 24 h.

4. Conditioned media experiments.

Primary neurons, astrocytes and microglia were seeded separately, at a density of $1x10^6$ cells in Petri dishes, 60 mm in diameter. One day later, medium was replaced by serum-free B27 neurobasal, and cells were incubated for three days at 37ºC and 5% CO_2. Supernatants were collected, stored at -80ºC and filtered with a 22 µm nylon mesh before use.

5. Preparation of soluble oligomeric $A\beta_{1-42}$.

Synthetic Aβ oligomers were prepared as previously reported (Dahlgren *et al.*, 2002; Alberdi *et al.*, 2010). Briefly, $A\beta_{1-42}$ (Bachem, Switzerland) was dissolved in hexafluoroisopropanol (HFIP) (Sigma-Aldrich, MO, USA) to an initial concentration of 1 mM. It was distributed into aliquots and HFIP was removed under vacuum in a speed vac system before the peptide film was stored dry at -80ºC. For the aggregation protocol, the peptide was resuspended in anhydrous dimethylsulfoxide (DMSO) (Invitrogen, MA, USA) to a concentration of 5 mM. Hams F-12 pH 7.4 (Biowest, France) was added to reach the final concentration of 100 µM. Oligomers were obtained after incubating at 4ºC for 24 h.

6. Reagents.

For cell-based assays, the following compounds were used: ATL (5(S),6(R),15(R)-trihydroxy-7,9,13-trans-11-cis-eicosatetraenoic acid) (#90415, Cayman Chemical, MI, USA); peptide Boc-2 (Boc-Phe-Leu-Phe-Leu-Phe) (10 µM, #072-01, Phoenix Pharmaceuticals, CA, USA); NOX2 inhibitor gp91 ds-tat (1 µM, #AS-63818, Anaspec, Belgium) and scrambled gp91 ds-tat (1 µM, #AS-63821, Anaspec, Belgium); general NOX inhibitor diphenyleneiodonium chloride (DPI) (0.5 µM, D2926, Sigma-Aldrich, MO, USA); serine and cysteine protease inhibitor leupeptin (100 µM, #78435, Thermo Fisher Scientific, MA, USA); and XVA143 (1 µM, kindly provided by Hoffmann-La Roche). 0.05% ethanol was used as vehicle for ATL.

7. Cellular viability and toxicity assays.

7.1. Calcein AM and Ethidium homodimer-1 quantification.

Cell viability assays were performed as previously described (Davenport *et al.*, 2010), with modifications. After treatment with compounds of interest for 24 h, cells were stained with Calcein AM (Thermo Fisher Scientific, MA, USA) to obtain the number of live cells, and NucBlue™ (Hoechst 33342) (Invitrogen, MA, USA) to stain nuclei and normalize the data. Cells were incubated with 1 nM Calcein AM and 4% NucBlue™ for 30 min at 37ºC, and then washed twice with

1X phosphate-buffered saline (PBS) (125 mM NaCl, 19 mM Na_2HPO_4, 8 mM KH_2PO_4 in double distilled water (ddH_2O), pH 7.4). Fluorescence was detected using a microplate reader Synergy HT and the software KC4 (BioTek, VT, USA). Excitation/emission ranges were 485/530 nm for Calcein AM and 360/460 nm for NucBlue™.

For cytotoxicity assays, primary microglia and BV2 cells were treated with increasing concentrations of XVA143 for 24 h. Then, they were incubated for 30 min at 37ºC with 2 µM Calcein AM and 4 µM Ethidium homodimer-1 (Thermo Fisher Scientific, MA, USA) to obtain the number viable and dead cells, respectively. Cultures were washed twice with 1X PBS and fluorescence was detected using the excitation/emission ranges 485/530 nm for Calcein AM and 530/645 nm for Ethidium homodimer-1.

7.2. Propidium iodide quantification.

Corticostriatal slices were treated with 100 nM ATL and 3 µM oAβ for 24 h, being ATL added 1 h before the oAβ. Cell death was analyzed by quantifying the uptake of propidium iodide (PI). Slices were incubated with 10 µM PI for 2 h at 37ºC, and washed twice with neurobasal medium. Then, slices were washed with 1X PBS and slices were imaged using a fluorescence microscope Cell Observer Z1 (Zeiss, Germany) and captured using an EM CCD camera C9100-13 (Hamamatsu, Japan). PI was excited with 510-560 nm light and images were acquired at 610 nm. Images were analyzed using open source ImageJ/Fiji software, and the PI uptake was expressed as the mean integrated density per total area of each slice.

8. Measurement of Reactive Oxygen Species.

Primary neurons, primary microglia and corticostriatal slices were treated with 3 µM oAβ for 1 h and the corresponding reagents. Reagents were added 1 h before oAβ. Probes for ROS detection were added in the last 30 min of incubation. 5,6-chloromethyl-2'7dichlorodihydrofluorescein diacetate acetyl ester (CM-H2DCFDA) (30 µM, Invitrogen, MA, USA) was used to assess intracellular

ROS levels, and MitoSOX™ Red (5 µM, Invitrogen, MA, USA), to asses mitochondrial superoxide radicals. 4% NucBlue™ was also added for normalization. After the incubation, cultures were washed twice with 1X PBS and fluorescence was measured using a microplate reader Synergy HT and the software KC4. Excitation/emission ranges were 490/520 nm for CM-H2DCFDA, 510/580 nm for MitoSOX™, and 360/460 nm for NucBlue™.

Isolated mitochondria (50 µl per sample) were plated on a PLD-coated 48-well plate and centrifuged at 2,000 rpm (equivalent to approx. 300 g) for 20 min at 4ºC. Once attached to the plate, isolated mitochondria were incubated in Buffer A (composition below, section 15) with 1 µM MitoSOX™ at 37ºC for 30 min. The plate was washed twice with Buffer A and read using a microplate reader at 510/580 nm.

9. Measurements of oxygen consumption rate.

Oxygen consumption rate (OCR) in primary neurons and microglia was analyzed using an XF96 Extracellular Flux Analyzer and the XF Cell Mito Stress Test kit (Seahorse Bioscience, Agilent Technologies, CA, USA) as described previously (Alberdi *et al.*, 2018), and according to manufacturer's instructions. Before the addition of inhibitors, the baseline cellular OCR was measured, from which basal respiration (BR) was derived by deducting non-mitochondrial respiration. Then 2 µM oligomycin, which is a complex V inhibitor, was added and OCR was measured again. ATP-linked respiration (ATP), was calculated by deducting the oligomycin rate from the baseline cellular OCR, as well as proton leak respiration (PL), by deducting non-mitochondrial respiration from the oligomycin rate. Next, 2 µM carbonyl cyanide-p-trifluoromethoxyphenyl-hydrazone (FCCP), which is an uncoupling agent that collapses the proton gradient, was added. Maximal respiratory capacity (MUR) was derived by deducting non-mitochondrial respiration from the FCCP OCR rate. Lastly, 0.5 µM rotenone/antimycin A (Rot/AA), inhibitors of complexes I and III respectively, were added to derive non mitochondrial respiration (**Figure 12**).

Primary neurons and primary microglia ($2x10^4$ – $3x10^4$ cells per well) were seeded and cultured according to methods stated above, on PDL-coated XF96 plates (Seahorse Bioscience, Agilent Technologies, CA, USA). Cells were treated with 50 nM ATL and 3 μM oAβ in serum-free B27 neurobasal medium for 24 h. One hour before the OCR measurements, cells were incubated at 37ºC in absence of CO_2 with XF Base medium (Seahorse Bioscience, Agilent Technologies, CA, USA), supplemented with 1 mM pyruvate, 2 mM glutamine and 10 mM glucose. Baseline recordings of OCR were made, followed by the sequential addition and recordings of 2 μM oligomycin, 2 μM FCCP and 0.5 μM rot/AA. Measurements were normalized to the number of cells per well by staining nuclei with NucBlue™ like detailed above (section 6.1).

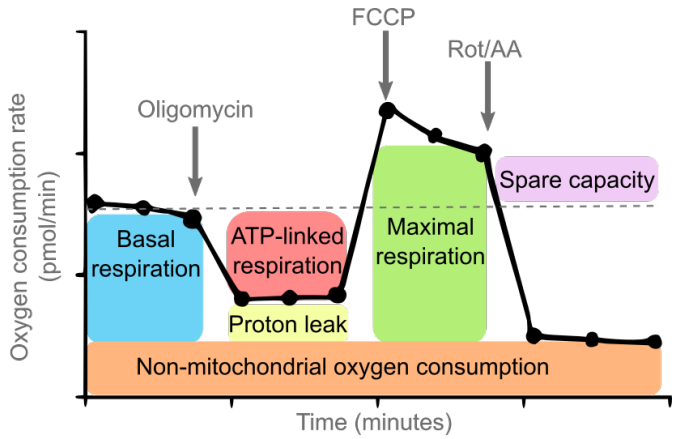

Figure 12. Mitochondrial respiration parameters, with Seahorse XF96 Extracellular Flux Analyzer. Basal respiration is calculated by deducting non-mitochondrial oxygen consumption to the baseline OCR (dashed line) rate. ATP-linked respiration is calculated by deducting the OCR rate after oligomycin to the baseline. Proton leak is calculated by deducting non-mitochondrial respiration from the oligomycin rate. Maximal respiratory capacity is calculated by deducting non-mitochondrial respiration from the OCR rate after FCCP. Non-mitochondrial oxygen consumption is the OCR rate after Rot/AA.

10. Superoxide dismutase activity assay.

Superoxide dismutase (SOD) activity was measured using a colorimetric assay based on tetrazolium salt WST-1 (ab65354, abcam, UK), following manufacturer's instructions. Primary neurons ($2x10^6$ per condition) and primary microglia ($5x10^5$ per condition) were treated with 100 nM ATL and 3 μM oAβ for 2 h, being ATL added 1 h before oAβ. Then, cells were harvested and lysed using Pierce™ RIPA buffer with Halt™ Protease & Phosphatase Inhibitor Cocktail

(Thermo Fisher Scientific, MA, USA), and centrifuged at 14,000 g for 5 min at 4ºC. Supernatants were collected for the colorimetric assay. Blanks and samples were added to a 96-well plate. 200 µl of WST working solution and 20 µl of enzyme working solution were added, and the plate was incubated at 37ºC for 20 min. Output was measured at OD450 nm on a microplate reader Synergy HT and the software KC4. SOD activity was also measured in isolated mitochondria and cytosolic fractions extracted from mouse brains, following the same protocol.

11. Scratch wound assay.

Cellular migration was assessed using scratch wound assay as previously described (Xu *et al.*, 2016). Primary microglia and BV2 cells were cultured in monolayer until 90-95% confluent. One day prior to the assay, serum-free medium was added to avoid more proliferation. The day of the assay, a scratch wound was produced in the center of each well using a 200 µl pipette tip. Cells were imaged at time point 0 h, using an EVOS® FL Cell Imaging System (Thermo Fisher Scientific, MA, USA). Immediately after, cultures were treated with 1 µM XVA143 for 16 h. Images were taken again at time 16 h, and the number of cells migrated to the wound were counted using open source ImageJ/Fiji software.

12. Transwell migration assay.

Transwell migration assay was performed as previously described (Choi *et al.*, 2015), with modifications. Primary microglia and BV2 cells ($4x10^4$ – $5x10^4$ cells per condition) were seeded onto Corning® Transwell membrane inserts (8 µm pore, Sigma-Aldrich, MO, USA). One day prior to the assay, serum-free medium was added to avoid proliferation. 1 µM XVA143 was put in the lower chamber and cells were incubated for 16 h. Cells that did not migrate from the top surface of the transwells were removed using a cotton swab. Cells that migrated to the bottom surface were fixed with 100% methanol for 10 min, then washed with 1X PBS and stained using Hematoxylin solution (Sigma-Aldrich, MO, USA) for 20 min. After washing twice with ddH_2O, cells were imaged using EVOS® FL Cell Imaging System. The number of cells that migrated to the bottom surface of the transwells were counted using open source ImageJ/Fiji software.

13. RNA extraction and RT-qPCR.

Primary microglia were cultured in 24-well plates ($1x10^5$ cells per condition) according to methods stated above. One day prior to treatment, serum-free B27 Neurobasal was added. Cells were treated with 1 μM XVA143 and 3 μM oAβ for 24 h. XVA143 was added one hour before oAβ. Then, cells were harvested using 300 μl of TRIzol™ reagent (Invitrogen, MA, USA) and kept at -80ºC before use.

RNA extractions and RT-qPCR were performed at the Unit of Gene expression, Service of genomics and proteomics, Sgiker General research services of the University of the Basque Country (UPV/EHU). RNA was extracted from the samples using chloroform and isopropanol, with glycogen RNA grade (Thermo Fisher Scientific, MA, USA) as carrier. Then, samples were washed twice with 75% ethanol, and pellet was resuspended in RNAse-free ultrapure H_2O. RNA quantity was measured using a fluorimeter QuBit 2.0 and the QuBit RNA BR Assay (Invitrogen, MA, USA). RNA quality and integrity was analyzed using LabChip GX Touch (PerkinElmer, Germany), in combination with a Standard RNA Reagent kit.

For the synthesis of cDNA, Fluidigm Reverse Transcription master mix kit (Fluidigm, CA, USA) was used. 10 ng of RNA were added, following the kit instructions, to obtain a final cDNA concentration of 2 ng/μl. Preamplification of the cDNA samples was required prior to qPCR. Multiplex PCR Kit (Qiagen, Germany) was used for preamplification, adding 1.25 μl of the original cDNA and 50 nM of primers in order to obtain a final volume of 5 μl per sample. The preamplification PCR protocol was: 15 min at 95ºC, 14 cycles of 15 s at 95ºC, 4 min at 60ºC and 4ºC ∞. After preamplification, samples were treated with Exonuclease I (Thermo Fisher Scientific, MA, USA) to remove unincorporated primers. The Exonuclease I protocol was: 30 min at 37ºC (digestion), 15 min at 80ºC (Exonuclease I inactivation), and 4ºC ∞. Finally, samples were diluted 1:5 with low EDTA TE buffer (10 mM Tris, 0.1mM EDTA, pH 8.0) prior to analysis.

The gene expression analysis was performed with BioMark HD nanofluidic qPCR kit (Fluidigm, CA, USA) in combination with 48.48 Dynamic Array™ IFC

(Fluidigm, CA, USA). Specific pairs of primers were designed using NCBI Primer-BLAST tool (**Table 2**).

Table 2. Primers used for RT-PCR.

#	Gene (rat)	ID NCBI	Forward (5' > 3')	Reverse (5' > 3')
1	B2M	24223	CACCGAGACCGATGTATATGCTT	TTACATGTCTCGGTCCCAGG
2	UbC	50522	CCTGACAGGCAAGACCATCAC	ACACCATTGAAAATGTCAAGGCA
3	GAPDH	24383	GAAGGTCGGTGTCAACGGATTT	CAATGTCCACTTTGTCACAAGAGAA
4	HPRT1	24465	ATGGACTGATTATGGACAGGACTGA	ACACAGAGGGCCACAATGTG
5	CicA	308435	CAAAGTTCCAAAGACAGCAGAAAA	CCACCCTGGCACATGAATC
6	ITGAM	25021	TACTTTGGGCAGTCTCTGAGTG	ATGGTTGCCTCCAGTCTCAGCA
7	ITGB2	309684	AGTCCCAGTGGAACAACGAC	AGCACTGGGGCTAGCTGTAA
8	IL1B	24494	TGTCTTGCCCGTGGAGCTT	AGGTCGTCATCATCCCACGA
9	TNFA	24835	GGTGTCTGTGCCTCAGCCTCTT	GCCATGGAACTGATGAGAGGGAG
10	IL10	25325	CTGCGACGCTGTCATCGATTT	AGTAGATGCCGGGTGGTTCAA
11	IFNg	25712	TAACTATTTTAACTCAAGTGGCATAGATGTG	GCCAGTTCCAGATATCCTCCAAG
12	CD40	171369	AAGGTGGTCAAGAAACCAAAGGA	GCTGACACCCATGCAACGTC
13	CD74	25599	GGACCCGTGAACTACCCACA	TGTCCAGTGGCTCTTTAGGTGG
14	TGFB1	59086	TGCCAACTTCTGTCTGGGGC	TGCGACCCACGTAGTAGACG
15	TGFB3	25717	AATCTGTTCCGGGCGGAGTT	GCGCTGCTTGGCTATGTGTT
16	MRC1	4360	AGGTTCCGGTTTGTGGAGCA	AGAGCCATCCATCTGACCGC
17	CD33	690492	GAGCAGGCGTCACTGTGGAA	TCAGGAGCTTGACTGCTGCC
18	CD36	29184	TGGCTAGCTGATTACTTCTGTGTAG	TGCAGCAGAATCAAGGAAGAGCA
19	AGER	81722	GCTATCGGAATTGTCGATGAGG	GCTGTGAGTTCAGAGGCAGGAT
20	PLAT	25692	ATCAGCTCAGCGCCAAGGAGAAG	TTTTGCTCCCCGTTTCTTCCGT
21	MMP2	81686	ATGCCTTTGCTCGGGCCTTA	CCGTCCTTGCCGTCAAATGG
22	MMP9	81687	AAAGGCCATTCGTTCACCGC	GCGGCAAGTCTTCGGTGTAG
23	IDE	25700	CAAACCTCTCCTTCCAAGTCAGC	TGTTCTCCGAGGTGCTCTGCAT
24	LAMP1	25328	GCCTACCTGCCGAGTAGCAA	GGGTTTGTGGGCACAAGTGG
25	C1QA	298566	CAAAGGAGAGAGAGGGGAGCC	GGTCCCTGATATTGCCCGGAT
26	C1QB	29687	AACCAGGCACTCCAGGGATAAA	TTGTAGTCTCCAGAGCCACCTT
27	C1QC	362634	GATGGACTTCAGGGGCCCAA	CATGGGGCCGTTTTTCCCAC
28	C2	24231	TGGGCATCAGTCGGAACAGA	CTCTCGCCGTCCTTCTTGGA
29	C3	24232	GAAGATCCTGAGTGCGCCAAG	CTTTGTCCATCCTCCTTTCCATCA
30	C4A	24233	GTCCTGTTGCAAGTTTGCTGAG	CGCACGAGAATGTCATCTTCATC
31	TYROBP	361537	TTCCTGTCCTCCTGACTGTGG	AGGAACATTCGCATCCTGGGTAA
32	SPI1	366126	TGGAGACAGCCATAGCGATCA	CAGCTCCGTGAAGTGGTTCT
33	STAT1	25124	GGAAGCACCAGAACCGATGGA	ATGGGAAGCAGGTTTTCTGTGC
34	IRF8	292060	CGTCCCCGAGGAAGAGCAAA	GCCACACTCCATCTCCGTGA
35	MSR1	498638	GACGCACGTTCCATGACAGC	AGAGCGACGAGGGCAACTTT

Detection of each amplification was performed using the non-specific fluorochrome EvaGreen® Master Mix SsoFastTM Supermix with Low ROX (Bio-Rad Laboratories, CA, USA). The final concentration of primers, both forward and reverse, was 200 nM. The RT-PCR protocol was: Stage 1, Hot Start 1 min at 95ºC, Ramp rate 5.5ºC/s; Stage 2, Ramp rate 5.5ºC/s, 30 cycles of 5 s at 96ºC, 20 s at 60ºC; Stage 3 (melting curve), 3 s at 60ºC, 60ºC-95ºC Ramp rate 1ºC/3 s. The software used to obtain Ct (cycle threshold) data was Real-Time PCR Analysis Software 4.1.3 (Fluidigm, CA, USA). Five housekeeping gene candidates were evaluated using GenEx vs 6.1 software (MultiD Analyses, Sweden). The most stable housekeeping genes were B2M and UbC, so their geometric means were used to normalize the Ct data from the target genes.

14. Sample collection from mice.

After the corresponding treatments, biological samples were harvested from mice (**Figure 13**). First, cerebrospinal fluid (CSF) was extracted from the cisterna magna, which is the space between the cerebellum and the dorsal surface of the medulla oblongata. Briefly, mice were anesthetized and placed on a platform with the head forming a 60º angle with the body. Layers of muscles in the back of the neck were carefully dissected using forceps and micro scissors. If bleeding occurred, cotton swabs were used to help stop it. Once the dura over the cisterna magna was exposed, a sharpened glass capillary (#3-000-203-G/X, Drummond Scientific Company, PA, USA) was inserted at a 35-45º angle. Typically, 2-10 µl of CSF were obtained, and stored at -80ºC. In the next step, blood was extracted from the heart and the mouse was transcardially perfused with 0.9% saline solution. Typically 400-700 µl of blood were obtained. Blood samples were collected in EDTA-coated tubes and centrifuged at 3,000 g for 15 min at 4ºC. Plasma (supernatants) and erythrocyte (pellets) samples were stored at -80ºC for further analysis. After this, brain hemispheres were dissected. One hemisphere was fixed by immersion in 4% paraformaldehyde (PFA) for 24 h at 4ºC, and sectioned into 40 µm thick slices using a vibratome (Leica VT 1200S). Slices were kept at -20ºC in storage solution (30% glycerol, 30% ethylene glycol, 10% PB 0.4M and 30% ddH_2O) until use for immunohistochemical staining. The other hemisphere was dissected into cortex, hippocampus, entorhinal cortex and cerebellum, frozen in dry ice and stored at -80ºC until use for protein extraction.

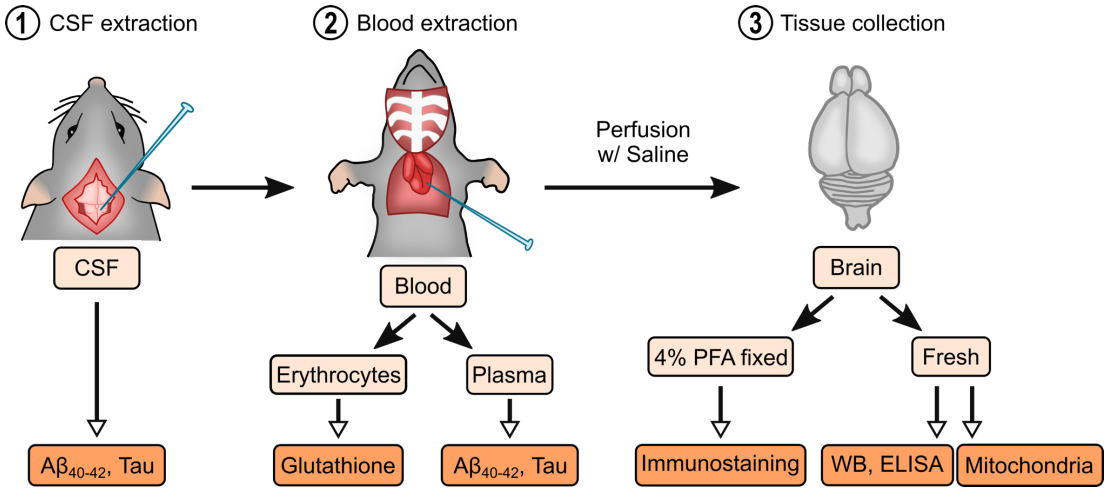

Figure 13. Diagram of the sample collection protocol in mice, and the experimental use of each sample. First, CSF was extracted from the cisterna magna. Then, blood samples were collected from the heart and mice were perfused with 0.9% saline solution. After centrifugation of blood samples collected in EDTA-coated tubes, plasma (supernatants) and erythrocyte (pellets) samples were obtained. After this, brains were dissected. One hemisphere was fixed in 4% PFA and sectioned into slices, and the other was dissected into cortex, hippocampus, entorhinal cortex and cerebellum and stored fresh. CSF and plasma samples were used to quantify Aβ and tau, erythrocytes were used to quantify levels of oxidized/reduced glutathione. Brain slices were used for immunohistochemistry, and fresh brain tissue was used to isolate mitochondria, and to perform western blot (WB) and ELISA assays.

15. Mitochondria isolation from mouse brain.

Mitochondria were isolated from mouse brains as previously described (Xu *et al.*, 2018). 100-200 mg of brain tissue were washed twice with cold 1X PBS, and homogenized in 800 µl of 1X PBS with a glass homogenizer. Samples were centrifuged at 800 g for 5 min at 4ºC. Supernatants (~0.5 ml) were transferred to new tubes containing 1.5 ml of cold Buffer A (0.5 mM EGTA, 250 mM mannitol, 5 mM HEPES, 0.1% bovine serum albumin (BSA), 1% Halt™ Protease & Phosphatase Inhibitor Cocktail in ddH_2O, pH 7.4), and centrifuged at 15,000 g for 10 min at 4ºC. Supernatants were collected as cytosolic fractions, and pellets were collected as mitochondrial fractions. Mitochondrial fractions were washed twice with 1 ml of Buffer A, recentrifuged at 15,000 g for 10 min at 4ºC, and resuspended in 0.5 ml of Buffer A. Protein concentrations were determined by DC Protein Assay (Bio-Rad Laboratories, CA, USA), based on the Lowry assay. Samples were immediately used to perform ROS detection assays, and the rest was stored at -80ºC for further analysis. For western blotting, samples were diluted in 2X sodium dodecyl sulfate (SDS) sample buffer and boiled at 95°C for 5 min before use.

16. Glutathione quantification in erythrocyte samples.

Total glutathione (γ-L-glutamyl-L-cysteinylglycine) and its oxidized form were quantified in mouse erythrocyte samples using a colorimetric assay based on 5,5'-dithiobis-(2-nitrobenzoic acid) (#38185, Sigma-Aldrich, MO, USA), following manufacturer's instructions. Erythrocyte samples were centrifuged at 1,000 g for 10 min at 4ºC. Supernatants were discarded, and four times the

sample volume of 5% 5-sulfosalicylic acid (SSA) was added to lyse the erythrocytes. Samples were centrifuged at 8,000 g for 10 min at 4ºC, and supernatants were transferred to new tubes. Ten times the sample volume of ddH_2O was added to reduce the concentration of SSA to 0.5%, and samples were used at a 1:10 dilution for the assay. Two sets of samples were prepared (200 µl each); one to measure oxidized glutathione (GSSG), and the other to measure total glutathione. The first set was treated with 4 µl of masking solution to mask reduced glutathione (GSH), while the other set was untreated. Standard curves for GSSG and GSH were prepared. 40 µl of standard solutions and the two sets of samples were added to a 96-well plate, and incubated with 120 µl of Buffer solution at 37ºC for 1 h. Then, 20 µl of substrate, 20 µl of coenzyme and 20 µl of enzyme were added to each well. After incubation at 37ºC for 10 min, absorbance was read at 412 nm using a microplate reader Synergy HT and the software KC4. GSSG and GSH concentrations in each sample were calculated using the equation of the best-fit straight line through the standard points for each case. Total glutathione concentration was calculated as the sum of GSSG plus GSH.

17. Protein extraction and detection by western blotting.

17.1. Protein extraction from cell cultures.

Lysates from cell cultures were prepared using a cell scraper (Corning, NY, USA) and Pierce™ RIPA buffer, with Halt™ Protease & Phosphatase Inhibitor Cocktail and 0.5 M EDTA solution (Thermo Fisher Scientific, MA, USA). Protein concentrations were determined by DC Protein Assay. Samples were diluted in 2X SDS sample buffer and boiled at 95°C for 5 min before use.

17.2. Biotinylation of cellular membranes.

Biotinylation assays were performed in order to examine proteins localized on the cell surface, as described previously (Arancibia-Cárcamo *et al.*, 2006). Primary microglia were seeded as described above ($2x10^5$ cells per condition). One day prior to treatment, serum-free medium was added to the cultures. Cells were treated with 100 nM ATL or 1 µM XVA143, and 3 µM oAβ for 24 h. ATL and XVA143 were added one hour before oAβ. After the treatment, cells were cooled

on ice to prevent receptor endocytosis during the biotinylation protocol, and washed three times in cold rinsing buffer (1 mM $CaCl_2$, 0.5 mM $MgCl_2$ in 1X PBS pH 7.4). Then, cultures were incubated in rinsing buffer containing 1 mg/ml sulfo-NHS-SS-biotin (Thermo Fisher Scientific, MA, USA) for 30 min at 4ºC with gentle agitation. After the biotinylation step, cells were washed three times in cold quenching buffer (50 mM glycine, 0.5% BSA in rinsing buffer), and incubated with quenching buffer for 30 min at 4ºC with gentle agitation, in order to remove non-incorporated biotin. After the quenching step, cells were washed twice with 1X PBS and lysed using Pierce™ RIPA buffer, with Halt™ Protease & Phosphatase Inhibitor Cocktail and 0.5 M EDTA (100 µl per condition). Lysates were transferred to tubes and incubated for 1 h at 4ºC using a rotating mixer. Afterwards, samples were centrifuged at 12,000 g for 20 min. 10 µl of the supernatant was used as total lysate fraction. The remaining 90 µl were incubated with NeutrAvidin™ UltraLink™ Resin beads (Thermo Fisher Scientific, MA, USA) overnight at 4ºC (30-35 µl per sample) using a rotating mixer. Samples were washed twice with Pierce™ RIPA buffer, twice with high-salt Pierce™ RIPA buffer (500 mM NaCl in RIPA pH 7.5), and twice with 1X PBS, each step followed by a quick centrifugation at 1,000 rpm (equivalent to approx. 200 g), for 1 min. Finally, biotinylated proteins were eluted with 2X SDS sample buffer by heating at 95ºC for 5 min, and centrifuged at 15,000 g for 5 min. Biotinylated fractions were normalized using α-tubulin in their corresponding total lysate fractions.

17.3. Protein extraction from mouse tissue.

Brain tissue was homogenized using Pierce™ RIPA buffer, with Halt™ Protease & Phosphatase Inhibitor Cocktail and 0.5 M EDTA. Tissue samples were homogenized in 200 µl of RIPA with a glass homogenizer, and sonicated with an ultrasonic cell disrupter (25 pulses, 80% amplitude and 0.6 cycle). Then, tubes were centrifuged at 12,000 g for 15 min at 4ºC. Supernatants (RIPA fractions) were transferred to new tubes and pellets were further processed for insoluble Aβ detection. Pellets were extracted with 400 µl 2% SDS buffer and sonicated (10 s, 80% amplitude and 12% power). Samples were heated for 5 min at 90ºC and centrifuged at 100,000 g for 30 min. Supernatants (SDS fractions) were transferred to new tubes and stored at -80ºC until use. Protein

concentrations were determined by DC Protein Assay in the RIPA fractions. Samples were diluted in 2X SDS sample buffer and boiled at 95°C for 5 min before use for western blotting.

17.4. Western blotting.

Protein lysates were separated by SDS-PAGE. For a low number of samples, Bolt™ 4 to 12%, Bis-Tris, mini protein gels and Bolt™ MES SDS Running buffer (Invitrogen, MA, USA) were used for electrophoresis, and transferred to iBlot™ 2 PVDF or nitrocellulose membranes (Invitrogen, MA, USA), followed by immunoblotting. For a high number of samples, Any kD™ Criterion™ TGX Stain-Free™ midi protein gels (Bio-Rad Laboratories, CA, USA) and Tris-Glycine buffer (25 mM Tris pH 8.3, 192 mM glycine, 0.1% SDS in ddH_2O) were used. Gels were transferred to Trans-Blot Turbo Midi Nitrocellulose transfer packs (Bio-Rad Laboratories, CA, USA).

Membranes were blocked in 1X tris-buffered saline (TBS) (20 mM Tris, 137 mM NaCl in ddH_2O pH 7.4), with 0.05% Tween-20 (TBS-T) (Acros organics, Belgium) and 5% fat-free milk for 1 h at room temperature (RT). Membranes were incubated overnight with primary antibodies in the same solution at 4ºC, then washed three times with TBS-T and incubated with horseradish peroxidase-linked (HRP) secondary antibodies for 1 h at RT (**Table 3**). Finally, membranes were washed three times with TBS-T. Immunoreactive bands were detected using enhanced electrochemical luminescence SuperSignal™ West Dura or Femto (Thermo Fisher Scientific, MA, USA) and a ChemiDoc™ MP Imaging System (Bio-Rad Laboratories, CA, USA). Band intensities were quantified using the company's Image Lab® software. All protein intensities were divided by the corresponding α-tubulin or Glyceraldehyde-3-phosphate dehydrogenase (GAPDH) measurement for normalization, unless otherwise stated. In the case of protein samples from isolated mitochondria, target proteins were normalized using mitochondrial marker voltage-dependent anion channel 1 (VDAC1). When needed, membranes were stripped of antibodies using Restore™ Western Blot Stripping Buffer (Thermo Fisher Scientific, MA, USA) for 15-20 min at RT, followed by two washes with 1X TBS and reblotting. Quantification of respiratory

chain components was carried out using Total OXPHOS rodent WB antibody cocktail (abcam, UK) and AffiniPure Goat secondary antibody according to manufacturer's instructions.

Table 3. Antibodies used for Western blotting.

Antibody	Supplier	Cat. #	Conc.	RRID
Rabbit anti-CD11b	abcam	ab128797	1:500	Not found
Mouse anti-IL1β	Cell Signaling	#12242	1:500	AB_2715503
Rat anti-Caspase 1 (4B4.2.1)	Gift by Genentech	-	1:1,000	Not found
Mouse anti-NLRP3	AdipoGen	AG-20B-0014	1:1,000	AB_2490202
Rabbit anti-ASC/TMS1	Cell Signaling	#67824	1:1,000	AB_2799736
Mouse anti-α Tubulin	abcam	ab7291	1:2,000	AB_2241126
Mouse OXPHOS WB Cocktail	abcam	ab110413	1:250	AB_2629281
Rabbit anti-VDAC	Cell Signaling	#4866	1:500	AB_2272627
Mouse anti-DRP1	Santa Cruz Bio.	sc-271583	1:200	AB_10659110
Mouse anti-MFN2	abcam	ab56889	1:500	AB_2142629
Rabbit anti-CD18	Invitrogen	PA5-95027	1:500	AB_2806833
Rabbit anti-PSD95	abcam	ab18258	1:500	AB_444362
Mouse anti-VGlut1	Synaptic Systems	#135511	1:750	AB_887879
Rabbit anti-MRC1	abcam	ab64693	1:1,000	AB_1523910
Mouse anti-Argl	Santa Cruz Bio.	sc-166920	1:200	AB_10609486
Rabbit anti-Iba1	Wako	016-20001	1:500	AB_839506
Mouse anti-GAPDH	Sigma-Aldrich	MAB374	1:2,000	AB_2107445
HRP Sheep anti-mouse IgG	Sigma-Aldrich	A6782	1:5,000	AB_258315
HRP Goat anti-rabbit IgG	Cell Signaling	#7074	1:5,000	AB_2099233
AffiniPure Goat anti-mouse IgG	Jackson Immuno	115-035-003	1:5,000	AB_10015289

18. Preparation of tissue extracts from human samples.

Frozen samples from human prefrontal cortex (**Table 1**) were lysed with the non-denaturing buffer Lysis Buffer 3 (IS007, Cloud-Clone Corp., TX, USA). They were rinsed in cold 1X PBS and weighed. Lysis Buffer was added in a 1:20 ratio (1 ml of Lysis Buffer for 20 mg of tissue). Samples were homogenized with a glass homogenizer and sonicated with an ultrasonic cell disrupter (25 pulses, 80% amplitude and 0.6 cycle). Homogenates were centrifuged at 10,000 g for 5 min at 4ºC, and supernatants were collected. Protein concentrations were determined by DC Protein Assay.

19. ELISA Assays.

19.1. Quantification of IL-1β in cell culture supernatants.

Pro-inflammatory cytokine IL-1β present in supernatants was measured using an appropriate ELISA kit (ab100767, abcam, UK), following manufacturer's instructions. Supernatant samples from cell cultures (density of $1x10^5$ - $1x10^6$ cells) were used undiluted. In brief, 100 µl of standards and samples were added into a 96-well plate pre-coated for rat IL-1β and incubated for 2.5 h at RT with gentle shaking. The plate was washed with Washing solution, and 100 µl of Biotinylated IL-1β detection antibody were added to each well. After incubating for 1 h at RT with gentle shaking, the plate was washed again, and 100 µl of HRP-Streptavidin solution were added to each well. The plate was incubated for 45 min at RT with gentle shaking and washed before adding 100 µl of TMB One-Step substrate reagent to each well. After a 30 min incubation at RT with gentle shaking in darkness, 50 µl of Stop solution were added and the plate was read immediately in a fluorimeter at 450 nm. The standard curve was obtained plotting the standard concentration (pg/ml) on the x-axis and absorbance on the y-axis. IL-1β concentrations in each sample were calculated using the equation of the best-fit straight line through the standard points.

19.2. Quantification of TGF-β1 in cell culture supernatants.

Transforming Growth Factor-β1 (TGF-β1) in supernatants was measured by an ELISA kit (ab119558, abcam, UK), following manufacturer's instructions. Amicon® Ultracel® 3K centrifuge filters (EMD Millipore, MA, USA) were used to concentrate the amount of proteins present in the cell culture supernatants (density of $1x10^5$ - $1x10^6$ cells), due to low levels of TGF-β1. For the ELISA assay, 20 µl of all samples were prediluted with 180 µl of Assay buffer plus 20 µl of 1N HCl for 1h, and then neutralized with 20 µl 1N NaOH. 100 µl of standards and samples were added into a 96-well plate pre-coated for rat TGF-β1 and incubated for 2 h at RT with gentle shaking. The plate was washed with Washing solution, and 100 µl of Biotin-Conjugated Antibody were added to each well. After incubating for 1 h at RT with gentle shaking, the plate was washed again, and 100 µl of Streptavidin-HRP solution were added to each well. The plate was

incubated for 30 min at RT with gentle shaking and washed before adding 100 µl of TMB Substrate Solution to each well. After a 30 min incubation at RT with gentle shaking in darkness, 100 µl of Stop solution were added and the plate was read immediately in a fluorimeter at 450 nm. The standard curve was obtained plotting the standard concentration (pg/ml) on the x-axis and absorbance on the y-axis. TGF-β1 concentration in each sample was calculated using the equation of the best-fit straight line through the standard points.

19.3. Quantification of $A\beta_{42}$ in culture supernatants and mouse synaptosomes.

Supernatant samples from cell cultures (density of $1x10^5$ - $1x10^6$ cells) and supernatants from organotypic cultures (two slices per well) were quantified. $A\beta_{1-42}$ was also measured in post-synaptic synaptosomal fractions (PSD fractions) previously extracted from human cortices (**Table 1**) by Dr. Carolina Ortiz-Sanz (samples were diluted between 1:1 and 1:5 for the assay). Concentrations of human $A\beta_{1-42}$ were measured using an ELISA kit (KHB3441, Invitrogen, MA, USA), following manufacturer's instructions. In brief, 50 µl of standards and samples and 50 µl of human $A\beta_{42}$ detection antibody were added into a pre-coated 96-well plate and incubated for 3 h at RT with gentle shaking. The plate was washed with Washing solution, and 100 µl of anti-rabbit IgG HRP antibody were added to each well. After incubating for 30 min at RT with gentle shaking, the plate was washed again, and 100 µl of Stabilized chromogen solution were added to each well. The plate was incubated for 30 min at RT with gentle shaking in the dark. Finally, 100 µl of Stop solution were added and the plate was read immediately in a fluorimeter at 450 nm. The standard curve was obtained plotting the standard concentration (pg/ml) on the x-axis and absorbance on the y-axis. $A\beta_{1-42}$ concentrations in each sample were calculated using the equation of the best-fit straight line through the standard points.

19.4. Quantification of $A\beta_{42}$ in mouse brain tissue.

Concentrations of human $A\beta_{1-42}$ present in 3xTg mouse entorhinal cortex and hippocampus homogenates were measured using an ELISA kit (EZHS42,

EMD Millipore, MA, USA), following manufacturer's instructions. In brief, 50 µl of standards, quality controls and tissue homogenates (1 µg/µl per sample) plus 50 µl of Antibody Conjugate Solution were added into a pre-coated 96-well plate and incubated overnight at 4ºC without shaking. Next day, the plate was washed with Washing solution, and 100 µl of Enzyme Conjugate Solution were added to each well. After incubating for 30 min at RT with gentle shaking, the plate was washed again, and 100 µl of Substrate Solution were added to each well. The plate was incubated for 20-30 min at RT with gentle shaking in the dark. Finally, 100 µl of Stop solution were added and the plate was read immediately in a fluorimeter at 450 nm and 590 nm. Absorbance was calculated as the read at 450 minus the read at 590 nm. The standard curve was obtained plotting the standard concentration (pg/ml) on the x-axis and absorbance on the y-axis. $A\beta_{1-42}$ concentrations in each sample were calculated using the equation of the best-fit straight line through the standard points.

19.5. Multiplex quantification of cytokines in mouse brain tissue.

Pro-inflammatory cytokines IL-1β, IL-5, IL-6, KC/GRO and TNF-α were measured in mouse cortex and hippocampus using an MSD® Multi-spot panel based on electrochemiluminescence (K15048D, V-PLEX, Meso Scale Discovery, MD, USA), following manufacturer's instructions. Tissue homogenates (samples in Pierce™ RIPA buffer) were diluted 1:1 with Diluent 41. 50 µl of standards and samples were added into a pre-coated 96-well plate and incubated with shaking at room temperature for 2 h. Next, the plate was washed with 1X PBS plus 0.05% Tween-20, and 25 µl of Detection Antibodies were added to each well. After incubating with shaking at room temperature for 2 h, the plate was washed again, and 150 µl of 2X Read Buffer T were added per well. The plate was analyzed on a MESO QuickPlex SQ 120 (Meso Scale Discovery, MD, USA), which calculated the concentration of each target (pg/ml) using supplied in-assay standard curves.

19.6. Quantification of lipoxin LXA_4 in human samples.

Levels of endogenous lipoxin LXA_4 were measured in human cortices by an ELISA kit (CEB452Ge, Cloud-Clone Corp., TX, USA) based on competitive

inhibition, following manufacturer's instructions. For a total protein concentration range of 1-15 µg/µl, a dilution of 1:5 was performed before the assay. For the ELISA assay, 50 µl of standards and samples plus 50 µl of Detection Reagent A were added into a pre-coated 96-well plate, and incubated for 1 h at 37ºC. The plate was washed with Washing solution, and 100 µl of Detection Reagent B were added to each well. After incubating for 30 min at 37ºC, the plate was washed again, and 90 µl of Substrate solution were added to each well. The plate was incubated for 20 min at 37ºC in darkness. Finally, 50 µl of Stop Solution were added and the plate was read in a fluorimeter at 450 nm. The standard curve was obtained plotting the standard concentration (log pg/ml) on the x-axis and absorbance on the y-axis, taking into account that the intensity of color developed was inversely proportional to the concentration of LXA_4. LXA_4 concentration in each sample was calculated using the equation of the best-fit straight line through the standard points. Data was normalized using the weight of each tissue sample.

20. SIMOA Triplex assay in animal plasma and CSF samples.

EDTA plasma and CSF samples were thawed at RT and centrifuged at 10,000 g for 5 min at 4ºC prior to analysis. Levels of $A\beta_{40}$, $A\beta_{42}$ and total Tau (tTau) were measured using the Simoa® Human Neurology 3-Plex A assay (N3PA) (Quanterix, MA, USA) and the automated Simoa® HD-1 analyzer (Quanterix, MA, USA), and following the manufacturer's instructions. Plasma samples were loaded undiluted, and CSF samples were diluted 1:200 before loading. All samples went through a 1:4 on-board automated sample dilution, so that the final dilutions were 1:4 for plasma samples and 1:800 for CSF. All samples were analyzed in duplicate.

21. Immunofluorescence.

21.1. Cell culture immunostaining.

Cell culture coverslips were fixed in 4% PFA for 10 min, and washed twice with 1X TBS. Then, they were permeabilized and blocked in 1X TBS with 1% BSA, 0.5% normal goat serum (NGS) (Palex Medical, Spain) and 0.1% saponin for 1 h. Coverslips were incubated overnight at 4ºC in the same blocking solution with the corresponding primary antibodies (**Table 4**), washed with TBS-T and incubated with Alexa fluorophore-conjugated secondary antibodies at a dilution of 1:500 for 1h at RT (Invitrogen, MA, USA). Samples were mounted using Fluoromont-G (SouthernBiotech, AL, USA).

Table 4. Antibodies used for immunocytochemistry (ICC) and immunohistochemistry (IHC).

Antibody	Supplier	Cat. #	Applic.	Conc.	RRID
Mouse anti-AT8	Invitrogen	MN1020	IHC	1:500	AB_223647
Chicken anti-Synaptophysin	Synaptic Systems	#101006	IHC	1:500	AB_2622239
Rabbit anti-Homer1	Synaptic Systems	#160003	ICC, IHC	1:500	AB_887730
Rabbit anti-C1q	abcam	ab182451	ICC, IHC	1:500	AB_2732849
Rabbit anti-S100β	Dako	GA50461-2	IHC	1:400	AB_2811056
Rabbit anti-GFAP	Dako	Z0334	IHC	1:4,000	AB_10013382
Rat anti-mouse CD11b	Bio-Rad	MCA711	IHC	1:250	AB_321292
Rabbit anti-Iba1	Wako	019-19741	IHC	1:1,000	AB_839504
Guinea pig anti-Iba1	Synaptic Systems	#234004	ICC	1:500	AB_2493179
Rabbit anti-CD11b	abcam	ab128797	ICC	1:500	Not found
Texas Red™-X phalloidin	Invitrogen	T7471	ICC	1:100	Not found
Mouse anti-Aβ [6e10]	BioLegend	803015	ICC	1:500	AB_2565328
Mouse anti-rat CD11b	Bio-Rad	MCA275	IHC	1:500	AB_321300
Mouse anti-Synaptophysin	BioLegend	#837101	ICC, IHC	1:1,000	AB_2565370
Mouse anti-GFAP	Sigma-Aldrich	MAB3402	ICC	1:1,000	AB_94844
Mouse anti-MAP2	Sigma-Aldrich	M9942	ICC	1:1,000	AB_477256
Rabbit anti-CD18	Invitrogen	PA5-95027	ICC	1:500	AB_2806833
Mouse anti-iNOS	BD Biosciences	#610329	ICC	1:200	AB_397719
Mouse anti-AMIGO2	Santa Cruz Bio.	sc-373699	ICC	1:250	AB_10920216
Rabbit anti-C3	abcam	ab11887	ICC	1:100	AB_298669
Rabbit anti-PSD95	abcam	ab18258	IHC	1:500	AB_444362

21.2. Organotypic cultures immunostaining.

Organotypic hippocampal slices were fixed in 4% PFA for 40 min, and washed twice with 1X PBS. Samples were permeabilized and blocked for 3 h at RT in 1X PBS with 5% NGS and 0.5% Triton-X. Then, they were incubated overnight at 4ºC in 1X PBS 1% NGS and 0.1% Triton-X with primary antibodies

(**Table 4**), washed with 1X PBS and incubated with Alexa fluorophore-conjugated secondary antibodies at a dilution of 1:500 for 2h at RT. Slices were mounted using a bridge mounting technique (Yoon *et al.*, 2010), where two 22 mm x 22 mm coverslips were glued to each end of a glass slide. Organotypic slices were mounted using Fluoromont-G, and a 40 mm x 22 mm coverslip was placed to bridge the gap between the two coverslips without smashing the samples.

21.3. Mouse tissue immunostaining.

Free floating sections of brain tissue were washed three times with 0.1 M PB (23 mM Na_2HPO_4, 90 mM NaH_2PO_4 in ddH_2O, pH 7.4). They were permeabilized and blocked in 0.1 M PB with 4% BSA and 0.25% Triton-X for 1 h, and then incubated overnight at 4ºC in 0.1 M PB with 4% BSA with the corresponding primary antibodies (**Table 4**). Next, sections were washed with 0.1 M PB and incubated with Alexa fluorophore-conjugated secondary antibodies at a dilution of 1:500 for 1h at RT. Samples were mounted using Fluoromont-G. In the case of staining with Thioflavin S (ThS) (Sigma-Aldrich, MO, USA), slices were incubated with 0.001% ThS in PB for 15 min, and then washed twice with PB before mounting.

22. Confocal microscopy and image processing.

Images were acquired using Leica TCS STED CW SP8X confocal microscope (Leica, Germany). In experiments with multiple fluorophores, channels were scanned sequentially to avoid crosstalk. The same settings were applied to all images within the same experiment. All analyses were carried out using open source ImageJ/Fiji software.

22.1. Synaptic marker analysis.

Synaptic markers were quantified in neuritic segments of primary neurons. In each condition, images were acquired on random fields, and neuritic segments (20 µm in length) were selected from areas where a single process could be outlined. After the background was subtracted and a threshold was applied,

integrated density of each neuritic segment was quantified. For each condition, individual segments were grouped and averaged per field, and all the per field averages were used to calculate the group mean and standard deviation for each condition and experiment. A macro was developed in ImageJ/Fiji software to automate the analysis.

For synaptic puncta colocalization studies, random fields in hippocampal organotypic slices were imaged with the 63X objective and 4X zoom in Leica TCS STED CW SP8X confocal microscope. Each image was deconvoluted to better distinguish synaptic puncta using Huygens Professional software (Scientific Volume Imaging, Netherlands). The number of pre-synaptic, post-synaptic and colocalized puncta (spots where the two synaptic channels overlapped) was determined for each image. The values from each image were averaged to obtain the group mean and standard deviation for each condition and experiment. A macro was developed in ImageJ/Fiji software to automate the analysis.

For synapse quantification in mouse brain tissue, hippocampal CA1 areas were imaged with the 63X objective and 2X zoom in Leica TCS STED CW SP8X confocal microscope. Each image was deconvoluted with Huygens Professional software. The integrated density and the area occupied by the staining were determined for each image. The values from each image were averaged to obtain the group mean and standard deviation for each condition and experiment.

22.2. Neuronal morphology.

For neuronal morphology analyses, Microtubule-Associated Protein 2 positive ($MAP2^+$) cells were used. Single neurons were selected in areas where a single cell could be identified. Images were converted to binary and then skeletonized. The function Summarize skeleton in ImageJ/Fiji software was used to obtain the average branch length, the number of branches and the number of junctions in each neuron. The values of each individual cell were used to obtain the group mean and standard deviation for each condition and experiment.

22.3. Glial morphology.

In order to study astrocytic morphology *in vitro*, GFAP was used to stain astrocytes. They were selected in areas where a single astrocyte could be identified. After images of individual cells were transformed into binary, the tool Outline was used to automatically draw the cell shape. Morphology parameters like density (number of pixels of foreground color divided by the total number of pixels in the convex hull), span ratio (a measure of shape, as ratio of major and minor axes for the convex hull) and circularity were quantified using the Fractal Analysis FracLac plugin available in ImageJ/Fiji software as previously described (Young & Morrison, 2018). The values from individual cells were averaged to obtain the group mean and standard deviation for each condition and experiment.

For glial morphology in mouse brain tissue, $GFAP^+$ astrocytes and $Iba1^+$ microglia were quantified. Stack images were taken in hippocampal CA1 areas, and they were deconvoluted using Huygens Professional software. Next, maximal projections of the stack images were obtained, and individual cells were cropped. These crops were converted to binary and then skeletonized. The function Summarize skeleton in ImageJ/Fiji software was used to obtain the average branch length, the number of branches and the number of junctions in each cell. The same crop images were used to obtain the cells' outlines and measure morphological parameters using the FracLac plugin as described above. The values of each individual cell were used to obtain the group mean and standard deviation for each condition and experiment.

22.4. Quantification of areas and intensities.

To quantify the expression levels of targets in cell cultures, the specific markers MAP2, GFAP and Iba1 were used to identify and define the area occupied by neurons, astrocytes and microglia, respectively. Then, the integrated density of each target was measured inside that delimited area. Images were acquired on random fields. A minimum of 20 individual cells were analyzed per condition. The integrated density of individual cells was averaged and divided by the total number of cells to obtain the integrated density per cell group mean and standard deviation for each condition and experiment.

In order to quantify the area occupied by astrocytes (marked with S100β and GFAP) and microglia (marked with CD11b and Iba1) in mouse brain tissue, as well as C1q puncta, stack images of hippocampal CA1 area and cortex were taken and then deconvoluted using Huygens Professional software. Mean projections of the stacks were used to determine area occupied and integrated density data.

For ThS stainings, stack images of the subiculum area were taken. Maximal projections of the stacks were used to determine the number of Aβ plaques and the area occupied by those plaques. In the case of AT8 stainings, images of the hippocampal pyramidal layer were used to determine area and integrated density.

23. Statistical analysis.

GraphPad Prism 8 software was used to perform all statistical analyses (GraphPad Software, CA, USA). In graphs, data were presented as mean ± standard error of the mean (SEM), and scaled so that the average value for the corresponding control was 100%. Each independent experiment was coded with a different color for better visualization in the case of experiments with paired sets of data. All data sets were tested for normality and homoscedasticity. Two-tailed Student's t test was used to compare two experimental groups. Comparisons between more than two groups were performed by one-way Analysis of variance (ANOVA), followed by post hoc test. If one or more data points were missing when comparing more than two groups, mixed-effect model was used to perform the analysis. Statistical significance was represented as $p<0.05$ (*), $p<0.01$ (**), $p<0.001$ (***) and $p<0.0001$ (****).

Results

Results

1. Pro-resolving mediator ATL reduces oxidative stress, mitochondrial dysfunction and AD neuropathology.

1.1. $A\beta_{1-42}$ oligomers increase ROS generation through NOX2 enzyme.

Aβ oligomers induce ROS generation in neurons and glial cells via nicotinamide adenine dinucleotide phosphate oxidases (NOX), mainly NOX2 (Shelat *et al.*, 2008; Li *et al.*, 2013). In order to validate this, we used primary cultures of neurons and microglia to measure intracellular ROS generation after treatment with oAβ and two different NOX inhibitors. DPI is a potent inhibitor of the NOX family that engages their heme and flavin cofactors, while peptide gp91 ds-tat is a specific NOX2 inhibitor that blocks the interaction between the transmembrane domain and its activator $p47^{phox}$ (Reis *et al.*, 2020). In primary neurons, we found that 3 μM oAβ for 1 h significantly increased intracellular ROS generation compared with controls (135.1 ± 9.6 vs 100 ± 6.0%; $p<0.01$; n = 5), while the presence of 1 μM gp91 ds-tat and 0.5 μM DPI prevented this increase. Besides, oAβ was still able to increase ROS generation in the presence of scrambled peptide gp91 ds-tat (113.2 ± 13.3 vs 85.5 ± 11.3%; $p<0.01$; n = 5), which confirmed the specificity of this inhibitor (**Figure 14A**). We made similar observations in primary microglia, where oAβ significantly increased intracellular ROS (130.1 ± 6.8 vs 100 ± 3.3%; $p<0.05$; n = 5), and treatment with gp91 ds-tat and DPI blocked this effect. With scrambled gp91 ds-tat, oAβ still increased intracellular ROS (125.6 ± 9.6 vs 104.1 ± 5.6%; $p<0.05$; n = 5) (**Figure 14B**). These results support the idea that oAβ stimulates ROS production mediated by NADPH oxidase NOX2, both in neurons and microglia.

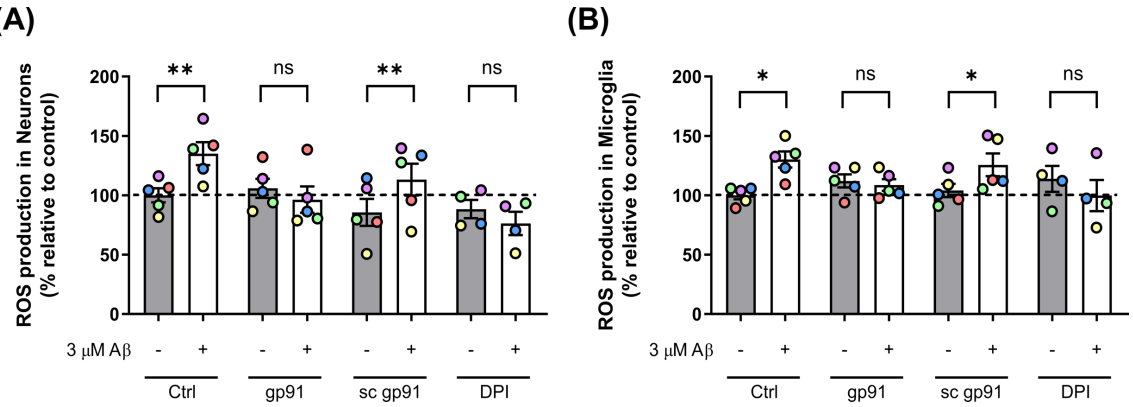

Figure 14. $A\beta_{1-42}$ increases ROS generation by enzyme NOX2 in primary neurons and microglia. Quantification of intracellular ROS with fluorescent probe CM-H2DCFDA in **(A)** primary neurons (n = 5) and **(B)** primary microglia (n = 5). ROS were measured after treating cells for 1 h with 3 μM oAβ, 1 μM gp91 ds-tat, 1 μM scrambled gp91 ds-tat, and 0.5 μM DPI. Values were normalized with the number of cells per condition. Each bar represents the mean ± SEM. * $p<0.05$; ** $p<0.01$; ^{ns} not significant; mixed-effect model. gp91 = gp91 ds-tat; sc gp91 = scrambled gp91.

1.2. Lipoxin ATL ameliorates Aβ-induced ROS accumulation by reducing their production and enhancing their elimination.

Oxidative stress and neuroinflammation can potentiate each other under pathological conditions, so we hypothesized that facilitating inflammation resolution could have a positive effect on Aβ-induced ROS accumulation. In order to test this hypothesis, we focused our attention on lipoxins. We used aspirin-triggered 15-epi-LXA_4 or ATL (5(S),6(R),15(R)-trihydroxy-7,9,13-trans-11-cis-eicosatetraenoic acid), which is a stable and potent analog of LXA_4 (Fierro *et al.*, 2003). The main lipoxins receptor is ALX/FPR2 (Wang *et al.*, 2011; Romano *et al.*, 2015), so we included ALX/FPR2 antagonist Boc-2 in the experimental design in order to confirm the specificity of our target.

Firstly, we performed cell viability assays to ensure non-cytotoxic concentrations of ATL and Boc-2. None of the analyzed concentrations reduced the viability of either neurons or microglia (**Figure 15A, B**), so we decided to choose 100 nM for ATL and 10 μM for Boc-2, based on previous publications (Wu *et al.*, 2012*b*; Zhou *et al.*, 2020). Once we decided the working concentrations, we analyzed the effect of ATL on Aβ-induced ROS generation. We quantified intracellular ROS in primary neurons and microglia after treatment with 3 μM oAβ,

100 nM ATL, or 100 nM ATL together with 10 μM for Boc-2 for 1 h. In primary neurons, we observed that oAβ significantly increased ROS generation compared with controls (132.8 ± 5.6 vs 100 ± 5.8%; p<0.01; n = 4), while ATL prevented this increase. Boc-2 effectively blocked ATL effect, so oAβ was still able to increase ROS compared with Boc-2 alone (136.7 ± 5.4 vs 111.0 ± 5.5%; p<0.01; n = 4) (**Figure 15C**). In the case of primary microglia, intracellular ROS was increased with oAβ (134.8 ± 11.2 vs 100 ± 18.8%; p<0.05; n = 4), while ATL prevented this increase. Boc-2 blocked the action of ATL, which allowed oAβ to increase ROS generation (130.6 ± 14.5 vs 100.7 ± 19.9%; p<0.05; n = 4) compared with Boc-2 alone (**Figure 15D**).

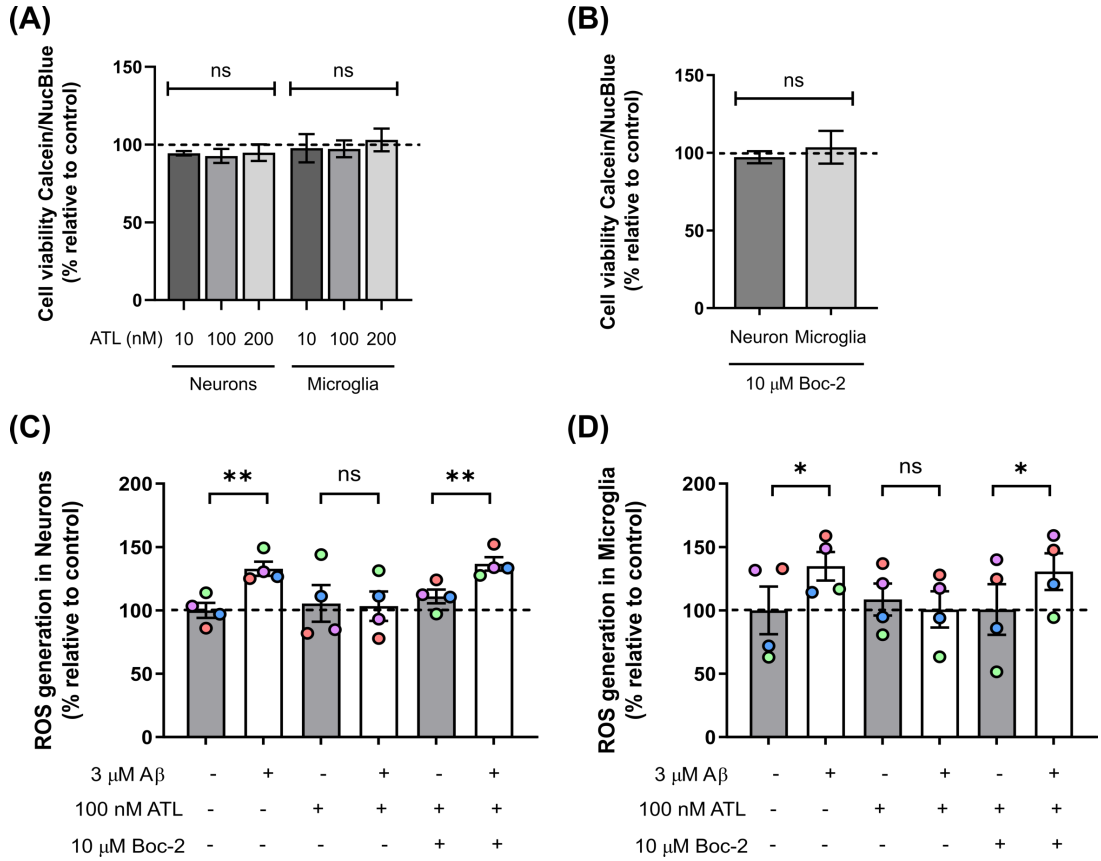

Figure 15. Lipoxin ATL prevents Aβ-induced ROS generation in a receptor-specific manner. (A) Toxicity assay for ATL using fluorescent probe Calcein AM in primary neurons and microglia 24 h after treatment (n = 3). Paired one-way ANOVA. **(B)** Toxicity assay for Boc-2 with Calcein AM in primary neurons and microglia 24 h after treatment (n = 3). Paired Student's t test. **(C, D)** Quantification of intracellular ROS with fluorescent probe CM-H2DCFDA in primary neurons and primary microglia, respectively. Cells were treated with 3 μM oAβ, 100 mM ATL, and 10 μM Boc-2 for 1 h (n = 4). Values were normalized with the number of cells per condition. Paired one-way ANOVA. Each bar represents the mean ± SEM. * p<0.05; ** p<0.01; ^{ns} not significant;

In addition to primary cultures, we analyzed the effects of ATL in corticostriatal organotypic cultures, given that previous work in our lab demonstrated that oAβ induces ROS generation and cellular death in organotypic slices (Alberdi *et al.*, 2018). We measured intracellular ROS after treating organotypic slices with 3 μM oAβ and 100 nM ATL for 1 h. We observed that oAβ significantly increased ROS production (130.4 ± 7.2 vs 100 ± 1.5%; $p<0.05$; n = 5), while ATL prevented this increase (**Figure 16A, B**). In addition, we assessed Aβ-induced cell death by measuring PI uptake. Treatment with 3 μM oAβ for 24 h significantly increased PI uptake compared with control slices (147.4 ± 19.8 vs 100 ± 6.2%; $p<0.05$; n = 5). ATL was able to reduce Aβ-induced cell death to levels slightly below its control (83.9 ± 5.7 vs 96.8 ± 6.9%; p = 0.0527; n = 5), although it was not statistically significant (**Figure 16C, D**).

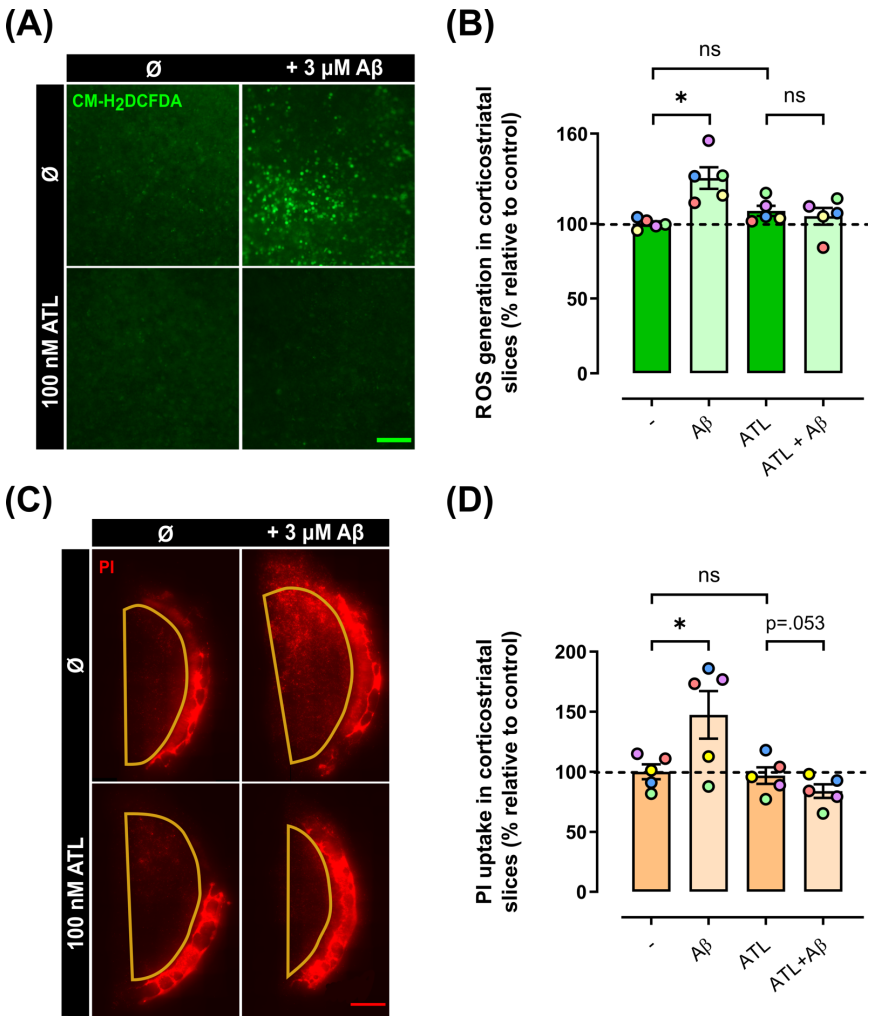

Figure 16. ATL reduces Aβ-induced ROS generation and cell death in corticostriatal organotypic cultures. (A) Representative image of intracellular ROS detected with CM-H2DCFDA in organotypic slices. Scale bar = 40 µm. **(B)** Quantification of intracellular ROS after treatment with 3 µM oAβ and 100 nM ATL for 1 h (n = 5). **(C)** Representative image of PI uptake as measure of cell death in organotypic slices. The area delimited by yellow lines was quantified to avoid nonspecific signal in slice edges. Scale bar = 1000 µm. **(D)** Quantification of PI uptake after treatment with 3 µM oAβ and 100 nM ATL for 24 h (n = 5). Values were normalized with the total area of each slice. Each bar represents the mean ± SEM. * $p<0.05$; ^{ns} not significant; paired one-way ANOVA.

After we demonstrated that ATL is able to reduce intracellular ROS generation in neurons and microglia, we asked ourselves whether ATL could be modulating NOX2 upstream mechanisms in microglia. Previous reports have linked complement receptor CR3 to NOX2 activation. Antibody neutralization or genetic ablation of CR3 subunit CD11b attenuates NOX2 assembly and activation induced by α-synuclein (Hou *et al.*, 2018). With this in mind, we analyzed the potential effect of lipoxin ATL on microglial CD11b expression. We treated primary microglia with 3 µM oAβ and 100 nM ATL for 24 h and performed a biotinylation protocol to obtain fractions enriched in membrane proteins to analyze CD11b expression in the cell surface. We found that oAβ increased CD11b both in the cell surface (133.8 ± 2.8 vs 109.9 ± 3.3%; $p<0.05$; n = 3) and total lysates (119.7 ± 15.7 vs 100 ± 17.2%; $p<0.05$; n = 3), compared with controls. Additionally, ATL significantly reduced CD11b in the cell surface (98.7 ± 8.3 vs 109.9 ± 3.3%; $p<0.05$; n = 3) and total lysates (79.5 ± 11.5 vs 100 ± 17.2%; $p<0.05$; n = 3), compared with oAβ alone (**Figure 17A, B**). These results suggest that ATL is able to reduce the Aβ-induced expression of CD11b, which in turn would mediate NOX2 activation and ROS generation in microglia.

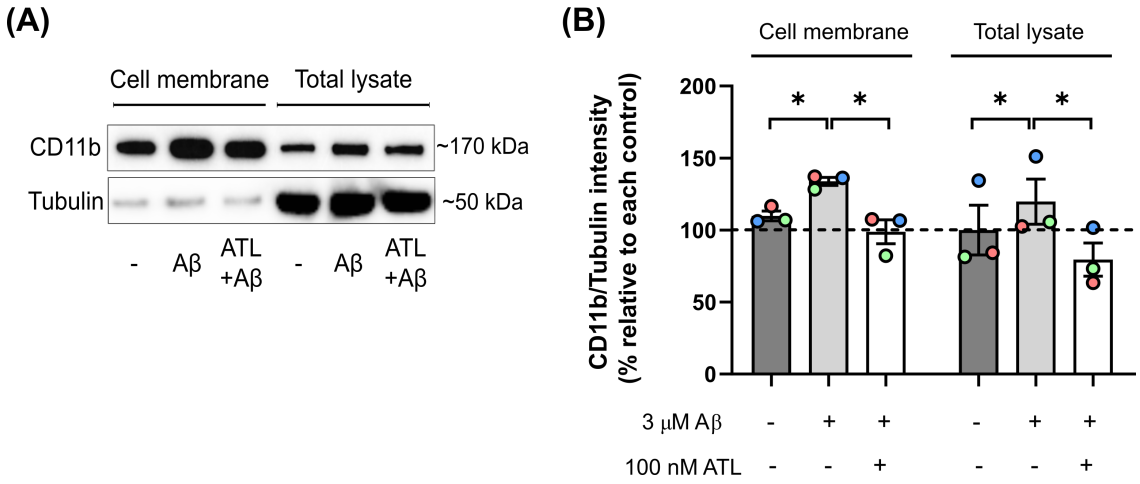

Figure 17. ATL reduces Aβ-induced CD11b in the cell membrane of primary microglia. (A) Western blot image of microglial activation marker CD11b in cellular surfaces and total lysates of primary microglia. **(B)** Quantification of CD11b after treatment with 3 μM oAβ and 100 nM ATL for 24 h (n = 3). Raw data was normalized using α-tubulin in the total lysate fraction. Each bar represents the mean ± SEM. * $p<0.05$; ^{ns} not significant; paired one-way ANOVA.

Once we observed that ATL is able to reduce ROS generation, we asked whether ATL would also have a positive effect on ROS elimination. Primary neurons can reduce SOD activity in the presence of oAβ (Alberdi *et al.*, 2018), and previous reports suggest that LXA_4 can stimulate SOD after spinal cord injury (Liu *et al.*, 2015). Here, we wanted to analyze the effect of ATL on Aβ-induced SOD activity impairment. We treated primary neurons and microglia with 5 μM oAβ and 100 nM ATL for 2 h and then measured the activity of the enzyme. In primary neurons, we observed a significant reduction of SOD activity with oAβ compared to controls (83.7 ± 7.7 vs 100 ± 7.4%; $p<0.05$; n = 5), while ATL prevented this reduction (**Figure 18A**). We found similar results in primary microglia, where oAβ significantly reduced SOD activity (64.4 ± 7.1 vs 100 ± 9.3%; $p<0.01$; n = 5), and ATL kept it in levels similar to controls (**Figure 18B**). Considering these results, ATL effectively decreases Aβ-induced oxidative stress by reducing NOX2-mediated ROS generation and enhancing SOD-mediated ROS detoxification.

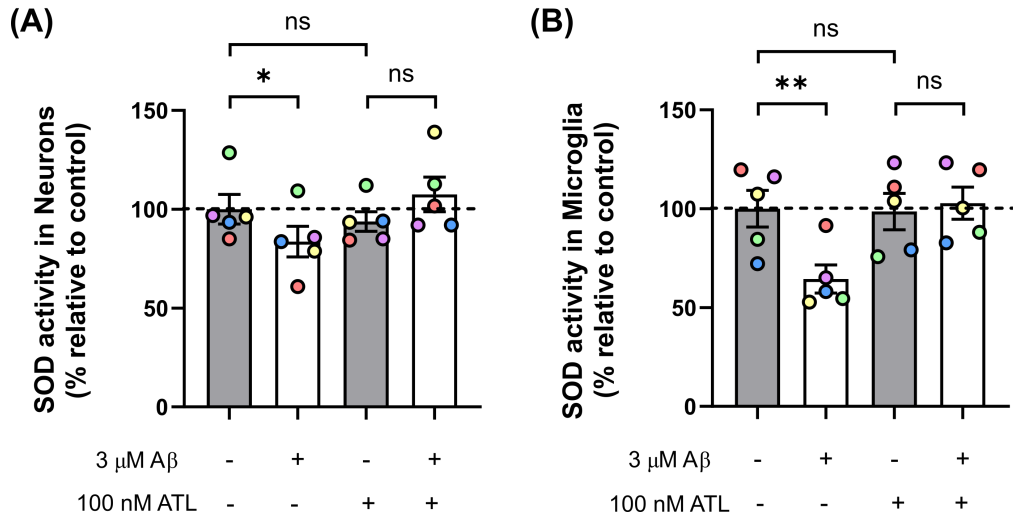

Figure 18. $A\beta_{1-42}$ impairs SOD activity, but ATL restores it to control levels in primary neurons and microglia. (A, B) Quantification of SOD activity in primary neurons and primary microglia, respectively. Cells were treated with 5 μM oAβ and 100 nM ATL for 2 h before measuring SOD activity (n= 5). Each bar represents the mean ± SEM. * p<0.05; ** p<0.01; ^{ns} not significant; paired one-way ANOVA.

1.3. ATL reduces Aβ-induced ROS in the mitochondria and restores impaired respiration.

It has been reported that LXA_4 can reduce mitochondrial ROS and restore mitochondrial respiration in a rat model of gastric ulcer (Madi *et al.*, 2020), so we hypothesized that lipoxin ATL could prevent Aβ-induced mitochondrial dysfunction in the 3xTg model. In order to test our hypothesis, we analyzed Aβ-induced mitochondrial ROS generation. First, we quantified mitochondrial superoxide radicals in primary neurons and microglia, after treatment with 3 μM oAβ, 100 nM ATL, or 100 nM ATL together with 10 μM for Boc-2 for 1 h. Regarding primary neurons, we observed that oAβ significantly increased superoxide radicals compared with controls (130.9 ± 7.8 vs 100 ± 7.7%; p<0.05; n = 4), while ATL prevented this increase. With ATL antagonist Boc-2, oAβ was still able to increase superoxide radicals (123.2 ± 5.9 vs 109.4 ± 2.5%; p<0.05; n = 4) (**Figure 19A**). In primary microglia, oAβ also increased superoxide radicals (113.2 ± 8.5 vs 100 ± 8.2%; p<0.01; n = 4) compared with controls, and ATL restored it to levels similar to controls. Boc-2 effectively blocked ATL, and oAβ was still able to increase superoxide radicals (113.6 ± 1.8 vs 96.2 ± 0.5%; p<0.01;

n = 4) (**Figure 19B**). In addition to primary cultures, we analyzed Aβ-induced mitochondrial ROS in corticostriatal organotypic slices. After treating slices with 3 µM oAβ, 100 nM ATL, or 100 nM ATL together with 10 µM Boc-2 for 1 h, we saw an increase of mitochondrial superoxide radicals with oAβ (129.2 ± 14.2 vs 100 ± 11.1%; p<0.05; n = 3), that was prevented by ATL (**Figure 19C, D**).

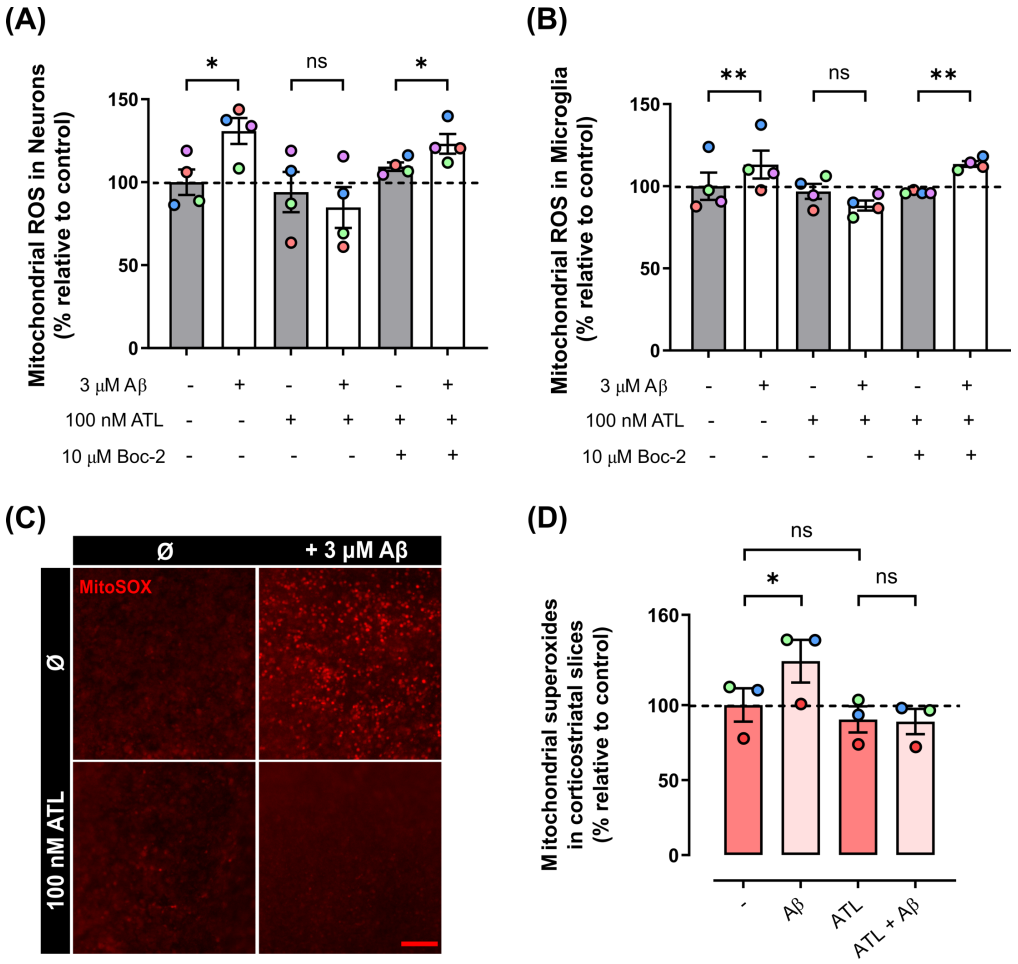

Figure 19. Lipoxin ATL decreases Aβ-induced superoxide radicals in the mitochondria of neurons and microglia, as well as in corticostriatal organotypic cultures. (A, B) Quantification of superoxide radicals in the mitochondria with fluorescent probe MitoSOX™ in primary neurons and primary microglia, respectively. Before quantification, cells were treated with 3 µM oAβ, 100 nM and 10 µM Boc-1 for 1 h (n = 4). Values were normalized with the number of cells per condition. **(C)** Representative image of MitoSOX™ in corticostriatal organotypic slices. Scale bar = 40 µm. **(D)** Quantification of mitochondrial superoxide radicals after treatment with 3 µM oAβ and 100 nM ATL for 1 h (n = 3). Values were normalized with the total area of each slice. Each bar represents the mean ± SEM. * p<0.05; ** p<0.01; ns not significant; paired one-way ANOVA.

Once we corroborated that ATL effectively reduced mitochondrial ROS generation, we considered whether this could be reflected on mitochondrial function. To investigate this, we treated cultures with 3 μM oAβ and 50 nM ATL for 1 h, and then analyzed respiration parameters using Seahorse XF96 Extracellular Flux Analyzer to measure OCR as detailed in Experimental procedures, section 8. In primary neurons, we observed that oAβ significantly impaired basal respiration (14.8 ± 1.7 vs 20.9 ± 1.1 pmol/min; $p<0.001$; n = 6) and maximal respiration capacity (22.5 ± 4.1 vs 39.2 ± 4.3 pmol/min; $p<0.01$; n = 6), compared with controls. ATL was able to recover basal respiration to control levels, and maximal respiration capacity to levels slightly lower than its control (32.0 ± 6.2 vs 39.8 ± 6.7 pmol/min; $p<0.05$; n = 6) (**Figure 20A, B**). OCR linked to ATP production and proton leak were also significantly lower with oAβ (9.8 ± 1.9 vs 14.0 ± 1.8 pmol/min; $p<0.01$; n = 6) and (4.9 ± 0.8 vs 6.8 ± 1.0 pmol/min; $p<0.01$; n = 6), respectively, while ATL returned both parameters to control levels (**Figure 20C**). We made similar observations in primary microglia, where oAβ significantly reduced basal respiration (13.6 ± 1.6 vs 18.7 ± 1.6 pmol/min; $p<0.05$; n = 7) and maximal respiration capacity and (35.8 ± 7.9 vs 46.7 ± 8.7 pmol/min; $p<0.05$; n = 7), compared with controls. ATL recovered both parameters to control levels (**Figure 20D, E**). Finally, OCR liked to ATP production was significantly reduced with oAβ (8.1 ± 1.3 vs 11.9 ± 1.2 pmol/min; $p<0.05$; n = 7), and ATL prevented this reduction (**Figure 20F**).

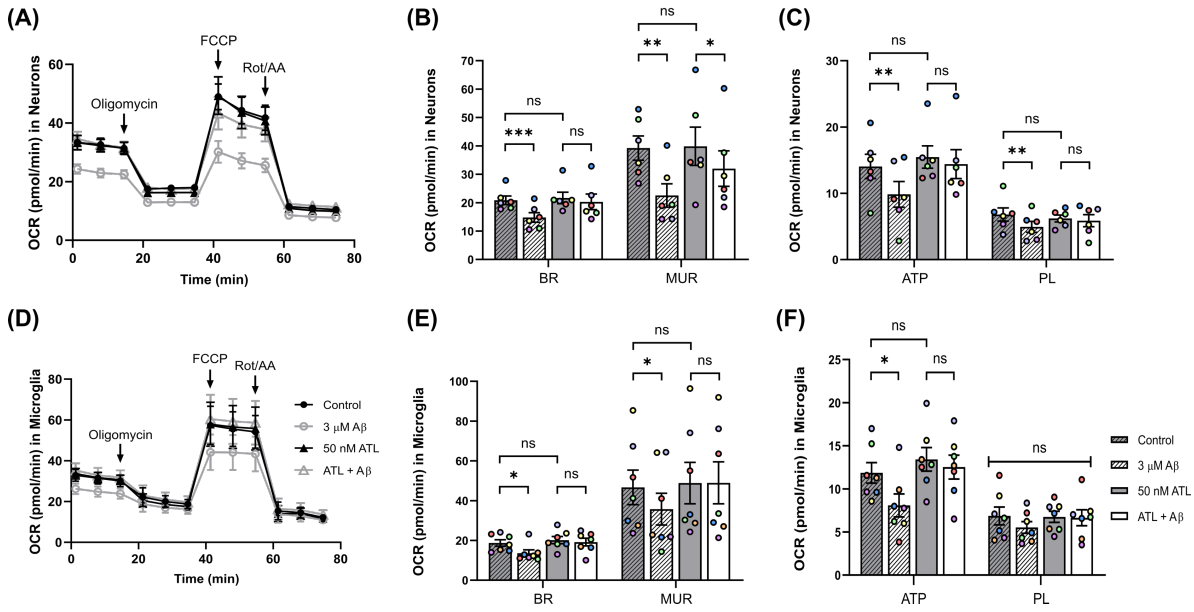

Figure 20. ATL recovers respiration parameters altered by $A\beta_{1-42}$ in primary neurons and microglia. Analysis of mitochondrial respiration using Agilent Seahorse XF Cell Mito Stress Test. Data was normalized with the number of cells per condition. **(A)** Oxygen consumption rate (OCR) over time in primary neurons treated with 3 μM oAβ and 50 nM ATL for 1 h. **(B)** Quantification of OCR linked to basal respiration (BR) and maximal respiration capacity (MUR) in primary neurons (n = 6). **(C)** Quantification of OCR linked to ATP production (ATP) and proton leak (PL) in primary neurons (n=6). **(D)** OCR over time in primary microglia treated with 3 μM oAβ and 50 nM ATL for 1 h. **(E)** Quantification of BR and MUR in primary microglia (n = 7). **(F)** Quantification of ATP and PL in primary microglia (n = 7). Each bar represents the mean ± SEM. * $p<0.05$; ** $p<0.01$;*** $p<0.001$; ^{ns} not significant; paired one-way ANOVA.

All of these results suggest that ATL can counteract Aβ-induced ROS generation and respiratory chain impairment in the mitochondria. Together with our previous observations, ATL seems to have the capacity to reduce ROS accumulation and oxidative damage in the mitochondria in primary neurons, microglia and organotypic cultures.

1.4. Endogenous LXA_4 is low and inversely correlates with synaptic Aβ levels in prefrontal cortices of AD patients.

Previous studies have linked low LXA_4 levels with neurodegenerative diseases. LXA_4 is reduced in CSF and hippocampi of AD patients, and it positively correlates with MMSE scores (Wang *et al.*, 2015*b*). In order to complement previous reports, we analyzed LXA_4 levels in cortical samples of a cohort of control individuals and AD patients in V-VI Braak stages of the disease. We found that LXA_4 was significantly reduced in AD patients compared with control individuals (25.2 ± 3.1 vs 34.5 ± 2.6 pg/mg; $p<0.05$; n = 7-9/group) (**Figure 21A**). Next, we asked ourselves whether LXA_4 levels would be linked to Aβ accumulation. To answer this question, we used post-synaptic fractions from the same cohort of patients (previously isolated by Dr. Carolina Ortiz-Sanz in our laboratory) to quantify the accumulation of $A\beta_{1-42}$. Linear regression analysis revealed a statistically significant negative correlation between LXA_4 levels in the cortex and Aβ accumulation in post-synapses ($R = -0.57$; $p = 0.021$ n = 7-9/group) (**Figure 21B**). In summary, we found low levels of lipoxin LXA_4 in the cortex of AD patients, which negatively correlate with $A\beta_{1-42}$ in post-synapses.

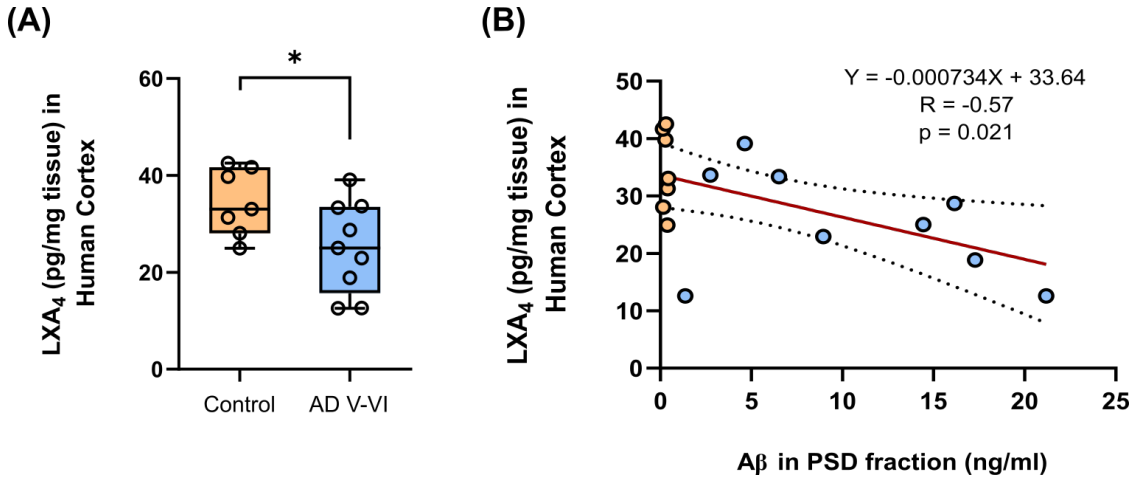

Figure 21. Endogenous lipoxin LXA_4 is reduced in cortical samples of AD patients. **(A)** Quantification of LXA_4 in cortical samples of control individuals and AD patients in V-VI Braak stages (n = 7-9/group). Data were normalized using the weight (mg) of each tissue sample. Each boxplot represents the median and its respective quartiles. * $p<0.05$; unpaired Student's t test. **(B)** Negative correlation between LXA_4 levels and $A\beta_{1-42}$ accumulated in post-synaptic fractions. Orange dots = controls; Blue dots = AD V-VI patients; PSD fraction = post-synaptic fraction. The dashed lines in the regression analysis represent 95% confidence intervals.

1.5. Effects of ATL treatment in the 3xTg mouse model.

Since we observed that lipoxin LXA_4 is reduced in AD patients, and that ATL is able to reduce ROS generation and mitochondrial dysfunction *in vitro*, we decided to study the effect of ATL in the 3xTg mouse model of AD, focusing on glial activation and mitochondrial function. Based on existing *in vivo* studies where ATL was administered alone (Medeiros *et al.*, 2013), or in combination with other pro-resolving mediator (Kantarci *et al.*, 2018), we treated female WT 129 and 3xTg animals, 16-17 months old, with one daily intraperitoneal injection of 10 µg/kg ATL or vehicle (0.05% ethanol) in saline for two months (**Figure 22**).

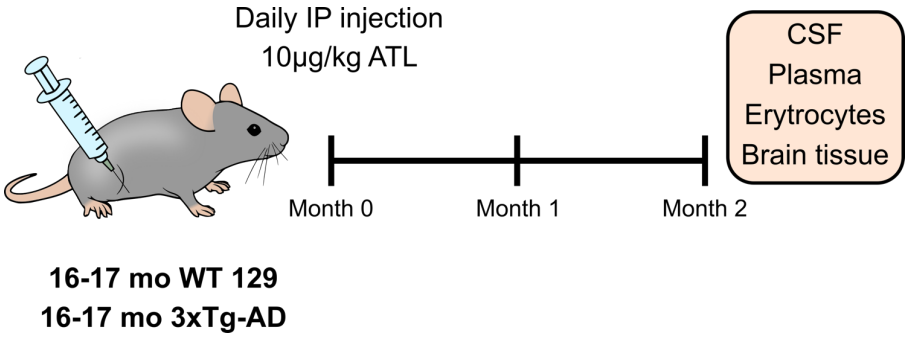

Figure 22. Diagram of ATL treatment in 3xTg female mice. Animals were treated with one daily intraperitoneal injection of 10 µg/kg ATL or 0.05% ethanol in saline for two months. Four groups were used: WT mice with vehicle (n = 4), WT mice with ATL (n = 4), 3xTg mice with vehicle (n = 7) and 3xTg mice with ATL (n =7). IP = intraperitoneal.

1.5.1. ATL reduces amyloid and tau pathology.

First, we analyzed the effect of ATL on amyloid pathology. Previous reports with higher doses of this lipoxin revealed that ATL reduces Aβ oligomers, fibrils and senile plaques in mouse models of AD (Medeiros *et al.*, 2013; Kantarci *et al.*, 2018). Thus, in our 3xTg model, we quantified ThS positive plaques, as well as Aβ levels in entorhinal cortex, hippocampus, CSF and plasma samples. We found a drastic ~80% reduction in the number of ThS^+ amyloid plaques per area in the subiculum of the animals treated with ATL compared to vehicles (122.0 ± 83.9 vs 808.0 ± 293.3 plaques/μm^2; $p<0.05$; n = 7/group) (**Figure 23A, B**). We also found that soluble $A\beta_{1-42}$, mainly monomeric and oligomeric forms soluble in RIPA buffer, was reduced in the entorhinal cortex of ATL treated mice (194.9 ± 59.8 vs 362.3 ± 41.4 pg/ml; $p<0.05$; n = 7/group), compared with vehicles (**Figure 23C**). Insoluble $A\beta_{1-42}$ in the hippocampus, which was extracted using 2% SDS buffer, was significantly reduced in ATL treated 3xTg mice (17.4 ± 0.5 vs 20.0 ± 0.1 ng/ml; $p<0.001$; n = 7/group), compared to vehicles (**Figure 23D**). Finally, levels of $A\beta_{40}$ and $A\beta_{42}$, as well as the ratio $A\beta_{42}/A\beta_{40}$ were analyzed in CSF and plasma samples using Quanterix Simoa® HD-1 analyzer. Neither the individual levels (data not shown) nor the $A\beta_{42}/A\beta_{40}$ ratio were altered with the ATL treatment (**Figure 23E, F**).

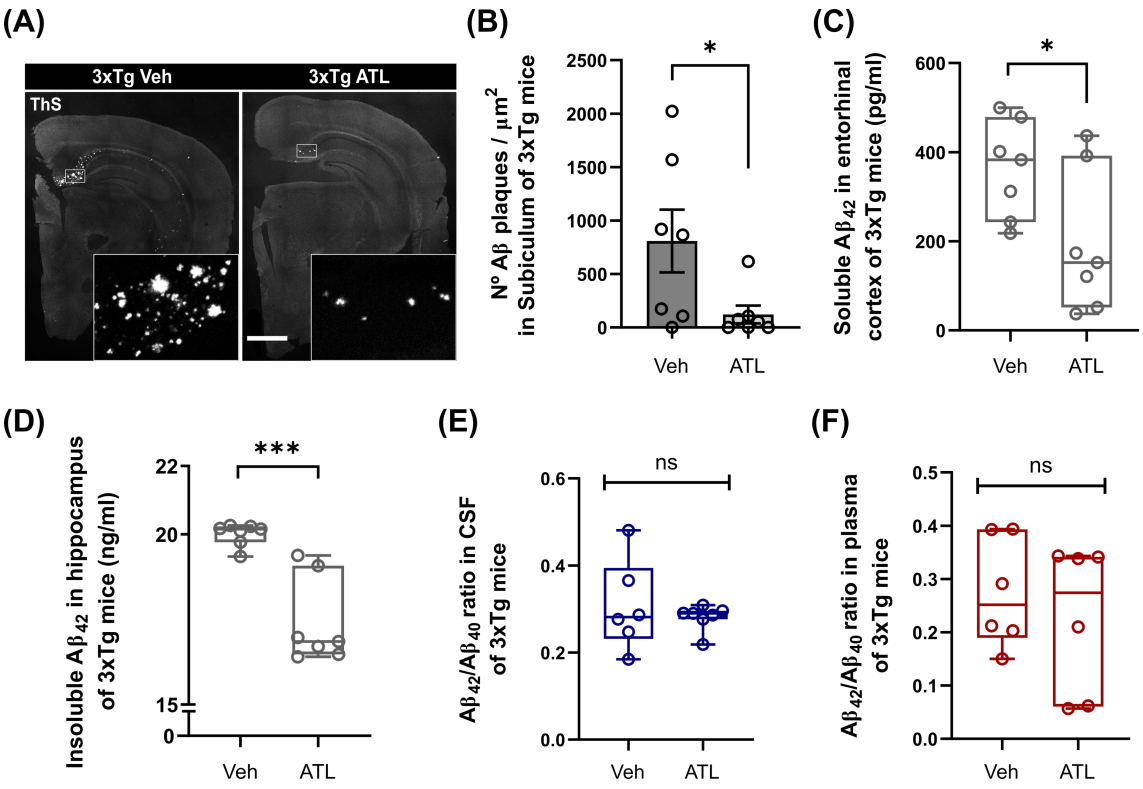

Figure 23. Lipoxin ATL reduces plaque load and Aβ$_{1-42}$ in 3xTg mice. (A) Representative images of amyloid plaques in the subiculum area, stained with ThS. Scale bar = 1 mm. **(B)** Number of plaques per unit of area in animals treated with ATL or with vehicle (n = 7/group). **(C)** ELISA quantification of soluble Aβ$_{1-42}$ (RIPA fractions) in the entorhinal cortex (n = 7/group). **(D)** ELISA quantification of insoluble Aβ$_{1-42}$ (SDS fractions) in the hippocampus (n = 7/group). **(E, F)** SIMOA quantification of Aβ$_{42}$/Aβ$_{40}$ ratio in CSF and plasma samples, respectively (n = 7/group). Each bar represents the mean ± SEM. Each boxplot represents the median and its respective quartiles. * p<0.05; *** p<0.001; ^{ns} not significant; unpaired Student's t test. Veh = vehicle.

Previous studies using the same 3xTg model and higher doses of this lipoxin demonstrated that ATL reduces tau phosphorylation (Dunn *et al.*, 2015). Based on this information, we quantified tau phosphorylation in the CA1 hippocampal area using antibody AT8. We found that the area occupied by AT8 was significantly reduced by ~0.5 fold in ATL treated animals compared with vehicles (3.9 ± 0.7 vs 6.3 ± 0.7 µm^2; p<0.05; n = 7/group) (**Figure 24A, B**). In addition to phosphorylated tau in the hippocampus, total tau in CSF is a good indicator of tau pathology in AD mouse models. For instance, previous reports have shown a steady increase of total tau in CSF with age in APP/PS1 mice compared to non-transgenic littermates (Schelle *et al.*, 2017; Kaeser *et al.*, 2021). Considering this, we assessed total tau levels in CSF and plasma samples using

Quanterix Simoa® HD-1 analyzer. Total tau levels in CSF were reduced by ~80% in 3xTg animals treated with ATL (112.6 ± 29.2 vs 642.2 ± 160.8 pg/ml; p<0.01; n = 7/group), compared with animals treated with vehicle (**Figure 24C**). No differences were found in total tau levels in plasma samples (**Figure 24D**).

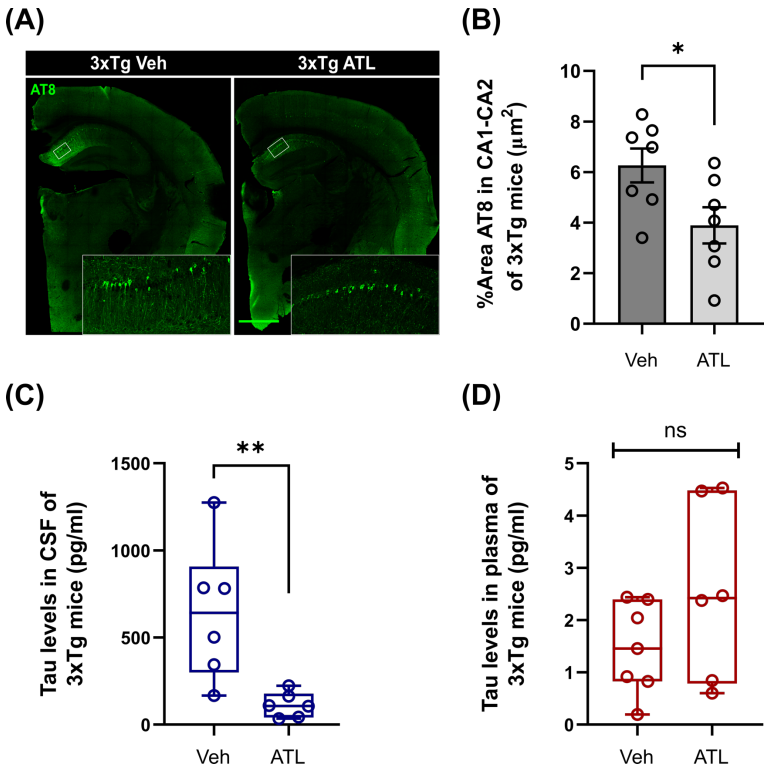

Figure 24. ATL reduces phosphorylated tau in hippocampus and total tau levels in CSF of 3xTg mice. (A) Representative images of phosphorylated tau in hippocampus stained with AT8. Scale bar = 1 mm. **(B)** Quantification of the area occupied by AT8 in hippocampus of animals treated with ATL or vehicle (n = 7/group). **(C,D)** SIMOA quantification of total tau in CSF and plasma samples, respectively (n = 7/group). Each bar represents the mean ± SEM. Each boxplot represents the median and its respective quartiles. * p<0.05; ** p<0.01; ns not significant; unpaired Student's t test. Veh = vehicle.

In summary, all of these results suggest that ATL effectively reduces soluble and insoluble forms of Aβ, as well as senile plaque deposition and tau pathology in the brain and CSF of 3xTg mice.

1.5.2. Hippocampal synaptic loss is prevented by ATL.

Along with amyloid and tau pathology, synaptic loss is a key pathological feature of AD. Sustained neuroinflammation contributes to synaptic dysfunction and elimination, and it has been proposed as a therapeutic candidate to reduce AD-related synaptic loss by reducing pro-inflammatory cytokines and microglial activation (reviewed in Ardura-Fabregat et al., 2017). Microglia can directly participate in synaptic elimination via the complement cascade and C1q deposition in synapses (Hong *et al.*, 2016; Bie *et al.*, 2019). Thus, we wanted to study in detail the effects of lipoxin ATL on synaptic loss in the 3xTg mouse model. We quantified pre-synaptic marker Synaptophysin, post-synaptic marker Homer scaffold protein 1 (Homer1) and synapse-associated C1q in hippocampal CA1 and cortex of WT and 3xTg mice treated with ATL or vehicle. In CA1, we found that the area occupied by Synaptophysin puncta was significantly reduced by ~0.5 fold in 3xTg compared with WT animals (57.8 ± 3.7 vs 100 ± 2.5%; $p<0.001$; n = 4-7/group). In addition, Synaptophysin area increased in 3xTg mice treated with ATL (99.7 ± 6.6 vs 57.8 ± 3.7%; $p<0.001$; n = 7/group) compared with vehicles (**Figure 25A, B**). We also observed that the area occupied by Homer1 puncta was reduced by ~0.5 fold in 3xTg (54.8 ± 3.0 vs 100 ± 3.1%; $p<0.001$; n = 4-7/group), compared with WT mice. ATL recovered Homer1 area in 3xTg animals (82.8 ± 2.6 vs 54.8 ± 3.0%; $p<0.001$; n = 7/group) compared with vehicles (**Figure 25C, D**). Regarding C1q, we found a significant increase in CA1 in the area occupied by C1q puncta in 3xTg (173.4 ± 8.1 vs 100 ± 1.8%; $p<0.001$; n = 4-7/group), compared with WT mice. ATL reduced C1q area in 3xTg mice (94.3 ± 4.6 vs 173.4 ± 8.1%; $p<0.001$; n = 7/group) compared with 3xTg mice treated with vehicle (**Figure 25E, F**).

In addition to CA1, we quantified synaptic markers and C1q in the cortex. Unfortunately, we did not see any differences in Synaptophysin, Homer1 or C1q levels between 3xTg and WT animals. Accordingly, we could not observe any differences between vehicle and ATL treatments (**Figure 26A-F**).

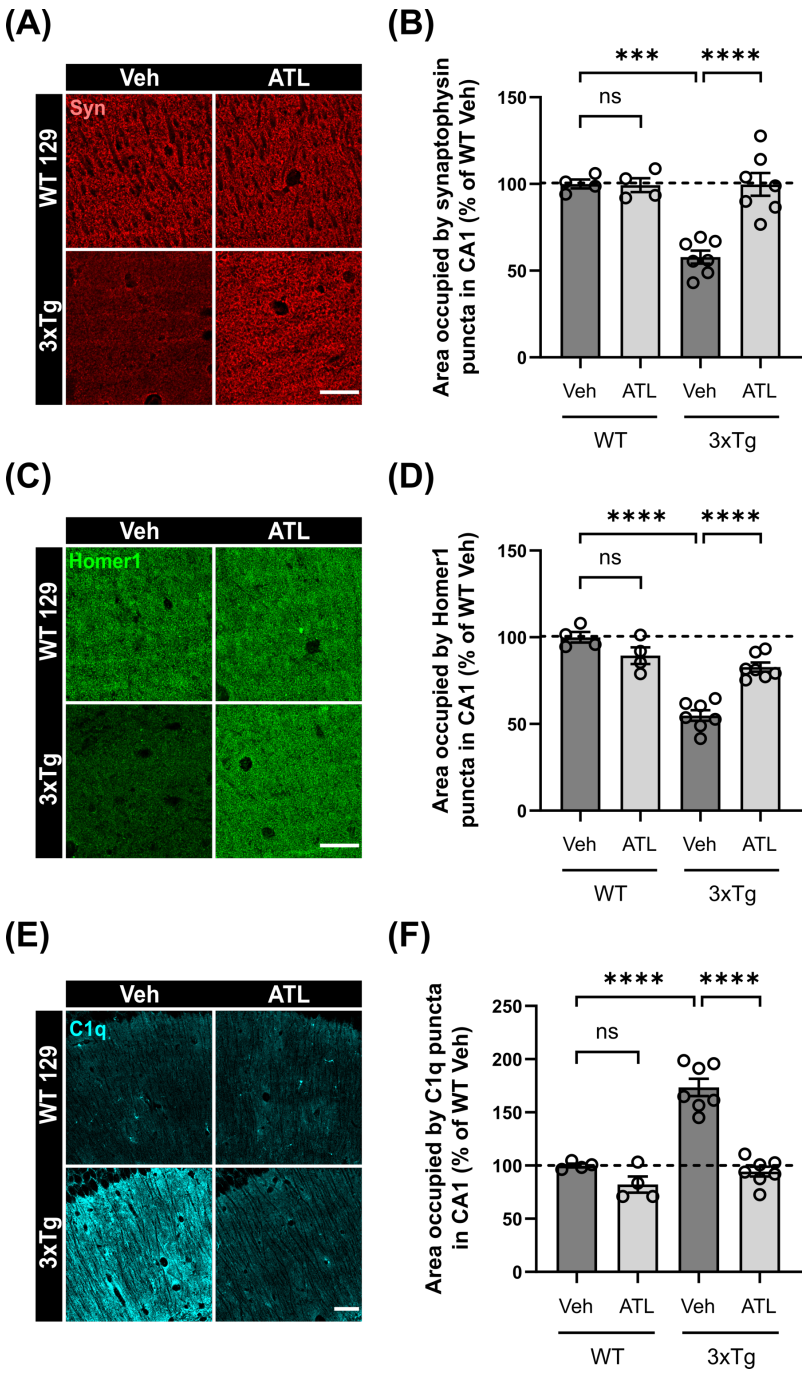

Figure 25. Lipoxin ATL recovers synaptic loss and lowers C1q puncta in 3xTg mouse hippocampi. (A) Representative images of pre-synaptic marker Synaptophysin in CA1 hippocampal area. Scale bar = 20 µm. **(B)** Quantification of the area occupied by Synaptophysin puncta in WT and 3xTg mice treated with vehicle or ATL (n = 4-7/group). **(C)** Representative images of post-synaptic marker Homer1 in CA1. Scale bar = 20 µm. **(D)** Quantification of the area occupied by Homer1 puncta (n = 4-7/group). **(E)** Representative images of C1q staining in CA1. Scale bar = 40 µm. **(F)** Quantification of the area occupied by C1q puncta (n = 4-7/group). Each bar represents the mean ± SEM. *** $p<0.001$; **** $p<0.0001$; ^{ns} not significant; one-way ANOVA. Syn = Synaptophysin.

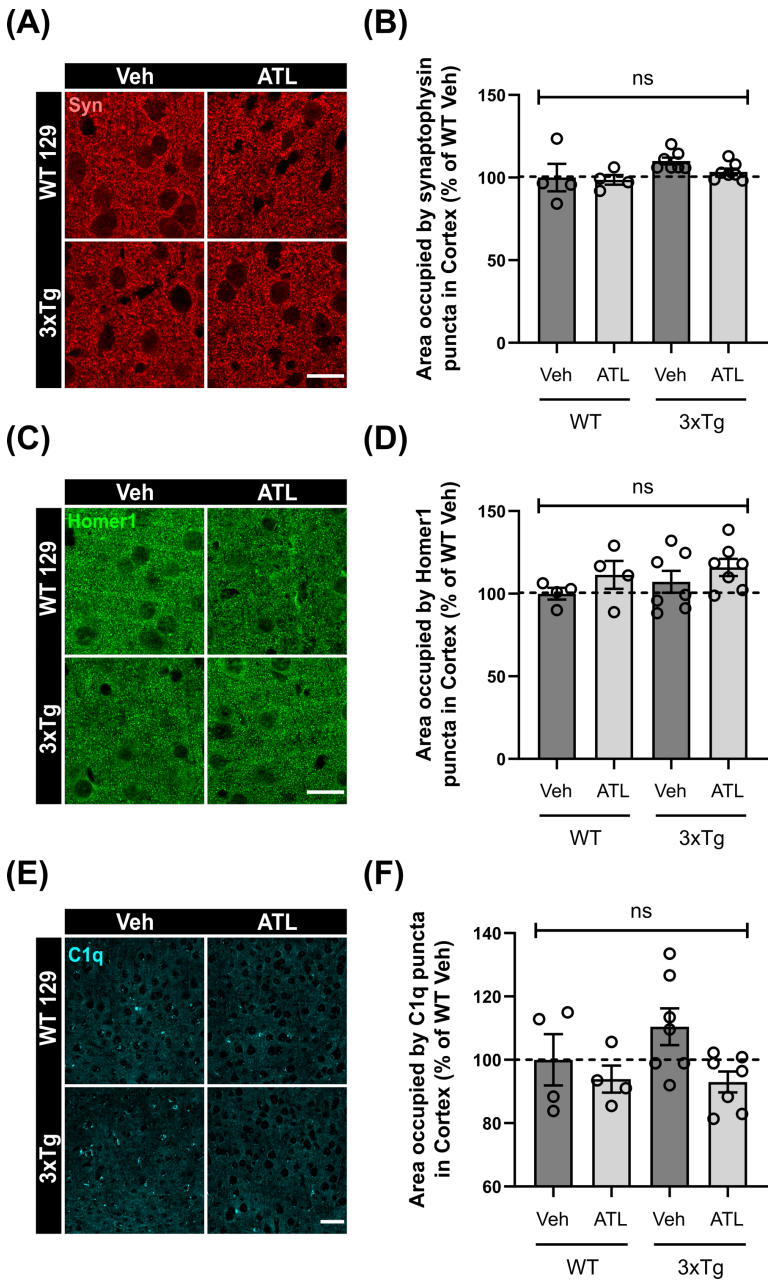

Figure 26. No synaptic loss in the cortex of 3xTg mice. (A) Representative images of Synaptophysin in cortex of WT and 3xTg mice treated with ATL or vehicle. Scale bar = 20 µm. **(B)** Area occupied by Synaptophysin puncta (n = 4-7/group). **(C)** Representative images of Homer1 in cortex. Scale bar = 20 µm. **(D)** Area of Homer1 puncta (n = 4-7/group). **(E)** Representative images of C1q. Scale bar = 40 µm. **(F)** Area occupied by C1q puncta (n = 4-7/group). Each bar represents the mean ± SEM. ^{ns} not significant; one-way ANOVA. Syn = Synaptophysin.

In summary, we found a noteworthy complement-related synaptic loss in the hippocampus of 3xTg mice, with reduction of Synaptophysin and Homer1, accompanied by increased C1q puncta. Our treatment with ATL was able to lower C1q deposition, and recover synaptic loss.

1.5.3. ATL reduces pro-inflammatory markers in brain and blood.

As part of their anti-inflammatory functions, lipoxins can regulate the production and secretion of cytokines. Previous publications have reported that ATL can lower LPS-induced production of cytokines IL-1β and TNF-α in BV2 cells (Wang *et al.*, 2011). Similarly, LXA_4 reduces the expression of IL-1β and TNF-α in Aβ-stimulated BV2 cells and in AD mouse models (Wu *et al.*, 2011; Medeiros *et al.*, 2013). Taking this into account, we decided to evaluate both inflammatory cytokines and the inflammasome, key mediator if the inflammatory response. In order to address this, I stayed for 3 months at the German center for neurodegenerative diseases DZNE (Bonn, Germany) in the laboratory of Dr. Michael T. Heneka, expert in neuroinflammation in AD.

First, we quantified several pro-inflammatory cytokines (IL-1β, KC/GRO, TNF-α, IL-5 and IL-6) in hippocampus and cortex samples of the WT and 3xTg animals treated with ATL or vehicle. In hippocampus, IL-1β showed a ~2 fold increase in 3xTg (0.27 ± 0.05 vs 0.10 ± 0.02 pg/mg; $p<0.05$; n = 4-7/group) compared with WT mice. This increase was significantly reduced with the ATL treatment compared with vehicles (0.10 ± 0.02 vs 0.27 ± 0.05 pg/mg; $p<0.01$; n = 7/group) (**Figure 27A**). KC/GRO was increased in 3xTg mice compared with WT (2.6 ± 0.3 vs 1.4 ± 0.1 pg/mg; $p<0.05$; n = 4-7/group), and ATL showed a trend to decrease it, although it was not statistically significant (**Figure 27B**). 3xTg mice also displayed a ~7 fold increased in TNF-α levels compared with WT mice (0.21 ± 0.05 vs 0.02 ± 0.003 pg/mg; $p<0.01$; n = 4-7/group). ATL was able to significantly reduce TNF-α in 3xTg animals compared with vehicles (0.03 ± 0.01 vs 0.21 ± 0.05 pg/mg; $p<0.01$; n = 7/group) (**Figure 27C**). Cytokines IL-5 and IL-6 did not show any differences between any of the groups (**Figure 27D, E**). Regarding cortex, 3xTg mice showed a ~2 fold reduction of IL-1β (0.11 ± 0.02 vs 0.3 ± 0.06 pg/mg; $p<0.01$; n = 4-7/group) compared with WT, and ATL did not have any effect (**Figure 28A**). KC/GRO showed a non-significant trend to increase in 3xTg mice compared with WT, and ATL did not have any effect (**Figure 28B**). Cytokines TNF-α, IL-5 and IL-6 did not reveal any differences between any of the groups (**Figure 28C-E**).

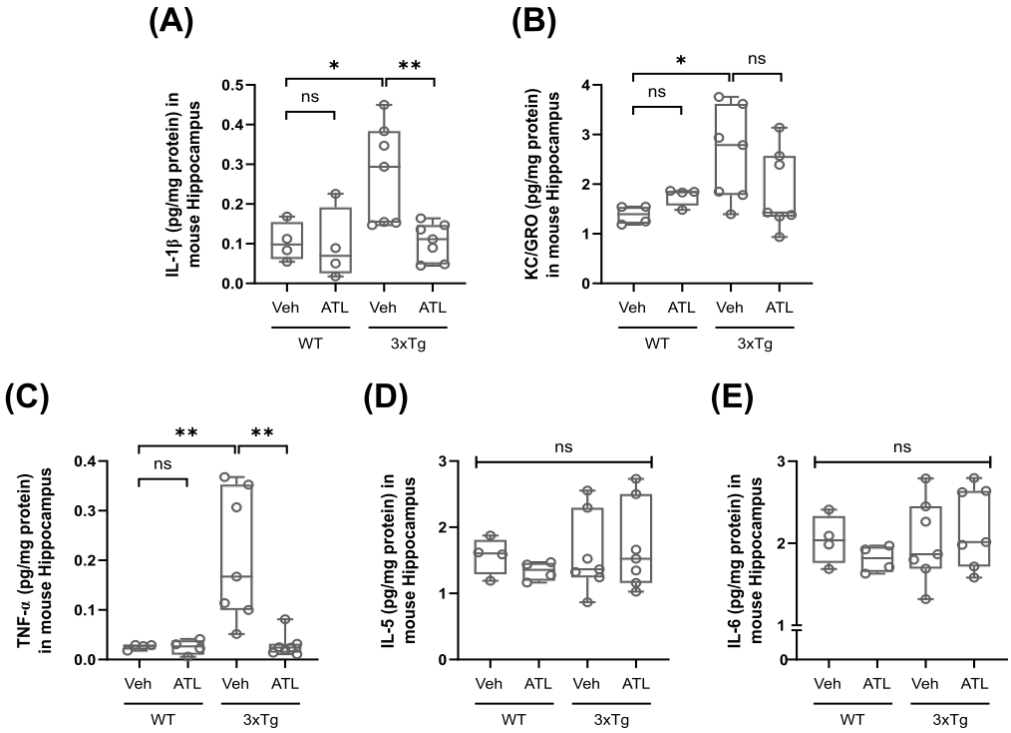

Figure 27. Lipoxin ATL reduces cytokines IL-1β and TNF-α in 3xTg mouse hippocampi. Analysis of pro-inflammatory cytokines in tissue extracts, using a multiplex system MSD® Multi-spot panel. Data were normalized using protein concentrations. Quantification of cytokines **(A)** IL-1β, **(B)** KC/GRO, **(C)** TNF-α, **(D)** IL-5, and **(E)** IL-6 in WT and 3xTg animals treated with ATL of vehicle (n = 4-7/group). Each boxplot represents the median and its respective quartiles. * p<0.05; ** p<0.01; ns not significant; one-way ANOVA.

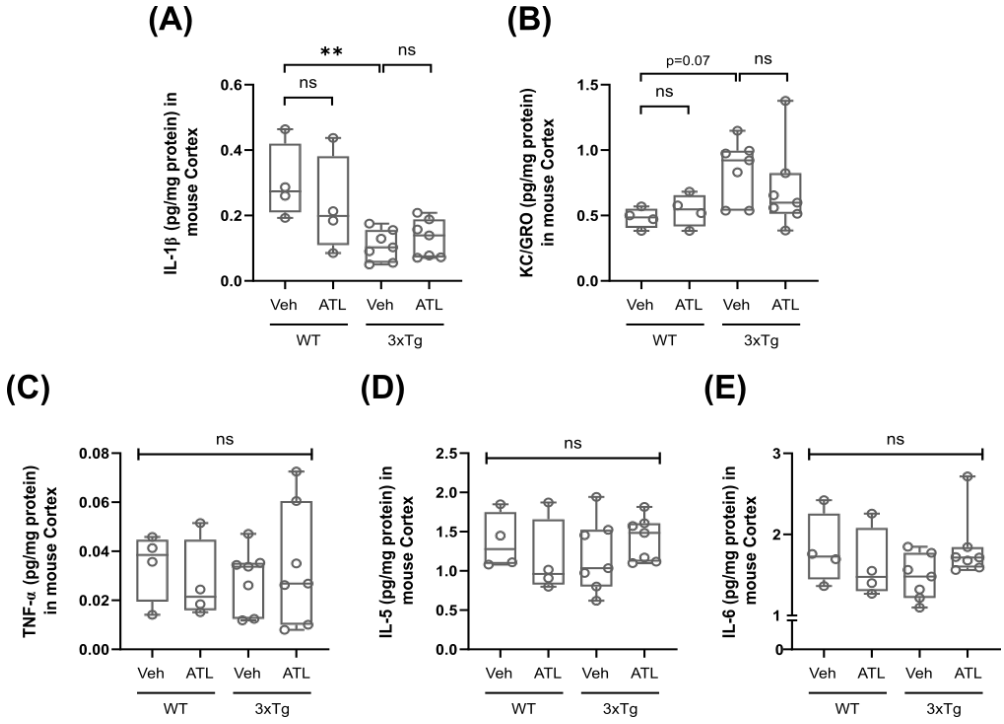

Figure 28. Lipoxin ATL does not alter cytokines in 3xTg mouse cortex. Analysis of pro-inflammatory cytokines in cortical tissue extracts, using a multiplex system MSD® Multi-spot panel. Data were normalized using protein concentrations. Quantification of cytokines **(A)** IL-1β, **(B)** KC/GRO, **(C)** TNF-α, **(D)** IL-5, and **(E)** IL-6 in WT and 3xTg animals treated with ATL of vehicle (n = 4-7/group). Each boxplot represents the median and its respective quartiles. ** $p<0.01$; ^{ns} not significant; one-way ANOVA.

Next, we analyzed inflammasome NLRP3, which is a protein complex consisting of NLRP3, ASC and cleaved caspase-1. NLRP3 is activated by Aβ, and it is associated with senile plaques in AD patients (reviewed in Venegas and Heneka, 2019). Several publications have suggested that lipoxins can inhibit the function of the inflammasome. For instance, LXA_4 can reduce the expression of NLRP3 and caspase-1 in *in vitro* LPS-treated macrophages (Zhao *et al.*, 2021). Thus, we asked ourselves whether ATL could modulate inflammasome NLRP3 in our model. We quantified ASC, NLRP3 and cleaved caspase-1 in cortex and hippocampus of WT and 3xTg mice treated with ATL or vehicle. Unfortunately, we found little evidence of inflammasome activation in 3xTg animals. There was a significant increase of ASC in 3xTg mice compared with WT, both in cortex (135.9 ± 11.1 vs 100 ± 3.2%; $p<0.05$; n = 4-7/group) and hippocampus (149.3 ± 7.9 vs 100 ± 7.7%; $p<0.05$; n = 4-7/group), although ATL did not have an effect in any of the groups (**Figure 29A-C**). Quantification of NLRP3 did not reveal differences between 3xTg and WT animals, neither in cortex nor in hippocampus (**Figure 29A, D, E**). No differences were found in cleaved caspase-1 levels between any of the groups analyzed (**Figure 29F-H**).

All of these results suggest that, even though ATL did not have a direct effect on inflammasome NLRP3 in our conditions, it was able to dramatically reduce the production of pro-inflammatory cytokines IL-1β and TNF-α in hippocampi of 3xTg mice.

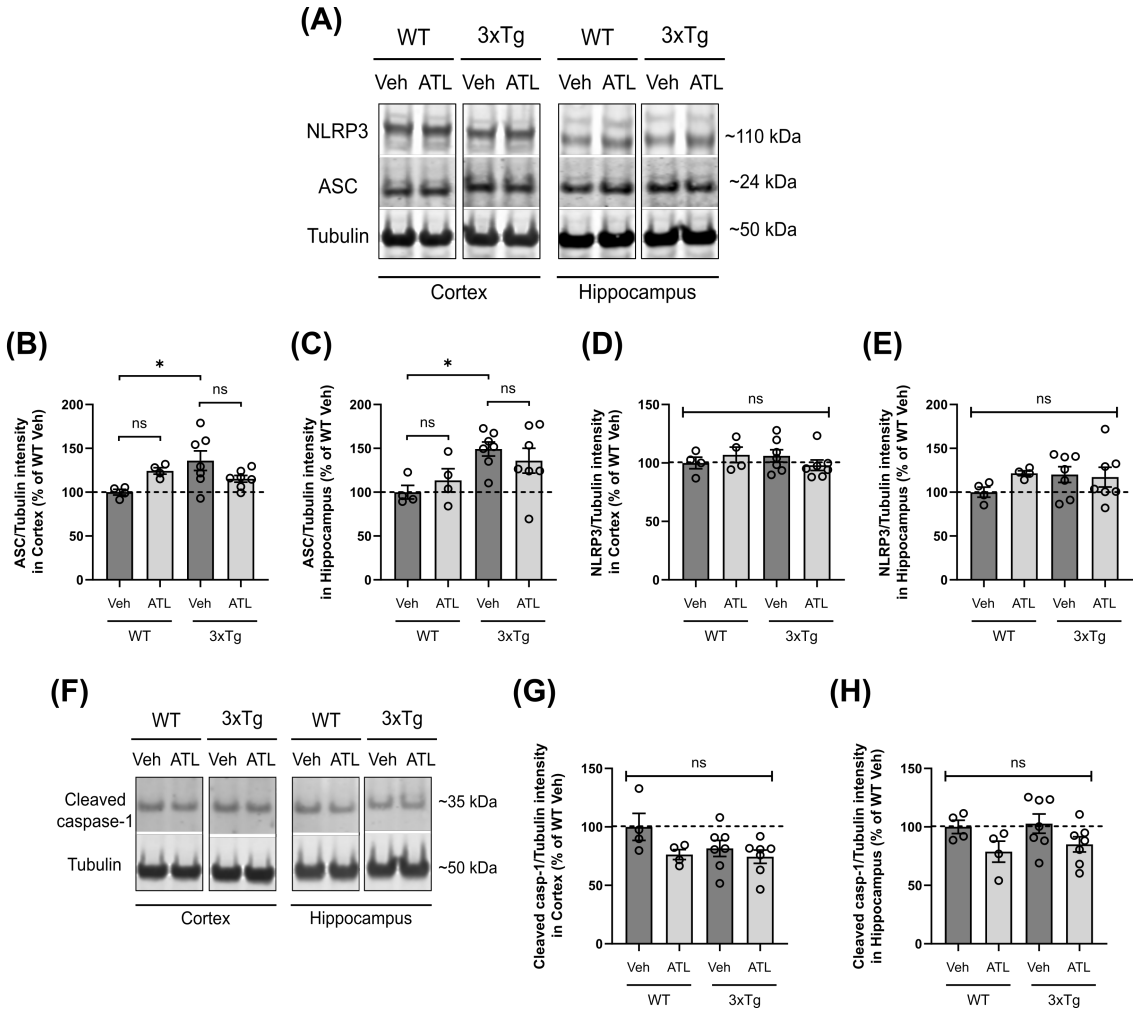

Figure 29. ATL does not have an effect on inflammasome activation in 3xTg mice. **(A)** Western blot image of inflammasome components NLRP3 and ASC in cortex and hippocampus. **(B, C)** Quantification of ASC in cortex and hippocampus, respectively (n = 4-7/group). **(D, E)** Quantification of NLRP3 in cortex and hippocampus, respectively (n = 4-7/group). **(F)** Western blot image of cleaved caspase-1. **(G, H)** Quantification of cleaved caspase-1 in cortex and hippocampus, respectively (n = 4-7/group). Raw data was normalized using α-tubulin. Each bar represents the mean ± SEM. * $p<0.05$; ^{ns} not significant; one-way ANOVA.

Once we analyzed the anti-inflammatory properties of ATL in the brain, we wanted to know if we could see an effect on the general redox state of the animals. Previous reports suggested the use of glutathione oxidized form GSSG as biomarker of AD, given the high GSSG levels found in erythrocyte samples of AD patients (Bermejo *et al.*, 2009). With this in mind, we quantified total glutathione and GSSG levels in erythrocyte samples from WT and 3xTg mice treated with ATL or vehicle. Although we found no differences in total glutathione levels in any of the animal groups (**Figure 30A**), there was a significant increase

of GSSG in 3xTg mice compared to WT (6.6 ± 0.3 vs 4.9 ± 0.4 µmol/l; p<0.05; n = 4-7/group). Besides, ATL significantly reduced the levels of GSSG in 3xTg animals compared with 3xTg vehicles (5.1 ± 0.3 vs 6.6 ± 0.3 µmol/l; p<0.01; n = 7/group) (**Figure 30B**).

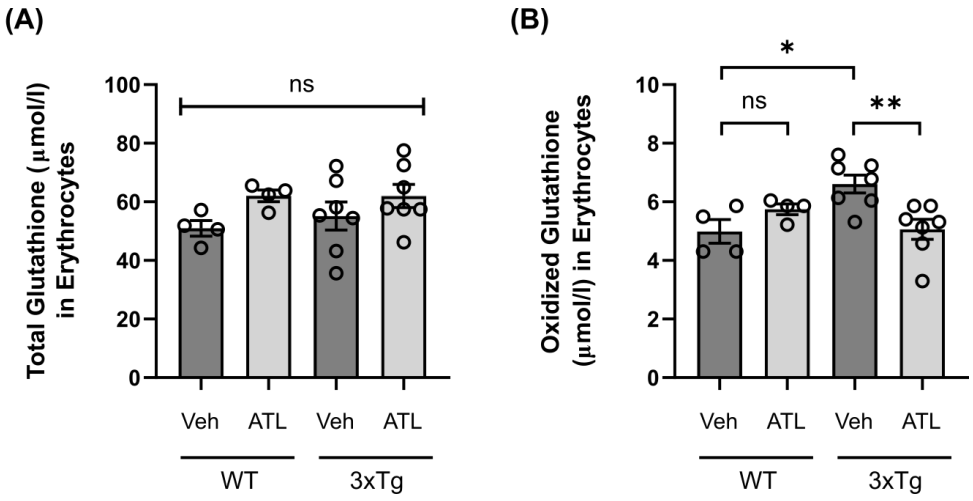

Figure 30. ATL reduces the amount of oxidized glutathione in peripheral erythrocytes of 3xTg mice. (A) Quantification of total glutathione in erythrocyte samples (n = 4-7/group). **(B)** Quantification of oxidized glutathione GSSG in erythrocyte samples (4-7/group). Each bar represents the mean ± SEM. * p<0.05; ** p<0.01; ^{ns} not significant; one-way ANOVA.

These results suggest that, as well as cytokines IL-1β and TNF-α in the hippocampus, ATL can reduce GSSG in the blood. This emphasizes the anti-inflammatory properties of lipoxin ATL and its potential to treat inflammation and oxidative stress driven neurodegeneration.

1.5.4. ATL reduces microgliosis and astrogliosis in hippocampus.

Previous publications have demonstrated that lipoxin ATL can reduce gliosis markers such as GFAP$^+$, CD11b$^+$ and CD45$^+$ immunoreactivity in Tg2576 and 3xTg mice (Medeiros *et al.*, 2013; Dunn *et al.*, 2015). In order to further explore the effects of ATL on gliosis, we quantified microgliosis and astrogliosis markers in the CA1 hippocampal area of WT and 3xTg mice treated with ATL or vehicle, focusing our attention in morphological alterations.

Firstly, we analyzed microglia using markers CD11b and Iba1. We found that the area occupied by CD11b was increased in 3xTg mice compared with WT (151.8 ± 8.7 vs 100 ± 9.9%; p<0.001; n = 4-7/group). 3xTg animals treated with ATL significantly reduced this area compared with vehicles (105.7 ± 3.9 vs 151.8 ± 8.7%; p<0.001; n = 7/group) (**Figure 31A, B**). Likewise, the area occupied by Iba1 was higher in 3xTg mice compared to WT (140.8 ± 6.8 vs 100 ± 17.0%; p<0.05; n = 4-7/group), and ATL reduced this area in 3xTg mice (106.2 ± 6.3 vs 140.8 ± 6.8%; p<0.05; n = 7/group) compared with vehicles (**Figure 31C, D**).

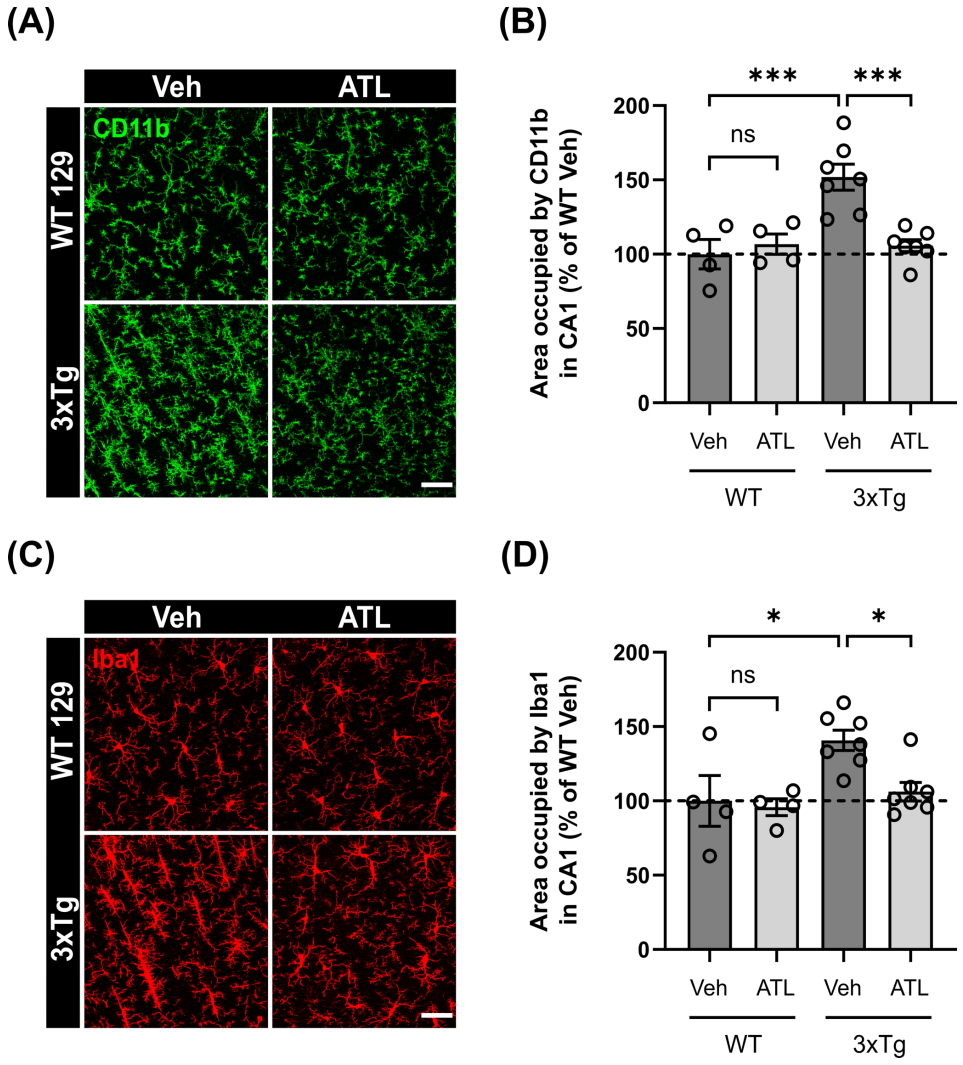

Figure 31. Lipoxin ATL reduces the area of microglial markers CD11b and Iba1 in 3xTg mouse hippocampi. (A) Representative images of microglial marker CD11b in CA1 hippocampal area. Scale bar = 40 µm. **(B)** Quantification of area occupied by CD11b in WT and 3xTg mice treated with ATL or vehicle (n = 4-7/group). **(C)** Representative images of microglial marker Iba1 in CA1. Scale bar = 40 µm. **(D)** Quantification of Iba1 area (n = 4-7/group). Each bar represents the mean ± SEM. * p<0.05; *** p<0.001; ^{ns} not significant; one-way ANOVA.

Once we confirmed that $CD11b^+$ and $Iba1^+$ microglia were reduced with ATL, we asked ourselves whether this lipoxin could also affect microglial morphology. We noticed that 3xTg mice presented rod-shaped microglia in CA1, with elongated cellular bodies and short processes (Taylor *et al.*, 2014). Thus, we wanted to know if ATL was able to revert this morphology. Using Z-stacks of $Iba1^+$ microglia, we isolated individual cells and measured several morphological parameters (**Figure 32A**) as described in Experimental procedures, section 21.3. We found several morphological alterations in the microglia of 3xTg mice, compared with WT animals. The mean number of branches per cell was increased in 3xTg mice compared with WT, although it was not statistically significant. Nonetheless, ATL did significantly reduce the number of branches in 3xTg mice compared with vehicles (81.7 ± 8.5 vs 114.8 ± 7.5%; $p<0.05$; n = 7/group) (**Figure 32B**). The mean number of junctions per cell also increased in a non-significant way in 3xTg mice compared with WT mice, and ATL significantly reduced this number of junctions in 3xTg compared with vehicles (110.2 ± 9.6 vs 189.4 ± 19.3%; $p<0.05$; n = 7/group) (**Figure 32C**). The mean branch length was significantly increased by ATL in 3xTg mice compared with vehicles (114.4 ± 4.8 vs 94.5 ± 2.5%; $p<0.01$; n = 7/group) (**Figure 32D**). Another parameter that was measured was the circularity of the cells. Microglia of 3xTg mice had significantly reduced circularity compared with WT (91.5 ± 2.0 vs 100 ± 1.7%; $p<0.05$; n = 4-7/group), and ATL was able to restore this circularity (98.3 ± 1.5 vs 91.5 ± 2.0%; $p<0.05$; n = 7/group) (**Figure 32E**). The span ratio, which is an inverse parameter of circularity, was significantly increased in microglia of 3xTg mice compared with WT (127.2 ± 7.4 vs 100 ± 2.6%; $p<0.05$; n = 4-7/group). ATL reduced this span ratio in 3xTg mice compared with vehicles (99.3 ± 5.4 vs 127.2 ± 7.4%; $p<0.01$; n = 7/group) (**Figure 32F**). In summary, we found that lipoxin ATL significantly reduced microgliosis and restored morphological alterations in hippocampi of 3xTg mice.

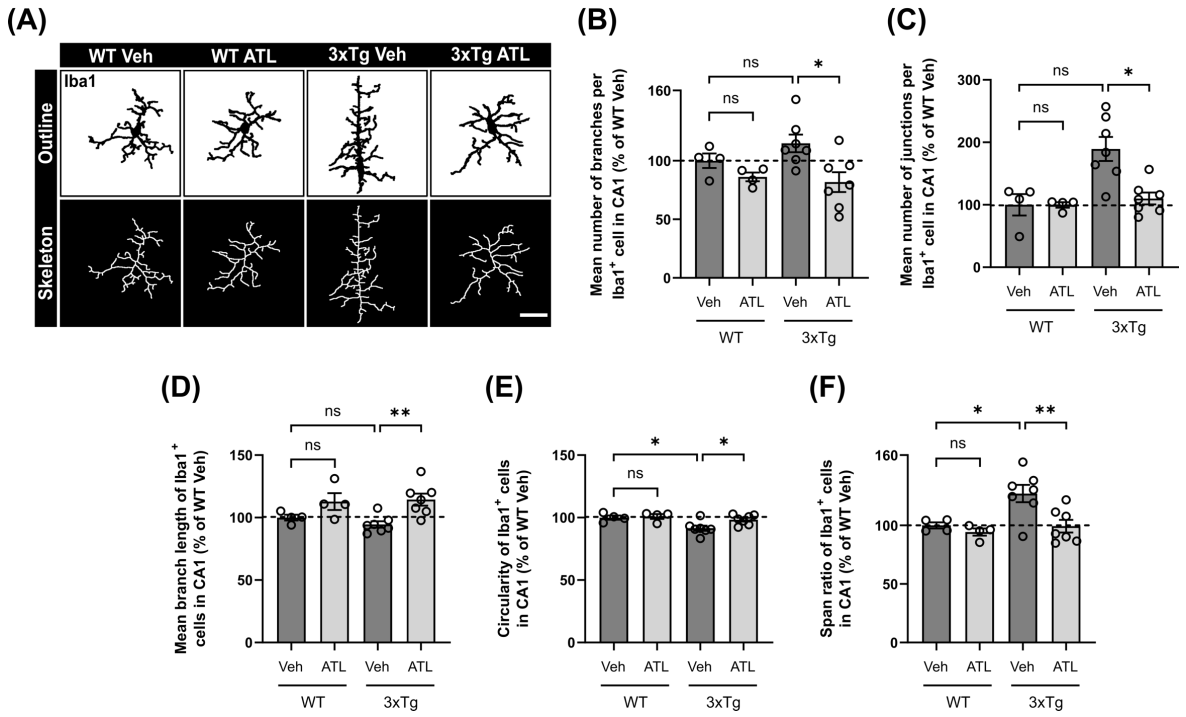

Figure 32. ATL reverts morphological alterations in hippocampal microglia of 3xTg mice. (A) Representative images of Iba1$^+$ microglia in CA1 hippocampal area of WT and 3xTg treated with ATL of vehicle (n = 4-7/group). The outline of individual cells, as well as their skeletons, were used to quantify morphological parameters. Scale bar = 20 µm. **(B)** Mean number of branches per Iba1$^+$ cell. **(C)** Mean number of junctions per Iba1$^+$ cell. **(D)** Mean branch length in Iba1$^+$ cells. **(E)** Quantification of Iba1$^+$ cells circularity. **(F)** Quantification of span ratio of Iba1$^+$ cells. Each bar represents the mean ± SEM. * p<0.05; ** p<0.01; ^{ns} not significant; one-way ANOVA.

After addressing microgliosis, we focused our attention on astrogliosis. In AD patients, astrocytes become hypertrophic, with increased ramifications and high expression of GFAP (Beach and McGeer, 1988; Simpson *et al.*, 2010; Zhou *et al.*, 2019). Based on this, we quantified astrocytic markers S100β and GFAP in the CA1 area of WT and 3xTg animals treated with ATL or vehicle. We found that the area occupied by S100β was higher in 3xTg mice compared with WT (125.5 ± 5.9 vs 100 ± 5.7%; p<0.03; n = 4-7/group). ATL reduced the S100β area in 3xTg mice compared with vehicles (85.5 ± 5.1 vs 125.5 ± 5.9%; p<0.001; n = 7/group) (**Figure 33A, B**). In addition, the area occupied by GFAP was significantly higher in 3xTg mice (158.6 ± 7.7 vs 100 ± 4.2%; p<0.001; n = 4-7/group) compared with WT, while ATL was able to reduce this GFAP area in 3xTg mice (107.5 ± 5.2 vs 158.6 ± 7.7%; p<0.001; n = 7/group) (**Figure 33C, D**).

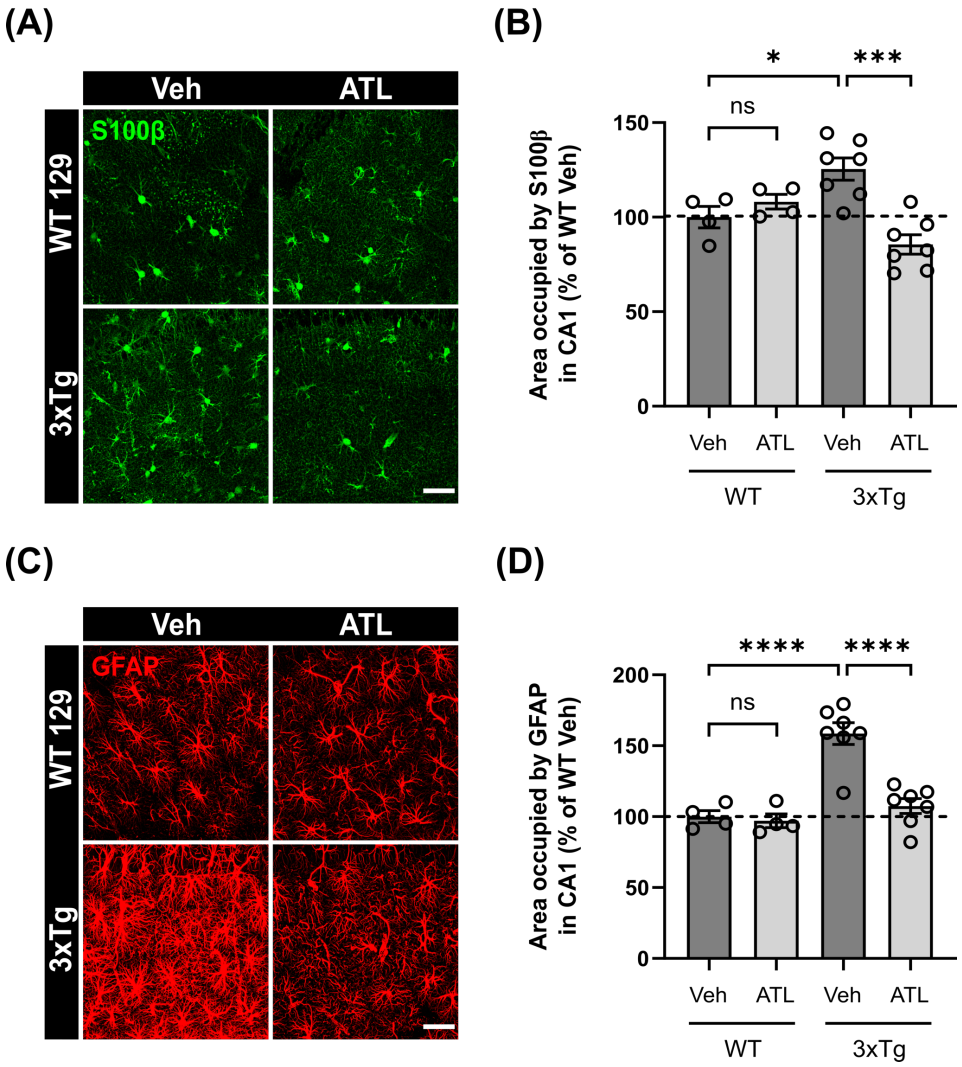

Figure 33. ATL reduces the area occupied by astrocytic markers S100β and GFAP in 3xTg mouse hippocampi. (A) Representative images of astrocytic marker S100β in CA1 hippocampal area. Scale bar = 40 µm. **(B)** Quantification of S100β area (n = 4-7/group). **(C)** Representative images of astrocytic marker GFAP in CA1. Scale bar = 40 µm. **(D)** Quantification of area occupied by GFAP staining (n = 4-7/group). Each bar represents the mean ± SEM. * $p<0.05$; *** $p<0.001$; **** $p<0.0001$; ^{ns} not significant; one-way ANOVA.

As with microglia, we thought that ATL would also have a positive effect on astrocytic morphological alterations. We used Z-stacks of GFAP$^+$ astrocytes and followed the same protocol to quantify morphological parameters (**Figure 34A**). We found that the mean number of branches per cell was significantly increased in 3xTg mice compared with WT (160.4 ± 15.2 vs 100 ± 3.5%; $p<0.01$; n = 4-7/group). ATL was able to reduce this number of branches in 3xTg mice compared with vehicles (96.0 ± 7.7 vs 160.4 ± 15.2%; $p<0.01$; n = 7/group) (**Figure 34B**). The mean number of junctions per cell was also significantly higher

in 3xTg compared with WT mice (165.8 ± 16.9 vs 100 ± 3.4%; p<0.01; n = 4-7/group), and ATL was able to decrease this number compared with vehicles (96.4 ± 8.4 vs 165.8 ± 16.9%; p<0.01; n = 7/group) (**Figure 34C**). The mean branch length was reduced in 3xTg mice compared with WT (88.4 ± 3.2 vs 100 ± 1.9%; p<0.05; n = 4-7/group). ATL restored this value in 3xTg mice compared with vehicles (102.0 ± 1.8 vs 88.4 ± 3.2%; p<0.01; n = 7/group) (**Figure 34D**). Parameters such as the circularity and the span ratio of astrocytes were not altered in any of the animal groups analyzed (**Figure 34E, F**).

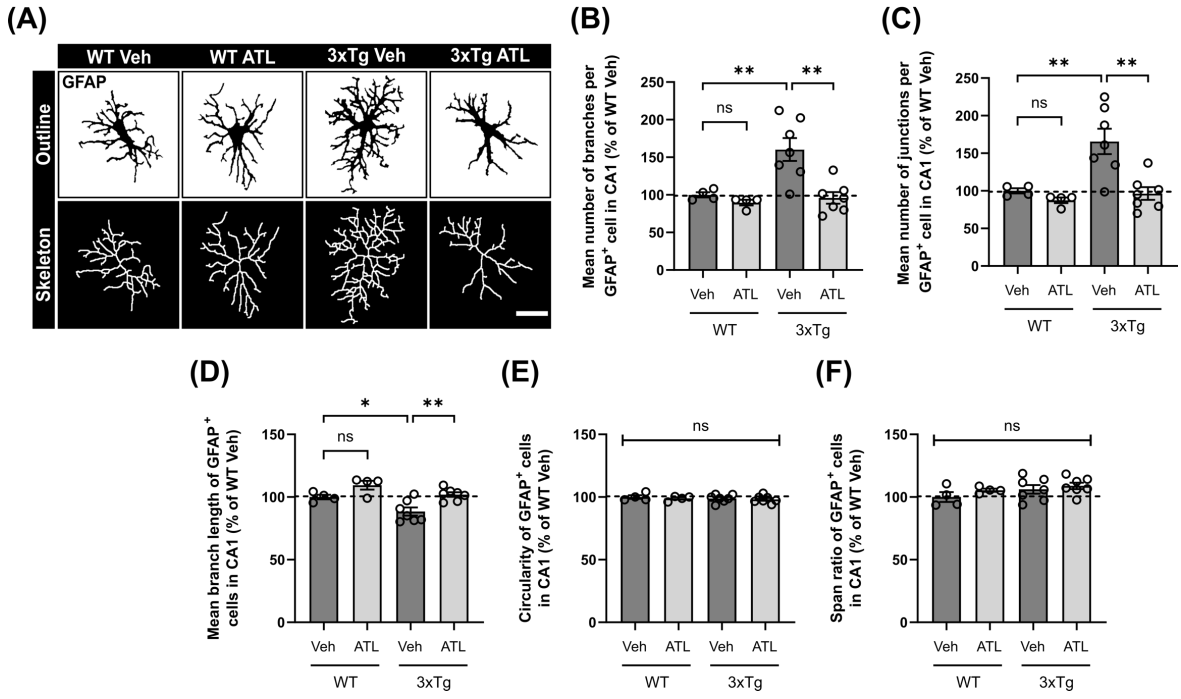

Figure 34. ATL prevents morphological alterations in hippocampal astrocytes of 3xTg mice. (A) Representative images of GFAP$^+$ astrocytes in CA1 hippocampal area of WT and 3xTg mice treated with ATL or vehicle (n =4-7/group). The outline of individual cells, as well as their skeletons, were used to quantify morphological parameters. Scale bar = 20 µm. **(B)** Quantification of the mean number of branches per GFAP$^+$ cell **(D)** Mean branch length of GFAP$^+$ cells. **(E, F)** Quantification of circularity and span ratio of GFAP$^+$ cells, respectively. Each bar represents the mean ± SEM. * p<0.05; ** p<0.01; ^{ns} not significant; one-way ANOVA.

All of these results suggest that ATL effectively reduces microgliosis and astrogliosis. This lipoxin is also able to avoid morphological alterations such as rod-shape microglia and hypertrophic astrocytes in 3xTg mice.

1.5.5. ATL restores mitochondrial dynamics and ROS generation.

Our previous results with *in vitro* models suggest that lipoxin ATL has a direct effect on mitochondrial function. Impaired mitochondrial respiration has been reported in female 3xTg mice, together with increased ROS production (Yao *et al.*, 2009; Djordjevic *et al.*, 2020). Considering this, we isolated mitochondria from WT and 3xTg mice treated with ATL or vehicle, and analyzed the respiratory chain components, as well as mitochondrial ROS accumulation. First, we quantified the expression of respiratory chain complexes I-V. Regarding complexes I, II and III (NDUFB8, SDHB and UQCRC2, respectively), we found a tendency to be reduced in 3xTg mice compared with WT mice, although it was not statistically significant (**Figure 35A-D**). Complex IV (MTCO1) was significantly reduced in 3xTg mice compared with WT (70.9 ± 4.8 vs 100 ± 14.6%; $p<0.05$; n = 4-7/group). However, ATL did not recover its expression (**Figure 35E**). Complex V (ATP synthase ATPS5A) was also significantly reduced in 3xTg compared with WT mice (67.1 ± 8.6 vs 100 ± 8.0; $p<0.05$; n = 4-7/group), although ATL did not recover its expression compared with vehicles (**Figure 35F**).

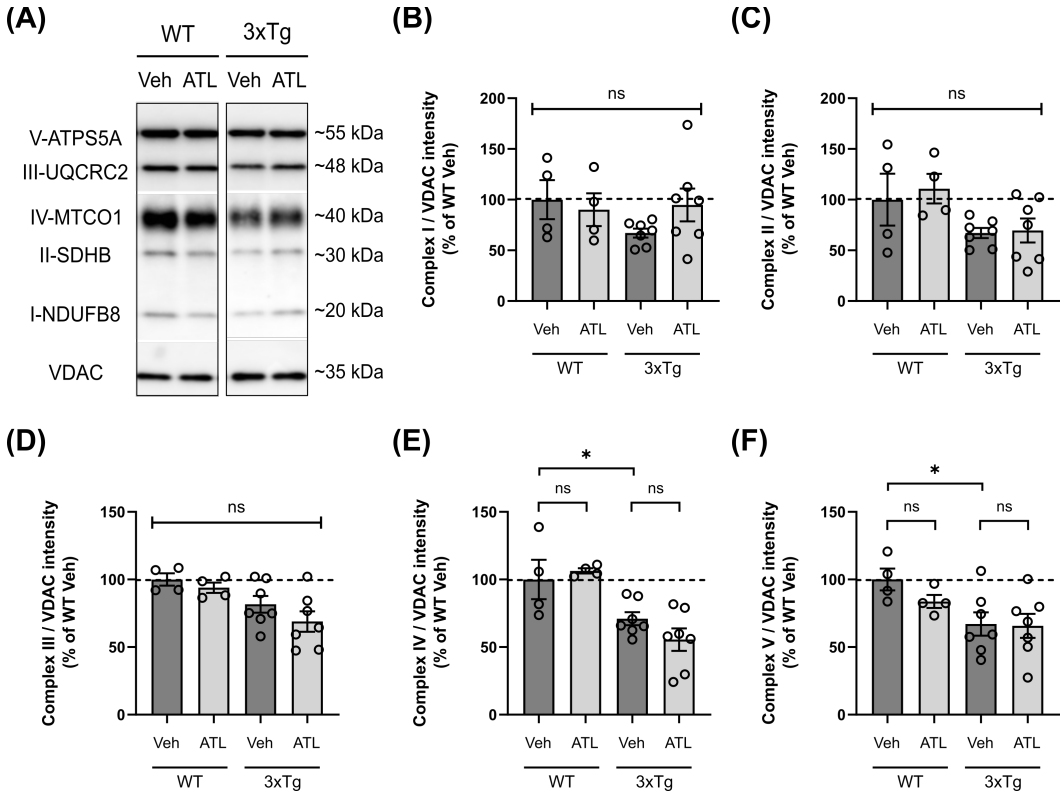

Figure 35. ATL does not have an effect on the expression of respiratory chain components in 3xTg mice. (A) Western blot of respiratory chain components (I-V) in isolated mitochondria from whole brain fractions. **(B-F)** Quantification of complex I, complex II, complex III, complex IV and complex V. Raw data was normalized with mitochondrial marker VDAC (n = 4-7/group). Each bar represents the mean ± SEM. * $p<0.05$; ^{ns} not significant; one-way ANOVA.

Next, we asked ourselves whether ATL could have an effect on mitochondrial ROS. To answer that question, we quantified both superoxide radical generation and SOD activity in the mitochondria. We observed significantly higher levels of superoxide radicals in the mitochondria of 3xTg mice compared with WT (122.9 ± 3.4 vs 100 ± 2.5%; $p<0.05$; n = 4-7/group). In addition, ATL treatment reduced this ROS production compared to vehicles (101.4 ± 8.5 vs 122.9 ± 3.4%; $p<0.05$; n = 7/group) (**Figure 36A**). On the other hand, SOD activity was lower in 3xTg mice than in WT mice, although not statistically significant. ATL did increased SOD activity in 3xTg mice compared to vehicles (126.5 ± 14.4 vs 78.4 ± 4.3%; $p<0.05$; n = 7/group) (**Figure 36B**). No differences were found in SOD activity in cytosolic fractions (**Figure 36C**).

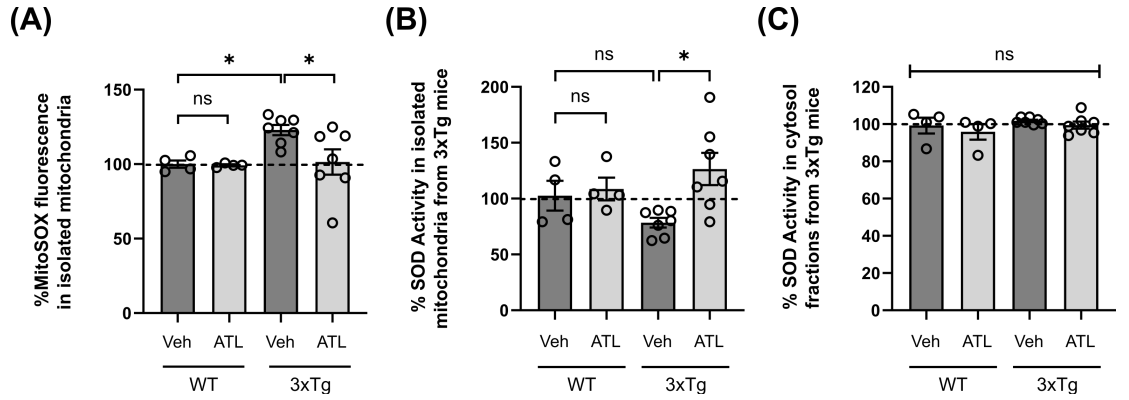

Figure 36. Lipoxin ATL reduces ROS production and enhances SOD activity in mitochondria of 3xTg mice. (A) Quantification of superoxide radicals with MitoSOX^{TM} probe in isolated mitochondria (n = 4-7/group). **(B, C)** Quantification of SOD activity in isolated mitochondria and cytosolic fractions, respectively (n = 4-7/group). Each bar represents the mean ± SEM. * $p<0.05$; ^{ns} not significant; one-way ANOVA.

In addition to respiration, mitochondrial dynamics are also altered in the 3xTg model, with favored mitochondrial fission (Djordjevic *et al.*, 2020). In order to see the effect of ATL on mitochondrial dynamics, we quantified fission marker

DRP1 and fusion marker MFN2 in isolated mitochondria of WT and 3xTg mice treated with ATL or vehicle. We found that DRP1 was increased in 3xTg compared with WT (155.6 ± 13.5 vs 100 ± 10.9%; p<0.05; n = 4-7/group), while ATL significantly lowered its expression (90.9 ± 9.8 vs 155.6 ± 13.5%; p<0.01; n = 7/group) (**Figure 37A, B**). On the other hand, MFN2 was significantly reduced in 3xTg mice compared with WT mice (74.3 ± 2.3 vs 100 ± 4.5%; p<0.01; n = 4-7/group), while ATL recovered its expression compared to vehicles (96.1 ± 5.3 vs 74.3 ± 2.3%; p<0.01; n = 7/group) (**Figure 37C, D**).

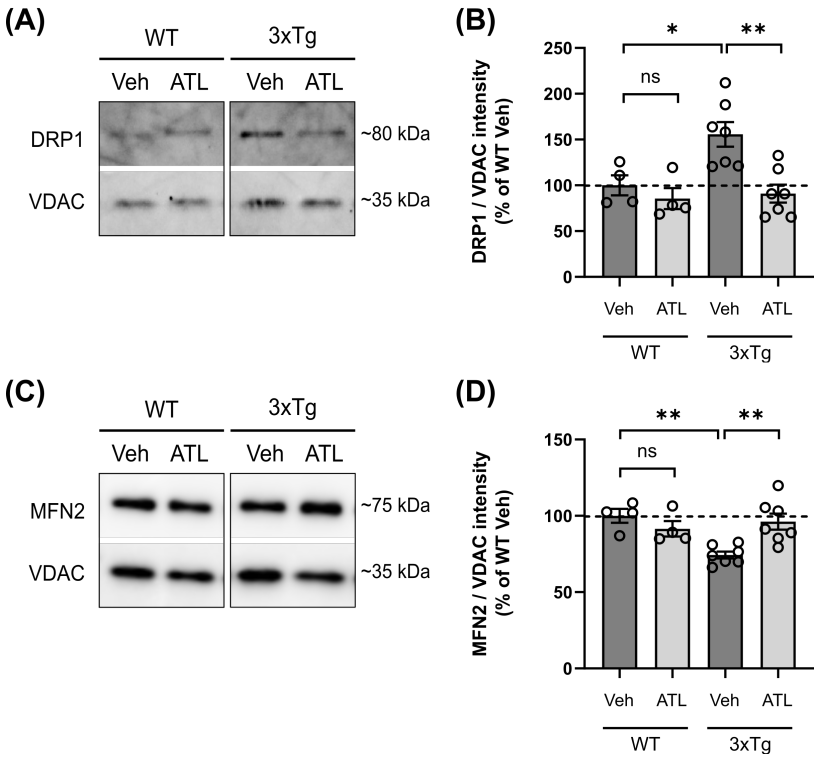

Figure 37. ATL restores the balance between mitochondrial fusion and fission processes in 3xTg mice. (A) Western blot of fission marker DRP1 in isolated mitochondria from WT and 3xTg mice treated with ATL or vehicle, and **(B)** quantification (n = 4-7/group). **(C)** Western blot of fusion marker Mitofusin 2 in isolated mitochondria and **(D)** quantification. Raw data was normalized using mitochondrial marker VDAC. Each bar represents the mean ± SEM. * p<0.05; ** p<0.01; ^{ns} not significant; one-way ANOVA. MFN2 = mitofusin 2.

In summary, 3xTg mice display reduced expression of respiratory complexes IV and V, along with increased mitochondrial ROS and high mitochondrial fission. ATL was able to reduce ROS generation and increase ROS detoxification, and it recovered mitochondrial fission/fusion balance.

In this first part of the thesis, we studied the effect of pro-resolution mediator lipoxin ATL on neuroinflammation, mitochondrial dysfunction and AD pathology (**Figure 38**). Using *in vitro* and *in vivo* models, we found that ATL reduces AD neuropathological features such as plaque deposition, tau hyperphosphorylation, synaptic loss and pro-inflammatory cytokine release. ATL is also able to reduce the activation of microglia and astrocytes, as well as their pathology-associated morphological alterations. Lastly, ATL restores ROS accumulation in the mitochondria, and rebalances fusion/fission dynamics.

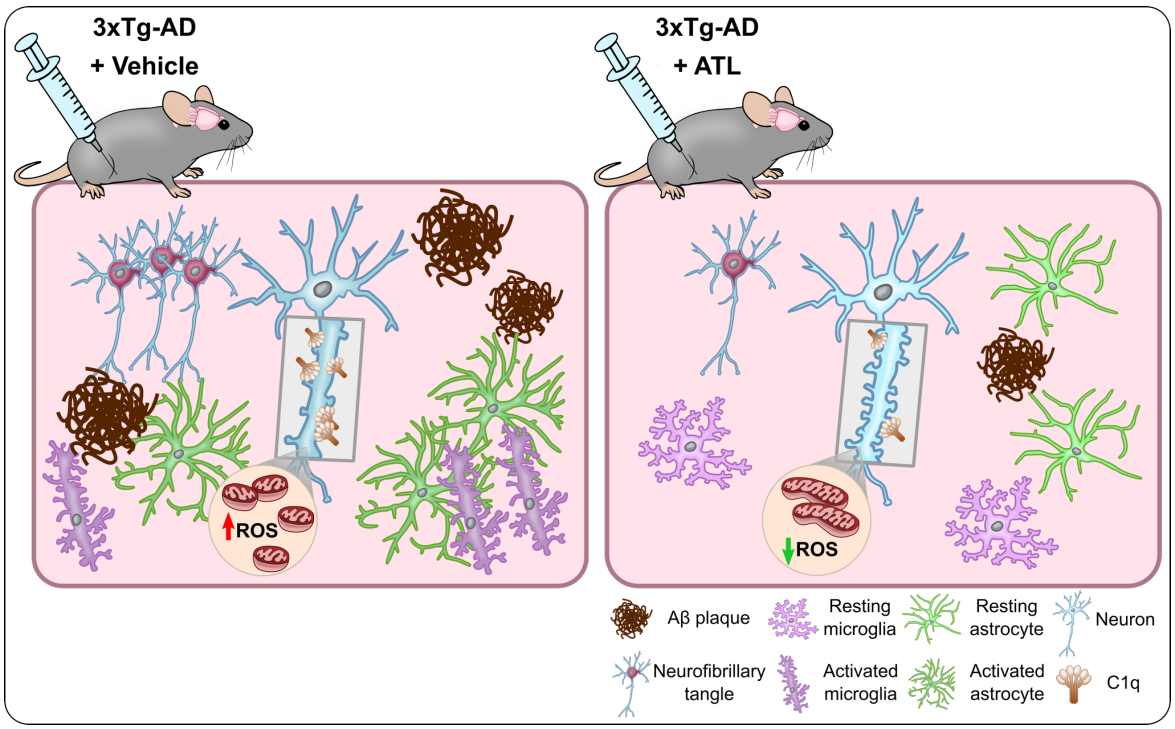

Figure 38. Lipoxin ATL attenuates AD pathology, gliosis and mitochondrial dysfunction in 3xTg mice. (Left) 3xTg mice display AD neuropathological features such as senile plaques, hyperphosphorylated tau and synapse loss. There is extensive microgliosis (rod-shape microglia) and astrogliosis (hypertrophic astrocytes) in the hippocampi of these animals, along with increased levels of pro-inflammatory cytokines IL-1β, KC/GRO and TNF-α. In addition, mitochondrial dynamics are altered, with increased mitochondrial fission and elevated ROS generation. **(Right)** 3xTg mice treated with lipoxin ATL exhibit low plaque deposition and tau hyperphosphorylation, as well as reduced C1q-dependent synaptic elimination. Mice treated with ATL also display lower levels of pro-inflammatory cytokines IL-1β and TNF-α, along with significantly reduced microgliosis and astrogliosis. Finally, ATL restores mitochondrial fusion/fission balance, and decreases ROS generation.

2. Microglial complement receptor CR3 inhibition with small molecule XVA143 reveals transcriptomic changes and alterations in cellular migration and Aβ internalization.

Complement receptor CR3 participates in diverse inflammation processes (reviewed in Ricklin *et al.*, 2010), and both subunits CD11b and CD18 are elevated in the cortex of AD patients (Akiyama and McGeer, 1990). Genetic ablation of CD11b reduces uptake of fibrillar $A\beta_{1-42}$ (Fu *et al.*, 2012; Czirr *et al.*, 2017), and also diminishes microglia-mediated synaptic elimination (Hong *et al.*, 2016; Merlini *et al.*, 2019). These studies support the crucial role of CR3 in AD progression and, consequently, its potential as therapeutic target. To explore this premise, we evaluated the relationship between CR3 and microglial function.

2.1. Compound XVA143 effectively reduces complement receptor CR3 in the cell membrane of primary microglia.

As a tool to analyze how CR3 could modulate microglial function, we used XVA143, an allosteric CR3 antagonist that binds to CD18 subunit (Shimaoka *et al.*, 2003). Firstly, we performed cell viability and cell death assays to ensure non-cytotoxic concentrations of the compound, both in primary microglia and the BV2 cell line. After treating cells with 1 and 5 μM XVA143 for 24 h, we measured cell viability using Calcein AM, and cell death using Ethidium homodimer-1. We found that only 5 μM XVA143 significantly reduced cell viability in primary microglia (86.6 ± 9.9 vs 100 ± 11.9%; $p<0.05$; n = 5), while it did not affect BV2 cells (**Figure 39A**). Accordingly, 5 μM XVA143 increased cellular death in primary microglia (129.3 ± 12.3 vs 100 ± 11.8%; $p<0.05$; n = 5), and it did not affect BV2 cells (**Figure 39B**). Thus, 1 μM XVA143 was used in the following experiments, agreeing with previous studies performed in human lymphocytes (Salas *et al.*, 2004). Next, we asked ourselves whether XVA143 was able to reduce the expression of CR3. To answer this question, we quantified subunits CD11b and CD18 at the gene expression and protein expression levels. We did not observe any changes in the gene expression of either CD11b (ITGAM gene) or CD18

(ITGB2 gene) with 1 μM XVA143 for 24 h (n = 4) (**Figure 39C, D**). At the protein level, we quantified both subunits in total lysates and in cell membrane samples, extracted by biotinylation, after treatment with 1 μM XVA143 for 24 h. We also added 3 μM oAβ to induce a basal increase of CR3. We found that oAβ significantly increased CD11b both in total lysates (161.7 ± 30.5 vs 100 ± 11.7%; $p<0.05$; n = 5) and the cellular membrane compared with controls (302.9 ± 49.3 vs 226.4 ± 51.3%; $p<0.05$; n = 5). At the same time, XVA143 drastically reduced CD11b in total lysates (20.6 ± 13.9 vs 100 ± 11.7%; $p<0.01$; n = 5) and the cell membrane (71.9 ± 26.9 vs 226.4 ± 51.3%; $p<0.05$; n = 5) (**Figure 39E, F**). Regarding CD18, oAβ increased its expression only in the cellular membrane (222.7 ± 43.8 vs 122.6 ± 24.4%; $p<0.05$; n = 6), compared with controls. XVA143 significantly reduced CD18 by ~0.5 fold in total lysates (44.2 ± 9.9 vs 100 ± 28.8%; $p<0.05$; n = 6) and the cell membranes (48.1 ± 15.3 vs 122.6 ± 24.4%; $p<0.05$; n = 6), compared with controls. Additionally, oAβ still increased CD18 in the cell membrane (91.0 ± 14.4 vs 48.1 ± 15.3%; $p<0.05$; n = 6) in the presence of XVA143 (**Figure 39E, G**). These results suggest that XVA143 can effectively reduce CR3 in the cell surface of primary microglia, while it does not alter gene expression.

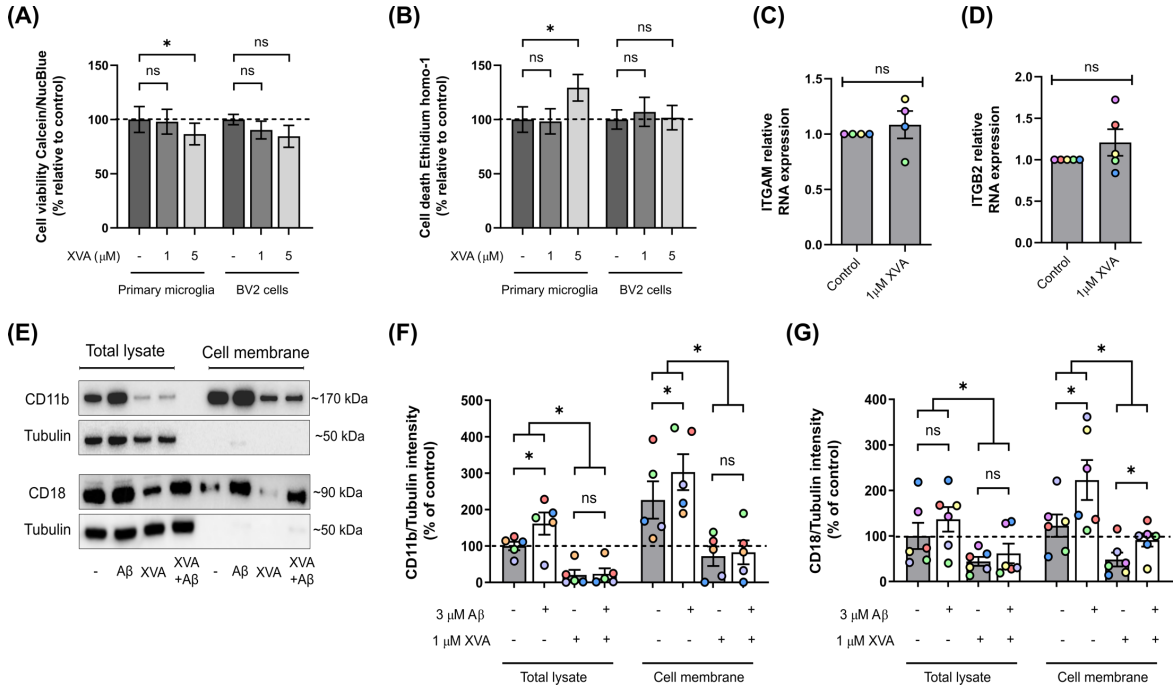

Figure 39. XVA143 reduces CR3 subunits CD11b and CD18 in primary microglia. **(A)** Cell viability assay for XVA143 using fluorescent probe Calcein AM in primary microglia and the cell line BV2, 24 h after treatment (n = 5). **(B)** Cell death assay for XVA143 using fluorescent probe Ethidium homodimer-1 in primary microglia and BV2 cells, 24 h after treatment (n = 5). Data was normalized with the number of cells per condition. Paired one-way ANOVA. **(C)** Gene expression of ITGAM/CD11b and **(D)** ITGB2/CD18 in primary microglia after 1 μM XVA143 for 24 h (n = 4). RNA relative expression was represented as fold change. Paired Student's t test. **(E)** Western blot of CD11b and CD18 in cellular surfaces and total lysates of primary microglia. **(F, G)** Quantification of CD11b (n = 5) and CD18 (n = 6), respectively, after treatment with 3 μM oAβ and 1μM XVA143 for 24 h. Raw data was normalized using α-tubulin. Each bar represents the mean ± SEM. * $p<0.05$; ^{ns} not significant; paired one-way ANOVA. XVA = XVA143.

2.2. XVA143 alters microglial morphology and migration capacity.

After we proved that 1 μM XVA143 does not reduce cellular viability, and that it reduces CR3 expression, we wanted to know if this small molecule could affect microglial morphology and motility. CR3 is part of the integrin β_2 family, and it takes part in cell adhesion, cytoskeleton support and migration processes (reviewed in Fagerholm *et al.*, 2019). Previous studies have reported that XVA143 induces a round morphology and reduces adhesion in monocytes and lymphocytes (Yang *et al.*, 2006), so we analyzed the effect of the compound in primary microglia. First, we quantified microglial morphology after treating the cells with 1 μM XVA143 for 24 h. We observed a significant reduction of the area occupied by Iba1$^+$ cells with XVA143 (77.0 ± 5.9 vs 100 ± 11.1%; $p<0.05$; n = 5) compared to controls (**Figure 40A, B**). The number of Iba1$^+$ cells per area unit was also significantly lower in the presence of XVA143 (77.4 ± 6.8 vs 100 ± 5.8%; $p<0.05$; n = 5) (**Figure 40A, C**). To evaluate changes in the cytoskeleton, we stained microglia with phalloidin to detect filamentous actin (F-actin). We found that the area occupied by F-actin per CD11b$^+$ cell was significantly reduced by ~0.5 fold with XVA143 (41.7 ± 6.6 vs 100 ± 15.9%; $p<0.01$; n = 5), compared with controls (**Figure 40D, E**). Finally, and in agreement with Yang *et al.*, the circularity of CD11b$^+$ cells was significantly increased with XVA143 (166.1 ± 23.6 vs 100 ± 14.4%; $p<0.05$; n = 5), compared with controls (**Figure 40D, F**).

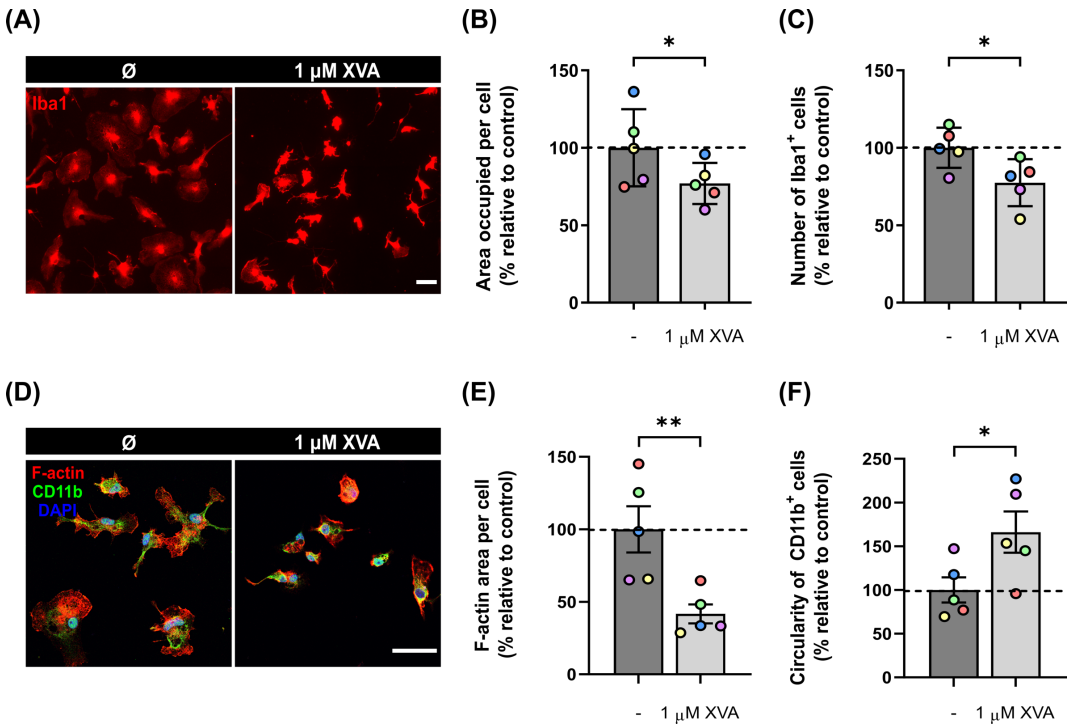

Figure 40. XVA143 induces morphological alterations in primary microglia. (A) Representative image of Iba1$^+$ primary microglia. Scale bar = 200 μm. **(B, C)** Quantification of the area per Iba1$^+$ cell and the number of Iba1$^+$ cells, respectively, after treatment with 1 μM XVA143 for 24 h (n = 5). Paired Student's t test. **(D)** Representative image of CD11b$^+$ primary microglia stained with phalloidin for F-actin. Scale bar = 40 μm. **(E)** Area occupied by F-actin per cell after treatment with 1 μM XVA143 for 24 h (n = 5). **(F)** Circularity of CD11b$^+$ cells (n = 5). Each bar represents the mean ± SEM. * p<0.05; ** p<0.01; paired Student's t test.

Several authors have reported that, along with morphology alterations, XVA143 can reduce lymphocyte rolling adhesion and migration (Salas *et al.*, 2004; Yang *et al.*, 2006). Thus, we analyzed cellular migration in both primary microglia and the BV2 cell line, using the scratch wound assay and the transwell migration assay after treating the cells with 1 μM XVA143 for 16 h. In primary microglia, XVA143 was able to significantly reduce cellular migration compared with controls, both in the scratch wound assay (61.9 ± 12.0 vs 100 ± 25.6%; p<0.05; n = 4) (**Figure 41A, B**), and the transwell migration assay (54.1 ± 6.8 vs 100 ± 13.4%; p<0.01; n = 4) (**Figure 41C, D**). We made the same observations in BV2 cells, where XVA143 effectively reduced cellular migration compared with controls both in the scratch wound assay (56.8 ± 10.5 vs 100 ± 5.6%; p<0.05; n = 4) (**Figure 41E, F**) and the transwell assay (50.1 ± 11.3 vs 100 ± 28.3%; p<0.01; n = 3) (**Figure 41G, H**).

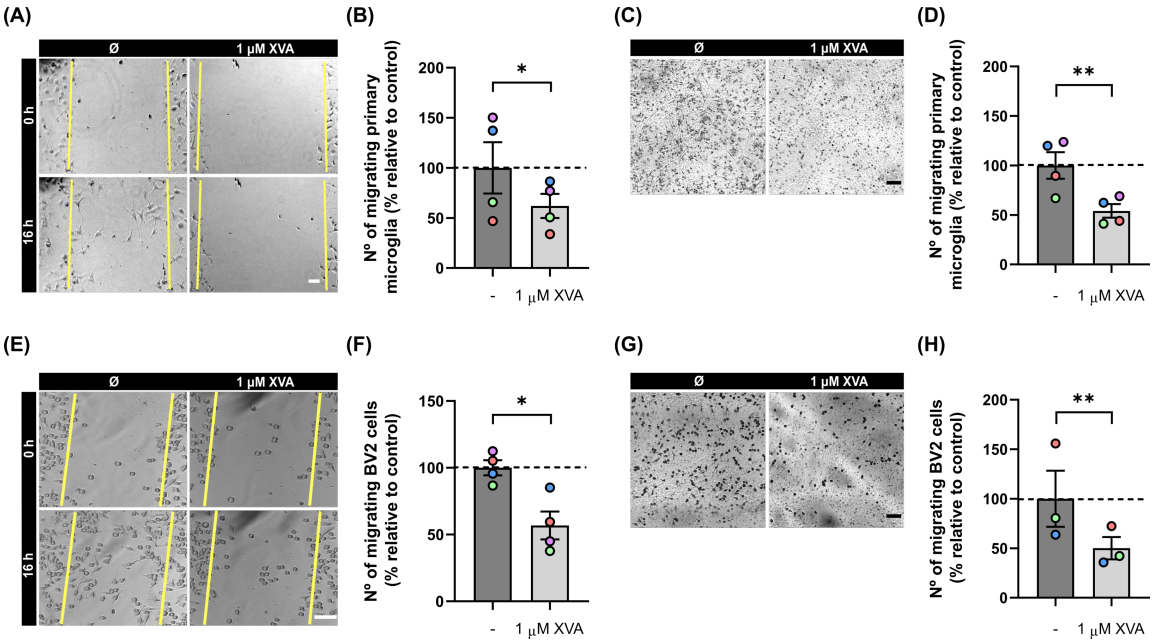

Figure 41. XVA143 impairs cellular migration in primary microglia and BV2 cells. **(A, B)** Representative image of the scratch wound assay and quantification in primary microglia (n = 4), after treatment with 1 µM XVA143 for 16 h. Scale bar = 50 µm. **(C, D)** Transwell migration assay and quantification in primary microglia (n = 4), after treatment with 1 µM XVA143 for 16 h. Scale bar = 100 µm. **(E, F)** Representative image of scratch wound assay and quantification in the BV2 cell line (n = 4), after treatment with 1 µM XVA143 for 16 h. Scale bar = 50 µm. **(G, H)** Transwell migration assay and quantification in BV2 cells (n = 3), after treatment with 1 µM XVA143 for 16 h. Scale bar = 100 µm. Each bar represents the mean ± SEM. * $p<0.05$; ** $p<0.01$; paired Student's t test.

In summary, we found that the inhibition of CR3 by XVA143 changes microglial morphology to a more rounded shape, and impairs cellular migration both in primary microglia and BV2 cells.

2.3. Characterization of transcriptomic changes induced by XVA143 in primary microglia.

Several studies performed in peripheral immune cells involve CR3 in the regulation of anti-inflammatory cytokines, so we analyzed the expression of inflammation-related genes. After we treated primary microglia with 1 µM XVA143 for 24 h, we quantified gene expression for pro-inflammatory cytokines IL-1γ, TNF-α and IFN-γ, and anti-inflammatory cytokines IL-10, TGF-β1 and TGF-β3. We also included in the analysis markers typically associated with pro-

inflammatory microglia, CD40 (tumor necrosis factor receptor superfamily, member 5) and CD74 (HLA class II histocompatibility antigen γ chain); as well as markers typically associated with anti-inflammatory microglia, MRC1 (Mannose Receptor C-type 1) and CD33 (sialic acid-binding Ig-like lectin 3). We found that XVA143 significantly upregulated the expression of IL-1β by ~4 fold (5.0 ± 1.8 vs 1.0 ± 0.0 a.u.; $p<0.05$; n = 5), compared with controls. CD40 was also upregulated with XVA143 compared with controls, although it was not statistically significant (1.5 ± 0.2 vs 1.0 ± 0.0%; p = 0.06; n = 5). Expression of TNF-α, IL-10, IFN-γ, CD74, TGF-β1, TGF-β3, MRC1 and CD33 was not changed with XVA143 (**Figure 42A, B**).

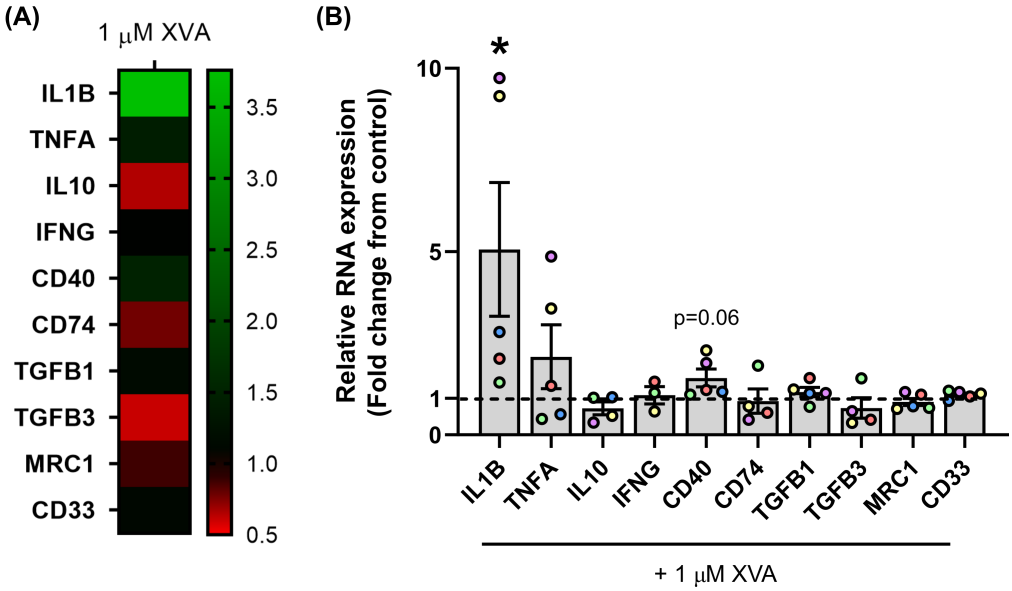

Figure 42. XVA143 upregulates the gene expression of IL-1β in primary microglia. **(A)** Heat map of inflammation-related gene expression in microglia control and treated with 1 μM XVA143 for 24 h. **(B)** Relative expression of genes IL1B, TNFA, IL10, IFNG, CD40, CD74, TGFB1, TGFB3, MRC1 and CD33. Data represented as fold change from controls (n = 5). Statistical analysis was performed with raw logarithmic data independently for each gene. Each bar represents the mean ± SEM. * $p<0.05$; paired Student's t test.

As it was mentioned before, CR3 is involved in Aβ clearance. To figure out whether XVA143 could affect Aβ elimination, we analyzed the gene expression of several membrane receptors associated with Aβ internalization and extracellular degrading enzymes associated with extracellular Aβ degradation. We quantified CD36 (scavenger receptor B) and AGER (RAGE, Receptor for

Advanced Glycosylation End-products), implicated in Aβ binding and internalization, as well as LAMP1 (Lysosomal Associated Membrane Protein 1), involved in lysosomal Aβ degradation. We also quantified extracellular Aβ-degrading enzymes PLAT, MMP2, MMP9 (Matrix metalloproteinases 2 and 9), and IDE (Insulin Degrading Enzyme). XVA143 significantly downregulated AGER compared with controls (0.5 ± 0.02 vs 1.0 ± 0.0 a.u.; p<0.01; n = 3). MMP2 also displayed a downregulation trend with XVA143, although it was not statistically significant (0.6 ± 0.1 vs 1.0 ± 0.0 a.u.; p = 0.068; n = 5). Expression of CD36, PLAT, MMP9, IDE and LAMP1 was not altered (**Figure 43A, B**).

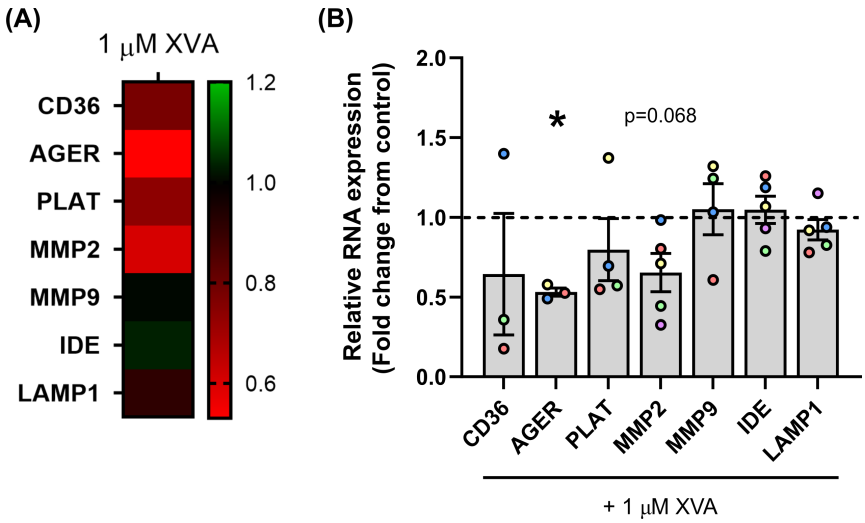

Figure 43. XVA143 downregulates the gene expression of AGER in primary microglia. (A) Heat map of Aβ clearance-related gene expression in microglia control and treated with 1 μM XVA143 for 24 h. **(B)** Relative expression of genes CD36, AGER, PLAT, MMP2, MMP9, IDE and LAMP1. Data represented as fold change from controls (n = 5). Statistical analysis was performed with raw logarithmic data independently for each gene. Each bar represents the mean ± SEM. * p<0.05; paired Student's t test.

Finally, we addressed if modulation of CR3 had an effect on other components of the complement system. Given that the inhibition with XVA143 drastically reduced the expression of CR3 itself on the cell surface, we asked whether it could also affect the expression of components of the complement cascade. To answer this, we quantified the gene expression of C1qA, C1qB, C1qC, C2, C3, C4a and TYROBP (Tyrosine kinase-binding protein or DAP12), which is an adapter for CR3 (Haure-Mirande *et al.*, 2017). We also analyzed transcription factors SPI1 (or PU.1), STAT1 (Signal Transducer and Activator of

Transcription 1) and IRF8 (Interferon Regulatory Factor 8), which have been reported to mediate C1q transcription (Chen *et al.*, 2011). We observed that XVA143 significantly downregulated the expression of C4a compared with control microglia (0.6 ± 0.1 vs 1.0 ± 0.0 a.u.; $p<0.05$; n = 4). TYROBP was also downregulated with XVA143 compared with controls (0.9 ± 0.04 vs 1.0 ± 0.0 a.u.; p = 0.07; n = 5), although it was not statistically significant. Interestingly, XVA143 induced a non-significant downregulation of C1qA, C1qB and C1qC, and a statistically significant downregulation of their transcription factor IRF8 (0.7 ± 0.09 vs 1.0 ± 0.0 a.u.; $p<0.05$; n = 5). Expression of C2, C3, SPI1 and STAT1 was not altered with XVA143 compared with control microglia (**Figure 44A, B**).

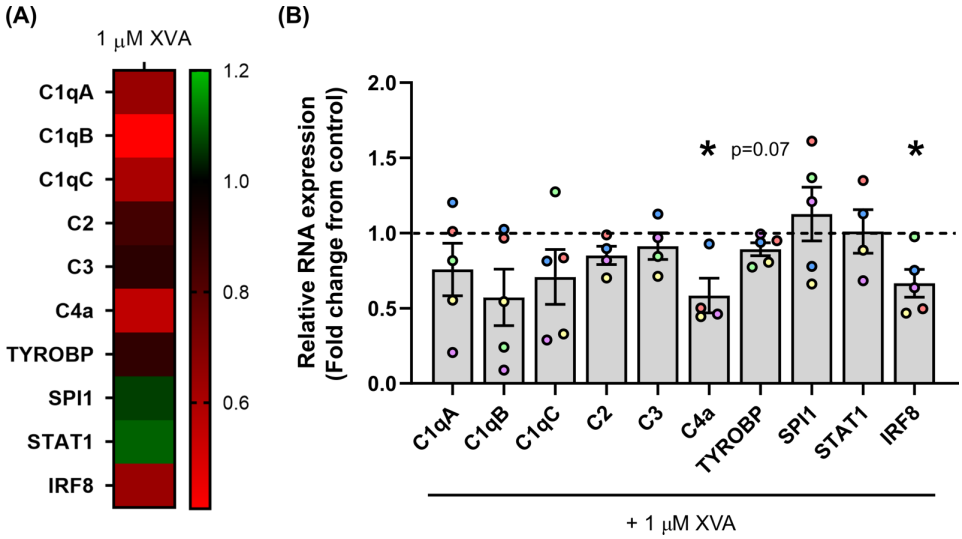

Figure 44. XVA143 downregulates gene expression of complement component C4a and transcription factor IRF8 in primary microglia. (A) Heat map of complement-related gene expression in microglia control and treated with 1 μM XVA143 for 24 h. **(B)** Relative expression of genes C1qA,B,C, C2, C3, C4a, TYROBP, SPI1, STAT1 and IRF8. Data represented as fold change from controls (n = 5). Statistical analysis was performed with raw logarithmic data independently for each gene. Each bar represents the mean ± SEM. * $p<0.05$; paired Student's t test.

In summary, these results suggest that XVA143 induces some transcriptomic changes in primary microglia related to the inflammatory response, Aβ clearance and the complement cascade. CR3 inhibition resulted in the upregulation of cytokine IL-1β, the downregulation of AGER, and the downregulation of C1q transcription factor IRF8.

2.4. XVA143 reduces extracellular $A\beta_{1-42}$ levels in primary microglia cultures while impairing its internalization.

Once we discovered that CR3 inhibition causes relevant modifications in microglial transcriptome, as well as alterations in morphology and migration capacity, we studied the effect of XVA143 in the context of amyloid pathology. CR3 deficiency reduces Aβ deposition in APP mice (Czirr *et al.*, 2017), so we hypothesized that XVA143 inhibition would also reduce oligomeric Aβ in our *in vitro* conditions. To test this hypothesis, we treated primary microglia and hippocampal organotypic cultures with 3 μM oAβ and 1 μM XVA143 for 24 h and then quantified extracellular $A\beta_{1-42}$ levels. In the case of primary microglia, we found that $A\beta_{1-42}$ was significantly reduced in supernatants with XVA143 (2786 ± 201.3 vs 3327 ± 312.5 ng/ml; $p<0.05$; n = 4), compared to controls (**Figure 45A**). In organotypic cultures, there was also a significant reduction in $A\beta_{1-42}$ levels in supernatants with the XVA143 treatment (1942 ± 210.6 vs 2337 ± 195.5 ng/ml; $p<0.05$; n = 7), compared to controls (**Figure 45B**). Once we saw that XVA143 was able to reduce extracellular $A\beta_{1-42}$, we tried to figure out what mechanisms would be involved in this Aβ clearance. First, we checked Aβ internalization. We quantified Aβ integrated density inside $Iba1^+$ microglia after treatment with 3 μM oAβ and 1 μM XVA143 for 24 h. Interestingly, we found a significant reduction of Aβ inside microglial cells with XVA143 (75.5 ± 4.5 vs 100 ± 10.5%; $p<0.05$; n = 4), compared to controls. To differentiate between internalization and degradation, we blocked degradation using 100 μM leupeptin, an inhibitor of lysosomal cysteine proteases. Aβ inside $Iba1^+$ cells was significantly higher with leupeptin compared with non-treated cells (152.7 ± 18.1 vs 171.2 ± 13.8%; $p<0.001$; n = 8), and we found no differences in the leupeptin group between control microglia and microglia treated with XVA143 (**Figure 45C, D**).

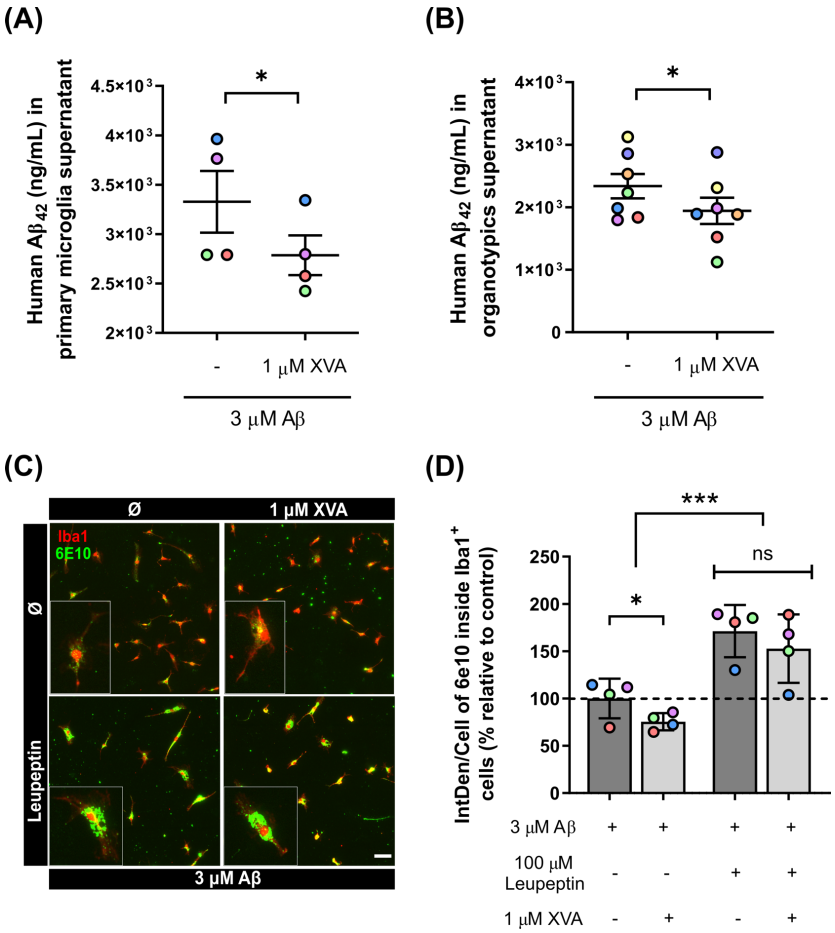

Figure 45. XVA143 reduces Aβ$_{1-42}$ levels in culture supernatants and reduces its internalization. (A, B) ELISA quantification of Aβ$_{1-42}$ in microglia supernatants (n = 4) and organotypic culture supernatants (n = 7), after treatment with 3 μM oAβ and 1 μM XVA143 for 24 h. Paired Student's t test. **(C)** Representative images of Iba1^{+} microglia and Aβ using 6E10. Scale bar = 200 μm. **(D)** Integrated density of 6E10 inside Iba1^{+} cells after treatment with 3 μM oAβ, 1 μM XVA143 and 100 μM leupeptin for 24 h (n = 4). Paired one-way ANOVA. Each bar represents the mean ± SEM. * p<0.05; *** p<0.001; ^{ns} not significant. IntDen = integrated density.

Next, we quantified the gene expression of Aβ internalization receptors MSR1 (Macrophage Scavenger Receptor 1), CD36 and AGER, and lysosomal marker LAMP1 after treatment with 3 μM oAβ and 1 μM XVA143 for 24 h. We did not find any differences in MSR1 and CD36, although CD36 showed a non-significant trend to increase in XVA143 treated microglia with oAβ compared with XVA143 alone (2.3 ± 1.1 vs 1.5 ± 0.9 a.u.; p = 0.08; n = 4). XVA143 significantly downregulated AGER (0.5 ± 0.02 vs 1.0 ± 0.0 a.u.; p<0.01; n = 3), although oAβ did not have any effect. Finally, the expression of LAMP1 showed a trend to decrease with oAβ (0.9 ± 0.03 vs 1.0 ± 0.0 a.u.; p = 0.06; n = 5) compared with control microglia, but it was not statistically significant (**Figure 46A, B**).

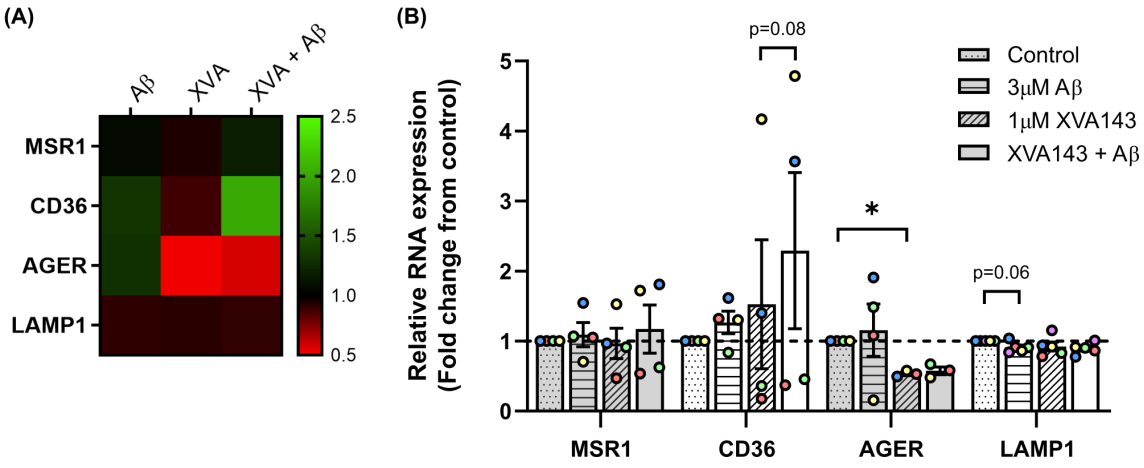

Figure 46. $A\beta_{1-42}$ does not alter the gene expression of internalization-related receptors with the presence of XVA143 in primary microglia. (A) Heat map of Aβ internalization and degradation genes in microglia treated with 3 μM oAβ and 1 μM XVA143 for 24 h. **(B)** Relative expression of genes MSR1, CD36, AGER and LAMP1. Data represented as fold change from controls (n = 5). Statistical analysis was performed with raw logarithmic data independently for each individual gene. Each bar represents the mean ± SEM. * $p<0.05$; ^{ns} not significant; paired Student's t test.

We found a reduction in Aβ internalization with XVA143, as well as a downregulation of Aβ-binding receptor AGER. This reduction in internalization agrees with previous studies reporting that CR3 deficiency impaired phagocytosis of fibrillar Aβ (Fu *et al.*, 2012), so we hypothesized that the reduction in extracellular Aβ that we observed could be due to increased secretion of extracellular degrading enzymes. To test this hypothesis, we quantified the gene expression of enzymes IDE, MMP2, MMP9 and PLAT, after treatment with 3 μM oAβ and 1 μM XVA143 for 24 h. We found that IDE was significantly downregulated in XVA143 treated microglia with oAβ compared with Aβ alone (0.9 ± 0.08 vs 1.1 ± 0.05 a.u.; $p<0.05$; n = 5). MMP2 displayed a non-significant downregulation trend with XVA143 (0.6 ± 0.1 vs 1.0 ± 0.0 a.u.; $p = 0.07$; n = 5) compared with controls, and it was not altered with oAβ. We did not find any differences in MMP9 and PLAT expression in any of the conditions analyzed (**Figure 47A, B**).

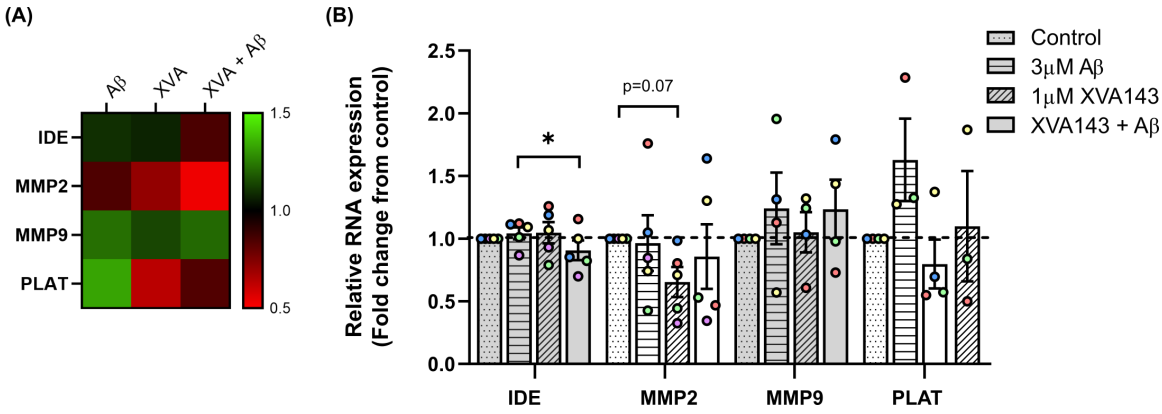

Figure 47. $A\beta_{1-42}$ does not alter the gene expression of extracellular degradation enzymes with XVA143 in primary microglia. (A) Heat map of extracellular enzyme genes in microglia treated with 3 μM oAβ and 1 μM XVA143 for 24 h. **(B)** Relative expression of genes IDE, MMP2, MMP9 and PLAT. Data represented as fold change from controls (n = 5). Statistical analysis was performed with raw logarithmic data independently for each individual gene. Each bar represents the mean ± SEM. * $p<0.05$; ^{ns} not significant; paired Student's t test.

Summarizing, we found that CR3 blockage significantly reduced extracellular Aβ in primary microglia and organotypic slices. At the same time, XVA143 lowered Aβ internalization and downregulated the gene expression of receptor AGER and extracellular enzyme IDE.

2.5. XVA143 reduces CD11b and complement component C1q in organotypic slices.

With the transcriptomic analysis, we found a novel relationship between CR3 and C1q. XVA143 inhibition of CR3 downregulated C1q components and IRF8, which partially regulates C1q gene expression. To confirm this finding, we used hippocampal organotypic slices. After treating the slices with 3 μM oAβ and 1 μM XVA143, we quantified CD11b and C1q by immunofluorescence. Treatment with oAβ significantly increased both the area occupied by CD11b (131.5 ± 11.4 vs 100 ± 5.7%; $p<0.05$; n = 4) and its integrated density (137.7 ± 12.3 vs 100 ± 10.2%; $p<0.05$; n = 4), compared with control slices. XVA143 was able to reduce both parameters to control levels (**Figure 48A-C**). In the case of C1q, we found that oAβ increased both the density of C1q puncta (113.3 ± 6.5 vs 100 ± 2.6%; $p<0.05$; n = 4) and its integrated density (126.6 ± 8.3 vs 100 ± 10.2%; $p<0.05$; n

= 4), compared with controls. In addition, XVA143 reduced C1q puncta density to levels lower that controls (92.2 ± 2.7 vs 100 ± 2.6%; p<0.001; n = 4), and the integrated density by ~0.5 fold (42.9 ± 10.5 vs 100 ± 10.2%; p<0.05; n = 4) (**Figure 48D-F**).

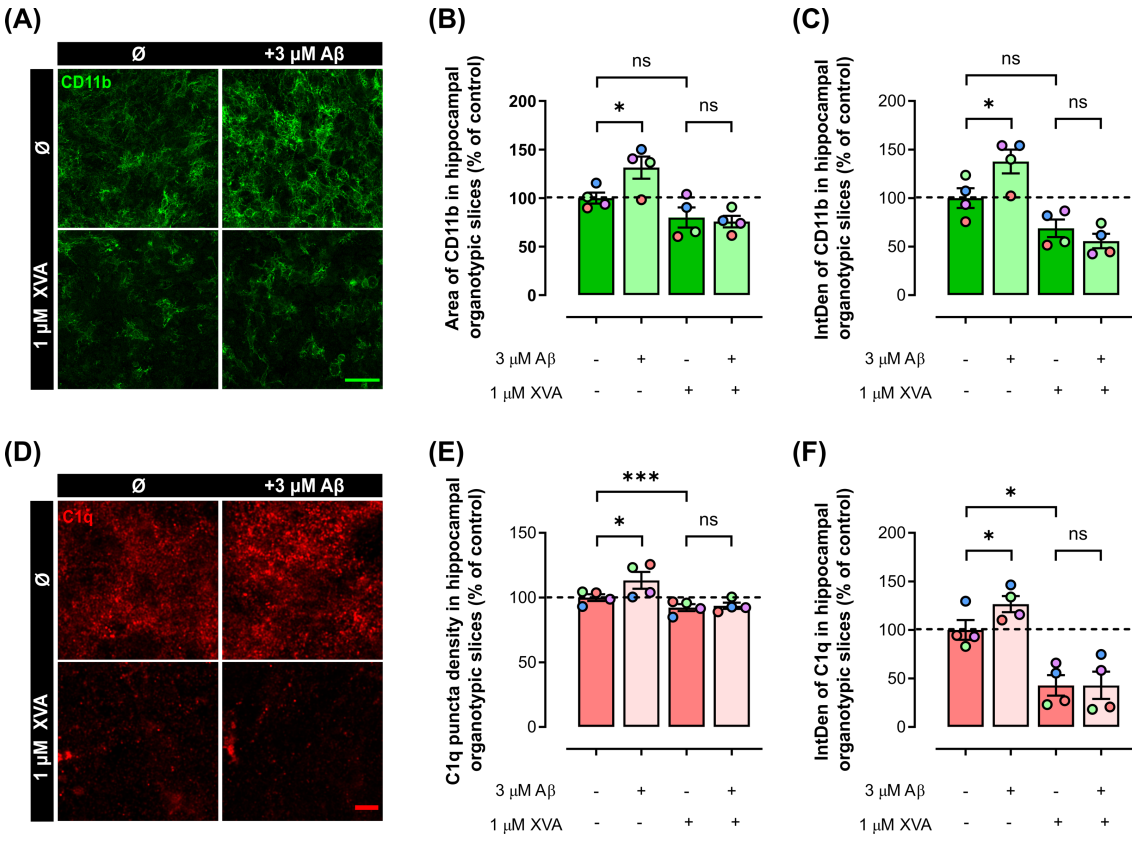

Figure 48. XVA143 reduces Aβ-induced CD11b and C1q levels in hippocampal organotypic slices. (A) Representative images of CD11b area in organotypic slices, after treatment with 3 µM oAβ and 1 µM XVA143 for 24 h. Scale bar = 40 µm. **(B, C)** Quantification of the area occupied by CD11b and its integrated density, respectively (n = 4). **(D)** Representative images of C1q puncta in organotypic slices. Scale bar = 5 µm. **(E, F)** Quantification of the density of C1q puncta and puncta integrated density, respectively (n = 4). Each bar represents the mean ± SEM. * p<0.05; *** p<0.001; ^{ns} not significant; paired one-way ANOVA. IntDen = integrated density.

These results, together with the gene expression data, suggest that XVA143 inhibition of CR3 induces a retrograde signaling that results in reduced expression of complement component C1q.

In this second part of the thesis, we analyzed the effects of XVA143 on microglial function (**Figure 49**). CR3 inhibition resulted in morphological alterations and impaired cellular migration, which supports the key role of CR3 in microglial response to injury and disease. Our results also suggest that XVA143 reduces Aβ internalization, at the same time that it reduces the levels of extracellular Aβ. Finally, our results indicate that CR3 could be involved in modulation of complement component C1q, a novel discovery that needs further investigation.

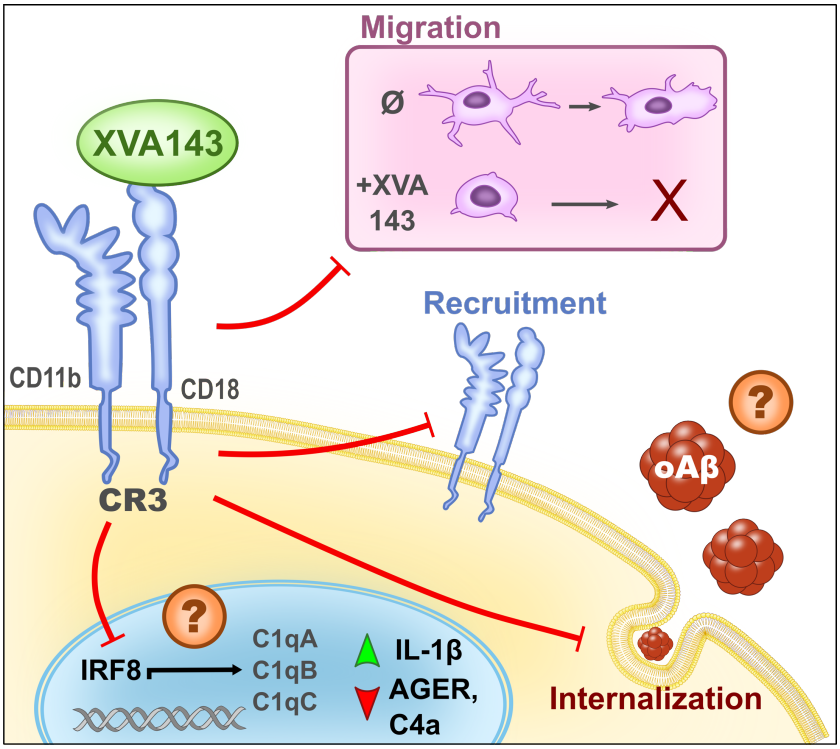

Figure 49. CR3 inhibition induces transcriptional changes and reduces cellular migration and Aβ internalization. The inhibition of CR3 with allosteric antagonist XVA143 results in alterations at multiple cellular levels in primary microglia. XVA143 reduces the recruitment of CR3 subunits CD11b and CD18 to the cellular surface. With XVA143, microglia becomes more rounded, and cellular migration is impaired. CR3 inhibition also induces changes at the transcriptional level, with increased IL-1β and reduced AGER and C4a. It also downregulates transcription factor IRF8, along with the expression of C1q components. The mechanism by which this regulation takes place is yet unknown. Finally, XVA143 seems to reduce both extracellular Aβ levels and Aβ internalization. This finding also needs further investigation to find an alternative mechanism for Aβ elimination.

3. A neuron, microglia and astrocyte triple co-culture model to study Alzheimer's disease.

After studying the role of lipoxins and complement receptor CR3 in AD neuroinflammation, we realized that available and affordable *in vitro* models to study neuron-glia interactions are limited. Thus, we decided to establish an *in vitro* model where we could study neuroinflammation in the context of neuron-glia communication. We established and characterized a straightforward murine triple co-culture model with neurons, astrocytes and microglia and added oAβ in order to recapitulate amyloid pathology and neurodegeneration (this work was accepted for publication on March 7, 2022 in the journal Frontiers in Aging Neuroscience, under the title "A neuron, microglia, and astrocyte triple coculture model to study Alzheimer´s disease".

3.1. Neurons increase synaptic markers and develop a more complex morphology when co-cultured with glial cells.

First of all, we performed a characterization of each cell type in the co-culture compared with primary cultures. Synapse formation and stabilization is promoted *in vitro* by astrocytes through secretion factors (Christopherson *et al.*, 2005). Thus, we analyzed whether neurons would develop more synapses in the triple co-culture environment. To do so, we quantified pre- and post-synaptic markers in our co-cultures. We found that post-synaptic markers Post-Synaptic Density protein 95 (PSD-95) (130.0 ± 9.1 vs 100 ± 7.1%; $p<0.05$; n = 4) and Homer1 (136.5 ± 10.5 vs 100 ± 11.9%; $p<0.01$; n = 6) were increased in the triple co-culture compared with primary neurons alone (**Figure 50A-D**). Both microglia and astrocytes had to be present to see this increase, because Homer1 was not altered in neuron-microglia or neuron-astrocyte co-cultures. Meanwhile, pre-synaptic markers Vesicular glutamate transporter 1 (VGlut1) and Synaptophysin were not different in the triple co-culture compared to primary neurons (**Figure 50E-H**).

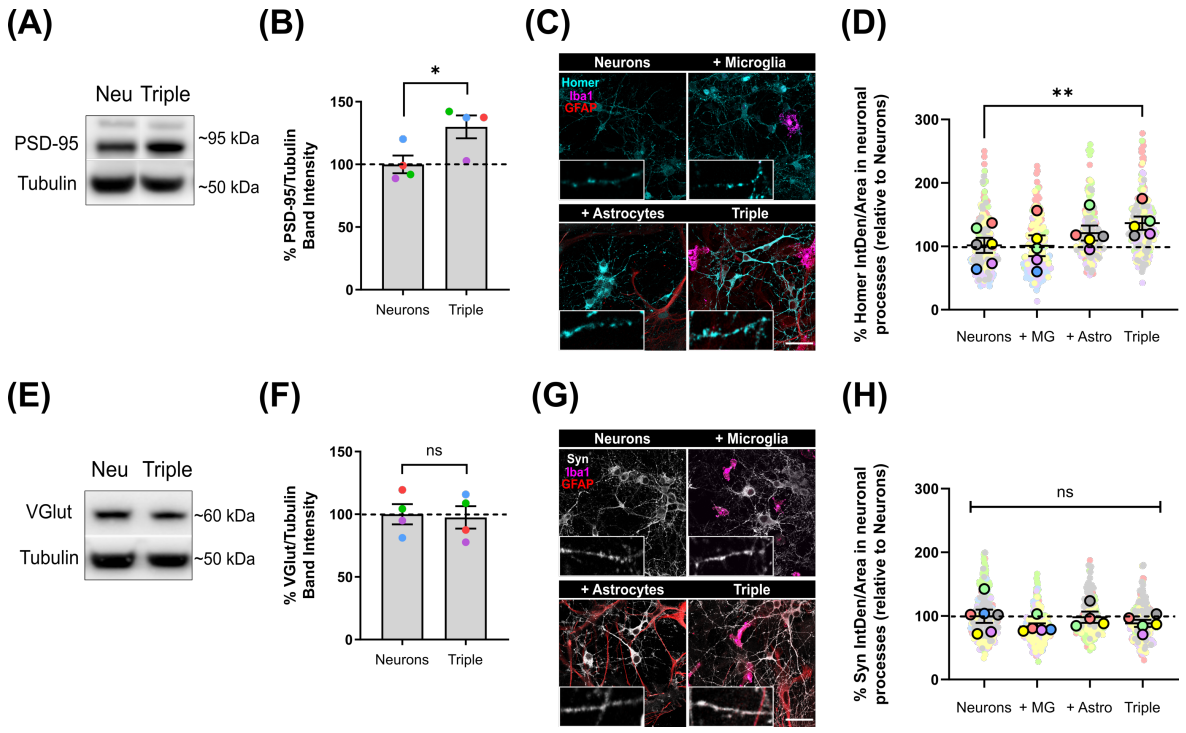

Figure 50. Neurons increase the expression of post-synaptic markers PSD-95 and Homer1 in the triple co-culture model. (A, B) Western blot of post-synaptic marker PSD-95 in total lysates and quantification in primary neurons and the triple co-culture (n = 4). Raw data was normalized using α-tubulin. Paired Student's t test. **(C)** Representative images of post-synaptic marker Homer1 in neuronal processes. In each condition, a zoom on a single neuronal process is displayed. Scale bar = 40 µm. **(D)** Quantification of Homer1 (n = 6). Mixed-effect model. **(E, F)** Western blot image of pre-synaptic marker VGlut1 in total lysates and quantification in primary neurons and the triple co-culture (n = 4). Paired Student's t test. **(G)** Representative images of pre-synaptic marker Synaptophysin in neuronal processes. In each condition, a zoom on a single neuronal process is shown. Scale bar = 40 µm. **(H)** Quantification of Synaptophysin (n = 6). Mixed-effect model. Each bar represents the mean ± SEM. Each scatter plot represents the mean ± SEM. * $p<0.05$; ** $p<0.01$; ^{ns} not significant. Neu = neurons; MG = microglia; Astro = astrocytes; Syn = Synaptophysin.

Studies carried out using dual co-cultures have suggested a change in neuronal morphology in the presence of microglia (Zhang and Fedoroff, 1996). Accordingly, we analyzed cellular morphology using the neuronal marker MAP2. In the triple co-culture, neurons displayed a higher number of branches (158.6 ± 23.3 vs 100 ± 16.3%; $p<0.05$; n = 4), as well as a higher number of junctions (162.6 ± 24.2 vs 100 ± 16.6%; $p<0.05$; n = 4). These branches were also significantly longer than primary neurons alone (112.8 ± 11.5 vs 100 ± 10.5%; $p<0.05$; n = 4) (**Figure 51**). Interestingly, astrocytes alone showed a trend to increase the number of branches and junctions in neurons, although it was not statistically significant.

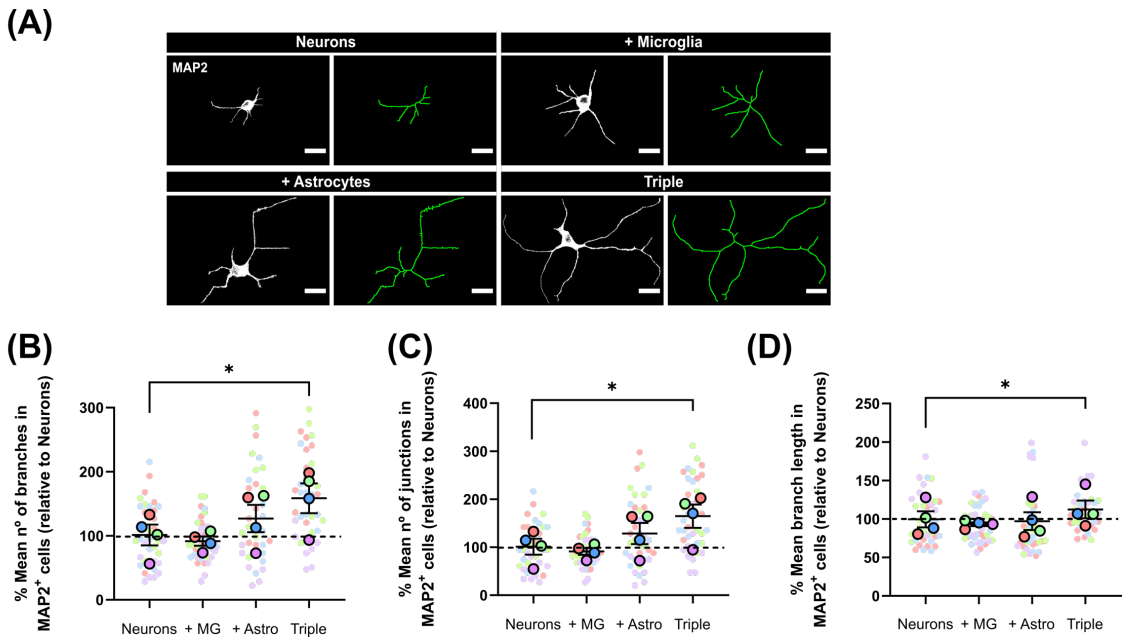

Figure 51. Neurons develop more and longer branches when co-cultured with glial cells. (A) Representative images of cellular morphology using the neuronal marker MAP2 and the function Skeletonize in FIJI software. Scale bar = 20 µm. **(B, C, D)** Quantification of the number of branches, the number of junctions and the mean branch length, respectively, in primary neurons and co-cultures (n = 4). Each bar represents the mean ± SEM. * p<0.05; paired one-way ANOVA. MG = microglia; Astro = astrocytes.

In summary, our results reveal that the conditions generated in the triple co-culture increase the number of post-synapses in neurons, as well as their cellular complexity.

3.2. Microglia becomes less inflammatory in the triple co-culture compared with primary microglia.

After observing that neurons exhibit different characteristics when glial cells are present, and given that microglial transcriptomic profiles are very dependent on the cellular environment (Schmid *et al.*, 2009), we analyzed the possible phenotypic changes that microglia could undergo in our triple co-culture. We quantified the expression of commonly used markers for pro- and anti-inflammatory microglial polarization. The typically anti-inflammatory marker Arginase I (ArgI) displayed a ~ 8-fold increase in the triple co-culture (898.2 ± 142.7 vs 100 ± 24.3%; p<0.01; n = 4), as well as in the microglia-neuron co-

culture (846.2 ± 147.3 vs 100 ± 24.3%; p<0.05; n = 4) compared with primary microglia alone (**Figure 52A, B**). No changes were found in the case of anti-inflammatory marker MRC1 (**Figure 52C**). We also found a ~ 2-fold increase in TGF-β1 in triple co-culture supernatants (422.2 ± 64.4 vs 182.7 ± 30.2 pg/ml; p<0.01; n = 5) compared with primary microglia supernatants (**Figure 52D**).

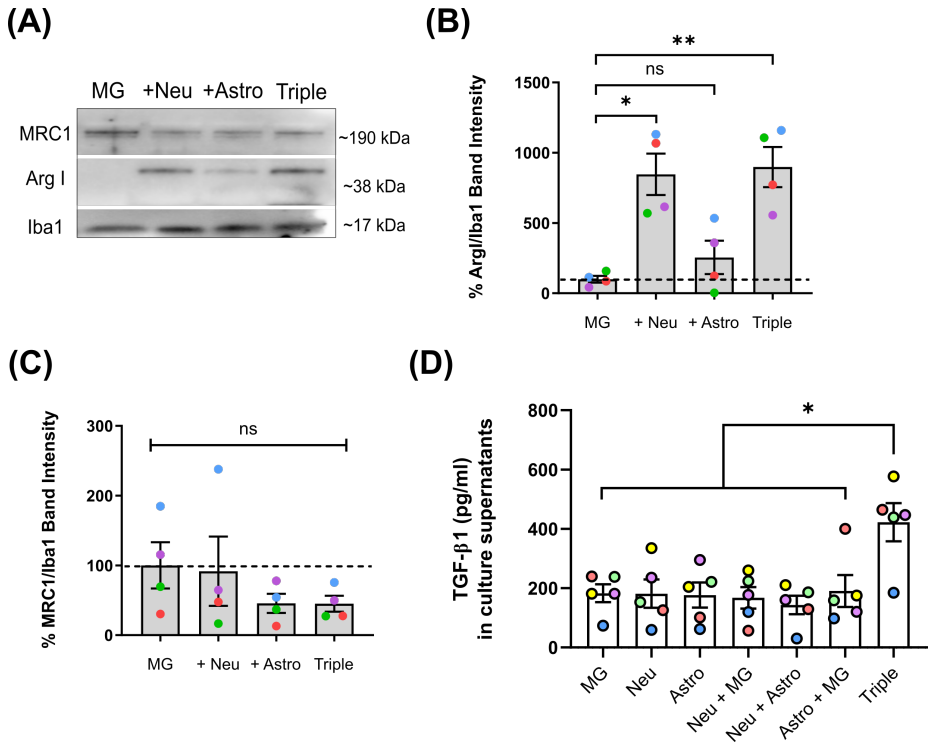

Figure 52. Microglia increase the expression of anti-inflammatory markers Argl and TGF-β1 in the triple co-culture. (A) Western blot of microglial anti-inflammatory markers in total cell lysates. **(B, C)** Quantification of Argl and MRC1 in primary microglia and co-cultures (n = 4). Data was normalized using the marker Iba1 in order to selectively control for microglia. **(D)** ELISA assay for TGF-β1 in supernatants of primary cultures and co-cultures (n = 5). Each bar represents the mean ± SEM. * p<0.05; ** p<0.01; ^{ns} not significant; paired one-way ANOVA. Neu = neurons; MG = microglia; Astro = astrocytes.

On the other hand, microglia decreased the secretion of pro-inflammatory cytokine IL-1β in the triple co-culture compared to primary microglia alone (18.6 ± 6.1 vs 47.1 ± 6.7 pg/ml; p<0.01; n = 5) (**Figure 53A**). No changes were found in microglial markers CD18 and Iba1 (**Figure 53B-D**). There was also a decrease of pro-inflammatory marker iNOS in the triple co-culture (56.6 ± 7.6 vs 100 ± 8.9%; p<0.01; n = 4) and the astrocyte-microglia co-culture compared with

microglia alone (66.3 ± 11.3 vs 100 ± 8.9%; p<0.05; n = 4). No changes were observed in microglial activation marker CD11b (**Figure 53E-G**).

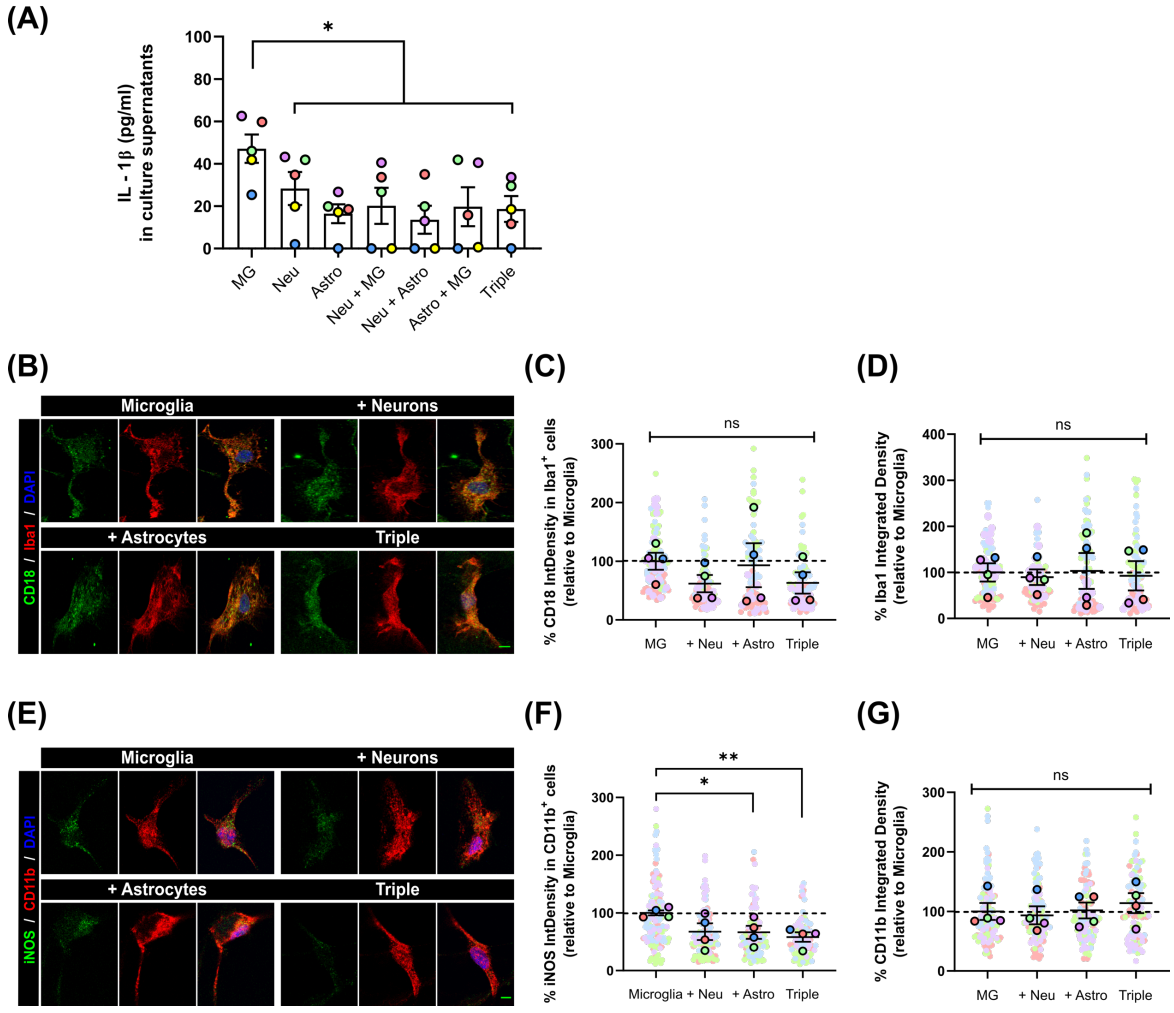

Figure 53. Microglia reduce the expression of pro-inflammatory markers IL-1β and iNOS in the triple co-culture model. (A) ELISA quantification of cytokine IL-1β in culture supernatants (n = 5). **(B)** Representative images of CD18 and Iba1 inside microglia. Scale bar = 10 µm. **(C,D)** Quantification of CD18 and Iba1 integrated density in primary microglia and co-cultures (n = 4). **(E)** Representative images of iNOS and CD11b in microglia. Scale bar = 10 µm. **(F, G)** Integrated density of iNOS inside $CD11b^+$ cells and CD11b in primary microglia and co-cultures (n = 4). Each bar represents the mean ± SEM. * p<0.05; ** p<0.01; ^{ns} not significant; paired one-way ANOVA. Neu = neurons; MG = microglia; Astro = astrocytes; IntDensity = integrated density.

In conclusion, microglia had a less inflammatory phenotype in the triple co-culture model compared with primary culture conditions, revealed by an increase of anti-inflammatory markers Argl and TGF-β1, and a decrease of pro-inflammatory markers IL-1β and iNOS.

3.3. Astrocytes undergo morphological changes and lower the expression of activation markers in the triple co-culture.

Once we observed that microglia were less inflammatory in the triple co-culture, we addressed astrocytic activation in the model. Besides, reactive microglia are necessary to induce neurotoxic reactive astrocytes in vitro via secreted signaling molecules (Liddelow *et al.*, 2017). Firstly, we analyzed astrocytic morphology as a measure of their activation state. We used the astrocytic marker GFAP to obtain morphological parameters. We observed that, in the triple co-culture, astrocytes significantly increased the parameters of density (118.9 ± 3.7 vs 100 ± 3.5%; $p<0.05$; n = 4) and span ratio (124.9 ± 6.4 vs 100 ± 1.5%; $p<0.05$; n = 4), while they reduced their circularity (88.1 ± 2.3 vs 100 ± 1.3%; $p<0.05$; n = 4) compared with primary astrocytes (**Figure 54**). These parameters in the triple co-culture reflect an increase in cellular ramifications, which resembles better the physiological resting state. The presence of neurons was enough to see a morphological change in astrocytes, although it was not statistically significant.

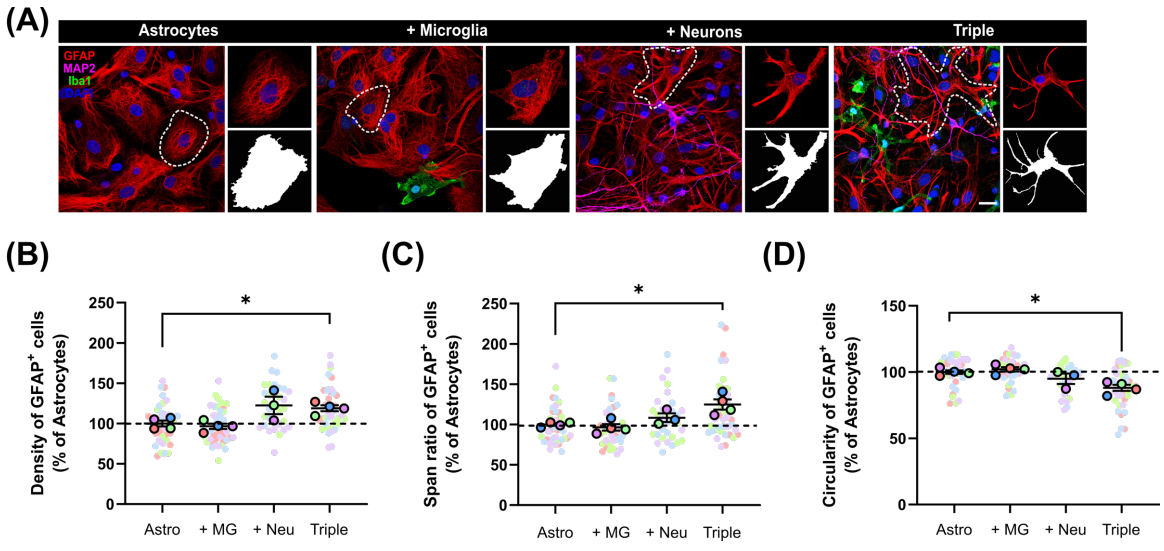

Figure 54. Astrocytes display a ramified morphology in the triple co-culture. (A) Representative images of the quantification of astrocytic morphology using GFAP and Fractal Analysis in FIJI Software. In each condition, a zoom of an individual cell and its outline are represented. Scale bar = 20 µm. **(B, C, D)** Quantification of density, span ratio and circularity, respectively, in primary astrocytes and co-cultures (n = 4). Each bar represents the mean ± SEM. * $p<0.05$; paired one-way ANOVA. Neu = neurons; MG = microglia; Astro = astrocytes.

We also quantified the expression of two astrocytic activation markers; Adhesion molecule with Ig like domain 2 (AMIGO2) and C3. In the triple co-culture, GFAP$^+$ astrocytes significantly decreased the expression of AMIGO2 compared with microglia-astrocyte co-culture (75.4 ± 13.4 vs 99.1 ± 13.9%; $p<0.05$; n = 3) and primary astrocytes (75.4 ± 13.4 vs 100 ± 12.6%; $p<0.05$; n = 3) (**Figure 55A, B**). In addition, C3 expression decreased in all of the co-cultures; in the microglia-astrocyte co-culture (57.1 ± 6.4 vs 100 ± 3.6%; $p<0.05$; n = 3), in the neuron-astrocyte co-culture (70.9 ± 12.3 vs 100 ± 3.6%; $p<0.05$; n = 3) and in the triple co-culture (67.1 ± 3.3 vs 100 ± 3.6%; $p<0.05$; n = 3) compared with primary astrocytes (**Figure 55C, D**). In order to analyze if astrocytic C3 was modulated via cell-to-cell contact or via secreted factors, we incubated primary astrocytes with conditioned media from neurons (NCM) or from microglia (MCM) and then quantified C3. We found no changes in C3 levels with NCM or MCM, so physical contact between cells was required to reduce C3 (**Figure 55E, F**).

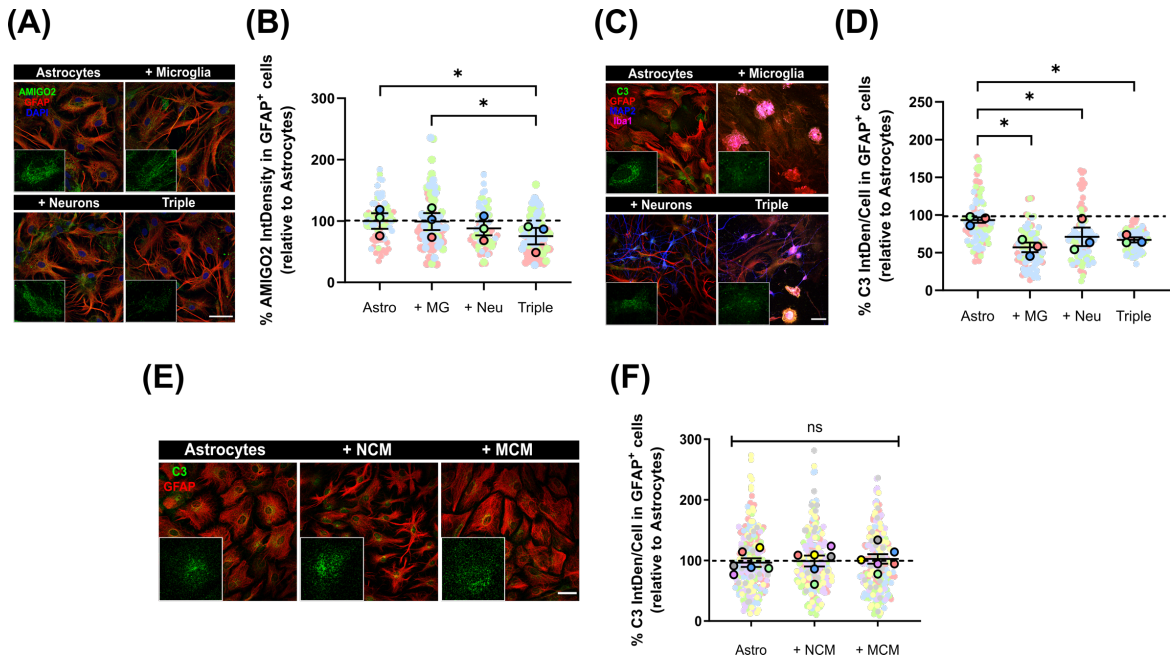

Figure 55. Astrocytes reduce activation markers AMIGO2 and C3 when co-cultured with microglia and neurons. (A) Representative images of marker AMIGO2. In each condition, a zoom on a single cell is displayed. Scale bar = 40 µm. **(B)** Quantification of AMIGO2 in primary astrocytes and co-cultures (n = 3). **(C, D)** Representative image of C3 and quantification (n = 3). Scale bar = 40 µm. **(E, F)** Representative image of C3 inside GFAP$^+$ astrocytes and quantification after conditioned media treatment. Scale bar = 40 µm. Each bar represents the mean ± SEM. * $p<0.05$; ^{ns} not significant; paired one-way ANOVA. Neu = neurons; MG = microglia; Astro = astrocytes; NCM = neuron conditioned media; MCM = microglia conditioned media; IntDen = integrated density.

In conclusion, astrocytes are less reactive in the triple co-culture environment, with a more ramified morphology and reduced expression of A1 markers AMIGO2 and C3.

3.4. Oligomeric $A\beta_{1-42}$ induces synaptic loss and microglial activation in the triple co-culture model.

Once we characterized the triple co-culture, we used it to establish a model where we could study AD *in vitro*, without the limitations of single primary cultures. We used oAβ as the stimulus to induce neurodegeneration, since oligomers seem to be the most neurotoxic amyloid species (reviewed in Glabe, 2006). We treated our triple co-cultures with 3 μM oAβ for 24 h, and then analyzed neurodegeneration features such as synaptic loss and neuroinflammation. We quantified pre- and post-synaptic markers in the neuronal processes using immunofluorescence and found that both Synaptophysin and Homer1 were reduced with the oAβ treatment (91.2 ± 8.1 vs 100 ± 6.2%; $p<0.05$; n = 5) and (83.3 ± 6.4 vs 100 ± 7.8%; $p<0.05$; n = 5) respectively, compared with controls (**Figure 56A-D**). Along with synapse loss, inflammation characterized by microglial CD11b increase is another key feature of Aβ-induced neurodegeneration (Zhang *et al.*, 2011). For that reason, we analyzed CD11b in total lysate samples with WB, as a measure of microglia-related inflammation. We observed that, while Iba1 expression did not change, CD11b increased in microglia with the oAβ treatment compared with controls (116.0 ± 14.2 vs 100 ± 16.5%; $p<0.01$; n = 4) (**Figure 56E-G**). Besides, there was a trend to decrease of anti-inflammatory cytokine TGF-β1 levels in the triple co-culture, although not statistically significant (**Figure 56H**).

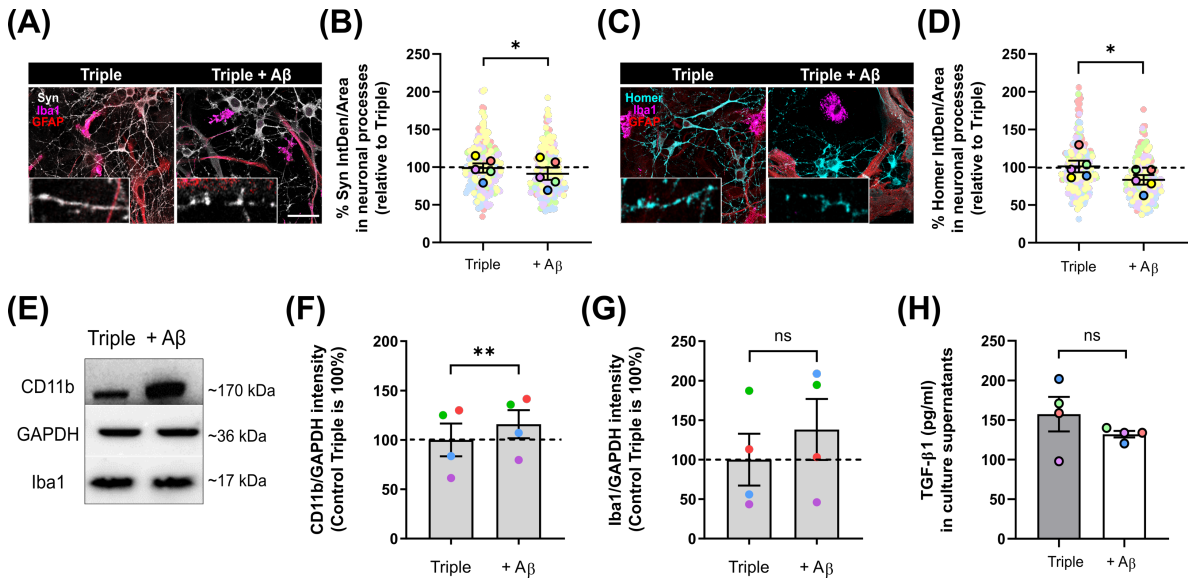

Figure 56. Oligomeric Aβ$_{1-42}$ reduces pre- and post-synaptic puncta and increases microglial marker CD11b in the triple co-culture model. (A) Representative image of Synaptophysin in neuronal processes. Scale bar = 40 µm. **(B)** Quantification of Synaptophysin after treatment with 3 µM oAβ for 24 h (n = 5). **(C)** Representative images of Homer1 in neuronal processes. Scale bar = 40 µm. **(D)** Quantification of Homer1 after treatment with 3 µM oAβ for 24 h (n = 5). **(E)** Western blot of microglial markers in total lysates. **(F, G)** Quantification of CD11b and Iba1 in triple co-cultures after treatment with 3 µM oAβ for 24 h (n = 4). Raw data was normalized using GAPDH. **(H)** ELISA assay for TGF-β1 in triple co-culture supernatants (n = 4). Each bar represents the mean ± SEM. * p<0.05; ** p<0.01; ^{ns} not significant; paired Student's t test. Syn = Synaptophysin; IntDen = integrated density.

To confirm our findings in the triple co-culture using a model with higher complexity, we used hippocampal organotypic cultures. We treated these organotypic cultures with the same conditions (3 µM oAβ for 24 h) and analyzed synaptic loss and neuroinflammation. Treatment with oAβ reduced the integrated density of Syn$^+$ pre-synaptic puncta (78.9 ± 12.4 vs 100 ± 7.6%; p<0.05; n = 4) and PSD-95$^+$ post-synaptic puncta (61.8 ± 12.8 vs 100 ± 11.4%; p<0.05; n = 4) compared with controls (**Figure 57A, B**). The puncta density was also decreased in the case of Synaptophysin (80.7 ± 6.4 vs 100 ± 2.2%; p<0.05; n = 4), which caused a reduction in the overall colocalization puncta (82.0 ± 8.1 vs 100 ± 4.5%; p<0.05; n = 4) (**Figure 57C**). Regarding microglial activation, we quantified CD11b$^+$ microglia in the organotypic slices. We found that oAβ increased both the area occupied by CD11b (131.5 ± 11.4 vs 100 ± 5.7%; p<0.05; n = 4) and its integrated density (137.7 ± 12.3 vs 100 ± 10.2%; p<0.05; n = 4) compared to controls (**Figure 57D-F**).

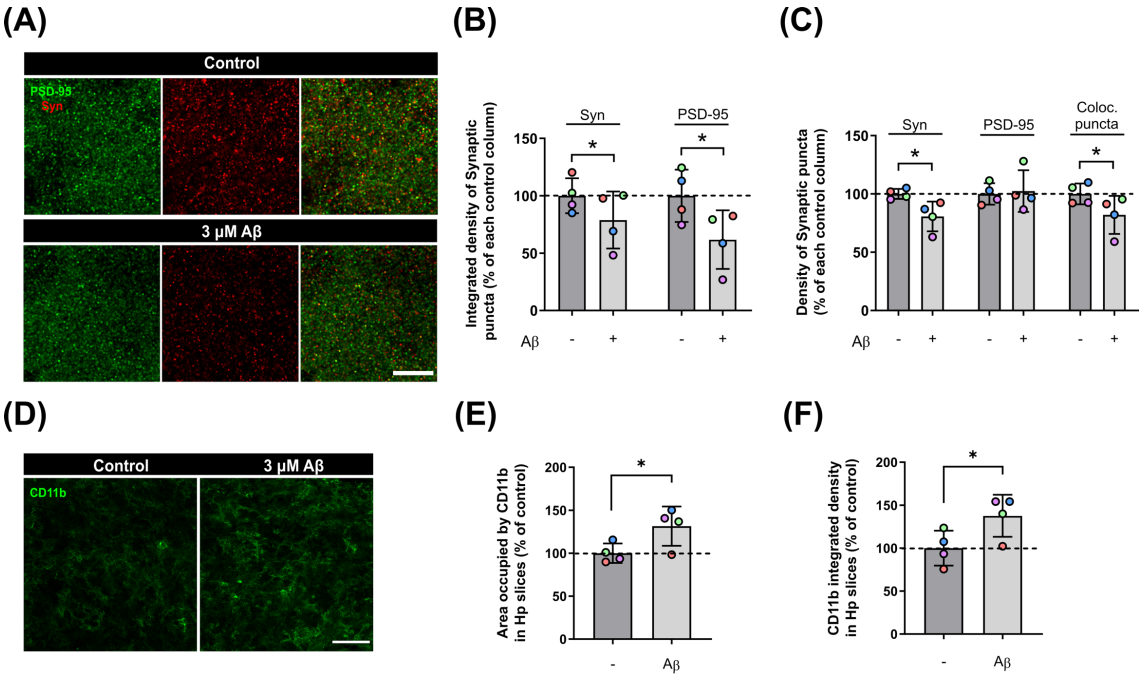

Figure 57. Oligomeric Aβ$_{1-42}$ decreases synaptic puncta and increases microglial CD11b in hippocampal organotypic slices. (A) Representative image of pre- and post-synaptic puncta in hippocampal organotypic slices. Scale bar = 10 µm. **(B)** Quantification of the integrated density of Synaptophysin and PSD-95 after treatment with 3 µM oAβ for 24 h (n = 4). **(C)** Density of Synaptophysin^{+}, PSD-95^{+} and colocalization puncta after treatment with 3 µM oAβ for 24 h (n = 4) **(D)** Representative images of CD11b staining in hippocampal organotypic slices. Scale bar = 40 µm. **(E, F)** Quantification of CD11b occupied area and integrated density, respectively, after treatment with 3 µM oAβ for 24 h (n = 4). Each bar represents the mean ± SEM. * $p<0.05$; paired Student's t test. Syn = Synaptophysin.

In conclusion, we were able to recapitulate Aβ-induced synaptic loss and microglial activation in our triple co-culture, and we confirmed these findings using hippocampal organotypic slices.

In this final part of the thesis, we developed a murine triple co-culture model including neurons, microglia and astrocytes, that holds physiological characteristics that are not present in classical primary cultures (**Figure 58**). Microglia are less inflammatory, astrocytes are less reactive and neurons display a more mature morphology than in individual primary cultures. With this model, we were able to recapitulate Aβ-induced AD pathological features like synaptic loss and microglial activation, which will allow us to study neurodegeneration and neuroinflammation processes relevant to AD progression.

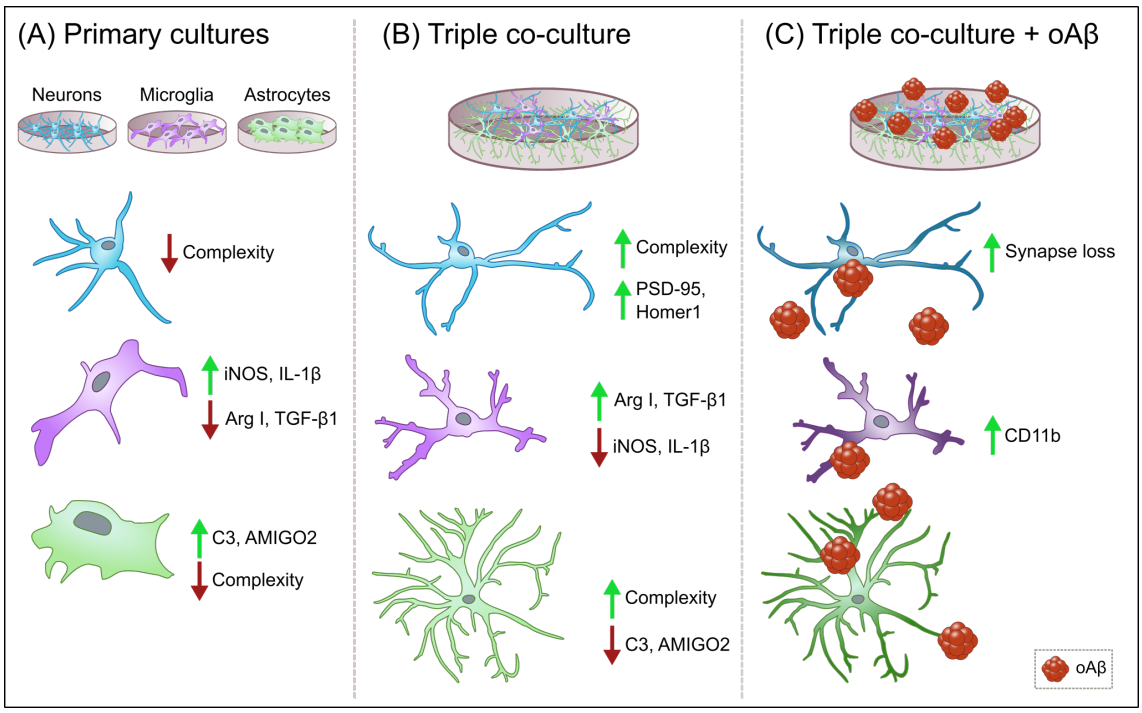

Figure 58. A neuron, microglia and astrocyte triple co-culture model to study Alzheimer's disease. (A) Classical individual primary cultures often exhibit significant alterations in comparison with cells in physiological conditions. Neurons and astrocytes display low morphological complexity, and both microglia and astrocytes increase the expression of pro-inflammatory markers iNOS, IL1β and C3, AMIGO2 respectively. **(B)** In our triple co-culture, neurons develop more complex morphologies and increase post-synaptic markers PSD-95 and Homer1. Microglia reduce their expression of pro-inflammatory markers such as iNOS and IL-1β, and increase anti-inflammatory markers Arg I and TGF-β1. Lastly, astrocytes reduce the expression of pro-inflammatory markers C3 and AMIGO2, while they develop ramifications that resemble physiological conditions. **(C)** In the triple co-culture, $A\beta_{1-42}$ oligomers are able to induce synaptic loss and increase microglial marker CD11b, which makes this triple co-culture a suitable model to study amyloid pathology associated changes in vitro. Blue cells = neurons; Purple cells = microglia; Green cells = astrocytes.

Discussion

Discussion

1. Pro-resolving mediator ATL reduces oxidative stress, mitochondrial dysfunction and AD neuropathology.

In the first part of this study, we explored the therapeutic potential of inflammation resolution in AD, mediated by aspirin-triggered 15-epi-LXA_4 or ATL. Using *in vitro* and *in vivo* models, we demonstrated that ATL ameliorates a number of neuropathological features including synapse loss, glial activation, oxidative stress and mitochondrial dysfunction, suggesting that enhancing inflammation resolution may be useful to prevent AD progression.

1.1. Lipoxin ATL reduces Aβ-induced oxidative stress, targeting ROS production and detoxification.

ROS accumulation and oxidative stress are key to AD progression, and can be both triggered and enhanced by neuroinflammation (Simpson and Oliver, 2020). Given this close interaction, we hypothesized that resolution of inflammation would have a positive impact on oxidative stress stimulated by amyloid pathology.

First, we observed that $A\beta_{42}$ oligomers directly upregulated ROS generation through the activation of NOX2 in primary neurons and microglia. This agrees with previous studies where, using the same NOX inhibitors that we used (DPI and gp91 ds-tat), authors demonstrated that Aβ oligomers induced NOX-mediated ROS production in cortical neuronal cultures (Shelat *et al.*, 2008) and microglia-like BV2 cells (Li *et al.*, 2013). Next, we analyzed the effect of ATL on this NOX2-mediated ROS generation. We found that ATL reduced ROS production triggered by $A\beta_{42}$ oligomers in primary neurons and microglia, as well as in organotypic cultures. This happened in a receptor-specific manner, given that Boc-2, antagonist of the main lipoxin receptor ALX/FPR2, blocked this effect. Besides, ATL has been shown to reduce NOX2 activation and ROS generation triggered by LPS in BV2 cells (Wu *et al.*, 2012*b*). Thus, ATL seems capable of

reducing ROS production triggered by LPS and $A\beta_{42}$ oligomers, suggesting a similar mechanism for NOX2 activation by both stimuli. Lipoxins can interact with diverse receptors in the CNS (Martini *et al.*, 2014). For instance, LXA_4 is an allosteric enhancer of CB2 cannabinoid receptors. Further investigation of the possible effects of ATL on receptors other than ALX/FPR2 is necessary to better understand its mechanisms of action.

Lipoxins can also have an effect on astrocytes, given that they express receptor ALX/FPR2 (Svensson *et al.*, 2007; Tiberi and Chiurchiù, 2021), and that they can release lipoxins LXA_4 and LXB_4 to induce neuroprotection (Livne-Bar *et al.*, 2017). Previous studies have demonstrated that, in LPS-stimulated astrocytes, ATL inhibits the production of nitric oxide and prostaglandins (Yao *et al.*, 2014), as well as the expression of inflammation marker aquaporin 4 and cytokines IL-1β and TNF-α (Wu *et al.*, 2019). In our study, we focused on neurons and microglia because our working concentration of $A\beta_{42}$ oligomers was not enough to trigger ROS production in primary astrocytes (data not shown). Previous studies in our laboratory did observe Aβ-induced ROS generation in astrocytes, although they used higher concentrations of $A\beta_{42}$ oligomers (Wyssenbach *et al.*, 2016). In future studies using astrocytes, it may be necessary to stimulate cells with higher concentrations of Aβ oligomers, or in combination with LPS, to be able to study ATL effects.

NOX2 activation is especially relevant for microglial immune response. LPS and pro-inflammatory cytokines like IL-1β and TNF-α can induce NOX2 via microglial activation (Yang *et al.*, 2007; Parajuli *et al.*, 2013). Previous studies have demonstrated that CR3, one of the receptors involved in microglial activation, can lead to NOX2-mediated ROS production in response to α-synuclein (Hou *et al.*, 2018). In our study, $A\beta_{42}$ oligomers increased the expression of CR3 subunit CD11b in the cell surface of primary microglia, while treatment with ATL reverted this increase. This observation suggests that, in microglia, ATL could indirectly reduce Aβ-mediated NOX2 activation via inhibition of CR3. In their studies with α-synuclein, Hou et al. (2018) proposed that CR3 could be acting on NOX2 via Src-ERK and Rho signaling pathways, so more analyses will be needed in order to find how CR3 and NOX2 communicate with each other in the context of amyloid pathology.

In addition to excessive ROS generation, oxidative stress can happen due to a defective ROS elimination. Aβ oligomers impair the activity of ROS detoxification enzymes like catalase and SOD in primary neurons (Alberdi *et al.*, 2018). In our case, SOD activity was indeed reduced both in primary neurons and microglia in response to $A\beta_{42}$ oligomers, and ATL was able to restore this activity to control levels. This agrees with a previous study where LXA_4 treatment stimulated SOD after spinal cord injury (Liu *et al.*, 2015). In summary, ATL was able to reduce ROS production by NOX2 and enhance ROS elimination by SOD, resulting in an effective reduction of Aβ-induced oxidative stress.

1.2. Resolution of inflammation ameliorates AD pathology.

Lipoxins have potent pro-resolution properties and researchers have reported low levels of this lipid mediator in situations of chronic neuroinflammation, like patients with post-stroke cognitive impairment (Wang *et al.*, 2021). Levels of LXA_4 also decline progressively with age (Gangemi *et al.*, 2005). In our study, we found a significant reduction of LXA_4 levels in the prefrontal cortex of AD patients compared to control individuals. These results agree with a previous study where researchers found lower levels of LXA_4 in the hippocampus and CSF of AD patients compared to controls, and LXA_4 positively correlated with MMSE scores (Wang *et al.*, 2015*b*). However, the same researchers also found no differences in LXA_4 levels in the entorhinal cortex (Zhu *et al.*, 2016), and another publication found no differences in LXA_4 levels in plasma and CSF of AD patients (Fraga *et al.*, 2019). These last studies displayed high variability within experimental groups, which would explain the discrepancy. It is also likely that lipoxin levels may vary depending on the brain area, the stage of the disease and other factors. In our study, we observed that LXA_4 levels negatively correlated with $A\beta_{42}$ deposited in post-synaptic compartments in the prefrontal cortex of AD patients. Given that $A\beta_{42}$ accumulation in post-synaptic terminals is linked to the initiation of tau pathology and synaptic dysfunction (Takahashi *et al.*, 2010), our results highlight the link between unsuccessful resolution of inflammation and AD progression.

Given the low levels of LXA_4 we found in AD patients, and the positive results that we obtained with ATL *in vitro*, we studied the effects of lipoxin ATL in the AD mouse model 3xTg. We observed that ATL effectively reduced the number of amyloid plaques in the brain, as well as the levels of soluble and insoluble $A\beta_{42}$ in the entorhinal cortex and hippocampus, respectively. On the contrary, we did not observe changes in the levels of $A\beta_{42}$, $A\beta_{40}$, or the $A\beta_{42}/A\beta_{40}$ ratio in CSF and plasma samples. These results might suggest that the reduction of Aβ accumulation in the brain could occur via CSF-independent mechanisms, for instance by enhanced microglial phagocytosis or extracellular enzymatic degradation. In fact, BV2 cells treated with ATL increase $A\beta_{42}$ phagocytosis in a dose-dependent manner (Medeiros *et al.*, 2013). Regarding tau protein, ATL reduced the area occupied by phosphorylated tau in the hippocampus, and the levels of total tau in CSF samples. It is well established that individuals with high levels of total tau in the CSF have higher risk of developing AD (Fagan *et al.*, 2007), and that tau is a strong predictor of neurodegeneration and cognitive decline in patients (Hanseeuw *et al.*, 2019). Thus, ATL ability to lower total tau in the CSF of 3xTg animals may suggest a reduction of neurodegeneration in these animals.

Synapse loss is also key to AD pathology, given that it is the best correlate of memory impairment in patients (DeKosky *et al.*, 1996; Sze *et al.*, 1997). In our study, we observed that 3xTg mice displayed significantly lower levels of pre- and post-synaptic markers in the CA1 hippocampal area, along with increased levels of complement C1q puncta. This observation agrees with previous studies where authors identified complement-related synapse loss in AD mouse models (Hong *et al.*, 2016). We also observed that ATL treatment recovered both pre- and post-synaptic markers to levels similar to WT mice and simultaneously reduced C1q puncta in the same area. These results suggest that ATL may be able to reduce synapse loss, which is partly mediated by the complement pathway.

Altogether, the reduction of amyloid and tau pathology, and the improvement of synapse loss with ATL are consistent with previous studies. In the first study performed with lipoxins in a mouse model of AD, Medeiros et al. (2013) discovered that ATL recovers pre- and post-synaptic markers in the cortex, and reduces amyloid plaques and soluble and insoluble $A\beta_{40}$ and $A\beta_{42}$ in

the brain of 12 months old male Tg2576 mice. In a publication by the same research group, ATL also reduced amyloid plaques and soluble and insoluble $A\beta_{40}$ and $A\beta_{42}$ in 14 months old 3xTg mice. The lipoxin treatment also reduced tau phosphorylation epitopes AT8, AT100, AT180, AT270 and PHF-1 (Dunn *et al.*, 2015). In a different publication using LXA_4 in combination with resolvin E1, $A\beta_{40}$ and $A\beta_{42}$ were reduced in 3 months old 5xFAD animals, although the effects were subtle (Kantarci *et al.*, 2018). In general, our results agree with previous publications that used diverse AD mouse models and different doses of ATL used. Medeiros et al. (2013) and Dunn et al. (2015) performed subcutaneous injections twice a day, with 15 µg/kg ATL for two months, while Kantarci et al. (2018) performed intraperitoneal injections three times a week, with 1.5 µg/kg LXA_4 for two months. We used an intermediate dose, giving one intraperitoneal injection per day with 10 µg/kg ATL for two months. We were fairly confident that this administration method was sufficient to deliver lipoxin to the brain, since intraperitoneal injections of a lower dose of LXA_4 significantly increased the amount of lipoxin in the hippocampus of 5xFAD animals (Kantarci *et al.*, 2018). With these conditions, we were able to obtain similar results to Dunn et al. (2015) using a 66% lower dose, thus reducing the cost of the treatment and its possible side effects. One should take into account that increasing the lipoxin synthesis pathway has the risk of increasing apoptosis via N-acetyl sphingosine, an enzyme responsible for COX-2 acetylation (Lee *et al.*, 2020). In the future, quantification of caspases will be necessary to make sure that our ATL treatment does not induce apoptosis.

1.3. ATL reduces gliosis and pro-inflammatory mediators.

Neuroinflammation is key to the progression of AD, and it is characterized by excessive secretion of pro-inflammatory cytokines (Lue *et al.*, 2001; Swardfager *et al.*, 2010). In a mouse model of amyloid pathology using $A\beta_{42}$ intracerebroventricular infusion, LXA_4 reduced gene expression and release of IL-1β and TNF-α (Wu *et al.*, 2011). Besides, ATL reduces cytokines IL-1β, TNF-α, IL-6, M-CSF and IFN-γ in Tg2576 and 5xFAD mice (Medeiros *et al.*, 2013; Kantarci *et al.*, 2018). In line with these results, we observed that 3xTg mice

display higher levels of cytokines IL-1β, KC/GRO and. TNF-α than WT mice in the hippocampus, and IL-1β and TNF-α were significantly reduced with the ATL treatment. These observations confirm that lipoxins regulate production and secretion of cytokines as part of their pro-resolution functions. In our study, we also analyzed pro-inflammatory cytokines in the cerebral cortex of 3xTg mice, although we only found a reduction of IL-1β compared to WT mice. This discrepancy could be explained because the methodology used for quantification is not specific for the active and inactive forms, so changes in the ratio of the two forms could not be detected.

Another neuroinflammation mechanism that lipoxins are capable of regulating is the activation of inflammasome NLRP3 (Zhao *et al.*, 2021). We analyzed each of the inflammasome components, although this analysis gave us limited results. Based on previous studies demonstrating that NLRP3 is involved in amyloid and tau pathology in mouse models (Heneka *et al.*, 2013; Ising *et al.*, 2019), we expected to find a robust activation of NLRP3 in 3xTg mice. Unfortunately, we only observed a significant increase of inflammasome component ASC in cortex and hippocampus of 3xTg mice compared to WT mice. We could not detect changes in NLRP3 protein or in cleaved caspase-1, and we could not see an effect of ATL in any of the components. This analysis was performed using western blotting in total tissue lysates, so it might be possible that the technique could not detect small changes in the inflammasome components. An analysis using more precise techniques such as immunohistochemistry could improve detection in the future.

In addition to measuring mediators of inflammation in the brain, we analyzed the effect of ATL on oxidative stress in the animals. We chose to measure the levels of oxidized glutathione in erythrocytes, based on the availability of the samples and the fact that oxidized glutathione is increased in AD patients in erythrocyte and plasma samples compared to controls (Calabrese *et al.*, 2006; Bermejo *et al.*, 2009). In our study, 3xTg mice displayed slightly higher levels of oxidized glutathione than WT mice, and ATL treatment was able to reduce this levels. A recent study has shown that LXA_4 can increase levels of the reduced form of glutathione in a rat model of skin transplantation (Xin *et al.*,

2020). Although, to our knowledge, our study is the first to link lipoxin ATL to a reduction in glutathione oxidation in the context of neurodegenerative diseases.

The main cellular mediators of neuroinflammation are microglia and astrocytes, and it is usual to find reactive microglia and astrocytes around senile plaques in AD patients (Vehmas *et al.*, 2003; Serrano-Pozo *et al.*, 2011). Since both cell types are susceptible to modulation by lipoxins, we analyzed the effects of ATL on microglia and astrocytes in the hippocampus of 3xTg animals. Specifically, we focused on the CA1 area, where we saw the greatest changes with our treatment. Both microglia and astrocytes occupied significantly more area in 3xTg mice compared to WT mice, as revealed by the microglial markers CD11b and Iba1, and the astrocytic markers S100β and GFAP. All of these glial markers were drastically reduced with ATL. Medeiros et al. (2013) and Dunn et al. (2015) also found a reduction of $GFAP^+$ astrocytes and $CD11b^+$, $CD45^+$ and $Iba1^+$ microglia in the brains of Tg2576 and 3xTg mice treated with ATL compared to mice treated with vehicle, although neither of the publications compared transgenic mice with their wild type counterparts (Medeiros *et al.*, 2013; Dunn *et al.*, 2015). Kantarci et al. (2018) did confirm an increase of GFAP and Iba1 staining in the cortex and hippocampus of 5xFAD mice compared to WT mice. Interestingly, gliosis was only reduced with the combination of ATL plus resolvin E1, and not with ATL alone, which could be explained by the low dose of ATL used in this study (Kantarci *et al.*, 2018). In a rat model of cerebral ischemia, LXA_4 reduced the area occupied by $GFAP^+$ astrocytes after the lesion, further supporting the role of lipoxins on reduction of glial activation (Wu *et al.*, 2012*a*).

In addition to changes in the area occupied by glial cells, we noticed differences in cellular morphology. Both astrocytes and microglia can display diverse morphologies depending on their function and their state of activation. (Oberheim *et al.*, 2012; Paasila *et al.*, 2019). In AD patients, microglial ramifications are reduced in number and length, and Iba1 labelling in those ramifications appears discontinuous (Davies *et al.*, 2017; Paasila *et al.*, 2019). The AD mouse model TgCRND8, which carries Swedish and Indiana APP mutations, also shows microglia with small cell bodies and reduced number of branches in the proximity of senile plaques (Plescher *et al.*, 2018). On the contrary, in our study we noticed that 3xTg mice displayed a rod-shape microglia

in the hippocampal CA1 area. These microglia had long cell bodies, all set in the same direction, with very short ramifications compared with WT mice. All of these parameters were restored to values similar to WT mice with the ATL treatment, suggesting that lipoxins are capable of reverting morphological alterations in microglia. One previous publication discovered that overexpression of sphingosine kinase type 1, an enzyme which acetylates COX-2 and stimulates the production of lipoxins and resolvins, induced the formation of amoeboid microglia in APP/PS1 mice (Lee *et al.*, 2018). This morphological change from ramified to amoeboid microglia does not agree with our study, which revealed a switch from rod-shape to ramified microglia. A possible explanation for this would be that Lee et al. (2018) analyzed microglia surrounding senile plaques, while we analyzed microglia in CA1, where no plaques were detected. This might suggest that microglia would undergo different morphological changes in response to lipoxins depending on their local environment. In addition, the question of what phenotypic modifications are associated with lipoxin-induced morphological changes in microglia requires further investigation.

Astrocytes also undergo morphological alterations under pathological conditions. In AD, reactive astrocytes are characterized by the overexpression of GFAP, and by adopting a hypertrophic morphology with enlarged cell bodies and increased number of ramifications (Serrano-Pozo *et al.*, 2011; Perez-Nievas and Serrano-Pozo, 2018). In the 3xTg mouse model, GFAP increases in the hippocampus after the onset of senile plaques (Oddo *et al.*, 2003*a*; Olabarria *et al.*, 2010). In our study, we found astrocytes with hypertrophic morphology and increased GFAP in CA1 of 3xTg animals that were clearly in a post-plaque stage, which agrees with these previous publications. Quantitatively, hypertrophic astrocytes in 3xTg mice had significantly higher numbers of junctions and branches, and these branches were significantly shorter compared to WT mice. Treatment with ATL reversed all of these parameters to values similar to WT mice, suggesting that lipoxins are able to reduce astrocytic activation and revert morphological alterations associated with AD.

1.4. Lipoxin ATL ameliorates mitochondrial dysfunction.

Mitochondrial dysfunction is a key hallmark of AD, and many of the physiological functions of this organelle, such as energy production, become compromised in early stages of the disease (reviewed in Cenini and Voos, 2019). Mitochondria are especially vulnerable to oxidative damage, and Aβ can increase ROS production and accumulation in this organelle (Manczak *et al.*, 2006; Wang *et al.*, 2009). In the context of AD, there is also excessive mitochondrial fragmentation and defective mitochondrial fusion, events that lead to mitochondrial impairment (Cai and Tammineni, 2017) In this study, we focused on how ATL could tackle oxidative stress and mitochondrial dynamics in AD.

Previous studies have demonstrated that $A\beta_{42}$ oligomers increase mitochondrial ROS in primary hippocampal neurons (Wang *et al.*, 2009), and 3xTg mice display increased mitochondrial H_2O_2 production and lipid peroxidation (Yao *et al.*, 2009). In agreement with these publications, we observed a significant increase in mitochondrial ROS generation, specifically in superoxide radicals, in response to $A\beta_{42}$ oligomers in primary neurons, primary microglia and organotypic cultures. We also observed an increase in mitochondrial ROS in 3xTg mice isolated mitochondria compared to WT mice. In all of the models, treatment with ATL reverted the excessive ROS generation. Besides, in the 3xTg animals, ATL restored SOD detoxification activity in the mitochondria, suggesting once again that lipoxins are able to ameliorate oxidative stress by targeting both ROS production and detoxification. Excessive ROS is linked to reduced energetic performance by mitochondria (Cortassa *et al.*, 2014). We found that $A\beta_{42}$ oligomers significantly impaired the normal function of oxidative phosphorylation, reducing basal respiration, maximal respiration capacity and ATP production in primary neurons and microglia. These results agree with previous work in our laboratory, where primary neurons showed reduced mitochondrial respiration in response to $A\beta_{42}$ oligomers, and it was recovered using antioxidant agents (Alberdi *et al.*, 2018). In our case, treating the cultures with ATL reduced Aβ-mediated ROS accumulation in the mitochondria, and recovered respiration parameters back to control levels. In addition to oxidative stress and impaired metabolism, mitochondrial dynamics are altered in AD, with inadequate fusion

and excessive fission (Wang *et al.*, 2008; Calkins *et al.*, 2011). In a previous publication, authors reported impaired mitochondrial respiration, as well as low levels of fusion marker MFN2 and high levels of fission marker DRP1 in cortex and hippocampus of 14 months old female 3xTg mice (Djordjevic *et al.*, 2020). In our study, we observed the same increase of DRP1 and decrease of MFN2 in 3xTg mice, and the treatment with ATL was able to restore both markers to levels similar to WT mice.

To the best of our knowledge, the role of lipoxins in mitochondrial regulation has not been addressed in AD as it has been in other pathologies. In a mouse model of glaucoma, lipoxin LXB_4 protects neurons from apoptosis caused by alterations in mitochondrial membrane potential (Livne-Bar *et al.*, 2017). LXA_4 also inhibits the activation of mitochondria-mediated apoptosis and attenuates ROS generation in macrophages, via the PI3K/Akt and ERK/Nrf-2 pathways (Prieto *et al.*, 2010). More recently, a publication has demonstrated that LXA_4 reduces mitochondrial ROS, restores mitochondrial membrane potential and respiration, and enhances mitochondrial fusion in a rat model of gastric ulcer (Madi *et al.*, 2020). A new preprint study (not peer reviewed) also suggests that LXA_4 improves mitochondrial fission caused by neonatal hyperoxia in pulmonary endothelial cells (Preprint B *et al.*, 2021). Our own results seem to go in line with these publications, with ATL recovering mitochondrial dynamics and function. This is the first time that ATL was used to reverse Aβ-induced mitochondrial damage, adding a new potential therapeutic target for lipoxins in the context of AD pathology that is worth investigating in depth.

2. Microglial complement receptor CR3 inhibition with small molecule XVA143 reveals transcriptomic changes and alterations in cellular migration and Aβ internalization.

The other therapeutic strategy explored in this thesis was complement receptor CR3 and its diverse roles in microglial function. In order to study this receptor, both in physiological and AD pathological conditions, we used small molecule XVA143, an allosteric CR3 antagonist.

Hoffmann-La Roche (Switzerland) developed this inhibitor more than a decade ago, but it has not been used in microglia until very recently. We performed a characterization of the compound in microglia, and found that XVA143 alters cellular migration and CR3 recruitment, and that it regulates the expression of a number of genes related to the inflammatory response. CR3 inhibition also modulates Aβ internalization and elimination by microglia, making XVA143 an interesting intervention to understand microglial activation and function in the context of AD and other neurodegenerative diseases.

2.1. CR3 inhibition alters multiple cellular functions in microglia.

Compound XVA143 has been extensively characterized from the biochemical point of view, mainly using human cell lines of lymphocytes and monocytes. XVA143 binds to the I-like domain of the β_2 chain (CD18 subunit) in receptor CR3 and the rest of the β_2 integrin family, specifically in the Metal Ion-Dependent Adhesion Site or MIDAS (Welzenbach *et al.*, 2002; Shimaoka *et al.*, 2003). This binding induces conformational changes that block transmission of activation signals to the α domain (CD11 subunit) (Schürpf and Springer, 2011). However, given the lack of publications that we found about the use of XVA143 in the CNS, we performed an initial characterization of the potential effects of this compound in microglia. First, we determined a suitable working concentration for *in vitro* cultures, both for primary microglia and for the immortalized BV2 cell line. Next, we observed that XVA143 induced a drastic reduction in the protein levels of both CR3 subunits CD11b and CD18, in total lysates and in the cell membrane of primary microglia. This reduction was not accompanied by a downregulation of the genes ITGAM and ITGB2, which encode for CD11b and CD18 respectively. Activation of receptor CR3, like the rest of the β_2 integrin family, requires the recruitment of its subunits from the cytoplasm, where they are stored under basal conditions, to the cell membrane (Sengeløv *et al.*, 1993; Vorup-Jensen and Jensen, 2018). Thus, our results suggest that XVA143 might reduce CR3 levels and recruitment of CR3 to the cell membrane by mechanisms different from gene expression. Further research is necessary to validate our observations, and to search for the mechanisms that mediate XVA143 modulation of CR3 expression.

Several authors have used XVA143 to study integrin-mediated cell adhesion and migration in the immune response against microbial infections. In order to explore these processes in microglia, we examined cellular morphology and migration in the presence of XVA143. The compound caused changes in cell morphology, with primary microglia adopting a round shape, and a reduction in the number of cells per area. A previous publication described a similar effect on XVA143-treated human lymphocytes, where cells reduced spreading and polarization and adopted a round morphology that reduced cell adhesion (Yang *et al.*, 2006). Numerous studies have confirmed that XVA143 promotes a reduction in cell firm adhesion in lymphocytes (Salas *et al.*, 2004; Chen *et al.*, 2006; Morin *et al.*, 2008), and in monocytes ability to bind adhesion ligands like intercellular adhesion molecule-1 and fibrinogen (Harokopakis *et al.*, 2006). In parallel with reduced adhesion, XVA143 promotes cell rolling *in vitro* (Salas *et al.*, 2004; Chen *et al.*, 2006; Yang *et al.*, 2006) and neutrophil migration in response to respiratory infections *in vivo* (Wilson *et al.*, 2017). In our study, we observed that XVA143 reduced cellular migration both in primary microglia and BV2 cells, which seems to contradict existing reports. Nonetheless, this difference could be explained by the methodologies used for quantification. We used scratch wound and transwell migration assays, and quantified the number of cells present before and after the XVA143 treatment. These methodologies rely on the capacity of the cells to remain attached to the analyzed surface after migrating. On the other hand, existing publications used methodologies that directly quantified migrating or rolling cells (Salas *et al.*, 2004; Chen *et al.*, 2006; Yang *et al.*, 2006). Therefore, our results would further confirm that XVA143 is capable of effectively reducing cellular adhesion, and more experimentation is required to elucidate the specific effect of XVA143 on microglial migration. It is worth mentioning that XVA143 has affinity for other members of the family apart from CR3, given that it binds the common subunit CD18. In addition to CR3, microglia constitutively express CR4 (CD11c/CD18) and LFA-1 (CD11a/CD18) (Kim and De Vellis, 2005), although recent research suggests that CD11a/CD18 is only expressed by peripheral immune cells and not by microglia (Shukla *et al.*, 2019). XVA143 is capable of inhibiting the function of LFA-1 and CR4 (Salas *et al.*, 2004; Nishida *et al.*, 2006), which participate in cell adhesion and phagocytosis in immune cells, so we

cannot completely rule out that compound XVA143 does not have an effect on these integrins in microglia.

In addition to cellular adhesion and migration, CR3 participates in a number of signaling pathways related to the immune response (Ross, 2002). For instance, in response to oral infections with *P. gingivalis*, CR3 promotes the release of pro-inflammatory cytokines TNF-α, IL-1β and IL-6 (Hajishengallis *et al.*, 2008), and XVA143 inhibition enhances pathogen clearance mediated by anti-inflammatory cytokine IL-12, via inhibition of the ERK1/2 pathway (Hajishengallis *et al.*, 2007). XVA143 also reduces the secretion of chemokine monocyte chemoattractant protein-1 in response to infection with *F. tularensis* (D'Elia et al., 2011). Based on this information, we performed a transcriptomic analysis in primary microglia treated with XVA143, in order to search for potential links between CR3 inhibition and expression of genes related to the inflammatory response, phagocytosis and the complement system. We analyzed the expression of ~25 genes, and found that XVA143 upregulated the expression of cytokine IL-1β, and downregulated the expression of AGER, IRF8 and C4a. These results are preliminary and will need to be validated by protein quantifications. Interestingly, a previous publication already observed that XVA143 reduced AGER expression in a model of lung injury inflammation (Parmley *et al.*, 2007). AGER encodes for the Receptor for Advanced Glycation End-products or RAGE, a receptor linked to Aβ binding and internalization (Donahue *et al.*, 2006).

Regarding the complement system, we observed a statistically significant reduction of IRF8 and C4a gene expression, but also a downregulation trend of C1q components A, B and C. IRF8 is a transcription factor regulated by IFN-γ that mediates the expression of gene networks related to microglial activation (Masuda *et al.*, 2012). It has been demonstrated that IRF8 participates in the synchronized transcription of the three C1q subunits (Chen *et al.*, 2011; Earley *et al.*, 2018), thus our results might suggest that CR3 inhibition using XVA143 reduces the transcription of C1q subunits via the inhibition of transcription factor IRF8. We also obtained evidence for this signaling between CR3 and C1q using organotypic cultures. We observed a significant increase in the area occupied by CD11b accompanied by an increase in C1q puncta in response to $A\beta_{42}$ oligomers

that was prevented by XVA143. To the best of our knowledge, this is the first time that a relationship between the inhibition of CR3 and the downregulation of C1q expression was reported, so more research needs to be done regarding the axis CR3, IRF8 and C1q.

Our results point towards the relevance of receptor CR3 in microglial activation through various cellular processes that need to be characterized in depth. In our particular case, XVA143 seems like a very useful tool for the study of amyloid pathology.

2.2. Relevance of CR3 modulation in AD pathology.

Once we characterized the effects of CR3 inhibition on microglia using compound XVA143, we performed preliminary studies in the context of amyloid pathology using $A\beta_{42}$ oligomers. Receptor CR3 actively participates in complement-mediated synapse elimination (Hong *et al.*, 2016) and Aβ phagocytosis (Fu *et al.*, 2012), In fact, Madore et al. (2020) reported that XVA143 blocks microglial phagocytosis *in vitro*, and reduces complement-mediated synaptic elimination during post-natal development in mouse pups (Madore *et al.*, 2020). Thus, we hypothesized that CR3 inhibition by XVA143 would have a positive effect on Aβ clearance. In line with our hypothesis, we observed that XVA143 treatment significantly reduced the levels of extracellular $A\beta_{42}$ in primary microglia and organotypic cultures. This reduction could be due to several processes. One possibility could be that, with the inhibition of CR3, microglia increased their ability to internalize extracellular Aβ. Microglia express receptors that promote clearance and phagocytosis of Aβ (Hickman *et al.*, 2008). However, we did not detect any changes in the gene expression of internalization receptors MSR1, CD36 and AGER after treatment with $A\beta_{42}$ oligomers. CR3 itself has been associated with the internalization of fibrillar Aβ (Fu *et al.*, 2012), and we observed that CR3 inhibition with XVA143 significantly reduced Aβ internalization by microglia. This observation also agrees with Czirr et al. (2017), who discovered that genetic ablation of CR3 resulted in reduced Aβ deposition, although this CR3 deficiency also reduced microglial phagocytic activity. Authors reported that, even though Aβ phagocytosis was impaired, microglia increased the secretion of

extracellular degrading enzymes that were able to degrade Aβ without internalization. In order to test this, we analyzed the expression of extracellular degrading enzymes IDE, MMP2, MMP9 and PLAT at the transcriptomic level, but did not find any differences between controls and cells treated with Aβ or with XVA143. Therefore, our results suggest that pharmacological inhibition of CR3 might be beneficial for Aβ clearance, although the mechanism by which XVA143 accomplishes its effect requires further investigation.

3. A neuron, microglia and astrocyte triple co-culture model to study Alzheimer's disease.

In order to provide a tool to study the complexity of neuroinflammation and neurodegeneration, we developed a murine triple co-culture model including neurons, microglia and astrocytes, which holds physiological characteristics that are lost in classical primary cultures. Microglia are less inflammatory, astrocytes are less reactive and neurons display a more mature morphology than in individual primary cultures. With this model, we were able to recapitulate Aβ-induced pathological features like synaptic loss and microglial activation, which will allow us to study neurodegeneration and neuroinflammation processes relevant to AD progression.

3.1. The triple co-culture is a straightforward and versatile model to study the communication between neurons and glial cells.

First, we optimized a straightforward triple co-culture with neurons, microglia and astrocytes. Previous studies have developed protocols for triple co-cultures where neurons were plated first, and glial cells were added after neuronal maturation (Lange *et al.*, 2018; Guttikonda *et al.*, 2021). In our hands, when neurons were plated first, adhesion of astrocytes to the plate was not optimal. On the contrary, when astrocytes were plated first, they were able to form a monolayer. Once we plated astrocytes first, we tried different proportions of each cell type. We decided to use a proportion of five neurons per two astrocytes, given

that lower numbers of neurons compromised their survival, and higher numbers of neurons would form big clusters of cells that did not allow adequate immunostaining and analysis (data not shown). Regarding microglia, previous publications with neuron-microglia co-cultures have used diverse ratios, ranging from two to thirty neurons per microglia (Zujovic *et al.*, 2000; Hernangómez *et al.*, 2012). We decided to use a proportion of five neurons per microglia, so that the number of microglia was not too high compared to physiological conditions. Nonetheless, given that the different cell types are added sequentially, the model allows the use of various cell ratios depending on the experimental needs.

Once the model was established, we characterized each cell type. In our triple co-culture, neurons developed a higher number of post-synapses, while pre-synapses remained unchanged. This finding would align with previous work indicating that astrocyte-secreted factors such as thrombospondins promote synaptogenesis (Christopherson *et al.*, 2005). Our model would allow further functional studies of neuronal activity, as well as the identification of glial factors with potential synaptogenic activity. We also observed that the presence of both microglia and astrocytes in the culture stimulated significant morphological change in neurons, which developed a higher number of branches that were also longer. These findings, along with previous studies demonstrating that the presence of astrocytes increases neuronal viability *in vitro* (Aebersold *et al.*, 2018), support our co-culture as a relevant system to study neuronal function in AD and other neurodegenerative diseases.

Microglial genomic and proteomic profile is very dependent on the environment. Previous studies have shown a differential gene expression in primary microglia as opposed to the adult CNS, revealed by a dedifferentiation of microglia in culture (Schmid *et al.*, 2009). The use of serum as a way to stimulate cell proliferation and survival *in vitro* also causes relevant phenotypic changes in microglia. Bohlen et al. (2017) demonstrated that serum induced significant alterations in microglial morphology and intrinsic phagocytic capacity, and that these alterations could be avoided using serum-free astrocyte conditioned media containing CSF-1/IL-34, TGF-β2, and cholesterol (Bohlen *et al.*, 2017). In the case of our triple co-culture model, we used serum-free neurobasal medium, which allowed us to avoid serum-related changes while maintaining neuronal

viability. In these serum-free co-culture conditions, microglia decreased the expression of pro-inflammatory markers iNOS and IL-1β, while increased the expression of anti-inflammatory marker ArgI. Anti-inflammatory cytokine TGF-β1 was also reduced. We consider that both the serum-free conditions and the presence of neurons and astrocytes, contributed to maintain microglia in a less reactive state compared with primary cultures. Previous studies performed with a triple co-culture that included microglial cells N11, neuroblastoma N2A cells and brain microvascular endothelial MVEC(B3) cells in a transwell system showed that microglial stimulation with LPS induced inflammatory pathways that resulted in neuron apoptosis and damaged endothelial integrity (Zheng *et al.*, 2021). Therefore, future studies including neuroinflammation induction (e.g. with LPS) would be required to have a more extensive phenotypic characterization of microglia in our model.

In our model, we observed that, microglia being less reactive, astrocytes had a ramified morphology and decreased the expression of activation markers AMIGO2 and C3. We did not observe any expression changes in astrocytic C3 with conditioned media. Liddelow et al. (2017) reported that condition media from LPS activated microglia, but not from control microglia, strongly induced reactive astrocytes. Our results go in line with these observations since under physiological conditions, without any external inflammatory stimulus such as LPS or oligomeric Aβ, only the soluble factors present in the microglial condition media are not enough to modified astrocytic C3 expression. However, our results seem to contradict a previous report that, using a tri-culture system with hPSC-derived microglia, astrocytes, and neurons, found an increase in astrocytic C3 in the presence of microglia and microglia conditioned media (Guttikonda *et al.*, 2021). This discrepancy could be explained because the authors quantified secreted C3, while we quantified C3 within astrocytes. Also, both optimal platting rates and the incubation time that cells and/or condition media were in contact with each other differ between our murine triple co-culture and the one derived from hPSCs, parameters that could also lead to different cellular responses. Thus, a more exhaustive analysis will be necessary to understand cellular communication.

Our model is complementary to existing triple models of neuroinflammation, and displays certain advantages. The morphological changes

that we observed in astrocytes were also reported in a previous publication that used rat triple co-cultures to model LPS and injury-induced neuroinflammation. In this publication, the triple co-culture was obtained from a pool of dissociated cortex tissue (Goshi *et al.*, 2020). In our case, we first cultured each cell type separately, which allows a better control over the number of cells seeded. A recently published triple co-culture model of LPS-induced neuroinflammation used immortalized cell lines in transwells, which allowed control over cell numbers, but did not allow physical contact between the cells (Zheng *et al.*, 2021). In our model, physical interaction between cells can be studied and compared with conditioned media. More advanced triple co-cultures use human PSCs. Guttikonda et al. (2021) developed a triple co-culture using PSC-derived neurons, astrocytes and microglia carrying the APP Swedish mutation to study complement C3 regulation by glial cells reciprocal signaling. Park et al. (2018) also used human PSCs with AD mutations to establish a 3D triple co-culture model in which they studied microglia migration and neurotoxicity. These models have the advantage of better recapitulating AD pathology in patients. However, human PSCs maintenance and 3D culture setups are more difficult and require more resources than murine cultures. Besides, the differentiation of each cell type is very time consuming, most of the time taking up to months. In comparison, our murine triple co-culture is easy to implement because it does not require sophisticated setups and needs reasonably short times, while it still allows studying AD pathology and cellular interactions.

3.2. Study of neurodegeneration and neuroinflammation using the triple co-culture model.

We used oligomeric $A\beta_{1-42}$ to model AD conditions. Exogenous addition of Aβ has been widely used in primary cultures to study amyloid pathology. Both Aβ oligomers and fibrils reduce neuronal viability (Ryan *et al.*, 2010; Janefjord *et al.*, 2014), and Aβ oligomers induce alterations in synaptic spine numbers and morphology in primary neurons (Calabrese *et al.*, 2007; Lacor *et al.*, 2007). Aβ oligomers also increase pro-inflammatory cytokine release (Li *et al.*, 2013) and activate the inflammasome in microglia cultures (Lučiūnaitė *et al.*, 2020). CD11b

increase has been reported in AD patients and in cultured microglia in response to Aβ fibrils (Akiyama and McGeer, 1990; Jana *et al.*, 2008; Zhang *et al.*, 2011), and it has been associated as potential AD risk gene (Salih *et al.*, 2019). Severity of microglial activation is reflected by the increased on CD11b expression in LPS induced inflammation (Roy *et al.*, 2008). In primary astrocytes, Aβ oligomers can reduce cell viability and increase activation markers like GFAP (Hou *et al.*, 2011; Alberdi *et al.*, 2013). In our triple co-culture, addition of exogenous Aβ oligomers promoted pre- and post-synaptic loss, as well as an increase in microglial marker CD11b. Guttikonda et al. (2021) reported that astrocytes secrete high levels of C3 upon LPS stimulation in the triple AD co-culture derived from human PSC. Interestingly, our results are complementary to those ones, since we report high levels of CD11b, one of the subunits of C3 receptor CR3. Both microglia and astrocytes can participate in synaptic elimination via the complement system (Hong *et al.*, 2016) and MEGF10/MERTK pathways (Chung *et al.*, 2013), respectively. Therefore, our model could be useful to further study the role of these pathways in Aβ-induced synaptic loss. We used a more complex model such as hippocampal organotypic cultures to confirm our findings and observed the same negative effects of oligomeric Aβ on synaptic loss and neuroinflammation. Compared with organotypic cultures, our triple co-culture model has a defined concentration of each cell type that can be easily manipulated, becoming a complementary model for mechanistic studies.

Altogether, our findings suggest that the neuron, microglia, and astrocyte triple co-culture model we developed is reliable, affordable and a useful tool for the study of mechanisms implicated in AD neurodegeneration. In agreement with previous reports with *in vitro* models, ours also closely mimics the *in vivo* environment, where the cross talk between neurons and glial cells contributes to neuroinflammation processes (Goshi *et al.*, 2020), and where alterations in glial cells can lead to neurodegeneration (Lange *et al.*, 2018). Our model can also be potentially used in high throughput screening setups, so we expect that it will help finding new therapeutic targets for AD and other neurodegenerative diseases.

4. Concluding remarks.

With this work, we have provided evidence that strongly supports the essential role of neuroinflammation in AD progression in a variety of experimental models. Neuroinflammation is a multifactorial process that encompasses numerous cell types, soluble mediators and signaling pathways, and microglia is one of the main actor in this process (Rubio-Perez and Morillas-Ruiz, 2012; Heneka *et al.*, 2015). In this study, we have taken two different approaches to tackle exacerbated inflammatory response and prevent the progression of AD, paying especial attention to Aβ-induced alterations. Our first approach was to restore resolution of inflammation using lipoxin ATL. This strategy was protective against AD pathology and synapse loss, it reduced pro-inflammatory mediators and reactive glial cells, and prevented oxidative stress damage and mitochondrial dysfunction. Together with the existing literature, our results suggest that enhancing the pro-resolution lipoxin pathway may be an effective therapeutic approach to treat AD progression. Our second strategy was to target microglia using CR3 inhibitor XVA143. This inhibitor drastically reduced the expression of CR3 itself, associated with microglial activation, and produced transcriptional and morphological changes that may affect microglial function. In addition, XVA143 enhanced Aβ clearance, and allowed us to observe a novel link between CR3 receptor and complement pathway initiator C1q that will be an important objective for future research. Finally, given the lack of available models to study the complexity of neuroinflammation, we developed a triple co-culture model consisting of neurons, astrocytes and microglia. This *in vitro* model, which retains cellular physiological characteristics that are lost in primary cultures, allowed us to recapitulate amyloid pathology and will be a useful tool to study the crosstalk between neurons and glial cells in order to understand the relationship between neuroinflammation and neurodegeneration.

Conclusions

Conclusions

1.1. ATL ameliorates Aβ-mediated oxidative stress and mitochondrial dysfunction by inhibiting NOX2 ROS production and enhancing SOD detoxification, which results in a recovery of oxidative phosphorylation and a rebalance of mitochondrial dynamics.

1.2. ATL reduces amyloid pathology, tau pathology and synapse loss mediated by the complement pathway C1q-CR3 axis in *in vitro* and *in vivo* AD models.

1.3. ATL mitigates neuroinflammation in the 3xTg AD mouse model by reducing pro-inflammatory mediators, inhibiting gliosis and reverting morphological alterations in astrocytes and microglia.

2.1. Inhibition of microglial CR3 using small molecule XVA143 alters cellular morphology, reduces migration capacity, induces transcriptomic changes in genes related to inflammation and phagocytosis, and modulates the expression of complement components C1q and C4.

2.2. XVA143 inhibition of CR3 impairs microglial internalization of $A\beta_{42}$ oligomers and reduces extracellular levels of $A\beta_{42}$ *in vitro* and *ex vivo*.

3.1. In the triple co-culture model, neurons and glia display characteristics similar to physiological conditions that are not preserved in primary cultures. Neurons develop a more mature morphology, microglia are less inflammatory and astrocytes are less reactive.

3.2. The addition of $A\beta_{42}$ oligomers to the triple co-culture model recapitulates Aβ pathology and neuroinflammation, and allows the study of communication between neurons and glial cells in the context of neurodegeneration.

This thesis provides evidence supporting the key role of neuroinflammation in the onset and progression of AD. We have investigated the effect of lipoxin ATL on the resolution of inflammation, which is impaired in AD patients, and we have demonstrated that this anti-inflammatory mediator has positive effects on the disease at multiple levels. In addition, we have characterized one of the most relevant receptors for microglial activation, CR3, with the help of a compound only recently used in the CNS. Finally, we have developed an *in vitro* model to study cell communication in the context of AD pathology. Our results highlight the relevance of microglia and neuroinflammation as therapeutic targets for AD, and let the door open to future research.

Bibliography

Bibliography

Abramov AY, Jacobson J, Wientjes F, Hothersall J, Canevari L, Duchen MR. Expression and modulation of an NADPH oxidase in mammalian astrocytes. J Neurosci 2005; 25: 9176–84.

Aebersold MJ, Thompson-Steckel G, Joutang A, Schneider M, Burchert C, Forró C, et al. Simple and Inexpensive Paper-Based Astrocyte Co-culture to Improve Survival of Low-Density Neuronal Networks. Front Neurosci 2018; 0: 94.

Afagh A, Cummings BJ, Cribbs DH, Cotman CW, Tenner AJ. Localization and Cell Association of C1q in Alzheimer's Disease Brain. Exp Neurol 1996; 138: 22–32.

Akama KT, Van Eldik LJ. β-Amyloid Stimulation of Inducible Nitric-oxide Synthase in Astrocytes Is Interleukin-1β- and Tumor Necrosis Factor-α (TNFα)-dependent, and Involves a TNFα Receptor-associated Factor- and NFκB-inducing Kinase-dependent Signaling Mechanism. J Biol Chem 2000; 275: 7918–24.

Akiyama H, McGeer PL. Brain microglia constitutively express β-2 integrins. J Neuroimmunol 1990; 30: 81–93.

Aksenov MY, Aksenova M V., Butterfield DA, Geddes JW, Markesbery WR. Protein oxidation in the brain in Alzheimer's disease. Neuroscience 2001; 103: 373–83.

Alberdi E, Sánchez-Gómez MV, Cavaliere F, Pérez-Samartín A, Zugaza JL, Trullas R, et al. Amyloid β oligomers induce Ca2+ dysregulation and neuronal death through activation of ionotropic glutamate receptors. Cell Calcium 2010; 47: 264–72.

Alberdi E, Sánchez-Gómez MV, Ruiz A, Cavaliere F, Ortiz-Sanz C, Quintela-López T, et al. Mangiferin and Morin Attenuate Oxidative Stress, Mitochondrial Dysfunction, and Neurocytotoxicity, Induced by Amyloid Beta Oligomers. Oxid Med Cell Longev 2018; 2018: 2856063.

Alberdi E, Wyssenbach A, Alberdi M, S?nchez-G?mez M V., Cavaliere F, Rodr?guez JJ, et al. Ca $^{2+}$ -dependent endoplasmic reticulum stress correlates with astrogliosis in oligomeric amyloid ?-treated astrocytes and in a model of Alzheimer's disease. Aging Cell 2013; 12: 292–302.

Almeida CG, Tampellini D, Takahashi RH, Greengard P, Lin MT, Snyder EM, et al. Beta-amyloid accumulation in APP mutant neurons reduces PSD-95 and GluR1 in synapses. Neurobiol Dis 2005; 20: 187–98.

Alzheimer, A. Über eine eigenartige Erkrankung der Hirnrinde Allgemeine Zeitschrift fur Psychiatrie und Psychisch-gerichtliche Medizin. Psychiatry (Edgmont) 1907; 64: 146–8.

Apelt J, Bigl M, Wunderlich P, Schliebs R. Aging-related increase in oxidative stress correlates with developmental pattern of beta-secretase activity and beta-amyloid plaque formation in transgenic Tg2576 mice with Alzheimer-like pathology. Int J Dev Neurosci 2004; 22: 475–84.

Apostolova LG. Alzheimer Disease. Contin Lifelong Learn Neurol 2016; 22: 419.

Arancibia-Cárcamo IL, Fairfax BP, Moss SJ, Kittler JT. Studying the Localization, Surface Stability and Endocytosis of Neurotransmitter Receptors by Antibody Labeling and Biotinylation Approaches. Dyn Synap Mol Methods Ionotropic Recept Biol 2006: 91–118.

Ardura-Fabregat A, Boddeke EWGM, Boza-Serrano A, Brioschi S, Castro-Gomez S, Ceyzériat K, et al. Targeting Neuroinflammation to Treat Alzheimer's Disease. CNS Drugs 2017 3112 2017; 31: 1057–82.

Asai H, Ikezu S, Tsunoda S, Medalla M, Luebke J, Haydar T, et al. Depletion of microglia and inhibition of exosome synthesis halt tau propagation. Nat Neurosci 2015; 18: 1584–93.

Aschenbrenner AJ, Gordon BA, Benzinger TLS, Morris JC, Hassenstab JJ. Influence of tau PET, amyloid PET, and hippocampal volume on cognition in Alzheimer disease. Neurology 2018; 91: e859–66.

B Y, Z L, J Z, B P, X W, R H, et al. Lipoxin A4 Ameliorates Lung Development in Neonatal Rats with Hyperoxia-induced Bronchopulmonary Dysplasia by Reducing Mitochondrial Fission. 2021

Bachstetter AD, Ighodaro ET, Hassoun Y, Aldeiri D, Neltner JH, Patel E, et al. Rod-shaped microglia morphology is associated with aging in two human autopsy series. Neurobiol Aging 2017; 52: 98.

Ballatore C, Lee VMY, Trojanowski JQ. Tau-mediated neurodegeneration in Alzheimer's disease and related disorders. Nat Rev Neurosci 2007 89 2007; 8: 663–72.

Beach TG, McGeer EG. Lamina-specific arrangement of astrocytic gliosis and senile plaques in Alzheimer's disease visual cortex. Brain Res 1988; 463: 357–61.

Belenguer P, Duarte JMN, Schuck PF, Ferreira GC. Mitochondria and the Brain: Bioenergetics and Beyond. Neurotox Res 2019 362 2019; 36: 219–38.

Belfiore R, Rodin A, Ferreira E, Velazquez R, Branca C, Caccamo A, et al. Temporal and regional progression of Alzheimer's disease-like pathology in 3xTg-AD mice. Aging Cell 2019; 18: e12873.

Benzing WC, Wujek JR, Ward EK, Shaffer D, Ashe KH, Younkin SG, et al. Evidence for glial-mediated inflammation in aged APPSW transgenic mice. Neurobiol Aging 1999; 20: 581–9.

Bermejo P, Martín-Aragón S, Benedí J, Susín C, Felici E, Gil P, et al. Peripheral levels of glutathione and protein oxidation as markers in the development of Alzheimer's disease from Mild Cognitive Impairment. Free Radic Res 2009; 42: 162–70.

Della Bianca V, Dusi S, Bianchini E, Dal Prà I, Rossi F. β-Amyloid Activates the O÷2 Forming NADPH Oxidase in Microglia, Monocytes, and Neutrophils: A POSSIBLE INFLAMMATORY MECHANISM OF NEURONAL DAMAGE IN ALZHEIMER'S DISEASE *. J Biol Chem 1999; 274: 15493–9.

Bie B, Wu J, Foss JF, Naguib M. Activation of mGluR1 Mediates C1q-Dependent Microglial Phagocytosis of Glutamatergic Synapses in Alzheimer's Rodent Models. Mol Neurobiol 2019; 56:

5568–85.

Billings LM, Oddo S, Green KN, McGaugh JL, LaFerla FM. Intraneuronal Aβ Causes the Onset of Early Alzheimer's Disease-Related Cognitive Deficits in Transgenic Mice. Neuron 2005; 45: 675–88.

Bloom GS. Amyloid-β and Tau: The Trigger and Bullet in Alzheimer Disease Pathogenesis. JAMA Neurol 2014; 71: 505–8.

Bobba A, Amadoro G, Valenti D, Corsetti V, Lassandro R, Atlante A. Mitochondrial respiratory chain Complexes I and IV are impaired by β-amyloid via direct interaction and through Complex I-dependent ROS production, respectively. Mitochondrion 2013; 13: 298–311.

Bohlen CJ, Bennett FC, Tucker AF, Collins HY, Mulinyawe SB, Barres BA. Diverse Requirements for Microglial Survival, Specification, and Function Revealed by Defined-Medium Cultures. Neuron 2017; 94: 759-773.e8.

Braak H, Braak E. Staging of alzheimer's disease-related neurofibrillary changes. Neurobiol Aging 1995; 16: 271–8.

Brandes RP, Weissmann N, Schröder K. Nox family NADPH oxidases: Molecular mechanisms of activation. Free Radic Biol Med 2014; 76: 208–26.

Breijyeh Z, Karaman R. Comprehensive Review on Alzheimer's Disease: Causes and Treatment. Mol 2020, Vol 25, Page 5789 2020; 25: 5789.

Breitner JC, Baker LD, Montine TJ, Meinert CL, Lyketsos CG, Ashe KH, et al. Extended results of the Alzheimer's disease anti-inflammatory prevention trial. Alzheimer's Dement 2011; 7: 402–11.

Brelstaff J, Tolkovsky AM, Ghetti B, Goedert M, Spillantini MG. Living Neurons with Tau Filaments Aberrantly Expose Phosphatidylserine and Are Phagocytosed by Microglia. Cell Rep 2018; 24: 1939-1948.e4.

Bresciani G, da Cruz IBM, González-Gallego J. Manganese Superoxide Dismutase and Oxidative Stress Modulation. Adv Clin Chem 2015; 68: 87–130.

Brewer GJ, Torricelli JR, Evege EK, Price PJ. Optimized survival of hippocampal neurons in B27-supplemented neurobasal™, a new serum-free medium combination. J Neurosci Res 1993; 35: 567–76.

Bronzuoli MR, Iacomino A, Steardo L, Scuderi C. Targeting neuroinflammation in Alzheimer's disease. J Inflamm Res 2016; 9: 199.

Burdick D, Soreghan B, Kwon M, Kosmoski J, Knauer M, Henschen A, et al. Assembly and aggregation properties of synthetic Alzheimer's A4/beta amyloid peptide analogs. J Biol Chem 1992; 267: 546–54.

Burns ME, Augustine GJ. Synaptic structure and function: Dynamic organization yields architectural precision. Cell 1995; 83: 187–94.

Cai Q, Tammineni P. Mitochondrial Aspects of Synaptic Dysfunction in Alzheimer's Disease. J Alzheimers Dis 2017; 57: 1087.

Calabrese B, Shaked GM, Tabarean I V., Braga J, Koo EH, Halpain S. Rapid, Concurrent Alterations in Pre- and Postsynaptic Structure Induced by Soluble Natural Amyloid-β Protein. Mol Cell Neurosci 2007; 35: 183.

Calabrese V, Sultana R, Scapagnini G, Guagliano E, Sapienza M, Bella R, et al. Nitrosative Stress, Cellular Stress Response, and Thiol Homeostasis in Patients with Alzheimer's Disease. Antioxid Redox Signal 2006; 8: 1975–86.

Calkins MJ, Manczak M, Mao P, Shirendeb U, Reddy PH. Impaired mitochondrial biogenesis, defective axonal transport of mitochondria, abnormal mitochondrial dynamics and synaptic degeneration in a mouse model of Alzheimer's disease. Hum Mol Genet 2011; 20: 4515–29.

Calsolaro V, Edison P. Neuroinflammation in Alzheimer's disease: Current evidence and future directions. Alzheimer's Dement 2016; 12: 719–32.

Cardozo PL, Lima IBQ de, Maciel EMA, Silva NC, Dobransky T, Ribeiro FM. Synaptic Elimination in Neurological Disorders. Curr Neuropharmacol 2019; 17: 1071.

Carpanini SM, Torvell M, Morgan BP. Therapeutic inhibition of the complement system in diseases of the central nervous system. Front Immunol 2019; 10: 362.

Catalá I, Ferrer I, Galofré E, Fábregues I. Decreased numbers of dendritic spines on cortical pyramidal neurons in dementia. A quantitative Golgi study on biopsy samples. Hum Neurobiol 1988; 6: 255–9.

Cenini G, Voos W. Mitochondria as potential targets in Alzheimer disease therapy: An update. Front Pharmacol 2019; 10: 902.

Chan DC. Fusion and Fission: Interlinked Processes Critical for Mitochondrial Health. Annu Rev Genet 2012; 46: 265–87.

Chandrasekharan JA, Sharma-Wali N. Lipoxins: Nature's way to resolve inflammation. J Inflamm Res 2015; 8: 181–92.

Chartier-Harlin MC, Crawford F, Houlden H, Warren A, Hughes D, Fidani L, et al. Early-onset Alzheimer's disease caused by mutations at codon 717 of the beta-amyloid precursor protein gene. Nature 1991; 353: 844–6.

Cheignon C, Tomas M, Bonnefont-Rousselot D, Faller P, Hureau C, Collin F. Oxidative stress and the amyloid beta peptide in Alzheimer's disease. Redox Biol 2018; 14: 450–64.

Chen G, Tan CS, Teh BK, Lu J. Molecular Mechanisms for Synchronized Transcription of Three Complement C1q Subunit Genes in Dendritic Cells and Macrophages. J Biol Chem 2011; 286: 34941–50.

Chen JF, Yang W, Kim M, Carman C V., Springer TA. Regulation of outside-in signaling and affinity by the β2 I domain of integrin αLβ2. Proc Natl Acad Sci 2006; 103: 13062–7.

Chiang N, Hurwitz S, Ridker PM, Serhan CN. Aspirin has a gender-dependent impact on antiinflammatory 15-epi-lipoxin A4 formation: A randomized human trial. Arterioscler Thromb Vasc Biol 2006; 26

Choi I, Kim B, Byun JW, Baik SH, Huh YH, Kim JH, et al. LRRK2 G2019S mutation attenuates microglial motility by inhibiting focal adhesion kinase. Nat Commun 2015; 6: 1–13.

Christie R, Yamada M, Moskowitz M, Hyman B. Structural and Functional Disruption of Vascular Smooth Muscle Cells in a Transgenic Mouse Model of Amyloid Angiopathy. Am J Pathol 2001; 158: 1065.

Christopherson KS, Ullian EM, Stokes CCA, Mullowney CE, Hell JW, Agah A, et al. Thrombospondins are astrocyte-secreted proteins that promote CNS synaptogenesis. Cell 2005; 120: 421–33.

Chung W-S, Clarke LE, Wang GX, Stafford BK, Sher A, Chakraborty C, et al. Astrocytes mediate synapse elimination through MEGF10 and MERTK pathways. Nature 2013; 504: 394–400.

Correa FG, Hernangómez M, Guaza C. Co-culture Systems to Analysis Microglia Interactions with Other Cell Types. In: Bertrand J, Venero JL, editor(s). Microglia: Methods and protocols. New York: Springer-Human Press; 2013. p. 215–30

Cortassa S, O'Rourke B, Aon MA. Redox-Optimized ROS Balance and the relationship between mitochondrial respiration and ROS. Biochim Biophys Acta - Bioenerg 2014; 1837: 287–95.

Cummings J, Lee G, Ritter A, Sabbagh M, Zhong K. Alzheimer's disease drug development pipeline: 2020. Alzheimer's Dement Transl Res Clin Interv 2020; 6: e12050.

Czirr E, Castello NA, Mosher KI, Castellano JM, Hinkson I V., Lucin KM, et al. Microglial complement receptor 3 regulates brain Aβ levels through secreted proteolytic activity. J Exp Med 2017; 214: 1081–92.

D'Elia R, Jenner DC, Laws TR, Stokes MGM, Jackson MC, Essex-Lopresti AE, et al. Inhibition of Francisella tularensis LVS infection of macrophages results in a reduced inflammatory response: evaluation of a therapeutic strategy for intracellular bacteria. FEMS Immunol Med Microbiol 2011; 62: 348–61.

Daborg J, Andreasson U, Pekna M, Lautner R, Hanse E, Minthon L, et al. Cerebrospinal fluid levels of complement proteins C3, C4 and CR1 in Alzheimer's disease. J Neural Transm 2012; 119: 789–97.

Dagher NN, Najafi AR, Kayala KMN, Elmore MRP, White TE, Medeiros R, et al. Colony-stimulating factor 1 receptor inhibition prevents microglial plaque association and improves cognition in 3xTg-AD mice. J Neuroinflammation 2015; 12

Dahlgren KN, Manelli AM, Blaine Stine W, Baker LK, Krafft GA, Ladu MJ. Oligomeric and Fibrillar Species of Amyloid-β Peptides Differentially Affect Neuronal Viability *. J Biol Chem 2002; 277: 32046–53.

Darocha-Souto B, Scotton TC, Coma M, Serrano-Pozo A, Hashimoto T, Serenó L, et al. Brain Oligomeric β-Amyloid but Not Total Amyloid Plaque Burden Correlates With Neuronal Loss and Astrocyte Inflammatory Response in Amyloid Precursor Protein/Tau Transgenic Mice. J Neuropathol Exp Neurol 2011; 70: 360–76.

Davenport CM, Sevastou IG, Hooper C, Pocock JM. Inhibiting p53 pathways in microglia attenuates microglial-evoked neurotoxicity following exposure to Alzheimer peptides. J Neurochem 2010; 112: 552–63.

Davies CA, Mann DMA, Sumpter PQ, Yates PO. A quantitative morphometric analysis of the neuronal and synaptic content of the frontal and temporal cortex in patients with Alzheimer's disease. J Neurol Sci 1987; 78: 151–64.

Davies DS, Ma J, Jegathees T, Goldsbury C. Microglia show altered morphology and reduced arborization in human brain during aging and Alzheimer's disease. Brain Pathol 2017; 27: 795–808.

Dejanovic B, Huntley MA, De Mazière A, Meilandt WJ, Wu T, Srinivasan K, et al. Changes in the Synaptic Proteome in Tauopathy and Rescue of Tau-Induced Synapse Loss by C1q Antibodies. Neuron 2018; 100: 1322-1336.e7.

DeKosky ST, Scheff SW, Styren SD. Structural Correlates of Cognition in Dementia: Quantification and Assessment of Synapse Change. Neurodegeneration 1996; 5: 417–21.

Dickson DW. The Pathogenesis of Senile Plaques. J Neuropathol Exp Neurol 1997; 56: 321–39.

Dickson DW, Farlo J, Davies P, Crystal H, Fuld P, Yen SH. Alzheimer's disease. A double-labeling immunohistochemical study of senile plaques. Am J Pathol 1988; 132: 86.

Djordjevic J, Roy Chowdhury S, Snow WM, Perez C, Cadonic C, Fernyhough P, et al. Early Onset of Sex-Dependent Mitochondrial Deficits in the Cortex of 3xTg Alzheimer's Mice. Cells 2020, Vol 9, Page 1541 2020; 9: 1541.

Dohi K, Ohtaki H, Nakamachi T, Yofu S, Satoh K, Miyamoto K, et al. Gp91phox(NOX2) in classically activated microglia exacerbates traumatic brain injury. J Neuroinflammation 2010; 7: 1–11.

Donahue JE, Flaherty SL, Johanson CE, Duncan JA, Silverberg GD, Miller MC, et al. RAGE, LRP-1, and amyloid-beta protein in Alzheimer's disease. Acta Neuropathol 2006; 112: 405–15.

Dringen R. Glutathione metabolism and oxidative stress in neurodegeneration. Eur J Biochem 2000; 267: 4903–4903.

Du F, Yu Q, Chen A, Chen D, ShiDu Yan S. Astrocytes Attenuate Mitochondrial Dysfunctions in Human Dopaminergic Neurons Derived from iPSC. Stem Cell Reports 2018; 10: 366–74.

Duffield JS, Hong S, Vaidya VS, Lu Y, Fredman G, Serhan CN, et al. Resolvin D Series and Protectin D1 Mitigate Acute Kidney Injury. J Immunol 2006; 177: 5902–11.

Dunn HC, Ager RR, Baglietto-Vargas D, Cheng D, Kitazawa M, Cribbs DH, et al. Restoration of

Lipoxin A4 Signaling Reduces Alzheimer's Disease-Like Pathology in the 3xTg-AD Mouse Model. J Alzheimer's Dis 2015; 43: 893–903.

Earley AM, Graves CL, Shiau CE. Critical Role for a Subset of Intestinal Macrophages in Shaping Gut Microbiota in Adult Zebrafish. Cell Rep 2018; 25: 424–36.

Ehehalt R, Keller P, Haass C, Thiele C, Simons K. Amyloidogenic processing of the Alzheimer beta-amyloid precursor protein depends on lipid rafts. J Cell Biol 2003; 160: 113–23.

Emsley JG, Macklis JD. Astroglial heterogeneity closely reflects the neuronal-defined anatomy of the adult murine CNS. Neuron Glia Biol 2006; 2: 175.

Escartin C, Galea E, Lakatos A, O'Callaghan JP, Petzold GC, Serrano-Pozo A, et al. Reactive astrocyte nomenclature, definitions, and future directions. Nat Neurosci 2021 243 2021; 24: 312–25.

Esposito L, Raber J, Kekonius L, Yan F, Yu GQ, Bien-Ly N, et al. Reduction in Mitochondrial Superoxide Dismutase Modulates Alzheimer's Disease-Like Pathology and Accelerates the Onset of Behavioral Changes in Human Amyloid Precursor Protein Transgenic Mice. J Neurosci 2006; 26: 5167–79.

Fagan AM, Mintun MA, Mach RH, Lee SY, Dence CS, Shah AR, et al. Inverse relation between in vivo amyloid imaging load and cerebrospinal fluid Aβ42 in humans. Ann Neurol 2006; 59: 512–9.

Fagan AM, Roe CM, Xiong C, Mintun MA, Morris JC, Holtzman DM. Cerebrospinal Fluid tau/β-Amyloid42 Ratio as a Prediction of Cognitive Decline in Nondemented Older Adults. Arch Neurol 2007; 64: 343–9.

Fagerholm SC, Guenther C, Asens ML, Savinko T, Uotila LM. Beta2-Integins and interacting proteins in leukocyte trafficking, immune supression, and immunodeficiency disease. Front Immunol 2019; 10: 254.

Färber K, Cheung G, Mitchell D, Wallis R, Weihe E, Schwaeble W, et al. C1q, the recognition subcomponent of the classical pathway of complement, drives microglial activation. J Neurosci Res 2009; 87: 644–52.

Fernández-Fernández D, Dorner-Ciossek C, Kroker KS, Rosenbrock H. Age-related synaptic dysfunction in Tg2576 mice starts as a failure in early long-term potentiation which develops into a full abolishment of late long-term potentiation. J Neurosci Res 2016; 94: 266–81.

Fierro IM, Colgan SP, Bernasconi G, Petasis NA, Clish CB, Arita M, et al. Lipoxin A4 and aspirin-triggered 15-epi-lipoxin A4 inhibit human neutrophil migration: comparisons between synthetic 15 epimers in chemotaxis and transmigration with microvessel endothelial cells and epithelial cells. J Immunol 2003; 170: 2688–94.

Floden AM, Li S, Combs CK. β-Amyloid-Stimulated Microglia Induce Neuron Death via Synergistic Stimulation of Tumor Necrosis Factor α and NMDA Receptors. J Neurosci 2005; 25:

2566–75.

Fonseca MI, Chu SH, Hernandez MX, Fang MJ, Modarresi L, Selvan P, et al. Cell-specific deletion of C1qa identifies microglia as the dominant source of C1q in mouse brain. J Neuroinflammation 2017; 14: 1–15.

Forloni G, Demicheli F, Giorgi S, Bendotti C, Angeretti N. Expression of amyloid precursor protein mRNAs in endothelial, neuronal and glial cells: modulation by interleukin-1. Mol Brain Res 1992; 16: 128–34.

Fossati S, Ramos Cejudo J, Debure L, Pirraglia E, Sone JY, Li Y, et al. Plasma tau complements CSF tau and P-tau in the diagnosis of Alzheimer's disease. Alzheimer's Dement Diagnosis, Assess Dis Monit 2019; 11: 483–92.

Fraga VG, Magalhães CA, Loures C de MG, de Souza LC, Guimarães HC, Zauli DAG, et al. Inflammatory and Pro-resolving Mediators in Frontotemporal Dementia and Alzheimer's Disease. Neuroscience 2019; 421: 123–35.

Freeman LC, Ting JPY. The pathogenic role of the inflammasome in neurodegenerative diseases. J Neurochem 2016; 136: 29–38.

Freire MO, Van Dyke TE. Natural resolution of inflammation. Periodontol 2000 2013; 63: 149–64.

Fricker M, Oliva-Martín MJ, Brown GC. Primary phagocytosis of viable neurons by microglia activated with LPS or Aβ is dependent on calreticulin/LRP phagocytic signalling. J Neuroinflammation 2012; 9: 1–12.

Fu H, Liu B, Frost JL, Hong S, Jin M, Ostaszewski B, et al. Complement component C3 and complement receptor type 3 contribute to the phagocytosis and clearance of fibrillar Aβ by microglia. Glia 2012; 60: 993–1003.

Fukuyama R, Izumoto T, Fushiki S. The cerebrospinal fluid level of glial fibrillary acidic protein is increased in cerebrospinal fluid from Alzheimer's disease patients and correlates with severity of dementia. Eur Neurol 2001; 46: 35–8.

Furman JL, Sama DM, Gant JC, Beckett TL, Murphy MP, Bachstetter AD, et al. Targeting Astrocytes Ameliorates Neurologic Changes in a Mouse Model of Alzheimer's Disease. J Neurosci 2012; 32: 16129–40.

Gangemi S, Pescara L, D'Urbano E, Basile G, Nicita-Mauro V, Davì G, et al. Aging is characterized by a profound reduction in anti-inflammatory lipoxin A4 levels. Exp Gerontol 2005; 40: 612–4.

Garden GA, Möller T. Microglia biology in health and disease. J Neuroimmune Pharmacol 2006; 1: 127–37.

Garwood CJ, Pooler AM, Atherton J, Hanger DP, Noble W. Astrocytes are important mediators of Aβ-induced neurotoxicity and tau phosphorylation in primary culture. Cell Death Dis 2011 26 2011; 2: e167–e167.

Gasparini L, Ongini E, Wilcock D, Morgan D. Activity of flurbiprofen and chemically related anti-inflammatory drugs in models of Alzheimer's disease. Brain Res Rev 2005; 48: 400–8.

Ge Y, Zhang S, Wang J, Xia F, Wan JB, Lu J, et al. Dual modulation of formyl peptide receptor 2 by aspirin-triggered lipoxin contributes to its anti-inflammatory activity. FASEB J 2020; 34: 6920–33.

Geula C, Wu CK, Saroff D, Lorenzo A, Yuan M, Yankner BA. Aging renders the brain vulnerable to amyloid β-protein neurotoxicity. Nat Med 1998 47 1998; 4: 827–31.

Gezen-Ak D, Dursun E, Hanağasi H, Bilgiç B, Lohman E, Araz ÖS, et al. BDNF, TNFα, HSP90, CFH, and IL-10 serum levels in patients with early or late onset Alzheimer's disease or mild cognitive impairment. J Alzheimers Dis 2013; 37: 185–95.

Ghebrehiwet B. The complement system: an evolution in progress. F1000Research 2016; 5: 2840.

Girard SD, Jacquet M, Baranger K, Migliorati M, Escoffier G, Bernard A, et al. Onset of hippocampus-dependent memory impairments in 5XFAD transgenic mouse model of Alzheimer's disease. Hippocampus 2014; 24: 762–72.

Glabe CG. Common mechanisms of amyloid oligomer pathogenesis in degenerative disease. Neurobiol Aging 2006; 27: 570–5.

Glenner GG, Wong CW. Alzheimer's disease: Initial report of the purification and characterization of a novel cerebrovascular amyloid protein. Biochem Biophys Res Commun 1984; 120: 885–90.

Gold M, El Khoury J. β-amyloid, microglia, and the inflammasome in Alzheimer's disease. Semin Immunopathol 2015; 37: 607–11.

Gomez-Arboledas A, Davila JC, Sanchez-Mejias E, Navarro V, Nuñez-Diaz C, Sanchez-Varo R, et al. Phagocytic clearance of presynaptic dystrophies by reactive astrocytes in Alzheimer's disease. Glia 2018; 66: 637–53.

Gong CX, Liu F, Iqbal K. Multifactorial Hypothesis and Multi-Targets for Alzheimer's Disease. J Alzheimer's Dis 2018; 64: S107–17.

Goshi N, Morgan RK, Lein PJ, Seker E. A primary neural cell culture model to study neuron, astrocyte, and microglia interactions in neuroinflammation. J Neuroinflammation 2020; 17: 155.

Gosselin D, Skola D, Coufal NG, Holtman IR, Schlachetzki JCM, Sajti E, et al. An environment-dependent transcriptional network specifies human microglia identity. Science 2017; 356: 1248–59.

Grundke-Iqbal I, Iqbal K, Quinlan M, Tung YC, Zaidi MS, Wisniewski HM. Microtubule-associated protein tau. A component of Alzheimer paired helical filaments. J Biol Chem 1986; 261: 6084–9.

Guttikonda SR, Sikkema L, Tchieu J, Saurat N, Walsh R, Harschnitz O, et al. Fully defined human pluripotent stem cell-derived microglia and tri-culture system model C3 production in Alzheimer's disease. Nat Neurosci 2021; 24: 343.

Haass C, Schlossmacher MG, Hung AY, Vigo-Pelfrey C, Mellon A, Ostaszewski BL, et al. Amyloid beta-peptide is produced by cultured cells during normal metabolism. Nature 1992; 359: 322–5.

Haass C, Selkoe DJ. Soluble protein oligomers in neurodegeneration: lessons from the Alzheimer's amyloid β-peptide. Nat Rev Mol Cell Biol 2007 82 2007; 8: 101–12.

Haenseler W, Sansom SN, Buchrieser J, Newey SE, Moore CS, Nicholls FJ, et al. A Highly Efficient Human Pluripotent Stem Cell Microglia Model Displays a Neuronal-Co-culture-Specific Expression Profile and Inflammatory Response. Stem Cell Reports 2017; 8: 1727–42.

Hajishengallis G, Shakhatreh M-AK, Wang M, Liang S. Complement Receptor 3 Blockade Promotes IL-12-Mediated Clearance of Porphyromonas gingivalis and Negates Its Virulence In Vivo. J Immunol 2007; 179: 2359–67.

Hajishengallis G, Wang M, Liang S, Shakhatreh MAK, James D, Nishiyama SI, et al. Subversion of Innate Immunity by Periodontopathic Bacteria via Exploitation of Complement Receptor-3. Adv Exp Med Biol 2008; 632: 203–19.

Han X, Yang L, Du H, Sun Q, Wang X, Cong L, et al. Insulin Attenuates Beta-Amyloid-Associated Insulin/Akt/EAAT Signaling Perturbations in Human Astrocytes. Cell Mol Neurobiol 2016; 36: 851.

Hanseeuw BJ, Betensky RA, Jacobs HIL, Schultz AP, Sepulcre J, Becker JA, et al. Association of Amyloid and Tau With Cognition in Preclinical Alzheimer Disease: A Longitudinal Study. JAMA Neurol 2019; 76: 915–24.

Hardy J, Selkoe DJ. The Amyloid Hypothesis of Alzheimer's Disease: Progress and Problems on the Road to Therapeutics. Science (80-) 2002; 297

Hardy JA, Higgins GA. Alzheimer's disease: the amyloid cascade hypothesis. Science (80-) 1992; 256: 184–6.

Harkany T, Ábrahám I, Timmerman W, Laskay G, Tóth B, Sasvári M, et al. β-Amyloid neurotoxicity is mediated by a glutamate-triggered excitotoxic cascade in rat nucleus basalis. Eur J Neurosci 2000; 12: 2735–45.

Harokopakis E, Albzreh MH, Martin MH, Hajishengallis G. TLR2 Transmodulates Monocyte Adhesion and Transmigration via Rac1- and PI3K-Mediated Inside-Out Signaling in Response to Porphyromonas gingivalis Fimbriae. J Immunol 2006; 176: 7645–56.

Hasturk H, Kantarci A, Ohira T, Arita M, Ebrahimi N, Chiang N, et al. RvE1 protects from local inflammation and osteoclastmediated bone destruction in periodontitis. FASEB J 2006; 20: 401–3.

Haure-Mirande JV, Audrain M, Fanutza T, Kim SH, Klein WL, Glabe C, et al. Deficiency of TYROBP, an adapter protein for TREM2 and CR3 receptors, is neuroprotective in a mouse model of early Alzheimer's pathology. Acta Neuropathol 2017; 134: 769–88.

He Y, Taylor N, Yao X, Bhattacharya A. Mouse primary microglia respond differently to LPS and poly(I:C) in vitro. Sci Reports 2021 111 2021; 11: 1–14.

Helmut K, Hanisch UK, Noda M, Verkhratsky A. Physiology of microglia. Physiol Rev 2011; 91: 461–553.

Heneka MT, Carson MJ, Khoury J El, Landreth GE, Brosseron F, Feinstein DL, et al. Neuroinflammation in Alzheimer's Disease. Lancet Neurol 2015; 14: 388.

Heneka MT, Kummer MP, Stutz A, Delekate A, Schwartz S, Vieira-Saecker A, et al. NLRP3 is activated in Alzheimer´s disease and contributes to pathology in APP/PS1 mice. Nature 2013; 493: 674.

Hensley K, Hall N, Subramaniam R, Cole P, Harris M, Aksenov M, et al. Brain Regional Correspondence Between Alzheimer's Disease Histopathology and Biomarkers of Protein Oxidation. J Neurochem 1995; 65: 2146–56.

Herms J, Anliker B, Heber S, Ring S, Fuhrmann M, Kretzschmar H, et al. Cortical dysplasia resembling human type 2 lissencephaly in mice lacking all three APP family members. EMBO J 2004; 23: 4106–15.

Hernangómez M, Mestre L, Correa FG, Loría F, Mecha M, Iñigo PM, et al. CD200-CD200R1 interaction contributes to neuroprotective effects of anandamide on experimentally induced inflammation. Glia 2012; 60: 1437–50.

Hickman S, Izzy S, Sen P, Morsett L, El Khoury J. Microglia in neurodegeneration. Nat Neurosci 2018 2110 2018; 21: 1359–69.

Hickman SE, Allison EK, El Khoury J. Microglial dysfunction and defective beta-amyloid clearance pathways in aging Alzheimer's disease mice. J Neurosci 2008; 28: 8354–60.

Hickman SE, Kingery ND, Ohsumi TK, Borowsky ML, Wang LC, Means TK, et al. The microglial sensome revealed by direct RNA sequencing. Nat Neurosci 2013 1612 2013; 16: 1896–905.

Hohsfield LA, Humpel C. Migration of blood cells to β-amyloid plaques in Alzheimer's disease. Exp Gerontol 2015; 65: 8–15.

Honda S, Sasaki Y, Ohsawa K, Imai Y, Nakamura Y, Inoue K, et al. Extracellular ATP or ADP Induce Chemotaxis of Cultured Microglia through Gi/o-Coupled P2Y Receptors. J Neurosci 2001; 21: 1975–82.

Hong S, Beja-Glasser VF, Nfonoyim BM, Frouin A, Li S, Ramakrishnan S, et al. Complement and microglia mediate early synapse loss in Alzheimer mouse models. Science (80-) 2016; 352: 712–6.

Honma T, Hatta K, Hitomi Y, Kambayashi Y, Hibino Y, Konoshita T, et al. Increased systemic inflammatory interleukin-1ß and interleukin-6 during agitation as predictors of Alzheimer's disease. Int J Geriatr Psychiatry 2013; 28: 233–41.

Hopperton KE, Mohammad D, Trépanier MO, Giuliano V, Bazinet RP. Markers of microglia in post-mortem brain samples from patients with Alzheimer's disease: a systematic review. Mol Psychiatry 2018 232 2017; 23: 177–98.

Hou L, Bao X, Zang C, Yang H, Sun F, Che Y, et al. Integrin CD11b mediates α-synuclein-induced activation of NADPH oxidase through a Rho-dependent pathway. Redox Biol 2018; 14: 600–8.

Hou L, Liu Y, Wang X, Ma H, He J, Zhang Y, et al. The effects of amyloid-β 42 oligomer on the proliferation and activation of astrocytes in vitro. Vitr Cell Dev Biol - Anim 2011; 47: 573–80.

Huang WJ, Zhang X, Chen WW. Role of oxidative stress in Alzheimer's disease (review). Biomed Reports 2016; 4: 519–22.

Hynes RO. Integrins: Bidirectional, allosteric signaling machines. Cell 2002; 110: 673–87.

Ibarretxe G, Sánchez-Gómez MV, Campos-Esparza MR, Alberdi E, Matute C. Differential oxidative stress in oligodendrocytes and neurons after excitotoxic insults and protection by natural polyphenols. Glia 2006; 53: 201–11.

Ishii T, Haga S. Immuno-electron-microscopic localization of complements in amyloid fibrils of senile plaques. Acta Neuropathol 1984; 63: 296–300.

Ising C, Venegas C, Zhang S, Scheiblich H, Schmidt S V., Vieira-Saecker A, et al. NLRP3 inflammasome activation drives tau pathology. Nature 2019; 575: 669–73.

Jana M, Palencia CA, Pahan K. Fibrillar Amyloid-β Peptides Activate Microglia via TLR2: Implications for Alzheimer's Disease. J Immunol 2008; 181: 7254–62.

Janefjord E, Mååg JLV, Harvey BS, Smid SD. Cannabinoid effects on β amyloid fibril and aggregate formation, neuronal and microglial-activated neurotoxicity in vitro. Cell Mol Neurobiol 2014; 34: 31–42.

Jiang H, Burdick D, Glabe CG, Cotman CW, Tenner AJ. beta-Amyloid activates complement by binding to a specific region of the collagen-like domain of the C1q A chain. J Immunol 1994; 152

Kaeser SA, Häsler LM, Lambert M, Bergmann C, Bottelbergs A, Theunis C, et al. CSF p-tau increase in response to Aβ-type and Danish-type cerebral amyloidosis and in the absence of neurofibrillary tangles. Acta Neuropathol 2021 2021; 1: 1–4.

Kang J, Lemaire HG, Unterbeck A, Salbaum JM, Masters CL, Grzeschik KH, et al. The precursor of Alzheimer's disease amyloid A4 protein resembles a cell-surface receptor. Nature 1987; 325: 733–6.

Kantarci A, Aytan N, Palaska I, Stephens D, Crabtree L, Benincasa C, et al. Combined administration of resolvin E1 and lipoxin A4 resolves inflammation in a murine model of Alzheimer's disease. Exp Neurol 2018; 300: 111–20.

Kato S, Gondo T, Hoshii Y, Takahashi M, Yamada M, Ishihara T. Confocal observation of senile plaques in Alzheimer's disease: Senile plaque morphology and relationship between senile plaques and astrocytes. Pathol Int 1998; 48: 332–40.

Kaur D, Sharma V, Deshmukh R. Activation of microglia and astrocytes: a roadway to neuroinflammation and Alzheimer's disease. Inflammopharmacology 2019 274 2019; 27: 663–77.

Kayed R, Lasagna-Reeves CA. Molecular Mechanisms of Amyloid Oligomers Toxicity. J Alzheimer's Dis 2013; 33: S67–78.

Kim DK, Mook-Jung I. The role of cell type-specific mitochondrial dysfunction in the pathogenesis of Alzheimer's disease. BMB Rep 2019; 52: 679.

Kim HG, Moon M, Choi JG, Park G, Kim AJ, Hur J, et al. Donepezil inhibits the amyloid-beta oligomer-induced microglial activation in vitro and in vivo. Neurotoxicology 2014; 40: 23–32.

Kim SU, De Vellis J. Microglia in health and disease. J Neurosci Res 2005; 81: 302–13.

Knopman DS, Jones DT, Greicius MD. Failure to demonstrate efficacy of aducanumab: An analysis of the EMERGE and ENGAGE trials as reported by Biogen, December 2019. Alzheimer's Dement 2021; 17: 696–701.

Koenigsknecht J, Landreth G. Microglial Phagocytosis of Fibrillar β-Amyloid through a β1 Integrin-Dependent Mechanism. J Neurosci 2004; 24: 9838–46.

Kozieł R, Pircher H, Kratochwil M, Lener B, Hermann M, Dencher NA, et al. Mitochondrial respiratory chain complex I is inactivated by NADPH oxidase Nox4. Biochem J 2013; 452: 231–9.

Kwon HS, Koh SH. Neuroinflammation in neurodegenerative disorders: the roles of microglia and astrocytes. Transl Neurodegener 2020 91 2020; 9: 1–12.

Lacor PN, Buniel MC, Furlow PW, Clemente AS, Velasco PT, Wood M, et al. Aβ Oligomer-Induced Aberrations in Synapse Composition, Shape, and Density Provide a Molecular Basis for Loss of Connectivity in Alzheimer's Disease. J Neurosci 2007; 27: 796–807.

LaFerla FM, Oddo S. Alzheimer's disease: Aβ, tau and synaptic dysfunction. Trends Mol Med 2005; 11: 170–6.

Lambert J-C, Heath S, Even G, Campion D, Sleegers K, Hiltunen M, et al. Genome-wide association study identifies variants at CLU and CR1 associated with Alzheimer's disease. Nat Genet 2009 4110 2009; 41: 1094–9.

Lambert MP, Barlow AK, Chromy BA, Edwards C, Freed R, Liosatos M, et al. Diffusible, nonfibrillar ligands derived from Aβ1–42 are potent central nervous system neurotoxins. Proc Natl Acad Sci 1998; 95: 6448–53.

Lamers C, Plüss CJ, Ricklin D. The Promiscuous Profile of Complement Receptor 3 in Ligand Binding, Immune Modulation, and Pathophysiology. Front Immunol 2021; 12

Lange J, Haslett LJ, Lloyd-Evans E, Pocock JM, Sands MS, Williams BP, et al. Compromised astrocyte function and survival negatively impact neurons in infantile neuronal ceroid lipofuscinosis. Acta Neuropathol Commun 2018; 6: 74.

Lanoiselée HM, Nicolas G, Wallon D, Rovelet-Lecrux A, Lacour M, Rousseau S, et al. APP, PSEN1, and PSEN2 mutations in early-onset Alzheimer disease: A genetic screening study of familial and sporadic cases. PLOS Med 2017; 14: e1002270.

Laske C, Stransky E, Hoffmann N, Maetzler W, Straten G, Eschweiler GW, et al. Macrophage Colony-Stimulating Factor (M-CSF) in Plasma and CSF of Patients with Mild Cognitive Impairment and Alzheimer's Disease. Curr Alzheimer Res 2010; 7: 409–14.

Le Y, Gong W, Tiffany HL, Tumanov A, Nedospasov S, Shen W, et al. Amyloid β42 Activates a G-Protein-Coupled Chemoattractant Receptor, FPR-Like-1. J Neurosci 2001; 21: RC123–RC123.

Lee J, Retamal C, Cuitiño L, Caruano-Yzermans A, Shin JE, Van Kerkhof P, et al. Adaptor Protein Sorting Nexin 17 Regulates Amyloid Precursor Protein Trafficking and Processing in the Early Endosomes. J Biol Chem 2008; 283: 11501–8.

Lee JY, Han SH, Park MH, Baek B, Song IS, Choi MK, et al. Neuronal SphK1 acetylates COX2 and contributes to pathogenesis in a model of Alzheimer's Disease. Nat Commun 2018 91 2018; 9: 1–14.

Lee JY, Han SH, Park MH, Song IS, Choi MK, Yu E, et al. N-AS-triggered SPMs are direct regulators of microglia in a model of Alzheimer's disease. Nat Commun 2020 111 2020; 11: 1–19.

Levy E, Carman MD, Fernandez-Madrid IJ, Power MD, Lieberburg I, Van Duinen SG, et al. Mutation of the Alzheimer's disease amyloid gene in hereditary cerebral hemorrhage, Dutch type. Science 1990; 248: 1124–6.

Li J, Yang JY, Yao XC, Xue X, Zhang QC, Wang XX, et al. Oligomeric aβ-induced microglial activation is possibly mediated by NADPH oxidase. Neurochem Res 2013; 38: 443–52.

Lian H, Litvinchuk A, Chiang AC-A, Aithmitti N, Jankowsky JL, Zheng H. Astrocyte-Microglia Cross Talk through Complement Activation Modulates Amyloid Pathology in Mouse Models of Alzheimer's Disease. J Neurosci 2016; 36: 577–89.

Lian H, Yang L, Cole A, Sun L, Chiang ACA, Fowler SW, et al. NFκB-Activated Astroglial Release of Complement C3 Compromises Neuronal Morphology and Function Associated with Alzheimer's Disease. Neuron 2015; 85: 101–15.

Liddelow SA, Guttenplan KA, Clarke LE, Bennett FC, Bohlen CJ, Schirmer L, et al. Neurotoxic reactive astrocytes are induced by activated microglia. Nat 2017 5417638 2017; 541: 481–7.

Liu L, Chan C. IPAF inflammasome is involved in IL-1β production from astrocytes, induced by palmitate; implications for Alzheimer's Disease. Neurobiol Aging 2014; 35: 309–21.

Liu ZQ, Zhang H Bin, Wang J, Xia LJ, Zhang W. Lipoxin A4 ameliorates ischemia/reperfusion induced spinal cord injury in rabbit model. Int J Clin Exp Med 2015; 8: 12826.

Livne-Bar I, Wei J, Liu HH, Alqawlaq S, Won GJ, Tuccitto A, et al. Astrocyte-derived lipoxins A4 and B4 promote neuroprotection from acute and chronic injury. J Clin Invest 2017; 127: 4403–14.

Long JM, Holtzman DM. Alzheimer Disease: An Update on Pathobiology and Treatment Strategies. Cell 2019; 179: 312–39.

Luchena C, Zuazo-Ibarra J, Alberdi E, Matute C, Capetillo-Zarate E. Contribution of neurons and

glial cells to complement-mediated synapse removal during development, aging and in Alzheimer's disease. Mediators Inflamm 2018; 2018

Lučiūnaitė A, McManus RM, Jankunec M, Rácz I, Dansokho C, Dalgėdienė I, et al. Soluble Aβ oligomers and protofibrils induce NLRP3 inflammasome activation in microglia. J Neurochem 2020; 155: 650–61.

Lue L-F, Rydel R, Brigham EF, Yang L-B, Hampel H, Murphy GM, et al. Inflammatory repertoire of Alzheimer's disease and nondemented elderly microglia in vitro. Glia 2001; 35: 72–9.

Lui H, Zhang J, Makinson SR, Cahill MK, Kelley KW, Huang HY, et al. Progranulin Deficiency Promotes Circuit-Specific Synaptic Pruning by Microglia via Complement Activation. Cell 2016; 165: 921–35.

Lukiw WJ, Cui JG, Marcheselli VL, Bodker M, Botkjaer A, Gotlinger K, et al. A role for docosahexaenoic acid–derived neuroprotectin D1 in neural cell survival and Alzheimer disease. J Clin Invest 2005; 115: 2774–83.

Lyman M, Lloyd DG, Ji X, Vizcaychipi MP, Ma D. Neuroinflammation: The role and consequences. Neurosci Res 2014; 79: 1–12.

Madi NM, Ibrahim RR, Alghazaly GM, Marea KE, El-Saka MH. The prospective curative role of lipoxin A4 in induced gastric ulcer in rats: Possible involvement of mitochondrial dynamics signaling pathway. IUBMB Life 2020; 72: 1379–92.

Madore C, Leyrolle Q, Morel L, Rossitto M, Greenhalgh AD, Delpech JC, et al. Essential omega-3 fatty acids tune microglial phagocytosis of synaptic elements in the mouse developing brain. Nat Commun 2020 111 2020; 11: 1–19.

Maier M, Peng Y, Jiang L, Seabrook TJ, Carroll MC, Lemere CA. Complement C3 Deficiency Leads to Accelerated Amyloid β Plaque Deposition and Neurodegeneration and Modulation of the Microglia/Macrophage Phenotype in Amyloid Precursor Protein Transgenic Mice. J Neurosci 2008; 28: 6333–41.

Majumdar A, Capetillo-Zarate E, Cruz D, Gouras GK, Maxfield FR. Degradation of Alzheimer's amyloid fibrils by microglia requires delivery of ClC-7 to lysosomes. Mol Biol Cell 2011; 22: 1664–76.

Manczak M, Anekonda TS, Henson E, Park BS, Quinn J, Reddy PH. Mitochondria are a direct site of Aβ accumulation in Alzheimer's disease neurons: implications for free radical generation and oxidative damage in disease progression. Hum Mol Genet 2006; 15: 1437–49.

Markesbery WR, Lovell MA. Four-Hydroxynonenal, a Product of Lipid Peroxidation, is Increased in the Brain in Alzheimer's Disease. Neurobiol Aging 1998; 19: 33–6.

Martini AC, Forner S, Bento AF, Rae GA. Neuroprotective Effects of Lipoxin A4 in Central Nervous System Pathologies. Biomed Res Int 2014; 2014

Massaad CA, Washington TM, Pautler RG, Klann E. Overexpression of SOD-2 reduces

hippocampal superoxide and prevents memory deficits in a mouse model of Alzheimer's disease. Proc Natl Acad Sci U S A 2009; 106: 13576.

Masuda T, Tsuda M, Yoshinaga R, Tozaki-Saitoh H, Ozato K, Tamura T, et al. IRF8 Is a Critical Transcription Factor for Transforming Microglia into a Reactive Phenotype. Cell Rep 2012; 1: 334–40.

Mathern DR, Heeger PS. Molecules Great and Small: The Complement System. Clin J Am Soc Nephrol 2015; 10: 1636–50.

Mawuenyega KG, Sigurdson W, Ovod V, Munsell L, Kasten T, Morris JC, et al. Decreased Clearance of CNS Amyloid-β in Alzheimer's Disease. Science 2010; 330: 1774.

McCarthy KD, De Vellis J. Preparation of separate astroglial and oligodendroglial cell cultures from rat cerebral tissue. J Cell Biol 1980; 85: 890–902.

McFarland KN, Ceballos C, Rosario A, Ladd T, Moore B, Golde G, et al. Microglia show differential transcriptomic response to Aβ peptide aggregates ex vivo and in vivo. Life Sci Alliance 2021; 4

McKhann G, Drachman D, Folstein M, Katzman R, Price D, Stadlan EM. Clinical diagnosis of Alzheimer's disease. Neurology 1984; 34: 939–939.

Mecocci P, Parnetti L, Romano G, Scarelli A, Chionne F, Cecchetti R, et al. Serum anti-GFAP and anti-S100 autoantibodies in brain aging, Alzheimer's disease and vascular dementia. J Neuroimmunol 1995; 57: 165–70.

Meda L, Baron P, Prat E, Scarpini E, Scarlato G, Cassatella MA, et al. Proinflammatory profile of cytokine production by human monocytes and murine microglia stimulated with β-amyloid[25–35]. J Neuroimmunol 1999; 93: 45–52.

Meda L, Cassatella MA, Szendrei GI, Otvos L, Baron P, Villalba M, et al. Activation of microglial cells by β-amyloid protein and interferon-γ. Nat 1995 3746523 1995; 374: 647–50.

Medeiros R, Kitazawa M, Passos GF, Baglietto-Vargas D, Cheng D, Cribbs DH, et al. Aspirin-Triggered Lipoxin A4 Stimulates Alternative Activation of Microglia and Reduces Alzheimer Disease?Like Pathology in Mice. Am J Pathol 2013; 182: 1780–9.

Merlini M, Rafalski VA, Rios Coronado PE, Gill TM, Ellisman M, Muthukumar G, et al. Fibrinogen Induces Microglia-Mediated Spine Elimination and Cognitive Impairment in an Alzheimer's Disease Model. Neuron 2019; 101: 1099-1108.e6.

Minter MR, Taylor JM, Crack PJ. The contribution of neuroinflammation to amyloid toxicity in Alzheimer's disease. J Neurochem 2016; 136: 457–74.

Mirra SS, Heyman A, McKeel D, Sumi SM, Crain BJ, Brownlee LM, et al. The Consortium to Establish a Registry for Alzheimer's Disease (CERAD). Neurology 1991; 41: 479–479.

Miyakawa T, Shimoji A, Kuramoto R, Higuchi Y. The relationship between senile plaques and cerebral blood vessels in Alzheimer's disease and senile dementia. Virchows Arch B 1982 401 1982; 40: 121–9.

Moore Z, Taylor JM, Crack PJ. The involvement of microglia in Alzheimer's disease: a new dog in the fight. Br J Pharmacol 2019; 176: 3533–43.

Morin NA, Oakes PW, Hyun YM, Lee D, Chin EY, King MR, et al. Nonmuscle myosin heavy chain IIA mediates integrin LFA-1 de-adhesion during T lymphocyte migration. J Exp Med 2008; 205: 195–205.

Morris JC, Roe CM, Grant EA, Head D, Storandt M, Goate AM, et al. Pittsburgh Compound B Imaging and Prediction of Progression From Cognitive Normality to Symptomatic Alzheimer Disease. Arch Neurol 2009; 66: 1469–75.

Mungarro-Menchaca X, Morán PFJ, Clorinda A. β-Amyloid peptide induces ultrastructural changes in synaptosomes and potentiates mitochondrial dysfunction in the presence of ryanodine. J Neurosci Res 2002; 68: 89–96.

Naj AC, Jun G, Beecham GW, Wang L-S, Vardarajan BN, Buros J, et al. Common variants in MS4A4/MS4A6E, CD2uAP, CD33, and EPHA1 are associated with late-onset Alzheimer's disease. Nat Genet 2011; 43: 436.

Nakamura Y, Si QS, Kataoka K. Lipopolysaccharide-induced microglial activation in culture: temporal profiles of morphological change and release of cytokines and nitric oxide. Neurosci Res 1999; 35: 95–100.

Neumann H, Schweigreiter R, Yamashita T, Rosenkranz K, Wekerle H, Barde YA. Tumor necrosis factor inhibits neurite outgrowth and branching of hippocampal neurons by a rho-dependent mechanism. J Neurosci 2002; 22: 854–62.

Nishida N, Xie C, Shimaoka M, Cheng Y, Walz T, Springer TA. Activation of Leukocyte β2 Integrins by Conversion from Bent to Extended Conformations. Immunity 2006; 25: 583–94.

Norling L V., Dalli J, Flower RJ, Serhan CN, Perretti M. Resolvin D1 limits polymorphonuclear leukocyte recruitment to inflammatory loci: Receptor-dependent actions. Arterioscler Thromb Vasc Biol 2012; 32: 1970–8.

O'Brien RJ, Wong PC. Amyloid Precursor Protein Processing and Alzheimer's Disease. http://dx.doi.org/101146/annurev-neuro-061010-113613 2011; 34: 185–204.

Oakley H, Cole SL, Logan S, Maus E, Shao P, Craft J, et al. Intraneuronal β-Amyloid Aggregates, Neurodegeneration, and Neuron Loss in Transgenic Mice with Five Familial Alzheimer's Disease Mutations: Potential Factors in Amyloid Plaque Formation. J Neurosci 2006; 26: 10129–40.

Oberheim NA, Goldman SA, Nedergaard M. Heterogeneity of Astrocytic Form and Function. Methods Mol Biol 2012; 814: 23.

Oddo S, Caccamo A, Kitazawa M, Tseng BP, LaFerla FM. Amyloid deposition precedes tangle formation in a triple transgenic model of Alzheimer's disease. Neurobiol Aging 2003; 24: 1063–70.

Oddo S, Caccamo A, Shepherd JD, Murphy MP, Golde TE, Kayed R, et al. Triple-Transgenic

Model of Alzheimer's Disease with Plaques and Tangles. Neuron 2003; 39: 409–21.

Olabarria M, Noristani HN, Verkhratsky A, Rodríguez JJ. Concomitant astroglial atrophy and astrogliosis in a triple transgenic animal model of Alzheimer's disease. Glia 2010; 58: 831–8.

Olah M, Biber K, Vinet J, W.G.M. Boddeke H. Microglia Phenotype Diversity. CNS Neurol Disord - Drug Targets 2011; 10: 108–18.

Oliver DMA, Reddy PH. Small Molecules as Therapeutic Drugs for Alzheimer'sDisease. Mol Cell Neurosci 2019; 96: 47.

Ortiz-Sanz C, Gaminde-Blasco A, Valero J, Bakota L, Brandt R, Zugaza JL, et al. Early Effects of Aβ Oligomers on Dendritic Spine Dynamics and Arborization in Hippocampal Neurons. Front Synaptic Neurosci 2020; 12: 2.

Ou Z, Kong X, Sun X, He X, Zhang L, Gong Z, et al. Metformin treatment prevents amyloid plaque deposition and memory impairment in APP/PS1 mice. Brain Behav Immun 2018; 69: 351–63.

Paasila PJ, Davies DS, Kril JJ, Goldsbury C, Sutherland GT. The relationship between the morphological subtypes of microglia and Alzheimer's disease neuropathology. Brain Pathol 2019; 29: 726–40.

Pan X, Zhu Y, Lin N, Zhang J, Ye Q, Huang H, et al. Microglial phagocytosis induced by fibrillar β-amyloid is attenuated by oligomeric β-amyloid: implications for Alzheimer's disease. Mol Neurodegener 2011; 6: 45.

Parajuli B, Sonobe Y, Horiuchi H, Takeuchi H, Mizuno T, Suzumura A. Oligomeric amyloid β induces IL-1β processing via production of ROS: implication in Alzheimer's disease. Cell Death Dis 2013 412 2013; 4: e975–e975.

Park J, Wetzel I, Marriott I, Dréau D, D'Avanzo C, Kim DY, et al. A 3D human triculture system modeling neurodegeneration and neuroinflammation in Alzheimer's disease. Nat Neurosci 2018 217 2018; 21: 941–51.

Parmley LA, Elkins ND, Fini MA, Liu YE, Repine JE, Wright RM. α-4/β-1 and α-L/β-2 integrins mediate cytokine induced lung leukocyte-epithelial adhesion and injury. Br J Pharmacol 2007; 152: 915–29.

Pascoal TA, Benedet AL, Ashton NJ, Kang MS, Therriault J, Chamoun M, et al. Microglial activation and tau propagate jointly across Braak stages. Nat Med 2021 279 2021; 27: 1592–9.

Patel MK, Riley MA, Hobbs S, Cortez-Cooper M, Robinson VJB. Can α-lipoic acid mitigate progression of aging-related decline caused by oxidative stress? South Med J 2014; 107: 780–7.

Perea G, Navarrete M, Araque A. Tripartite synapses: astrocytes process and control synaptic information. Trends Neurosci 2009; 32: 421–31.

Perez-Nievas BG, Serrano-Pozo A. Deciphering the astrocyte reaction in Alzheimer's disease. Front Aging Neurosci 2018; 10: 114.

Pike CJ, Walencewicz AJ, Glabe CG, Cotman CW. In vitro aging of ß-amyloid protein causes peptide aggregation and neurotoxicity. Brain Res 1991; 563: 311–4.

Plescher M, Seifert G, Hansen JN, Bedner P, Steinhäuser C, Halle A. Plaque-dependent morphological and electrophysiological heterogeneity of microglia in an Alzheimer's disease mouse model. Glia 2018; 66: 1464–80.

Pocernich CB, Butterfield DA. Elevation of glutathione as a therapeutic strategy in Alzheimer disease. Biochim Biophys Acta - Mol Basis Dis 2012; 1822: 625–30.

Possel H, Noack H, Jo¨ J, Putzke J, Wolf G, Sies H. Selective Upregulation of Inducible Nitric Oxide Synthase (iNOS) by Lipopolysaccharide (LPS) and Cytokines in Microglia: In Vitro and In Vivo Studies. 2000

Potter H, Woodcock JH, Boyd TD, Coughlan CM, O'Shaughnessy JR, Borges MT, et al. Safety and efficacy of sargramostim (GM-CSF) in the treatment of Alzheimer's disease. Alzheimer's Dement Transl Res Clin Interv 2021; 7: e12158.

Prieto P, Cuenca J, Través PG, Fernández-Velasco M, Martín-Sanz P, Boscá L. Lipoxin A4 impairment of apoptotic signaling in macrophages: implication of the PI3K/Akt and the ERK/Nrf-2 defense pathways. Cell Death Differ 2010 177 2010; 17: 1179–88.

Reines SA, Block GA, Morris JC, Liu G, Nessly ML, Lines CR, et al. Rofecoxib. Neurology 2004; 62: 66–71.

Reis J, Massari M, Marchese S, Ceccon M, Aalbers FS, Corana F, et al. A closer look into NADPH oxidase inhibitors: Validation and insight into their mechanism of action. Redox Biol 2020; 32: 101466.

Ricklin D, Hajishengallis G, Yang K, Lambris JD. Complement: a key system for immune surveillance and homeostasis. Nat Immunol 2010; 11: 785.

Rogers J, Cooper NR, Webster S, Schultz J, McGeer PL, Styren SD, et al. Complement activation by beta-amyloid in Alzheimer disease. Proc Natl Acad Sci 1992; 89: 10016–20.

Romano M, Cianci E, Simiele F, Recchiuti A. Lipoxins and aspirin-triggered lipoxins in resolution of inflammation. Eur J Pharmacol 2015; 760: 49–63.

Ross GD. Role of the lectin domain of Mac-1/CR3 (CD11b/CD18) in regulating intercellular adhesion. Immunol Res 2002; 25: 219–27.

Roy A, Jana A, Yatish K, Freidt MB, Fung YK, Martinson JA, et al. Reactive oxygen species up-regulate CD11b in microglia via nitric oxide: Implications for neurodegenerative diseases. Free Radic Biol Med 2008; 45: 686–99.

Rubio-Perez JM, Morillas-Ruiz JM. A review: Inflammatory process in Alzheimer's disease, role of cytokines. Sci World J 2012; 2012

Rui Y, Tiwari P, Xie Z, Zheng JQ. Acute Impairment of Mitochondrial Trafficking by β-Amyloid Peptides in Hippocampal Neurons. J Neurosci 2006; 26: 10480.

Ryan DA, Narrow WC, Federoff HJ, Bowers WJ. An Improved Method for Generating Consistent Soluble Amyloid-beta Oligomer Preparations for In Vitro Neurotoxicity Studies. J Neurosci Methods 2010; 190: 171.

Salas A, Shimaoka M, Kogan AN, Harwood C, Von Andrian UH, Springer TA. Rolling Adhesion through an Extended Conformation of Integrin αLβ2 and Relation to α I and β I-like Domain Interaction. Immunity 2004; 20: 393–406.

Salih DA, Bayram S, Guelfi S, Reynolds RH, Shoai M, Ryten M, et al. Genetic variability in response to amyloid beta deposition influences Alzheimer's disease risk. Brain Commun 2019; 1

Saresella M, La Rosa F, Piancone F, Zoppis M, Marventano I, Calabrese E, et al. The NLRP3 and NLRP1 inflammasomes are activated in Alzheimer's disease. Mol Neurodegener 2016; 11: 1–14.

Sasmita AO. Current viral-mediated gene transfer research for treatment of Alzheimer's disease. https://doi.org/101080/0264872520181523521 2018; 35: 26–45.

Sastre J, Pallardó F V., Viña J. The role of mitochondrial oxidative stress in aging. Free Radic Biol Med 2003; 35: 1–8.

Schafer DP, Lehrman EK, Kautzman AG, Koyama R, Mardinly AR, Yamasaki R, et al. Microglia Sculpt Postnatal Neural Circuits in an Activity and Complement-Dependent Manner. Neuron 2012; 74: 691–705.

Scheff SW, Price DA, Schmitt FA, Dekosky ST, Mufson EJ. Synaptic alterations in CA1 in mild Alzheimer disease and mild cognitive impairment. Neurology 2007; 68: 1501–8.

Schelle J, Häsler LM, Göpfert JC, Joos TO, Vanderstichele H, Stoops E, et al. Prevention of tau increase in cerebrospinal fluid of APP transgenic mice suggests downstream effect of BACE1 inhibition. Alzheimer's Dement 2017; 13: 701–9.

Scheuner D, Eckman C, Jensen M, Song X, Citron M, Suzuki N, et al. Secreted amyloid β–protein similar to that in the senile plaques of Alzheimer's disease is increased in vivo by the presenilin 1 and 2 and APP mutations linked to familial Alzheimer's disease. Nat Med 1996 28 1996; 2: 864–70.

Schmid CD, Melchior B, Masek K, Puntambekar SS, Danielson PE, Lo DD, et al. Differential gene expression in LPS/IFNγ activated microglia and macrophages: In vitro versus in vivo. In: Journal of Neurochemistry. John Wiley & Sons, Ltd; 2009. p. 117–25

Schürpf T, Springer TA. Regulation of integrin affinity on cell surfaces. EMBO J 2011; 30: 4712–27.

Selkoe DJ. The molecular pathology of Alzheimer's disease. Neuron 1991; 6: 487–98.

Selkoe DJ, Hardy J. The amyloid hypothesis of Alzheimer's disease at 25 years. EMBO Mol Med 2016; 8: 595–608.

Sengeløv H, Kjeldsen L, Diamond MS, Springer TA, Borregaard N. Subcellular localization and

dynamics of Mac-1 (alpha m beta 2) in human neutrophils. J Clin Invest 1993; 92: 1467.

Serhan CN, Chiang N, Dalli J, Levy BD. Lipid Mediators in the Resolution of Inflammation. Cold Spring Harb Perspect Biol 2015; 7: a016311.

Serhan CN, Jain A, Marleau S, Clish C, Kantarci A, Behbehani B, et al. Reduced Inflammation and Tissue Damage in Transgenic Rabbits Overexpressing 15-Lipoxygenase and Endogenous Anti-inflammatory Lipid Mediators. J Immunol 2003; 171: 6856–65.

Serrano-Pozo A, Mielke ML, Gómez-Isla T, Betensky RA, Growdon JH, Frosch MP, et al. Reactive Glia not only Associates with Plaques but also Parallels Tangles in Alzheimer's Disease. Am J Pathol 2011; 179: 1373–84.

Sevigny J, Chiao P, Bussière T, Weinreb PH, Williams L, Maier M, et al. The antibody aducanumab reduces Aβ plaques in Alzheimer's disease. Nat 2016 5377618 2016; 537: 50–6.

Shahidehpour RK, Higdon RE, Crawford NG, Neltner JH, Ighodaro ET, Patel E, et al. Dystrophic microglia are associated with neurodegenerative disease and not healthy aging in the human brain. Neurobiol Aging 2021; 99: 19–27.

Shankar GM, Bloodgood BL, Townsend M, Walsh DM, Selkoe DJ, Sabatini BL. Natural Oligomers of the Alzheimer Amyloid-β Protein Induce Reversible Synapse Loss by Modulating an NMDA-Type Glutamate Receptor-Dependent Signaling Pathway. J Neurosci 2007; 27: 2866–75.

Shelat PB, Chalimoniuk M, Wang JH, Strosznajder JB, Lee JC, Sun AY, et al. Amyloid beta peptide and NMDA induce ROS from NADPH oxidase and AA release from cytosolic phospholipase A2 in cortical neurons. J Neurochem 2008; 106: 45–55.

Shen Y, Li R, McGeer EG, McGeer PL. Neuronal expression of mRNAs for complement proteins of the classical pathway in Alzheimer brain. Brain Res 1997; 769: 391–5.

Shi Q, Chowdhury S, Ma R, Le KX, Hong S, Caldarone BJ, et al. Complement C3 deficiency protects against neurodegeneration in aged plaque-rich APP/PS1 mice. Sci Transl Med 2017; 9

Shi Q, Colodner KJ, Matousek SB, Merry K, Hong S, Kenison JE, et al. Complement C3-Deficient Mice Fail to Display Age-Related Hippocampal Decline. J Neurosci 2015; 35: 13029–42.

Shimaoka M, Salas A, Yang W, Weitz-Schmidt G, Springer TA. Small Molecule Integrin Antagonists that Bind to the β2 Subunit I-like Domain and Activate Signals in One Direction and Block Them in the Other. Immunity 2003; 19: 391–402.

Shimohama S, Tanino H, Kawakami N, Okamura N, Kodama H, Yamaguchi T, et al. Activation of NADPH Oxidase in Alzheimer's Disease Brains. Biochem Biophys Res Commun 2000; 273: 5–9.

Shinohara M, Mirakaj V, Serhan CN. Functional metabolomics reveals novel active products in the DHA metabolome. Front Immunol 2012; 3: 81.

Shukla AK, McIntyre LL, Marsh SE, Schneider CA, Hoover EM, Walsh CM, et al. CD11a expression distinguishes infiltrating myeloid cells from plaque-associated microglia in Alzheimer's

disease. Glia 2019; 67: 844–56.

Simpson DSA, Oliver PL. ROS Generation in Microglia: Understanding Oxidative Stress and Inflammation in Neurodegenerative Disease. Antioxidants 2020, Vol 9, Page 743 2020; 9: 743.

Simpson JE, Ince PG, Lace G, Forster G, Shaw PJ, Matthews F, et al. Astrocyte phenotype in relation to Alzheimer-type pathology in the ageing brain. Neurobiol Aging 2010; 31: 578–90.

Sims R, van der Lee SJ, Naj AC, Bellenguez C, Badarinarayan N, Jakobsdottir J, et al. Rare coding variants in PLCG2, ABI3, and TREM2 implicate microglial-mediated innate immunity in Alzheimer's disease. Nat Genet 2017 499 2017; 49: 1373–84.

Spangenberg EE, Green KN. Inflammation in Alzheimer's disease: Lessons learned from microglia-depletion models. Brain Behav Immun 2016

Spangenberg EE, Lee RJ, Najafi AR, Rice RA, Elmore MRP, Blurton-Jones M, et al. Eliminating microglia in Alzheimer's mice prevents neuronal loss without modulating amyloid-β pathology. Brain 2016; 139: 1265.

Stephan AH, Madison D V, Mateos JM, Fraser DA, Lovelett EA, Coutellier L, et al. A dramatic increase of C1q protein in the CNS during normal aging. J Neurosci 2013; 33: 13460–74.

Stewart PA, Hayakawa K, Akers MA, Vinters H V. A morphometric study of the blood-brain barrier in Alzheimer's disease. Lab Invest 1992; 67: 734–42.

Stoppini L, Buchs PA, Muller D. A simple method for organotypic cultures of nervous tissue. J Neurosci Methods 1991; 37: 173–82.

Strassnig M, Ganguli M. About a Peculiar Disease of the Cerebral Cortex: Alzheimer's Original Case Revisited. Psychiatry (Edgmont) 2005; 2: 30.

Suzuki N, Cheung TT, Cai XD, Odaka A, Otvos L, Eckman C, et al. An Increased Percentage of Long Amyloid β Protein Secreted by Familial Amyloid β Protein Precursor (βApp717) Mutants. Science (80-) 1994; 264: 1336–40.

Svensson CI, Zattoni M, Serhan CN. Lipoxins and aspirin-triggered lipoxin inhibit inflammatory pain processing. J Exp Med 2007; 204: 245–52.

Swardfager W, Lanctt K, Rothenburg L, Wong A, Cappell J, Herrmann N. A Meta-Analysis of Cytokines in Alzheimer's Disease. Biol Psychiatry 2010; 68: 930–41.

Sze CI, Troncoso JC, Kawas C, Mouton P, Price DL, Martin LJ. Loss of the Presynaptic Vesicle Protein Synaptophysin in Hippocampus Correlates with Cognitive Decline in Alzheimer Disease. J Neuropathol Exp Neurol 1997; 56: 933–44.

Takahashi RH, Capetillo-Zarate E, Lin MT, Milner TA, Gouras GK. Co-occurrence of Alzheimer's disease β-amyloid and tau pathologies at synapses. Neurobiol Aging 2010; 31: 1145.

Tammariello SP, Quinn MT, Estus S. t NADPH Oxidase Contributes Directly to Oxidative Stress and Apoptosis in Nerve Growth Factor-Deprived Sympathetic Neurons. J Neurosci 2000; 20:

RC53–RC53.

Taylor SE, Morganti-Kossmann C, Lifshitz J, Ziebell JM. Rod Microglia: A Morphological Definition. PLoS One 2014; 9: e97096.

Thal DR, Rüb U, Orantes M, Braak H. Phases of Aβ-deposition in the human brain and its relevance for the development of AD. Neurology 2002; 58: 1791–800.

Tiberi M, Chiurchiù V. Specialized Pro-resolving Lipid Mediators and Glial Cells: Emerging Candidates for Brain Homeostasis and Repair. Front Cell Neurosci 2021; 15: 136.

Tobin DM, Roca FJ, Oh SF, McFarland R, Vickery TW, Ray JP, et al. Host Genotype-Specific Therapies Can Optimize the Inflammatory Response to Mycobacterial Infections. Cell 2012; 148: 434–46.

Tong L, Balazs R, Soiampornkul R, Thangnipon W, Cotman CW. Interleukin-1 beta impairs brain derived neurotrophic factor-induced signal transduction. Neurobiol Aging 2008; 29: 1380–93.

Tu S, Okamoto S ichi, Lipton SA, Xu H. Oligomeric Aβ-induced synaptic dysfunction in Alzheimer's disease. Mol Neurodegener 2014; 9: 48.

Vasek MJ, Garber C, Dorsey D, Durrant DM, Bollman B, Soung A, et al. A complement–microglial axis drives synapse loss during virus-induced memory impairment. Nat 2016 5347608 2016; 534: 538–43.

Vehmas AK, Kawas CH, Stewart WF, Troncoso JC. Immune reactive cells in senile plaques and cognitive decline in Alzheimer's disease. Neurobiol Aging 2003; 24: 321–31.

Venegas C, Heneka MT. Inflammasome-mediated innate immunity in Alzheimer's disease. FASEB J 2019; 33: 13075–84.

Vinters H V., Secor DL, Read SL, Frazee JG, Tomiyasu U, Stanley TM, et al. Microvasculature in Brain Biopsy Specimens from Patients with Alzheimer's Disease: An Immunohistochemical and Ultrastructural Study. Ultrastruct Pathol 2009; 18: 333–48.

Vorup-Jensen T, Jensen RK. Structural immunology of complement receptors 3 and 4. Front Immunol 2018; 9

Walker DG, McGeer PL. Complement gene expression in human brain: comparison between normal and Alzheimer disease cases. Mol Brain Res 1992; 14: 109–16.

Wang SW, Wang YJ, Su YJ, Zhou WW, Yang SG, Zhang R, et al. Rutin inhibits β-amyloid aggregation and cytotoxicity, attenuates oxidative stress, and decreases the production of nitric oxide and proinflammatory cytokines. Neurotoxicology 2012; 33: 482–90.

Wang X, Miao Z, Xu X, Schultzberg M, Zhao Y. Reduced Levels of Plasma Lipoxin A4 Are Associated with Post-Stroke Cognitive Impairment. J Alzheimer's Dis 2021; 79: 607–13.

Wang X, Puerta E, Cedazo-Minguez A, Hjorth E, Schultzberg M. Insufficient Resolution Response in the Hippocampus of a Senescence-Accelerated Mouse Model — SAMP8. J Mol Neurosci 2015;

55: 396–405.

Wang X, Su B, Lee HG, Li X, Perry G, Smith MA, et al. Impaired Balance of Mitochondrial Fission and Fusion in Alzheimer's Disease. J Neurosci 2009; 29: 9090.

Wang X, Su B, Siedlak SL, Moreira PI, Fujioka H, Wang Y, et al. Amyloid-β overproduction causes abnormal mitochondrial dynamics via differential modulation of mitochondrial fission/fusion proteins. Proc Natl Acad Sci 2008; 105: 19318–23.

Wang X, Zhu M, Hjorth E, Cortés-Toro V, Eyjolfsdottir H, Graff C, et al. Resolution of inflammation is altered in Alzheimer's disease. Alzheimer's Dement 2015; 11: 40-50.e2.

Wang YP, Wu Y, Li LY, Zheng J, Liu RG, Zhou JP, et al. Aspirin-triggered lipoxin A4attenuates LPS-induced pro-inflammatory responses by inhibiting activation of NF-κB and MAPKs in BV-2 microglial cells. J Neuroinflammation 2011; 8

Weldon DT, Rogers SD, Ghilardi JR, Finke MP, Cleary JP, O'Hare E, et al. Fibrillar β-Amyloid Induces Microglial Phagocytosis, Expression of Inducible Nitric Oxide Synthase, and Loss of a Select Population of Neurons in the Rat CNS In Vivo. J Neurosci 1998; 18: 2161–73.

Welzenbach K, Hommel U, Weitz-Schmid G. Small Molecule Inhibitors Induce Conformational Changes in the I Domain and the I-like Domain of Lymphocyte Function-associated Antigen-1: MOLECULAR INSIGHTS INTO INTEGRIN INHIBITION. J Biol Chem 2002; 277: 10590–8.

Wenzel TJ, Klegeris A. Novel multi-target directed ligand-based strategies for reducing neuroinflammation in Alzheimer's disease. Life Sci 2018; 207: 314–22.

Westergard T, Rothstein JD. Astrocyte Diversity: Current Insights and Future Directions. Neurochem Res 2020; 45: 1298–305.

White JA, Manelli AM, Holmberg KH, Van Eldik LJ, LaDu MJ. Differential effects of oligomeric and fibrillar amyloid-β1–42 on astrocyte-mediated inflammation. Neurobiol Dis 2005; 18: 459–65.

Whittington RA, Planel E, Terrando N. Impaired Resolution of Inflammation in Alzheimer's Disease: A Review. Front Immunol 2017; 8: 1464.

Wierzba-Bobrowicz T, Gwiazda E, Kosno-Kruszewska E, Lewandowska E, Lechowicz W, Bertrand E, et al. Morphological analysis of active microglia--rod and ramified microglia in human brains affected by some neurological diseases (SSPE, Alzheimer's disease and Wilson's disease). Folia Neuropathol 2002; 40: 125–31.

Wilson ZS, Ahn LB, Serratelli WS, Belley MD, Lomas-Neira J, Sen M, et al. Activated β2 integrins restrict neutrophil recruitment during murine acute pseudomonal pneumonia. Am J Respir Cell Mol Biol 2017; 56: 620–7.

Wu J, Ding D, Wang X, Li Q, Sun Y, Li L, et al. Regulation of aquaporin 4 expression by lipoxin A4 in astrocytes stimulated by lipopolysaccharide. Cell Immunol 2019; 344: 103959.

Wu J, Wang A, Min Z, Xiong Y, Yan Q, Zhang J, et al. Lipoxin A4 inhibits the production of proinflammatory cytokines induced by β-amyloid in vitro and in vivo. Biochem Biophys Res

Commun 2011; 408: 382–7.

Wu L, Miao S, Zou LB, Wu P, Hao H, Tang K, et al. Lipoxin A 4 inhibits 5-lipoxygenase translocation and leukotrienes biosynthesis to exert a neuroprotective effect in cerebral ischemia/reperfusion injury. J Mol Neurosci 2012; 48: 185–200.

Wu Y, Zhai H, Wang Y, Li L, Wu J, Wang F, et al. Aspirin-triggered lipoxin A 4 attenuates lipopolysaccharide- induced intracellular ROS in BV2 microglia cells by inhibiting the function of NADPH oxidase. Neurochem Res 2012; 37: 1690–6.

Wyatt-Johnson SK, Herr SA, Brewster AL. Status epilepticus triggers time-dependent alterations in microglia abundance and morphological phenotypes in the hippocampus. Front Neurol 2017; 8: 700.

Wyss-Coray T, Loike JD, Brionne TC, Lu E, Anankov R, Yan F, et al. Adult mouse astrocytes degrade amyloid-β in vitro and in situ. Nat Med 2003 94 2003; 9: 453–7.

Wyss-Coray T, Yan F, Lin AHT, Lambris JD, Alexander JJ, Quigg RJ, et al. Prominent neurodegeneration and increased plaque formation in complement-inhibited Alzheimer's mice. Proc Natl Acad Sci 2002; 99: 10837–42.

Wyssenbach A, Quintela T, Llavero F, Zugaza JL, Matute C, Alberdi E. Amyloid β-induced astrogliosis is mediated by β1-integrin via NADPH oxidase 2 in Alzheimer's disease. Aging Cell 2016; 15: 1140–52.

Xin D, Quan R, Zeng L, Xu C, Tang Y. Lipoxin A4 protects rat skin flaps against ischemia-reperfusion injury through inhibiting cell apoptosis and inflammatory response induced by endoplasmic reticulum stress. Ann Transl Med 2020; 8: 1086–1086.

Xu F, Xu Y, Zhu L, Rao P, Wen J, Sang Y, et al. Fasudil inhibits LPS-induced migration of retinal microglial cells via regulating p38-MAPK signaling pathway. Mol Vis 2016; 22: 836–46.

Xu YJ, Mei Y, Qu ZL, Zhang SJ, Zhao W, Fang JS, et al. Ligustilide Ameliorates Memory Deficiency in APP/PS1 Transgenic Mice via Restoring Mitochondrial Dysfunction. Biomed Res Int 2018; 2018

Yang D, Elner SG, Bian ZM, Till GO, Petty HR, Elner VM. Pro-inflammatory Cytokines Increase Reactive Oxygen Species through Mitochondria and NADPH Oxidase in Cultured RPE Cells. Exp Eye Res 2007; 85: 462.

Yang W, Carman C V., Kim M, Salas A, Shimaoka M, Springer TA. A Small Molecule Agonist of an Integrin, αLβ2. J Biol Chem 2006; 281: 37904–12.

Yao C, Yang D, Wan Z, Wang Z, Liu R, Wu Y, et al. Aspirin-triggered lipoxin A4 attenuates lipopolysaccharide induced inflammatory response in primary astrocytes. Int Immunopharmacol 2014; 18: 85–9.

Yao J, Irwin RW, Zhao L, Nilsen J, Hamilton RT, Brinton RD. Mitochondrial bioenergetic deficit precedes Alzheimer's pathology in female mouse model of Alzheimer's disease. Proc Natl Acad

Sci 2009; 106: 14670–5.

Yasojima K, Schwab C, McGeer EG, McGeer PL. Up-Regulated Production and Activation of the Complement System in Alzheimer's Disease Brain. Am J Pathol 1999; 154: 927.

Yiannopoulou KG, Anastasiou AI, Zachariou V, Pelidou SH. Reasons for Failed Trials of Disease-Modifying Treatments for Alzheimer Disease and Their Contribution in Recent Research. Biomedicines 2019; 7

Yiannopoulou KG, Papageorgiou SG. Current and Future Treatments in Alzheimer Disease: An Update. J Cent Nerv Syst Dis 2020; 12: 1179573520907397.

Yin KJ, Cirrito JR, Yan P, Hu X, Xiao Q, Pan X, et al. Matrix metalloproteinases expressed by astrocytes mediate extracellular amyloid-β peptide catabolism. J Neurosci 2006; 26: 10939–48.

Yoon JJ, Nicholson LFB, Feng SX, Vis JC, Green CR. A novel method of organotypic brain slice culture using connexin-specific antisense oligodeoxynucleotides to improve neuronal survival. Brain Res 2010; 1353: 194–203.

Yoshiyama Y, Higuchi M, Zhang B, Huang SM, Iwata N, Saido TCC, et al. Synapse Loss and Microglial Activation Precede Tangles in a P301S Tauopathy Mouse Model. Neuron 2007; 53: 337–51.

Young-Pearse TL, Bai J, Chang R, Zheng JB, Loturco JJ, Selkoe DJ. A Critical Function for β-Amyloid Precursor Protein in Neuronal Migration Revealed by In Utero RNA Interference. J Neurosci 2007; 27: 14459–69.

Zafrilla P, Mulero J, Xandri JM, Santo E, Caravaca G, Morillas JM. Oxidative Stress in Alzheimer Patients in Different Stages of the Disease. Res Pract Alzheimers Dis 2007; 12: 82–7.

Zhang C, Rodriguez C, Spaulding J, Aw TY, Feng J. Age-Dependent and Tissue-Related Glutathione Redox Status in a Mouse Model of Alzheimer's Disease. J Alzheimers Dis 2012; 28: 655.

Zhang D, Hu X, Qian L, Chen S-H, Zhou H, Wilson B, et al. Microglial MAC1 receptor and PI3K are essential in mediating β-amyloid peptide-induced microglial activation and subsequent neurotoxicity. J Neuroinflammation 2011; 8: 3.

Zhang SC, Fedoroff S. Neuron-microglia interactions in vitro. Acta Neuropathol 1996; 91: 385–95.

Zhang W, Dallas S, Zhang D, Guo J-P, Pang H, Wilson B, et al. Microglial PHOX and Mac-1 are essential to the enhanced dopaminergic neurodegeneration elicited by A30P and A53T mutant alpha-synuclein. Glia 2007; 55: 1178–88.

Zhao J, Geng W, Wan K, Guo K, Xi F, Xu X, et al. Lipoxin A4 promotes autophagy and inhibits overactivation of macrophage inflammasome activity induced by Pg LPS. J Int Med Res 2021; 49: 1–14.

Zheng J yu, Sun J, Ji C mei, Shen L, Chen Z jun, Xie P, et al. Selective deletion of apolipoprotein

E in astrocytes ameliorates the spatial learning and memory deficits in Alzheimer's disease (APP/PS1) mice by inhibiting TGF-β/Smad2/STAT3 signaling. Neurobiol Aging 2017; 54: 112–32.

Zheng Y-F, Zhou X, Chang D, Bhuyan DJ, Zhang JP, Yu W-Z, et al. A novel tri-culture model for neuroinflammation. J Neurochem 2021; 156: 249–61.

Zhou B, Zuo YX, Jiang RT. Astrocyte morphology: Diversity, plasticity, and role in neurological diseases. CNS Neurosci Ther 2019; 25: 665–73.

Zhou Y, You H, Zhang A, Jiang X, Pu Z, Xu G, et al. Lipoxin A4 attenuates uric acid-activated, NADPH oxidase-dependent oxidative stress by interfering with translocation of p47phox in human umbilical vein endothelial cells. Exp Ther Med 2020; 20: 1682–92.

Zhu M, Wang X, Hjorth E, Colas RA, Schroeder L, Granholm AC, et al. Pro-Resolving Lipid Mediators Improve Neuronal Survival and Increase Aβ42 Phagocytosis. Mol Neurobiol 2016; 53: 2733–49.

Zujovic V, Jesu´ J, Benavides J, Vigé X, Carter C, Taupin R. Fractalkine Modulates TNF-Secretion and Neurotoxicity Induced by Microglial Activation. Glia 2000; 29: 305–15.

Search of: Suspended, Terminated, Withdrawn Studies | Interventional Studies | Alzheimer Disease - List Results - ClinicalTrials.gov [Internet]. [cited 2022 Jan 17] Available from: https://clinicaltrials.gov/ct2/results?cond=Alzheimer+Disease&recrs=g&recrs=h&recrs=i&age_v=&gndr=&type=Intr&rslt=&Search=Apply